Comparison of Two Vortex-In-Cell Schemes Implemented to a Three Dimensional Temporal Mixing Layer

Nabel Sadek

Thesis submitted to the
Faculty of Graduate and Postdoctoral Studies
in partial fulfillment of the requirements
for the PhD degree in Mechanical Engineering

Department of Mechanical Engineering
Faculty of Engineering
University of Ottawa

Acknowledgments

I offer my sincerest gratitude to my supervisor, Dr. Roger Milane, who has supported me throughout my thesis with his patience and knowledge whilst allowing me the room to work in my own way. One simply could not wish for a friendlier supervisor**.**

I am grateful to my family whose patience and support gave me the strength and persistence to complete this work.

Abstract

Numerical simulations are presented for three dimensional viscous incompressible free shear flows. The numerical method is based on solving the vorticity equation using Vortex-In-Cell method. In this method, the vorticity field is discretized into a finite set of Lagrangian elements (particles) and the computational domain is covered by Eulerian mesh. Velocity field is computed on the mesh by solving Poisson equation. The solution proceeds in time by advecting the particles with the flow. Second order Adam-Bashford method is used for time integration. Exchange of information between Lagrangian particles and Eulerian grid is carried out using the M'_4 interpolation scheme.

The classical inviscid scheme is enhanced to account for stretching and viscous effects. For that matter, two schemes are used. The first one used periodic remeshing of the vortex particles along with fourth order finite difference approximation for the partial derivatives of the stretching and viscous terms. In the second scheme, derivatives are approximated by least squares polynomial. The novelty of this work is signified by using the moving least squares technique within the framework of the Vortex-in-Cell method and implementing it to a three dimensional temporal mixing layer.

Comparisons of the mean flow and velocity statistics are made with experimental studies. The results confirm the validity of the present schemes. Both schemes also demonstrate capability to qualitatively capture significant flow scales, and allow gaining physical insight as to the development of instabilities and the formation of three dimensional vortex structures. The two schemes show acceptable low numerical diffusion as well.

Contents

Acknowledgments i
Abstract ii
Contents iii

Nomenclature vi
Roman Characters vi
Greek Symbols vii
Superscripts viii
Subscripts viii

List of Figures ix

CHAPTER 1 1

Introduction 1
1.1 Overview 1
1.2 Motivations and Objectives 4

CHAPTER 2 ..... ERROR! BOOKMARK NOT DEFINED.

Review of Literature 7
2.1 Introduction 7
2.2 Vortex Methods 9
2.2.1 Characteristics of Vortex Methods 9
2.2.2 Discretization of Vorticity Field 11
2.2.3 Solution of Poisson Equation 13
2.2.4 Desingularization Techniques 15
2.3 Vortex -In-Cell (VIC) Method 18
2.4 Viscous Schemes 22
2.4.1 Random Walk Method 22
2.4.2 Core Spreading Method 24
2.4.3 Particle Strength Exchange (PSE) Method 26
2.4.4 Fishlov Method 29
2.4.5 The Diffusion Velocity Method 30
2.4.6 The Moving Least Square Method 34
2.4.7 Finite Difference Scheme 35
2.3.3 Stretching and Tilting 35
2.5 Spatial Adaptation (Re-Meshing) 40
2.6 Relevant Literature on Vortex Methods 42

CHAPTER 3 47

Formulation and Mathematical Models 47
3.1 Introduction 47

3.2 Vorticity Equation 47
3.3 Vorticity-Velocity Formulation 52
3.4 Vortex Particle Method 53
3.5 Fractional Step Method 56
3.5.1 The Convection Substep 58
3.5.1.1 Interpolation Scheme 59
3.5.1.2 Calculation of Velocity 61
3.5.1.3 Stretching and Tilting 62
3.5.2 The Diffusion Sub-step 63
3.6 The Vorticity Correction 64

CHAPTER 4 67

Validation Tests for the Numerical Method 67
4.1 Introduction 67
4.2 Initial and Boundary Conditions 68
4.3 Development of Mean Flow 71
4.4 Velocity Statistics 74
4.5 Energy Spectra 76
4.6 Development of Vortical Structures 78

CHAPTER 5 81

Finite Difference Approximation with Remeshing 81
5.1 Introduction 81
5.2 Temporally Developing Mixing Layer 82
5.3 Remeshing 82
5.4 Evaluation of Derivatives 84
5.5 Initial and Boundary Conditions 85
5.6 Sequence of Computations over a Time Step 88
5.7 Results 91
5.7.1 Mixing Layer Evolution Parameters 91
5.7.2 Mean Flow and Velocity Statistics 94
5.7.3 Mixing Layer Three Dimensionality 96
5.7.4 Evolution of Instabilities in Three Dimensional Mixing Layers 98
5.7.4.1 Formation of Spanwise Vortices 98
5.7.4.2 Secondary Instability and the Formation of Streamwise Vorticity 100
5.7.5 Energy Spectra 102
5.7.6 Effect of Numerical Parameters 104
5.7.6.1 Mean Streamwise Velocity 105
5.7.6.2 Velocity Statistics 106
5.7.6.3 Power Spectra 107
5.7.7 Inviscid Run 107

CHAPTER 6 110

The Moving Least Square Method 110

6.1 Introduction 110
6.2 Description of the Solution Method 111
6.2.1 Implementation of the Moving Least Squares Method 113
6.2.2 Diffusion Computation 115
6.2.3 Initial and Boundary Conditions 116
6.3 Outline of Algorithm 117
6.4 Results 118
6.4.1 Particle and Filament Presentation 118
6.4.2 Growth Rates 120
6.4.3 Mean Flow and Velocity Statistics 121
6.4.4 Mixing Layer Three Dimensionality 122
6.4.5 Evolution of Instabilities in Three Dimensional Mixing Layers 124
6.4.5.1 Formation of Spanwise Vortices 124
6.4.5.2 Formation of Streamwise Vorticity-The Onset of Three Dimensionality 125
6.4.5.3 Three Dimensional Large Scale Structures 127
6.4.6 Energy Spectra 129
6.4.7 Effect of Numerical Parameters 130
6.4.7.1 Mean Streamwise Velocity 130
6.4.7.2 Velocity Statistics 131
6.4.7.3 Energy Spectra 131
6.4.8 Inviscid Run 132

CHAPTER 7 134

Numerical Performance of the Two Methods 134
7.1 Introduction 134
7.2 Comparison of Growth Parameters and Mean Velocity 135
7.3 Comparison of Velocity Statistics 136
7.4 Comparison of Power Spectra 136
7.5 Comparison of Vorticity Structures 137
7.6 Accuracy 138
7.7 Resolved Scales 141
7.8 CPU Time Comparison 142

CHAPTER 8 144

Summary, Conclusions and Recommendations 144
8.1 Closing Remarks 144
8.2 Two Dimensional Mixing Layer 145
8.3 Three Dimensional Mixing Layer 146
8.3.1 Mean Flow and Velocity Statistics 146
8.3.2 Energy Spectra 147
8.3.3 Spanwise Vortices 148
8.3.4 Streamwise Vortices 148
8.4 Recommendations for Future Work 149
References 151

Nomenclature

Roman Characters

A	Constant
$\vec{a}$, $\vec{b}$	General vector field
a_1, a_2, …	Least squares polynomial coefficients
AC	Autocovariance function
d_x,d_y,d_z	Particle spacing in x,y,z directions, respectively
E	Turbulence kinetic energy
erf	Error function
f	Function, frequency
$\vec{G}$	Green function of Laplace operator
g	Acceleration due to gravity
h_x, h_y, h_z	Grid size in x,y,z directions, respectively
$\vec{K}$	Curl of Green's function
L_x,L_y,L_z	Length of computational domain in x,y,z directions, respectively
M_x,M_y,M_z	Number of grid points in x,y,z directions, respectively
N_p	Number of vortex particles
p	

P_2	Pressure
r	Second order polynomial
Re	Velocity ratio u_1/u_2
RMS	Reynolds number
t	Root mean square
u,v,w	Time
u_{av}	Velocity components in x, y, z directions, respectively
$\vec{u}$	Average streamwise velocity
$\vec{x}$	Velocity vector
x,y,z	Position vector
	Cartesian coordinates

Greek Symbols

α	Particle circulation in two dimensions
$\vec{\alpha}$	Particle strength vector in three dimensions
ω_x, ω_y, ω_z	Vorticity components in x,y,z directions, respectively
$\vec{\omega}$	Vorticity vector
σ	Standard deviation, Spreading parameter of the velocity profile
ν	Kinematic viscosity
ν_{eff}	Effective Viscosity
δ	Vortex core size, Delta Dirac function
ξ	Gaussian random variable
φ	Interpolation kernel

ε_{ijk}	Alternating tensor
ρ	Density
Φ	Vector Potential
γ	Vorticity correction function
θ	Momentum thickness
δ_{ω}	Vorticity thickness
ς	Enstrophy
λ	Wave length

Superscripts

m	Integer exponent
*	Non-dimensionalized parameter
n	Time step

Subscripts

δ	Desingularized function
o	Initial value
i,j,k	Indices in x,y,z directions, respectively
p	Particle value

List of Figures

Fig. 2.1. Explanation of vorticity stretching. 159

Fig. 3.1 One dimensional Example of M'_4 interpolation scheme. 160

Fig. 3.2. 161

One dimensional kernel of M'_4 interpolation scheme. 161

Distribution of M'_4 scheme in two dimensions. 161

Isosurfaces of three dimensional M'_4 interpolation scheme. Fifty equally spaced levels are used. 161

Fig.4.1. Computational domain. 163

Fig.4.2. Profile of mean streamwise velocity. 163

Fig. 4.3. Grid size effect on mean velocity within similarity region. 164

Fig. 4.4. Grid size effect on $y_{0.5}$ 164

Fig. 4.5. Momentum thickness growth and its grid size sensitivity..... 165

Fig. 4.6. Profiles of root mean square streamwise velocity fluctuations. 165

Fig. 4.7. Sensitivity of root mean square streamwise velocity fluctuations to grid size. 166

Fig. 4.8. Profiles of root mean square of cross-stream velocity fluctuations..... 166

Fig. 4.9. Sensitivity of root mean square of cross stream velocity fluctuations to grid size. 167

Fig. 4.10. Profiles of *u'v'* cross-correlation. 167

Fig. 4.11. Sensitivity of *u'v'* cross-correlation to grid size..... 168

Fig. 4.12. Energy spectrum of fully developed two dimensional mixing layer. 168

Fig. 4.13. Sensitivity of energy spectrum to grid size. 169

Fig. 4.14. Initial perturbation of the vortex sheet. 170

Fig. 4.15. Development of instabilities described by particle location. 171

Fig. 4.16. Contour plot of spanwise vorticity, fifty contour levels are used with increment of 0.02, (a) at 14450 time steps, (b) at 15450 time steps. 172

Fig. 5.1. Particles affected by M'_4 remeshing scheme. 173

Fig. 5.2. Initial perturbation of particles. 173

Fig. 5.3. Computational domain of three dimensional temporal mixing layer. 174

Fig. 5.4. Temporal development of momentum thickness 175

Fig. 5.5. Temporal development of vorticity thickness. 175

Fig 5.6. Profiles of mean streamwise velocity. 176

Fig 5.7. Profiles of root mean square streamwise velocity fluctuations. 176

Fig. 5.8. Profiles of root mean square cross stream velocity fluctuations. 177

Fig. 5.9. Profiles of root mean square spanwise velocity fluctuations. 177

Fig. 5.10. Profiles of cross-correlation $u'v'$. 178

Fig. 5.11. Streamwise velocity contours showing flow three dimensionality at four times (a) $t\Delta u/\theta_o$=42.8, (b) $t\Delta u/\theta_o$=63.7, (c) $t\Delta u/\theta_o$=84.4 *and* (d) $t\Delta u/\theta_o$=105.2. Thirty equally distributed contour levels are used between u_{min} and u_{max}. Dotted lines represent negative velocity and continuous lines represent positive velocity 179

Fig. 5.12. Temporal growth of streamwise and spanwise vorticity. 180

Fig. 5.13. Temporal evolution of vorticity divergence. 180

Fig. 5.14. Development of spanwise vorticity contours at the mid spanwise plane z/L_z=0.5 and at five times $t\Delta u/\theta_o$=12.1, (b) $t\Delta u/\theta_o$=27.5, (c) $t\Delta u/\theta_o$=57.3, (d)

$t\Delta u/\theta_o$=87.4, *and* (e) $t\Delta u/\theta_o$=123.8. Ten equally spaced contour levels are used with $0.1\omega_{max}$ increment. 181

Fig. 5.14. For caption see previous page. 182

Fig. 5.15. Projection of velocity vector on x-y plane. Times and locations correspond to that of figure 5.14. 183

Fig. 5.15. For caption see previous page. 184

Fig. 5.16 Streamlines model for the onset of secondary (translative) instability in temporal mixing layer. 185

Fig. 5.17. Particles location at the same time and z plane as in figure 5.14. 186

Fig. 5.18 Streamwise vorticity contours at $t\Delta u/\theta_o$=42.8 and four streamwise locations (a)x/L_x=0.2, (b)x/L_x=0.4 , (c)x/L_x=0.6 , (d)x/L_x=0.8. Twenty equally distributed contour levels with 0.05 $(\omega_{max}- \omega_{min})$ increments are used. Dotted lines represent negative vorticity and continuous lines represent positive vorticity. 188

Fig. 5.19 Streamwise vorticity contours at $t\Delta u/\theta_o$=84.4 and four streamwise locations (a)x/L_x=0.2, (b)x/L_x=0.4 , (c)x/L_x=0.6 , (d)x/L_x=0.8. Twenty equally distributed contour levels with 0.05 $(\omega_{max}- \omega_{min})$ increments are used. Dotted lines represent negative vorticity and continuous lines represent positive vorticity. 189

Fig. 5.20 Streamwise vorticity contours at $t\Delta u/\theta_o$=123.8 and four streamwise locations (a)x/L_x=0.2, (b)x/L_x=0.4 , (c)x/L_x=0.6 , (d)x/L_x=0.8. Twenty equally distributed contour levels with 0.05 $(\omega_{max}- \omega_{min})$ increments are used. Dotted lines represent negative vorticity and continuous lines represent positive vorticity. 190

Fig. 5.21. Isosurfaces of streamwise vorticity at $t\Delta u/\theta_o$=84.4. 191

Fig. 5.22. Vorticity isosurface $\omega_x\theta_o/\Delta u$=0.004 at $t\Delta u/\theta_o$=84.4. 192

Fig. 5.23. velocity vector field (v,w) at $t\Delta u/\theta_o$=42.8 at four streamwise locations (a)x/L_x=0.2, (b)x/L_x=0.4 , (c)x/L_x=0.6 , (d)x/L_x=0.8 193

Fig. 5.24. velocity vector field (v,w) at $t\Delta u/\theta_o$=84.4 at four streamwise locations (a)x/L_x=0.2, (b)x/L_x=0.4 , (c)x/L_x=0.6 , (d)x/L_x=0.8 194

Fig. 5.25. velocity vector field (v,w) at $t\Delta u/\theta_o$=123.8 at four streamwise locations (a)x/L_x=0.2, (b)x/L_x=0.4 , (c)x/L_x=0.6 , (d)x/L_x=0.8 195

Fig. 5.26. Temporal Development of one dimensional streamwise energy spectrum at four times (a) $t\Delta u/\theta_o$=63.7, (b) $t\Delta u/\theta_o$=84.4, (c) $t\Delta u/\theta_o$=105.2, and (d) $t\Delta u/\theta_o$=123.8. Continuous line represents the -5/3 power law. 196

Fig. 5.27. Temporal Development of one dimensional spanwise energy spectrum at four times (a) $t\Delta u/\theta_o$=63.7, (b) $t\Delta u/\theta_o$=84.4, (c) $t\Delta u/\theta_o$=105.2, and (d) $t\Delta u/\theta_o$=123.8.. Continuous line represents the -5/3 power law. 196

Fig. 5.28. Sensitivity of mean velocity profile to grid size at $t\Delta u/\theta_o$=84.4. 197

Fig. 5.29. Sensitivity of root mean square streamwise velocity fluctuations to grid size at $t\Delta u/\theta_o$=84.4. 197

Fig. 5.30. Sensitivity of root mean square cross-stream velocity fluctuations to grid size at $t\Delta u/\theta_o$=84.4. 198

Fig. 5.31. Sensitivity of root mean square spanwise velocity fluctuations to grid size at $t\Delta u/\theta_o$=84.4. 198

Fig. 5.32. Sensitivity of cross correlation $u'v'$ to grid size at $t\Delta u/\theta_o$=84.4..... 199

Fig. 5.33. Sensitivity of streamwise energy spectrum to grid size at $t\Delta u/\theta_o$=84.4. 200

Fig. 5.34. Sensitivity of spanwise energy spectrum to grid size at $t\Delta u/\theta_o$=84.4. 200

Fig. 5.35. Temporal growth of momentum thickness. ----- (invisid run), _____ (viscous run). 201

Fig. 5.36. Temporal growth of vorticity thickness. ----- (invisid run), _____ (viscous run) 201

Fig. 5.37. Profiles of mean streamwise velocity in inviscid run at four times..... 202

Fig. 5.38. Temporal evolution of root mean square streamwise velocity fluctuations in inviscid run at four times. 202

Fig. 5.39. Temporal evolution of root mean square cross-stream velocity fluctuations in inviscid run at four times. 203

Fig. 5.40 Temporal evolution of root mean square streamwise velocity fluctuations in inviscid run at four times. 203

Fig. 5.41. Temporal evolution of cross correlation $u'v'$ in inviscid run at four times.... 204

Fig. 5.42. Temporal evolution of streamwise energy spectrum in inviscid run at four times. 205

Fig. 5.43. Temporal evolution of spanwise energy spectrum in inviscid run at four times. 205

Fig. 6.1 Temporal development of a vorticity filament. 206

Fig. 6.2 Temporal development of momentum thickness..... 207

Fig. 6.3 Temporal development of vorticity thickness. 207

Fig. 6.4. Profiles of mean streamwise velocity. 208

Fig. 6.5. Profiles of root mean square streamwise velocity fluctuations. 208

Fig. 6.6. Profiles of root mean square cross-stream velocity fluctuations. 209

Fig. 6.7. Profiles of root mean square spanwise velocity fluctuations. 209

Fig. 6.8. Profiles of cross-correlation *u'v'*. 210

Fig. 6.9. Streamwise velocity contours showing flow three dimensionality at four times (a) $t\Delta u/\theta_o$=43.1, (b) $t\Delta u/\theta_o$=63.2, (c) $t\Delta u/\theta_o$=89.4 *and* (d) $t\Delta u/\theta_o$=103.8. Thirty equally distributed contour levels are used between u_{min} and u_{max}. Dotted lines represent negative velocity and continuous lines represent positive velocity..... 211

Fig. 6.10 Temporal growth of streamwise and spanwise vorticity. 212

Fig. 6.11. Temporal evolution of vorticity divergence. 212

Fig. 6.12. Development of spanwise vorticity contours at the mid plane (z/L_z=0.5) at four times (a) $t\Delta u/\theta_o$=15.0, (b) $t\Delta u/\theta_o$=43.1, (c) $t\Delta u/\theta_o$=89.4 *and* (d) $t\Delta u/\theta_o$=121.6. 213

Fig 6.13. Projection of velocity vector field (u,v) on x-y plane. Times and locations correspond to that of figure 6.12..... 214

Fig. 6.14. Three dimensional perspectives of the particle field at four times (a) $t\Delta u/\theta_o$=43.1, (b) $t\Delta u/\theta_o$=63.2, (c) $t\Delta u/\theta_o$=89.4 *and* (d) $t\Delta u/\theta_o$=103.8 215

Fig. 6.15. Magnified view of the particle field for $0.3 \leq x/L_x \leq 0.7$ at the same times of figure 6.14. 216

Fig. 6.16. Growth of streamwise vorticity at four times (a) $t\Delta u/\theta_o$=43.1, (b) $t\Delta u/\theta_o$=63.2, (c) $t\Delta u/\theta_o$=89.4 *and* (d) $t\Delta u/\theta_o$=103.8. 217

Fig. 6.17. Streamwise vorticity contours at $t\Delta u/\theta_o$=43. 8 and four streamwise locations (a)x/L_x=0.2, (b)x/L_x=0.4 , (c)x/L_x=0.6 , (d)x/L_x=0.8. Twenty equally distributed contour levels with 0.05 $(\omega_{max}- \omega_{min})$ increments are used. Dotted lines represent negative vorticity and continuous lines represent positive vorticity. 218

Fig. 6.18. Streamwise vorticity contours at $t\Delta u/\theta_o$=63.28 and four streamwise locations (a)x/L_x=0.2, (b)x/L_x=0.4 , (c)x/L_x=0.6 , (d)x/L_x=0.8. Twenty equally distributed contour levels with 0.05 $(\omega_{max}- \omega_{min})$ increments are used. Dotted lines represent negative vorticity and continuous lines represent positive vorticity. 219

Fig. 6.19. Streamwise vorticity contours at $t\Delta u/\theta_o$=103.8 and four streamwise locations (a)x/L_x=0.2, (b)x/L_x=0.4 , (c)x/L_x=0.6 , (d)x/L_x=0.8. Twenty equally distributed contour levels with 0.05 $(\omega_{max}- \omega_{min})$ increments are used. Dotted lines represent negative vorticity and continuous lines represent positive vorticity. 220

Fig. 6.20. Projection of velocity vector field (v,w) on y-z plane at $t\Delta u/\theta_o$=43.1 *8* and four streamwise locations (a)x/L_x=0.2, (b)x/L_x=0.4 , (c)x/L_x=0.6 , (d)x/L_x=0.8. 221

Fig. 6.21. Projection of velocity vector field (v,w) on y-z plane at $t\Delta u/\theta_o$=63.1 and four streamwise locations (a)x/L_x=0.2, (b)x/L_x=0.4 , (c)x/L_x=0.6 , (d)x/L_x=0.8. 222

Fig. 6.22. Projection of velocity vector field (v,w) on y-z plane at $t\Delta u/\theta_o$=103.8 and four streamwise locations (a)x/L_x=0.2, (b)x/L_x=0.4 , (c)x/L_x=0.6 , (d)x/L_x=0.8. 223

Fig. 6.23. Projection of particle velocity field (v,w) on y-z plane of one grid size thick slice at x/L_x=0.6 at four times (a) $t\Delta u/\theta_o$=12.1, (b) $t\Delta u/\theta_o$=43.1, (c) $t\Delta u/\theta_o$=63.2 and (d) $t\Delta u/\theta_o$=103.8. 224

Fig. 6.24. Projection of particle location on y-z plane of one grid size thick slice at x/L_x=0.6 at four times (a) $t\Delta u/\theta_o$=12.1, (b) $t\Delta u/\theta_o$=43.1, (c) $t\Delta u/\theta_o$=63.2 *and* (d) $t\Delta u/\theta_o$=103.8. 225

Fig. 6.25. Temporal Development of one dimensional streamwise energy spectrum at four times (a) $t\Delta u/\theta_o$=43.1, (b) $t\Delta u/\theta_o$=63.2, (c) $t\Delta u/\theta_o$=89.4, and (d) $t\Delta u/\theta_o$=103.8. Continuous line represents the -5/3 power law. 226

Fig. 6.26 Temporal Development of one dimensional spanwise energy spectrum at four times (a) $t\Delta u/\theta_o$=43.1, (b) $t\Delta u/\theta_o$=63.2, (c) $t\Delta u/\theta_o$=89.4, and (d) $t\Delta u/\theta_o$=103.8. Continuous line represents the -5/3 power law. 226

Fig. 6.27. Sensitivity of mean velocity profile to grid size at $t\Delta u/\theta_o$=89.4. 227

Fig. 6.28. Sensitivity of root mean square streamwise velocity fluctuations to grid size at $t\Delta u/\theta_o$=89.4. 227

Fig. 6.29. Sensitivity of root mean square cross-stream velocity fluctuations to grid size at $t\Delta u/\theta_o$=89.4. 228

Fig. 6.30. Sensitivity of root mean square spanwise velocity fluctuations to grid size at $t\Delta u/\theta_o$=89.4. 228

Fig. 6.31. Sensitivity of cross correlation *u'v'* to grid size at $t\Delta u/\theta_o$=89.4..... 229

Fig. 6.32. Sensitivity of streamwise energy spectrum to grid size at $t\Delta u/\theta_o$=89.4. 230

Fig. 6.33 Sensitivity of spanwise energy spectrum to grid size at $t\Delta u/\theta_o$=89.4. 230

Fig. 6.34 Temporal growth of momentum thickness. ----- (invisid run), _____ (viscous run)..... 231

Fig. 6.35 Temporal growth of vorticity thickness. ---------- (invisid run), _____ (viscous run) 231

Fig. 6.36. Profiles of mean streamwise velocity in inviscid run at four times..... 232

Fig. 6.37. Temporal evolution of root mean square streamwise velocity fluctuations in inviscid run at four times. 232

Fig. 6.38. Temporal evolution of root mean square cross-stream velocity fluctuations in inviscid run at four times. 233

Fig. 6.39. Temporal evolution of root mean square spanwise velocity fluctuations in inviscid run at four times. 233

Fig. 6.40. Temporal evolution of cross correlation u'v' in inviscid run at four times.... 234

Fig. 6.41. Temporal evolution of streamwise energy spectrum in inviscid run at four times. 235

Fig. 6.42. Temporal evolution of spanwise energy spectrum in inviscid run at four times. 235

Fig, 7.1 Momentum Thickness 236

Fig. 7.2 Vorticity thickness..... 236

Fig. 7.3 Comparison of the profiles of mean streamwise velocity 237

Fig. 7.4 Comparison of the profiles of root mean square streamwise velocity fluctuations. 237

Fig. 7.5 comparison of profiles of root mean square cross-stream velocity fluctuations. 238

Fig. 7.6 Comparison of the profiles of root mean square spanwise velocity fluctuations. 238

Fig. 7.7 Comparison of the profiles of *u'v'* cross-correlation..... 239

Fig. 7.8 Comparison of the one dimensional energy spectra..... 240

Fig. 7.9 Comparison of the one dimensional energy spectra..... 240

Fig. 7.10 Comparison of the development of spanwise vorticity structures. For captions see figures 5.14 and 6.12..... 241

Fig. 7.11 Comparison of the streamwise vorticity structures. For captions see figures 5.20 and 6.19..... 242

Fig. 7.12. Temporal development of kinetic energy for the two schemes..... 243

Fig. 7.13. Temporal development of enstrophy for the two schemes..... 243

Fig. 7.14 Temporal development of relative diffusion error. 244

Fig. 7.15 Variation of the dissipation scales. 244

Fig. 7.16 Processing time for each time step. 245

Fig. 7.17 Cumulative processing time. 245

Chapter 1

Introduction

1.1 Overview

The complex flow phenomena observed in industrial applications and in nature are distinguished from the much simpler idealized potential flows by the existence of vorticity within the fluid. Vorticity is therefore of primary significance in the study of fluid dynamics both experimentally and computationally. Evidently, vorticity in the flow field contains all the dynamic information necessary to obtain velocity and pressure fields, (Leonard, 1980). However, typical flows of practical interest are characterized by small vortical (rotational) regions embedded in an otherwise vorticity-free (irrotational) fluid, or, in mathematical terminology, vorticity has "compact support" (Cottet and Koumoutsakos, 2000). As an example, in a flow caused by mixing two streams of different velocities downstream of a thin plate separating them, vorticity is confined to a thin layer adjacent to the plane where the two streams are merging together. Velocity, on the other hand, has non-zero values through out the region of the flow domain. This flow configuration is called mixing layer. Turbulent mixing layers occur in flow fields of

many engineering applications e.g., combustion chambers and premixers for gas turbines combustors. Certain flow features of mixing layers such as presence of large vortical structures and absence of bounding walls have made them attractive for both experimental and computational studies.

Another enticing feature of the vorticity field is that, in incompressible and inviscid flows, vorticity lines are material lines convected with the local fluid velocity. This statement was developed originally by Helmholtz and subsequently proven more concisely by Kelvin (Batchelor, 1979). The above two features of vorticity field, namely, compact support and Kelvin-Helmholtz theorem make it mathematically correct and often very convenient to consider fluid dynamics in terms of lumps of vorticity that induce motion on each other as an alternative to the traditional pressure-velocity consideration (Leonard,1985). Based on these premises, vortex methods emerged as a numerical tool to solve fluid dynamics problems. Thus, to simulate a flow problem by this method, the vorticity-containing regions are discretized into a finite number of vorticity-carrying elements and track, in Lagrangian frame, the translation and deformation of these elements. Consequently, in these methods, the computational elements automatically conform to the flow field dynamics, with little computational effort devoted to regions free of vorticity. Moreover, because of the kinematics and dynamics of the flow field, it is possible to obtain a complete description of the flow field by vortex methods.

Historically, vortex methods have been initiated in the early thirties of the last century as a tool to model two dimensional unsteady, incompressible and inviscid flows. A serious problem that precludes the general utilization of vortex methods for high Reynolds

number flows in the computational fluid dynamics community is the difficulty of approximating the derivatives that occur in the viscous diffusion and stretching (in three dimensional flows) terms of the vorticity transport equation.

Although no turbulence models are involved in the implementation of vortex methods these methods are in general viewed as good enough to reproduce motions having large and intermediate length scales of the turbulence spectrum (Cottet et al, 2002). Nevertheless, these methods provide a viable numerical tool able to qualitatively capture significant flow features such as, coherent structures, vortex roll-up, vortex pairing and vortex reconnection.

Vortex calculations based on the assumption of two dimensional flow do not in general accurately depict the dynamics of the flow. This is in part because they lack the ability to capture small scale structures that arise due to vortex stretching and tilting with respect to the main flow plane. The objective of this study is therefore to tackle the problem of stretching and diffusion simulation in the three dimensional vorticity transport equation in high Reynolds number flow. In standard three dimensional vortex methods, remeshing is needed when the particles become highly irregularly distributed. Remeshing proceeds by replacing the irregularly spaced vortex elements by a new set of particles located on a regularized lattice (mesh). Second and third order moment conserving interpolation (assignment) formulae are typically used in the remeshing (replacement) process. However, remeshing introduces additional computational cost and is known to bring in some errors due to interpolation. In this study, a new formulation of the Vortex-In-Cell method for incompressible flows is implemented. The general objective is to develop improvements in the vortex method to enhance its suitability for the computation of

incompressible flows. In the new approach, the need for remeshing is relaxed by utilizing the least squares method for evaluating partial derivatives that occur in the stretching and diffusion terms of the governing vorticity equation This method is implemented to a three dimensional temporally developing mixing layer within the frame work of the Vortex-In-Cell method.. The mixing layer has been selected because there is a massive body of research work, both numerical and experimental, that can be used to validate the present method. Also this flow configuration embodies most of the flow features encountered in any typical turbulent flow.

1.2 Motivations and Objectives

In order to obtain a full picture of the current state of the art of vortex methods, one needs to address step-by-step the different components of a reasonable implementation of the method and find where an opportunity for improvements is lying. To start, it is helpful to get a broad idea by considering the essential elements of any viscous vortex method implementation. The first basic element of a vortex method is the discretization, which implies accurate representation of a given initial vorticity field. In Vortex-In-Cell (VIC) method, which is to be used in this work, this stage represents the choice of coordinate system, particle location and the assignment scheme. Basically the assignment scheme is one of the general interpolation/approximation problem. Fortunately, a big body of research with remarkable results is available and the present work will make use of these results.

The next component of a successful vortex method implementation is the computation of velocity. In pure Lagrangian applications, the use of discrete Biot-Savart law gives rise to

very high computation cost due to the global influence of the particles. Two remedies have been developed to deal with this problem. The first technique is the fast multipole method. The method reduces the computation cost basically by approximating the effect of a cluster of particles at a certain distance by a finite series approximation (Cottet and Koumoutsakos, 2000). The second, the Vortex-In-Cell approach, replaces the Biot-Savart law by a numerical solution of Poisson equation on a grid system. The subject of numerical solution of Poisson equation is very well established and a variety of methods are available depending on the coordinate system, approximation technique and the computation architecture.

The essence of the vortex methods is the convection of the vortex element. The Lagrangian convection of the vortex particles involves appropriate integration scheme for time stepping and choosing the appropriate step size according to the flow characteristics. The present work will utilize available efficient techniques to solve Poisson equation for instantaneous velocity computation and second order Adam Bashford method for time integration (Moin, 2001). Nevertheless, these tasks require considerable programming efforts.

The last two components of a viable vortex method are the three dimensional effects (stretching) and the diffusion effects (viscous scheme). From the author's perspective and after comprehensive survey of literature, these two effects are still maturing and there is no consensus yet about the best viscous scheme and the best way to deal with stretching term. Also, deterioration of accuracy when the solution proceeds in time is attributed to the viscous and stretching schemes. That is the reason why it is believed that there is

room for improvements in these two components within the context of vortex method. Therefore the objectives of the present work are:

1. To build and validate a computer code for solving Poisson equation, with a diffusion term utilizing the M'_4 for information exchange between Eulerian and Lagrangian grids within the context of VIC method. These tasks have been realized in two dimensional spatially growing mixing layer and covered in Chapter 4.
2. To extend the code in objective (1) to a three dimensional VIC method and incorporate the stretching term using a high order finite difference scheme with spatial adaptation. Tasks of this objective are covered in Chapter 5.
3. To develop the moving least squares technique within the context of three dimensional VIC method to calculate first and second order partial derivatives encountered in stretching and diffusion terms. Tasks of this objective are covered in Chapter 6.
4. To compare the performance of the methods outlined in objectives 2 and 3 above. Tasks of this objective are covered in Chapter 7.

The flow configurations that will be used in this work as examples for testing the applicability of the proposed methodology is three dimensional temporally evolving mixing layers.

Chapter 2

Review of Literature

2.1 Introduction

The starting point for most studies of flows in the process industry and in engineering systems involves the analysis of turbulence. Since most of the transport processes are governed by turbulence, turbulence characteristics play a dominant role in determining their rates. Accuracy of numerical solution of turbulence problem is spread on a wide spectrum of approximations yielding different degrees of insight into the flow details. On one end of the spectrum, the Reynolds Averaged Navier-Stokes (RANS) techniques involve the solution of the governing equations to determine the mean values while all other scales are modeled. Because of their simplicity, RANS techniques are widely used in engineering applications. However, this approach suffers from one principal shortcoming, the fact that the model must represent a very wide range of scales, which can not be achieved by RANS models (Pope, 2000). On the other end of the numerical techniques lies the Direct Numerical Simulation (DNS) method. In DNS the governing equations are discretized and solved numerically and all scales of turbulence are resolved.

DNS is therefore considered as a reference technique, highly accurate but limited to very specific geometries, at least for straightforward implementations. Also, due to its computational cost, DNS application is limited to standard flows at relatively low Reynolds number. Intermediate between the above two techniques, namely RANS and DNS, is the Large Eddy Simulation LES. In LES, the contribution of large, energy-carrying structures is computed exactly and the effects of smallest scales on the large structures of turbulence are modeled (Pope, 2000). Vortex methods, the subject matter of this work, are accurate enough to produce acceptable statistics in the large and intermediate scales. They appear to behave as accurate as LES models in the sense that they avoid the accumulation of energy at the high- wave number end of the energy spectrum (Cottet et al, 2002).

The purpose of this survey is to put in perspective the state of development of three dimensional vortex methods as a numerical simulation tool and the many trials to incorporate viscous schemes in three dimensional vortex methods. Specifically, the focus of this review will be on viscous diffusion and stretching schemes in three dimensional vorticity transport equations in the context of vortex methods.

In the following sections, an overview of the vortex methods, Vortex-In-Cell method in three dimensional flows, stretching schemes and viscous schemes for vortex methods will be presented. Also, a review of the vortex method implemented to predict relevant free shear flows, particularly three dimensional mixing layers, will be discussed.

2.2 Vortex Methods

2.2.1 Characteristics of Vortex Methods

Broadly speaking, numerical techniques employed in fluid dynamics can be classified as Eulerian and Lagrangian. In the Eulerian type, flow quantities are defined as functions of position in space $(\vec{x})$ and time (t). This depiction provides the spatial distribution of flow properties at each instant during the motion. On the other hand, Lagrangian methods make use of the specifications of motions of particles. Flow properties, therefore, refer to a specific parcel of matter in addition to its spatial position at any particular time instant during the motion. Typically a fluid material element is specified by its position $(\vec{x}_o)$ at some initial time (t_o) and explicitly tracked as time proceeds. Accordingly, Lagrangian methods provide the dynamical history of this selected fluid element (Batchelor, 1979).

Vortex methods are a class of Lagrangian numerical methods for approximating the solution of Euler or Navier-Stokes equations. The first attempt to simulate a flow by a vortex method was done by Rosenhead (1932) to approximate the evolution of the two dimensional vortex sheet by point vortex approximation using hand calculations. Outlined in many reviews such as those by Leonard(1980 and 1985), (Puckett1993), Sarpkaya (1994), (Chorin,1996) and Winckelmans (2004), these methods can be regarded as a discretization of the equation of fluid motion in vorticity form rather than the velocity-pressure formulation, motivated by the following considerations.

In most high Reynolds number flows, the region of significant vorticity value comprises a small subset of the flow field; in other words, the flow field is characterized by regions of concentrated vorticity embedded in an effectively irrotational field. Consequently, most of the available computational resources are devoted to regions of significant vorticity which typically cover a small fraction of the computational domain.

The pressure term associated with the numerical methods using primitive variables, is known to be the source for many stability and convergence problems. This term is eliminated from the number of dependent variables in the vorticity equation. However, pressure can be obtained from the vorticity and the velocity field by solving the following Poisson equation (Marshall, 2001):

$$\nabla^2 p = \nabla \bullet (\vec{u} \times \vec{\omega}) \tag{2.1}$$

Generally speaking, all variations of vortex methods are characterized by the following three features:

- The underlying discretization is of the vorticity field rather than the velocity field. Usually this discretization is Lagrangian in nature and consists of a collection of elements which carry concentration of vorticity.
- An approximate velocity field is recovered from the discretized vorticity field by solving Poisson equation, which is derived from the solenoidality condition and Helmholtz vector field decomposition.

- The vorticity field then evolves in time according to this velocity field, plus corrections for boundary conditions by virtue of Kelvin-Helmholtz theorems.

A variety of solution techniques for three dimensional vortex methods have been proposed and implemented. Essentially, these methods are distinguished from one another by three features; the scheme of discretization of vorticity support, the method of solution of Poisson equation and the desingularization technique. In the following, a brief review of the state of the art of each of the features is discussed

2.2.2 Discretization of Vorticity Field

All vortex methods used currently in the literature descend from the line vortex method first used by Rosenhead (1932) to simulate a vortex sheet in two dimensional inviscid flow. His algorithm proceeded by discretizing the vorticity sheet into a finite number of point vortices and superimposing the velocity induced by interacting point vortices. The velocity induced by a point vortex at the origin $\vec{u}_\omega$ is given by

$$\vec{u}_\omega = \frac{\alpha}{2\pi\left(x^2 + y^2\right)}\begin{bmatrix} -y \\ x \end{bmatrix} \tag{2.2}$$

where α is the vortex strength (circulation). A point vortex induces a singular vorticity field. This singularity results in nonphysical solutions when approximated by superposition of a finite number of point vortices. To remove the velocity singularity of point vortices, Chorin (1973) simulated the flow around a two dimensional cylinder at high Reynolds number by using a finite vortex core for the discretized vorticity field.

Later, Ashurst and Meiberg (1988) and Inoue (1989) discretized the vorticity field of a three dimensional mixing layer into a finite set of vorticity filaments of finite core size. Every filament is further dicretized into a number of interconnected vorticity segments (elements), each defined by its end points. In this discretization technique the vorticity field is reconstructed every time step by reconnecting the points along every filament using a high order interpolating formula. Consequently stretching of the vorticity field is solved implicitly.

In their simulation of uniformly sheared flow, Milane and Abdolhoseini (2004) used the filament discretization scheme within the framework of Vortex-In-Cell method. The computational domain was covered by an Eulerian grid. The filaments core size was dictated by the grid size. Each filament was defined by a set of discrete Lagrangin points. And the information was exchanged between the Eulerian grid and the Lagrangian points by an interpolation scheme. A challenging feature of the filament discretization scheme is the ever increasing growth rate of filament length due to stretching that renders calculation very costly. Also, due to the fact that filaments exchange vorticity at a rate proportional to their distance as a result of diffusion, a unique value of circulation can not be defined along the filament. Therefore the filament method has proven difficult to extend successfully to viscous three dimensional flows, as discussed in Cottet and Koumoutsakos (2000). An alternative discretization scheme that does not suffer from the difficulties associated with filament method, discretize the vorticity field into a large number of disconnected vortex elements. These elements can be vortex blobs, usually known as vortons. Every blob is represented by a vector quantity at a point, or the vortex

element can be portrayed as a stick defined by a direction and a finite length (Micheal et al. 2000).

2.2.3 Solution of Poisson Equation

The Vorticity equation for a viscous incompressible flow is given by

$$\frac{\partial \vec{\omega}}{\partial t} + (\vec{u} \bullet \nabla)\vec{\omega} = (\vec{\omega} \bullet \nabla)\vec{u} + \nu \nabla^2 \vec{\omega} \qquad (2.3)$$

Equation (2.3) contains, besides the vorticity, the velocity as independent variable. Therefore it can not be solved without additional relationships. Within the framework of vortex methods, the Poisson equation is used to recover the velocity field from the vorticity field. It is derived by utilizing the incompressibility condition (divergence free) of the velocity field in the Helmholtz decomposition of a vector field. In analogy with the well known formula from electromagnetism, Biot-Savart law is used to solve Poisson equation for unbounded domain. Denoting the Green's function of Laplace operator by $\vec{G}(\vec{x})$, the velocity field can be recovered using Biot-Savart formula (Cottet and Koumoutsakos, 2000),

$$\vec{u}(\vec{x}) = \int_{-\infty}^{\infty} \left[\nabla \times \vec{G}(\vec{x} - \vec{x}')\right] \times \vec{\omega}(\vec{x}') dV(\vec{x}') = \int_{-\infty}^{\infty} \vec{k}(\vec{x} - \vec{x}') \times \vec{\omega}(\vec{x}') dV(\vec{x}') = \vec{k}(\vec{x}) * \vec{\omega}(\vec{x}) \qquad (2.4)$$

where * corresponds the convolution integral and $\vec{k}$ represents the rotational part of $\vec{G}$ i.e. $\vec{k} = \nabla \times \vec{G}$. The above convolution has to be understood in the sense of vector product. For example, in three dimensional unbounded flow,

$$\vec{k}(\vec{x}) * \vec{\omega}(\vec{x}) = \frac{-1}{4\pi} \int \frac{(\vec{x} - \vec{x}')}{|\vec{x} - \vec{x}'|^3} \times \vec{\omega}(\vec{x}') dV(\vec{x}') \tag{2.5}$$

The integration in equation (2.5) has to be performed over the whole fluid volume. In numerical computation and when the vorticity field is discretized into a finite number of particles, the integral operation in equation (2.4) is changed to summation, as

$$\vec{u}_i(\vec{x}_i) = \sum_{j \neq i} \vec{k}(\vec{x}_i - \vec{x}_j) \times \vec{\alpha}_j \tag{2.6}$$

where $\vec{\alpha} = \int \vec{\omega} dV$ is the strength of the point vortex. The physical meaning of equation (2.5) is that the velocity of any point vortex *i* is the accumulative effect of the induced velocity of all other vortex particles in the computational domain. Biot-Savart integral solution of Poisson equation, therefore, gives rise to N^2 operations at every time step when *N* vortex particles exist in the solution domain (Leonard, 1985). Consequently, a limited number of vorticity samples can be used in the simulation which affects the resolution this solution can provide. Two remedies have been developed in the literature to accelerate the velocity computation, both of which reduce the number of computations per time step to *O(NlogN)*. The first technique, due to Greengrad and Rokhlin (1987), is the fast multipole expansion. The basic idea of the fast multipole expansion is to divide the computational domain into a number of boxes which are considered the first

generation, and then every box is divided into a certain number of boxes to generate the second generation and so forth until a roughly specified number of Lagrangian points are contained in the last generation (smallest boxes). The next step is to replace the particle-particle interaction used in the Biot-Savart summation by a box-particle interaction approach in which the potential induced on a target point are computed based on the distance from the centroid of the box to that point. The second remedy is the Vortex-In-Cell (VIC) method. Derived from plasma physics by Christiansen (1973), this method replaces the Biot-Savart integral on Lagrangian points by solution of Poisson equation on an Eulerian mesh. Since this approach is adopted in this work an elaborate review of the method will be presented in section 2.3.

2.2.4 Desingularization Techniques

It is apparent from equations (2.5) that whenever two particle trajectories approach each other the denominator approches to zero and the velocity that each particle induces on the other goes to infinity. For this reason it was generally believed that the point vortex method was unstable and would not converge to solutions of incompressible vorticity equations. Chorin (1973) introduced the idea of replacing the function $\vec{k}$ in equation (2.6) by:

$$\vec{u}_i(\vec{x}_i) = \sum_{j \neq i} \vec{k}_\delta(\vec{x}_i - \vec{x}_j) \times \vec{\alpha} \tag{2.7}$$

where the new function $\vec{k}_\delta$ behaves similar to $\vec{k}$ except at the origin, i.e. $\vec{k}_\delta$ is bounded at the origin. $\vec{k}_\delta$ is typically obtained by convolving $\vec{k}$ with a smoothing (desingularization) kernel f_δ. The smoothing kernel is usually chosen to be radially symmetrical and must satisfy $\int_{-\infty}^{-\infty} f_\delta(\vec{x})d\vec{x} = 1$, (Cottet and Koumoutsakos, 2000). A typical example of the one dimensional smoothing kernel is the Gaussian distribution given by $\frac{1}{\delta\sqrt{2\pi}}\exp(\frac{-x^2}{2\delta^2})$. Following the notations used by Cottet and Koumoutsakos (2000), the three dimensional radially symmetrical desingularization function is obtained by the tensor product of its one dimensional counterpart as,

$$f_\delta(\vec{x}) = \frac{1}{\delta^3(2\pi)^{3/2}}\exp(\frac{-x^2}{2\delta^2})\exp(\frac{-y^2}{2\delta^2})\exp(\frac{-z^2}{2\delta^2}) \tag{2.8}$$

Integrating the above equation over the three dimensional space results in

$$\int_{-\infty}^{\infty} f_\delta(\vec{x})d\vec{x} = \frac{1}{\delta^3(2\pi)^{3/2}}\int_{-\infty}^{\infty}\int_{-\infty}^{\infty}\int_{-\infty}^{\infty}\exp(\frac{-x^2}{2\delta^2})\exp(\frac{-y^2}{2\delta^2})\exp(\frac{-z^2}{2\delta^2})dxdydz = 1 \tag{2.9}$$

The desingularized vorticity field is then given by

$$\vec{\omega}(\vec{x}) = \sum_j f_\delta(\vec{x} - \vec{x}_j)\vec{\alpha}_j \tag{2.10}$$

That is

$$\omega_x(\vec{x}) = \frac{1}{(2\pi)^{3/2}} \sum_j \frac{1}{\delta^3} \left[\exp \frac{-\left|\vec{x} - \vec{x}_j\right|^2}{2\delta^2} \right] \alpha_x \ , \tag{2.11}$$

$$\omega_y(\vec{x}) = \frac{1}{(2\pi)^{3/2}} \sum_j \frac{1}{\delta^3} \left[\exp \frac{-\left|\vec{x} - \vec{x}_j\right|^2}{2\delta^2} \right] \alpha_y \tag{2.12} ,$$

and

$$\omega_z(\vec{x}) = \frac{1}{(2\pi)^{3/2}} \sum_j \frac{1}{\delta^3} \left[\exp \frac{-\left|\vec{x} - \vec{x}_j\right|^2}{2\delta^2} \right] \alpha_z \tag{2.13}$$

The desingularization kernel serves the purpose of smoothing the vorticity associated with each element in a small neighborhood of the Lagrangian position of the element. A variety of smoothing kernels have been derived by Beale and Majda (1982). The order of these kernels is based on the moment conserving properties compared to the Dirac delta measure. A desingularization kernel is said to be of order *m* if the following hold, (Cottet and Koumoutsakos, 2000)

$$\int_{-\infty}^{\infty} \vec{x}^{\,j} f_\delta(\vec{x}) d\vec{x} = 0 \quad if \quad j \le m-1, \ and$$

$$\int_{-\infty}^{\infty} \vec{x}^{\,m} f_\delta(\vec{x}) d\vec{x} \qquad is \ finite \tag{2.14}$$

The above conditions signify that the desingularization function has, up to the power *m-1,* the same moment properties as the Dirac delta function. The desingularization kernels were tabulated and ever since used by many researchers to simulate different configurations of three dimensional flows. They have been used by Knio and Ghoniem (1990) for the simulation of three dimensional reacting shear layers, Knio and Ghoniem(1992) for predicting the three dimensional structure of periodic vorticity layers under non-symmetric conditions and Gharakhani and Ghoniem (1997) for three dimensional vortex simulation of time dependent internal viscous flow. Also, Ploumhans et al (2002) implemented these interpolation kernels in a direct numerical simulation of three dimensional flow around a sphere.

2.3 Vortex -In-Cell (VIC) Method

The computationally intensive part of vortex methods is the calculation of the velocity field. The classical computational cost of the method scales as $O(N^2)$, but it can be reduced to *NlogN* (for *N* vortex particles in the flow field) if the solution domain is covered by an Eulerian fixed mesh on which the velocity field can be determined as first proposed by Christiansen (1973). In the published literature, both Vortex-In-Cell (VIC) and Particle-In-Cell (PIC) are names used interchangeably to identify this method. The Lagrangian particles are then moved and tracked while information is exchanged between

the Lagrangian particles and the Eulerian grid. The VIC method has ever since been used successfully in two-dimensional flow cases where typically the vorticity-stream function formulation is implemented. This method has been implemented by, among many others, Aref and Siggia (1980) for shear layer flow and Chang and Chern (1991) for flow around an impulsively started circular cylinder.

In three-dimensional flows the vorticity is a vector. This implies that vorticity may be changed by stretching, tilting and diffusion. Three dimensional versions of VIC have been developed and used for inviscid flow by Couet et al (1981) simulating a periodic mixing layer flow and by Bretcht and Ferrante (1990) for bubble flow. It has also been used for viscous flow by Micheal et al (2000) for the diffusion of a line vortex and propagation of a vortex ring. Lui and Doorly (2000) used VIC to simulate a vortex flow in unbounded domain. The same group implemented VIC to simulate a vortex ring interaction with a wall (Lui, 2001) and later to simulate an unsteady shear flow induced by a vortex ring (Lui, 2002). Walther and Koumoutsakos (2001) also implemented the same methodology to solve for a particulate flow with two way coupling. Cottet and Poncet (2003) used it for three dimensional flows over a finite length cylinder using body fitted grid and immersed boundary for a vorticity ring impinging on a finite length cylinder. Recently Chatelain et al (2008) utilized an unprecedented billion vortex elements with a large parallel distributed memory code to simulate an aircraft wake at a Reynolds number of 6000.

In VIC method, the initial vorticity field is discretized into a finite set of particles, each of which is defined by its position and strength. The velocity field is computed by solving Poisson equation on the fixed grid. The vorticity then is advected explicitly by the

moving particles. Thus the grid-based computation of convection that causes the tainting of flow features is avoided. In comparison to pure Lagrangian methods, the grid system serves to, besides computing the velocity field, smoothing the vorticity over a blob of a dimension that depends on the interpolation scheme and grid spacing. Walther and Koumoutsakos (2001) used a uniform cubical grid in a particle-laden flow simulation. Micheal et al (2000) used a triangular grid in the simulation of a two-dimensional wake of a circular cylinder. The same authors used a tetrahedral grid system in the simulation of the three-dimensional propagation of a vortex ring.

A variety of methods has been proposed to solve the Poisson equation. Lui and Doorly (2000) used the seven point discretization of the second order derivatives in the equations. Micheal et al (2000) implemented the conjugate gradient solver with a piecewise linear finite element method. Fast Fourier Transform (FFT) is used by Walther and Koumoutsakos (2001) to solve the Poisson equation. The generalized minimal residual (GMRES) method, which is more suitable for parallel computing is used by Lui (2002). Chatelain et al (2008) used a periodic box for their computational domain which allowed a straightforward transformation and solution in the wave number space.

A crucial aspect of VIC method is the efficient and accurate exchange of information between the particle and mesh. The finite grid size produces a loss of the information contained in wave lengths shorter than the grid spacing. Longer wave length variations can be retrieved accurately by the assignment and interpolation schemes. Thorough analysis of these schemes in Fourier space is given by Hockney and Eastwood (1981). Following Hockney and Eastwood (1981), for a given grid size the best interpolating scheme would act as a band limited low-pass filter with a limit corresponding to the wave

number of the grid size. Unfortunately the optimal band limited transform corresponds to a sinc function which is not limited in the physical space (the sinc function is defined by $sinc(x)=sin(\pi x)/\pi x$). Such interpolation scheme will involve all the mesh points in the solution domain, which is computationally impractical. Practical scheme starts with the choice of grid based weighing function (or filter), that has a small compact support around the grid point. A family of these interpolation kernels are in use, every member of which is characterized by its accuracy (the number of grid points involved) and smoothness (the number of continuous derivatives shared by the interpolation kernel and sinc function). The interpolation scheme is constructed by the tensorial product of their one dimensional counterpart. The number of points involved is M^d, where M is the number of grid points involved in the interpolation kernel and d is 1, 2, or 3 corresponding to one, two, or three dimensional flow, respectively. The first of those interpolation kernels is the piecewise constant, which assigns the particle variable to the nearest grid point. The next in the line is the piecewise linear which interpolates the particle values to the nearest two grid points according to their distance from the particle. This scheme is termed as bilinear in one dimension, area weighing in two-dimensions and volume weighing in three dimensional flows and is used by many researchers such as Lui and Doorly (2000), Lui (2002) and Milane and Abdolhoseini (2004) as interpolation and smoothing formula. Monaghan (1985) proposed a one-dimensional moment-conserving B-spline interpolation formula that increases the accuracy without affecting the smoothness properties. It is known as M'_4 scheme and it was later applied to two and three dimensional vortex methods (Cottet and Koumoutsakos, 2000). This method is widely used in literature, for its accuracy and smoothness characteristics, see for example Cottet and Poncet (2003), Giovannini and Gagnon (2006) and Van Rees et al (2011). The

M'_4 scheme is adopted in this work and the details of their mathematical formulation will be presented in the next chapter dealing with the mathematical formulation.

2.4 Viscous Schemes

Vortex methods were originally derived as a tool to track the evolution of vorticity field in compliance with Kelvin-Helmholtz idealization of inviscid flows. This is the reason why there was always some inconvenience associated with the incorporation of diffusion effects into the vortex methods. However, diffusion of vortex sheets to non-zero thickness and vorticity filling significant regions of the flow field are direct consequences of non-zero viscosity. Therefore, viscosity effects are inevitable in almost every practical flow configuration. Many techniques have been developed to deal with the diffusion effects and will be discussed in the following sections.

2.4.1 Random Walk Method

The first successful addition of viscosity was made with the random walk of vortex position due to Chorin (1973), commonly known as random vortex method (RVM). The random vortex method acts by modifying the positions of the particles at each diffusion substep by adding a random walk, that is the particle locations are transformed using $\vec{x}_i^{n+1} = \vec{x}_i^n + \vec{\xi}_i^n$, where $\vec{\xi}_i^n$ are Gaussian independent random variables of zero mean and standard deviation equal to $\sqrt{2\nu\Delta t}$. This formula is based on the probabilistic interpretation of the diffusion equation, which says that the probability of finding a particle that moves at random in Brownian motion is given by the solution of the

diffusion equation. The fundamental solution of non dimensionalized one dimensional diffusion equation $\frac{\partial \omega^*}{\partial t^*} = \frac{1}{\mathrm{Re}} \frac{\partial^2 \omega^*}{\partial x^{*2}}$ in an unbounded domain for *t>0* (Saffman, 1992) is

$$\omega^*(x,t) = \sqrt{\frac{\mathrm{Re}}{4\pi t^*}} \exp\left(-\frac{\mathrm{Re}}{4t^*} x^{*2} \right) \tag{2.15}$$

The function above is the same as the probability density function of a Gaussian random variable with zero mean and standard deviation $\sigma = \sqrt{2t^*/\mathrm{Re}}$. Hence in three dimensions, the diffusion term is simulated stochastically by a displacement of the particles in three orthogonal directions, using three independent Gaussian random variable with zero mean and $\sigma = \sqrt{2\Delta t^*/\mathrm{Re}}$. Convergence of the method has been proven, but its slow rate means that a large number of particles are required to obtain reasonable accuracy. This makes the random walk method prohibitively costly when implemented in three dimensional flows. Also, the random walk method can only model slightly viscous flows, i.e.; laminar or transitional high Reynolds number flow and the solution given by equation (2.15) brings the effects of molecular and numerical (but not turbulent) diffusion into the numerical simulation of vorticity diffusion (Sarpkaya,1994). However, due to its locality and ease of implementation, the random walk method continues to find extensive use to this day. A more detailed description of this method, presentation of convergence analysis and aspects of numerical analysis are provided by Cottet and Koumatsakous (2000). Many research works can be cited for implementation of the random walk method. For example; flow around impulsively started cylinder at Re=300, 550, 3000,

9500 by Smith and Stansby (1988) and the wall bounded flow by Gharakhani and Ghoniem (1997), where the number of particles was of the order of 10^5.

2.4.2 Core Spreading Method

Core spreading scheme is another viscous vortex method which is apparently first presented by Leonard (1980). Viscous effects in this method are accounted for by changing the core size of vortex particles linearly with its age. This is to exactly match the diffusion of two dimensional line vortex (Lamb-Oseen vortex). This can be explained on the basis of the classical solution of Lamb-Oseen vortex, which is governed by the following partial differential equation (Green, 2001)

$$\frac{\partial \omega_z}{\partial t} = \nu \frac{\partial^2 \omega_z}{\partial |\vec{x}|^2} \tag{2.16}$$

The initial vorticity is zero everywhere except on the axis $|\vec{x}| = 0$, where there is a line vortex of strength α_o. This is a two dimensional flow with circular symmetry in which the streamlines are circles around the axis. The vorticity, which has one component parallel to the axis, is a function of the radial distance and time. Therefore, it can be treated as a scalar quantity. The vorticity field described by equation (2.16) is given by

$$\omega_z(\vec{x},t) = \frac{\alpha_o}{4\pi\nu t} \exp[\frac{-|\vec{x}|^2}{4\nu t}] \tag{2.17}$$

. If the discrete vorticity field of equation (2.10) is rewritten slightly different to express the core function dependence on time as

$$\vec{\omega}(\vec{x}) = \sum_j f_t\left(\vec{x} - \vec{x}_j\right)\vec{\alpha}_j \tag{2.18}$$

According to the core spreading method, the cut-off function is selected to be the solution of equation (2.16) with the initial condition f_o, that is the cut-off function at any time t is given by the convolution integral of the initial cut-off function and the Green's function of the diffusion equation (2.15):

$$f_t(\vec{x}) = \frac{1}{4\pi\nu}\int \exp[\frac{-\left|\vec{x} - \vec{x}'\right|^2}{4\nu t}] f_o(\vec{x}')d\vec{x}' \tag{2.19}$$

The core spreading is formulated to satisfy the diffusion part of the vorticity equation by linearly growing δ^2 according to Sarpkaya (1994) as

$$\frac{d\delta^2}{dt} = 4\nu \tag{2.20}$$

The above equation means that the core size must expand at every time step at a rate proportional to $\sqrt{\nu\Delta t}$ that is the core size of a vortex particle p at time $(t + \Delta t)$ is given by

$$\delta_p(t+\Delta t) = \delta_p(t) + 2\sqrt{\nu \Delta t} \tag{2.21}$$

The attraction of this formulation, apart from its simplicity, is that it is localized and it is fully deterministic, allowing for faster convergence. However research in its regard have seen a setback when Greengrad (1985) demonstrated the inconsistency of the core spreading method. He proved that the scheme converges to an equation different from Navier-Stokes equations. Greengrad (1985) derived the actual equation which is solved by the vorticity obtained by core spreading. It differs from the Navier-Stokes equation in the convection term only. As the convergence of a vortex method depends on core size sustainability, the method will clearly eventually break down as the core size keeps growing. This simple argument clarifies how a correction is implemented by splitting the blobs which have grown beyond a specified maximum into smaller elements. Rossi (1996) proposed a correction to the core spreading method with vortex splitting and provided details of implementation. He also proposed vortex merging as a means to control core size problem, as the splitting can rapidly increase the blob population.

2.4.3 Particle Strength Exchange (PSE) Method

Motivated by slow convergence of random walk method and the inconsistency of the core spreading method, the particle strength exchange (PSE) method was developed by Degond and Mas-Gallic (1989). It was introduced in the context of viscous splitting of the general particle method, in which the viscous and inviscid parts of the governing equations are taken into account as successive substeps. The principal feature of the particle strength exchange method is that the Laplacian operator in the diffusion term is

approximated by an integral operator. Given that the smoothing function f_δ satisfies the moment conditions given by equation (2.14), the Laplacian of vorticity can be approximated by

$$\nabla^2 \vec{\omega}(\vec{x}) \approx \frac{2}{\delta} \int f_\delta(\vec{x} - \vec{x}')[\vec{\omega}(\vec{x}) - \vec{\omega}(\vec{x}')] d\vec{x}' \tag{2.22}$$

When the vortex distribution within the smoothing function is Gaussian, then that is equivalent to the Green's function of the diffusion equation with a cut-off parameter δ expressed as

$$G_\delta(\vec{x}) = \frac{2}{\pi\delta^2} \exp\left(\frac{-|\vec{x}|^2}{2\delta^2} \right) \tag{2.23}$$

the Laplacian is approximated by

$$\nabla^2 \vec{\omega}(\vec{x}) \approx \frac{2}{\delta} \int G_\delta(|\vec{x} - \vec{x}'|)[\vec{\omega}(\vec{x}) - \vec{\omega}(\vec{x}')] d\vec{x} \tag{2.24}$$

Based on the length scale of the diffusion equation, the cut-off parameter δ is typically chosen to be $(2\nu\Delta t)^{1/2}$. The locations of the vortex particles are used as quadrature points

to approximate equation (2.22). Hence, for the case of unbounded flow, the diffusion substep obtained using the (PSE) method is discretized as

$$\frac{d\vec{\alpha}_p}{dt} = \nu \sum_{j=1}^{N} \left(\vec{\alpha}_j - \vec{\alpha}_p\right) G_\delta \left(\left|\vec{x}_j - \vec{x}_p\right|\right) \tag{2.25}$$

In summary, the main feature of the PSE method is the replacement of differential operators by integral operators, more suited to the particle representation of the data. The integral operators are discretized by quadrature on the locations of the particles, then the discrete integral operator for diffusion reduces to a contribution from nearby particles to a change of circulation on a given vortex blob. In equation (2.25) the strength exchange involves all particles; in practice, though, each vortex particle is allowed contributions to the change in its circulation strength from particles within a radius of typically 5δ as suggested by Ploumhans and Winckelmans (2000). The accuracy of (PSE) depends strongly on the quadrature rules used for the discretized integral, which means the accuracy is linked to having nearly uniformly spaced particles. That entails frequent remeshing of the particle field into a well-ordered field which undermines the grid free nature of the method.

In conclusion, the PSE method has been applied in many classic problems of flow past bluff bodies, as an example, the high resolution flow past a sphere at Reynolds numbers of 300, 500 and 1000 by Ploumhans et al (2002). Giovannini and Gagnon (2006) have implemented successfully the PSE method in an unbounded flow for two counter-rotating vorticity tubes.

2.4.4 Fishlov Method

There is yet another deterministic method proposed by Fishelov (1990) which is not based on the exchange of circulation. Her suggestion was to approximate the vorticity field by a convolution with a smoothing function

$$\vec{\omega} \approx f_{\delta} * \vec{\omega} \tag{2.26}$$

Then the Laplacian operator that represents the diffusion term in the vorticity equation is approximated analytically by differentiating the smoothing function as

$$\nabla^2 \vec{\omega} \approx \nabla^2 (f_{\delta} * \vec{\omega}) = (\nabla^2 f_{\delta}) * \vec{\omega} \tag{2.27}$$

Prior to Fishelov, the same concept was used by Anderson and Greengrad (1985) to compute derivatives in the stretching term in three dimensional flows as will be discussed in the next section. The method is proven to be stable if the Fourier transform of the smoothing function is non-negative. According to Fishelov's method, the viscous substep for Lagrangian particle representation when there are *N* particles in the computation domain is given by

$$\frac{d\vec{\omega}_p}{dt} = \nu \sum_{j=1}^{N} \nabla^2 f_{\delta}(\vec{x}_p - \vec{x}_j)\vec{\alpha}_j \tag{2.28}$$

Fishelov implemented this deterministic viscous approach to a step function initial vorticity problem and compared the results to that of Random Vortex Method (RVM). Numerical experiments for simple flow problems were carried out with this method and the results agreed well with the random walk method. Later Fishelov (1994) used her method for the simulation of flow around a sphere at Reynolds number of 3000. In this simulation, random walk method was utilized in the wall region with a boundary layer formulation whereas her method was used in regions away from the wall. The simulation seems to be unable to keep stability for long times and results looked coarse. Researches in this method appear to be scarce probably due to the fact that this method encounters difficulties when particles get distorted as computation proceeds in time.

2.4.5 The Diffusion Velocity Method

Introduced by Ogami and Akamatsu (1991), the diffusion velocity method was deduced by considering an arbitrary function *g(x,t)* moving in the x direction with a speed of *u(x,t)* which is not necessarily independent of *g*. The time variation of *g* over an element Δx for a short time interval Δt can be related to the difference between the incoming and outgoing quantities within the element Δx. This relationship was shown by Ogami and Akamatsu (1991) to be,

$$\frac{\partial g}{\partial t}\Delta t \cdot \Delta x \approx \left[ug - \left(u + \frac{\partial u}{\partial x}\Delta x \right)\left(g + \frac{\partial g}{\partial x}\Delta x \right) \right]\Delta t \tag{2.29}$$

When Δx and Δt approach zero and neglecting higher order terms, we get

$$\frac{\partial g}{\partial t}+\frac{\partial ug}{\partial x}=0 \tag{2.30}$$

Similarily the equation describing a function *g(x,y,t)* which moves in two dimensional space with a velocity *u(x,y,t)*, in the x direction and with a velocity *v(x,y,t)* can be written as ,

$$\frac{\partial g}{\partial t}+\frac{\partial ug}{\partial x}+\frac{\partial vg}{\partial y}=0 \tag{2.31}$$

Vorticity in two dimensional flows is a typical example of a scalar field and its equation can be written as

$$\frac{\partial \omega}{\partial t}+\frac{\partial}{\partial x}\left[\left(u-\frac{\nu}{\omega}\frac{\partial \omega}{\partial x}\right)\omega\right]+\frac{\partial}{\partial y}\left[\left(v-\frac{\nu}{\omega}\frac{\partial \omega}{\partial y}\right)\omega\right]=0 \tag{2.32}$$

Comparing equations (2.31) and (2.32), the contribution of diffusion $\vec{u}_d$ to the convective term is $\vec{u}_d=-\frac{\nu}{\omega}(\frac{\partial \omega}{\partial x},\frac{\partial \omega}{\partial y})$. Therefore the vorticity equation can be written in a conservative form as

$$\frac{\partial \omega}{\partial t}+\nabla\bullet\left(\vec{u}\omega+\vec{u}_d\omega\right)=0 \tag{2.33}$$

The concept of diffusion velocity implies that the net flow of vorticity is proportional to the vorticity gradient, which is analogous to Fick's law of diffusion with the diffusion coefficient ν/ω, where ν is the kinematic viscosity. The way the vorticity gradient is obtained in the diffusion velocity is by directly taking the derivatives of the cut off function in the discretized vorticity representation. The diffusion velocity also has the property that the circulation of any closed circuit is invariant if advected with the local fluid velocity and the diffusion velocity. With this property the diffusion effects can be amalgamated into the convection term. Ogami and Akamatsu (1991) examined the applicability of this method by applying it to an one dimensional diffusion test problem and two dimensional flow over a circular cylinder at Reynolds numbers 1200 and 40, which is below the limit of applicability of the random walk method. In a later work, Ogami and Ayano (1995) presented additional results for flow over a circular cylinder using the diffusion velocity method for a wide range of Reynolds number (10^{-1} – 10^{7}). According to the authors, the predicted variation of drag coefficient with Reynolds number shows good resemblance to the experimental data.

The diffusion velocity was also derived by a different approach, from fundamental principles, assuming that vortex elements are convected due to the usual convective velocity and due to the diffusion velocity as discussed in Kimpka and Strickland (1993), Strickland et al (1995) and Strickland et al (1996). Their argument was based on the premise that while the convective velocity is divergence free in incompressible flow, the diffusion velocity is not. This effect was not considered by Ogami and Akamatsu (1991). Therefore, in this approach vortex blobs change their location according to the diffusion velocity and change their size with time according to the divergence of the diffusion

velocity. Kimpka and Strickland (1993) have shown that for one-dimensional case their method provides an improvement over the diffusion velocity method proposed by Ogami and Akamatsu (1991) probably because it makes allowance for a change in vortex blob shape in a circular fashion. However, the formulation has a deficiency that it can not resolve the diffusion velocity in the direction of the vorticity vector. Consequently, it can only be applied to two dimensional flows since the velocity field is always perpendicular to the vorticity field in two dimensional flows.

The extension of the diffusion velocity method to three dimensional applications is quite problematic, due to the effect of the curvature of the vortex lines. When the previous two dimensional method is applied to three dimensional vorticity equation, three dimensional diffusion velocity will be introduced to every component of vorticity. This is not numerically applicable directly since a velocity is to be defined for the Lagrangian particle. The first attempt to introduce three dimensional diffusion velocity method was made by Rivoalen et al (1997, 1999). The authors decompose the vector field $\vec{\omega}$ into a vector parallel to the vorticity vector $\vec{\omega}_t$ and another orthogonal to it $\vec{\omega}_n$. With this decomposition and some vector algebra, they were able to rewrite the vorticity equation with the diffusion velocity term. However, it seems that their method was so computationally expensive, that the authors did not implement the method in a fully three dimensional problem. They have applied the method to an axisymmetric vortex ring.

A more computationally amenable formulation of the three dimensional diffusion velocity method is given by Marshall and Grant (1997) based on the assumption of local two dimensionality of the flow. Their argument was that the vorticity diffusion in most applications is dominantly two dimensional even in three dimensional flows. Diffusion of

vorticity sheet is a typical example of such flow. The same group has successfully applied this formulation of the diffusion velocity to two-phase particulate flows with two-way coupling (Chen and Marshall, 1999) and to three dimensional flow over a sphere using tetrahedral mesh (Marshall et al, 2000). In later study, Grant and Marshall (2005) have mathematically proven the existence of the diffusion velocity for a complex-lamellar vorticity field. In vector calculus jargon, a complex-lamellar is a vector field for which the curl of the vector is everywhere orthogonal to the vector itself (Aris, 1989).

2.4.6 The Moving Least Square Method

Another approach for inclusion of diffusion in vortex method is the moving least squares method. Marshall and Grant (1995) used this method within a fully Lagrangian context of the vortex method. The moving least squares method consists of fitting a polynomial of order two to the vorticity field in the neighbourhood of the point where derivatives are sought. It is one of the objectives of the present study to explore the validity of the moving least squares method within the Vortex-In-Cell frame work. The motivation behind this is the loss of accuracy in the calculation of partial derivatives when the solution proceed in time and the particles become irregularly spaced especially in highly strained flows. In fact, Lui and Doorly (2000) did not need to implement the moving least squares when they applied the particle-in-cell method to the flow of a vortex ring in unbounded domain, probably because the particles maintain their regularity in the flow configuration they were dealing with. The drawback of the moving least squares method is that one has to solve 10x10. linear equations in every time step of the solution for three dimensional flows. These linear equations are used to determine the coefficients of

the second order three dimensional polynomial utilized in this method. In a preliminary work by Sadek and Milane (2007), the Vortex-In-Cell method was used to simulate a three dimensional mixing layer together with the method of moving least squares. A discrepancy was observed in the root mean squares of spanwise velocity fluctuations when compared with the experiment of Oster and Wygnanski (1982) although it is in good agreement with the simulation of Inoue(1987) developed using the vortex method based on the fully Lagrangian filament approach.

2.4.7 Finite Difference Scheme

There is at least one more approach to incorporate diffusion effects in vortex method; that is the finite difference method. The accuracy and simplicity of this method are demonstrated by a recent validation study due to Van Rees et al (2011) This approach is particularly suitable for VIC method and is therefore adopted in Chapters 4 and 5 of this work. It has been employed by Lui and Doorly (2000), Lui (2002), Chatelain et al (2008). In this technique, the Laplacian operator of the diffusion term is approximated by a high order finite difference scheme using vorticity grid values. Vorticity increment is then used to update particle strength through back projection of grid values to the particle location using the interpolation scheme.

2.3.3 Stretching and Tilting

The stretching term in the vorticity equation is given by $(\vec{\omega}\bullet\nabla)\vec{u}$. To test the significance of this expression, let us take a coordinate system as shown in figure 2.1

with r direction along the vortex line s in the direction away from the center of the curvature of vortex line and t along the third normal (Kundu and Cohen, 2002). Then

$$(\vec{\omega} \bullet \nabla)\vec{u} = |\vec{\omega}| \frac{\partial \vec{u}}{\partial r} \tag{2.34}$$

The quantity $|\vec{\omega}| \frac{\partial \vec{u}}{\partial r}$ on the right hand side of equation (2.34) is a vector with three components. The first component $|\vec{\omega}| \frac{\partial u_r}{\partial r}$ represents the change of u_r along the vortex line, that is the stretching of vortex line according to the principle of conservation of angular momentum. The other two components $|\vec{\omega}| \frac{\partial u_s}{\partial r}$ and $|\vec{\omega}| \frac{\partial u_t}{\partial r}$ represent the change of normal velocity components along r and therefore, the rate of turning or tilting of vortex lines about s and t axes, respectively. For example, the turning of the vorticity vector toward the s-axis generates vorticity component along s.

Stretching is merely a characteristic of three-dimensional flows since the term representing stretching vanishes in two dimensional formulation of vorticity transport equation. The vorticity field in three-dimensional turbulent flows can be portrayed as tangled, spaghetti like filaments of concentrated vorticity. According to Biot-Savart law these filaments induce velocity on each other and cause some to stretch and tilt while convecting with the flow. In the absence of viscous dissipation, for the sake of this discussion, stretching of vorticity lines is associated with the enhancement of vorticity in compliance with the law of conservation of angular momentum. This intensification in vorticity results in thinning of vorticity tubes and increase in velocity gradients as

indicated by vorticity definition. This process is thought to be the main physical mechanism by which ever smaller scales of turbulence are produced and maintained (Mathieu and Scott, 2000).

From the computational stand point of three dimensional flows, if vortex elements are used to simulate a flow configuration, the strength of vortex elements must be updated in every time step to account for stretching and tilting. A variety of techniques have been proposed to compute the stretching and tilting. Essentially, stretching computation techniques are different from one another by the manner in which the vorticity field is discretized and the method used in computing the velocity derivatives. In filament method, the explicit computation of the spatial derivative of velocity in stretching term is avoided. This method was originally proposed by Chorin (1982) and later implemented by many researchers: Ashurst and Meiberg (1988) in three dimensional mixing layer simulation, Inoue (1989) for simulation of spatially growing mixing layer, Knio and Ghoniem (1989) for three dimensional vortex simulation of entrainment augmentation due to streamwise structures and Milane and Abdolhoseini (2004) for spatially growing uniformly sheared flow. In this method the vorticity field is approximated by a collection of interconnected vectors. Each vector is represented by two points considered to be the head and tail. The magnitude of vorticity is proportional to the distance between these two points. The stretching term is automatically accounted for by the relative movement of these points. In actual computations, vorticity intensification in general is associated with a rapid stretching and reorientation of these vector elements which result in irregular flow map and loss of accuracy of the solution as the time proceeds. This is the reason the filament vector is usually divided into two smaller vectors when the distance between the

two points becomes large and its circulation is divided between them in what is usually known as regridding step.

In contrast, when disconnected vortex elements are used to discretize the vorticity field, the redistribution of vorticity due to stretching and tilting is explicitly accounted for. Therefore a separate equation governing the change of particle vorticity due to stretching is needed. Several approaches have been developed to update the particle vorticity, leading to different approximations of the stretching term formulation. Anderson and Greengrad (1985) computed the velocity derivative tensor in the stretching term at the particle location in a fully Lagrangian manner. They differentiated analytically the velocity kernel resulted from Biot-Savart law, which is a known function of position and took the convolution summation with the particle vorticity. In this method the velocity derivatives in the stretching term are approximated by

$$\nabla \vec{u}(\vec{x},t) = \nabla \sum_j f_\delta(\vec{x} - \vec{x}_j)\vec{\alpha}_j(t) \tag{2.35}$$

Since f_δ is a known function of $\vec{x}$, the right hand side of equation (2.35) can be explicitly computed. This suggests that the change in particle vorticity due to stretching can be computed in a fractional step as

$$\frac{d\vec{\omega}_p}{dt} = (\vec{\omega}_p(t) \bullet \nabla) \sum_p f_\delta(\vec{x}_p - \vec{x}_j)\vec{\alpha}_j(t) \tag{2.36}$$

The method is later proven by Beale (1986) to converge to the exact solution of three-dimensional inviscid vorticity equation. A variant of this method based on the vector identity $\left(\nabla\vec{a} - (\nabla\vec{a})^T\right)\bullet\vec{b} = (\nabla\times\vec{a})\times\vec{b}$, for any vector fields $\vec{a}$ and $\vec{b}$ can also be used. If $\vec{a}$ is set as the velocity field and $\vec{b}$ as the vorticity field, the right hand side of the above identity will be identically zero and the velocity gradient tensor in the stretching term can be replaced by its transpose or any linear combination of them (Winckelmans and Leonard,1993), i.e. the stretching term can be written as $\left(\vec{\omega}\bullet\nabla^T\right)\vec{u}$ or $\frac{1}{2}\left(\vec{\omega}\bullet\left(\nabla+\nabla^T\right)\right)u$, where $\vec{\omega}$ and $\vec{u}$ are the vorticity and velocity fields, respectively. The first formulation is usually termed as the transpose scheme and the second is termed as the mixed scheme. Mixed scheme offers computational saving due to the symmetry of velocity kernels and transpose scheme conserve the total circulation. All the above schemes converge to the same solution for a divergence free (solenoidal) vorticity field, a condition that can not be kept in a discretized vorticity field (Winckelmans and Leonard, 1988).

When vortex particle method is used in highly strained flows, the calculation of stretching exhibits errors associated with severe distortion of the initial arrangement of vortex particles. Marshall and Grant (1997) proposed and implemented the moving least square technique to calculate derivatives in vorticity transport equation for fully Lagrangian method. They are obtained by locally fitting a polynomial function to a set of control points surrounding a given Lagrangian vortex particle at which the derivatives are required. The authors have used the least squares criterion to find the polynomial then analytically differentiate the polynomial to compute the derivatives. Chen and Marshall (1999) utilized the same technique in the simulation of two-way coupled particulate flow.

Later, Marshall et al (2000) used the moving least square method in three dimensional fully Lagrangian vortex method for the simulation of the flow around a sphere. In the present work, it is intended to extend the applicability of the least squares technique to the Eulerian-Lagrangian Vortex-In-Cell approach adopted by this study as a remedy for irregularity of the particle spacing.

In the context of Vortex-In-Cell (VIC) method, another approach to compute the stretching term is usually adopted. Vorticity difference due to stretching term in the vorticity transport equation is computed by a high order finite difference scheme on Eulerian grid points covering the computational domain. Grid values are then back projected to the particle locations to update their strength. This method is used by Lui and Doorly (2000), Micheal et al (2000), Lui (2001) and Lui (2002). A conservative variant of this method is implemented by Walther and Koumoutsakos (2001) in the simulation of two-way coupled particle-laden flow, by writing the stretching term in a conservative form, utilizing the solenoidality of the vorticity field. The grid values of the velocity and vorticity are multiplied and differentiated on the grid and finally interpolated back to the particles. They used this technique in the simulation of particle-laden flow with two-way coupling by a (VIC) method. Van Rees et al (2011) used the transpose formulation for the stretching term and discretized it with a fourth order finite difference scheme in their vortex method validation study applied to Taylor-Green vortex.

2.5 Spatial Adaptation (Re-Meshing)

Most vortex method applications incorporate some kind of spatial adaptation in the form of re-meshing or re-gridding algorithm. Re-meshing consists of many steps to restarting

the particle field on a regular grid every few time steps and recalculating the particle strength by interpolation or other means. A complete theory of stability and convergence of vortex methods for free space two and three dimensional vorticity equations have been developed by Beale and Majda (1982). Convergence requires vortex elements to overlap during the computation time. Nonetheless Beale and Majda (1986) have tested vortex methods with high-order cut off function and those numerical experiments confirm the theoretical prediction of the order of convergence for moderate times, however, at later times the high order accuracy progressively deteriorates. This seems to be due to the distortion of the Lagrangian grid; that, in general takes place as the initial grid is deformed by the flow. This leads to progressive loss of accuracy in the computation of velocities. Beale and Majda (1986) concluded that to obtain accurate solution for long integration times, re-meshing techniques are usually needed. Introducing re-meshing techniques decrease the local Lagrangian grid size and allow stability and accuracy for longer times. Unfortunately this introduces increasing levels of numerical diffusion, undermining the main feature of the vortex methods.

The current common approach of "remeshing" (also called "redistribution" by some workers) of the particle field consists of constructing a Cartesian lattice of new particle locations and obtaining the new strength values from the old particles by interpolation. The two dimensional or three dimensional interpolation rules are built by Cartesian tensor product of their one dimensional kernels. These kernels have been constructed of increasing order in terms of the number of particles involved in the interpolation formula and the highest order of vorticity moment conserved. The commonly used interpolation kernels are of two families, the "Λ" and the "M" family, as described in detail in Cottet

and Koumoutsakos (2000). Using any of the interpolation formulas φ, the remeshing schemes obtain the contribution of strength from the i[th] old vortex particle $\Delta\vec{\alpha}_{i,p}$ to the new vortex particle location $(\vec{x}_p)$, as will be discussed in section 5.2

$$\Delta\vec{\alpha}_{i,p} = \vec{\alpha}_i \varphi\left(\frac{x_p - x_i}{h}\right)\varphi\left(\frac{y_p - y_i}{h}\right)\varphi\left(\frac{z_p - z_i}{h}\right) \tag{2.37}$$

2.6 Relevant Literature on Vortex Methods

Among the many numerical and theoretical treatments of mixing layers one may distinguish two main approaches. The first school has chosen to rely on classical hydrodynamic stability theory. In this respect the mixing layer is conceptualized as a superposition of interacting instability waves that propagate and amplify in the downstream direction. Ho and Huerre (1984) have published an extensive review on two dimensional mixing layers within the frame work of stability theory. In their review they have shown the ability of stability analysis to describe very satisfactorily the initial development of mixing layer and reproduce the roll-up phenomenon. They also showed that beyond the region of exponential growth, Kelvin-Helmholtz instability waves evolve into a periodic array of compact spanwise vortices. Another approach provides a description in terms of the evolution of the vorticity field. This task can be conveniently accomplished by vortex methods, the focus of the present work.

A large body of research work has utilized vortex methods in different types of flow problems under different flow conditions. The present review will be limited to three

dimensional vortex methods and some two dimensional applications that have three dimensional character (axis-symmetric).

Inoue (1987) simulated incompressible mixing layer by a three dimensional vortex method by introducing three dimensional disturbances in an otherwise two dimensional flow field. He used vortex filament method, where each filament is represented by the sum of a two dimensional undisturbed part and a three dimensional perturbed part. Kinematic evolution of the filaments showed large scale spanwise variation of flow field produced as a result of amplification of initial disturbances. Pairs of streamwise vortices are formed at fixed spanwise locations that depend on initial disturbances. His results indicated also that the presence of background disturbances may be essential for the formation of streamwise vortices.

Ashurst and Meiberg (1988) have used vortex filament method to carry out numerical investigation of a temporally evolving three dimensional inviscid shear layer. They have included two signs of vorticiy to account for the weaker boundary layer leaving the splitter plate. They have found that the flow is initially dominated by the growth of two dimensional Kelvin-Hemholtz instability which leads to roll-up and the formation of spanwise structures. Their computations also showed concentrated streamwise vortices originated in the braid region between the spanwise rollers, whereas the translative core instability does grow beyond small amplitudes.

Knio and Ghoniem (1989) have extended the vortex methods to solve for scalar field besides the flow field. The method is termed transport element method. It is based on the discretization of the vorticity/scalar gradient vectors into finite overlapping elements. The method is applied to the simulation of three dimensional shear layers with high scalar

concentration in one stream. The flow is perturbed in streamwise and spanwise directions. Results show that the evolution of vorticity remains essentially two dimensional within the linear range of Kelvin-Helmholtz instability until the development of large scale spanwise structures connected by thin braids of vorticity, which will stimulate a strong streamwise vorticity. Entrainment is shown to increase by almost 25% over two dimensional simulations. In another work, Knio and Ghoniem (1990) have used three dimensional vortex method based on the discretization the vorticity field into vortex vector elements of finite spherical core for the simulation of propagation and stability of vortex ring. Results of unstable mode frequency and growth rate are in good agreement with analytical results. The late stages of evolution of instability showed the generation of small scales in the form of hair-pin vortex structure. In a later work, Knio and Ghoniem (1992) explored the effect of density variation on three dimensional shear layer using their modified vortex method (transport element method). Similar series of events have been observed in the case of variable density except that vorticity generation due to density variation leads to the formation of asymmetric cores whose volumetric composition are biased towards the lighter fluid.

Walther and Koumoutsakos (2001) utilized a three dimensional viscous vortex method for simulation of particulate flow with two-way coupling. The flow field is computed using purely Lagrangian vortex elements moving with the local velocity, while their strength is modified to account for viscous diffusion, vortex stretching and vorticity generation induced by the particles. They have used remeshing to accommodate vorticity generation and particle strength exchange (PSE) method to simulate viscous diffusion. The method was validated against finite difference study of swirling flow with particles.

Milane and Abdolhosseini (2004) used a mixed Eulerian- Lagrangian approach based on Vortex-In-Cell (VIC) method and vorticity- velocity formulation to solve three dimensional, incompressible, inviscid, spatially growing uniformly sheared flow. The vortex filaments were initially subjected to three dimensional random perturbations in order to simulate nearly isotropic conditions. Results showed qualitative agreements of the three components of energy ratio with other simulations and experiments.

Ploumhans et al (2002) have used fully Lagrangian vortex method along with the (PSE) diffusion technique to simulate flow around bluff bodies of a general three dimensional geometry. The method was applied to flow past a sphere at Reynolds numbers of 300, 500 and 1000, and was validated against experiments and numerical results.

Lakkis and Ghoniem (2003) have presented an axisymmetric vortex method for low Mack number diffusion controlled combustion. In their discretization, they have used vortex ring elements. An accurate solution for the diffusion term is also implemented. Results have shown very good agreement with finite difference solution of the same problem.

Giovannini and Gagnon (2006) developed a three dimensional Vortex-In-Cell method for two counter rotating vortex tubes. They validated their results by comparison to pseudo spectral code. Decay of kinetic energy and enstrophy were used as a diagnostic tool to quantify the dissipative behaviour of the vortex method. Their results demonstrated the ability of the vortex method to predict complex vortical flows.

Chatelain et al (2008) used the Parallel Particle Mesh (PPM) open source code to simulate three dimensional aircraft wake by vortex method. They utilized the mesh system to solve for the velocity, stretching and diffusion terms. They were able to use 1.6

billion particle and 2048x1024x768 grid points run on 4096 processors. Another validation study for the three dimensional vortex method utilizing the same (PPM) code was published recently by Van Rees et al (2011). In this work, vortex method was compared with the results of pseudo spectral method, where two vortical flows were tested; namely Taylor-Green vortex at Re=1600 and two colliding vortex tubes at Re=10000. Except for the smallest length scales, vortex method results matched that of pseudo spectral method.

To the author's knowledge, the Vortex-In-Cell (VIC) method has never been tested in a temporally developing viscous three dimensional mixing layer. It is one of the objectives of the present study to investigate the applicability of this method to such flow configuration.

Chapter 3

Formulation and Mathematical Models

3.1 Introduction

The most general starting points to solve any physical problem of incompressible shear flow type are the laws of nature arranged in two main groups; conservation of matter and conservation of momentum. These laws come together into the mathematical form of differential equations then a suitable solution technique is devoted to solve a specific problem. Our task in this chapter is to derive the differential equations governing the three dimensional shear flow phenomenon in a suitable coordinate system then to present a numerical solution method.

3.2 Vorticity Equation

The three dimensional incompressible flow of Newtonian viscous fluid may be described in terms of the velocity $\vec{u}(\vec{x},t)$ and pressure $p(\vec{x},t)$ of the flow by the momentum equation, written in an inertial frame of reference,

$$\frac{\partial \vec{u}}{\partial t} + (\vec{u} \bullet \nabla)\vec{u} = -\frac{1}{\rho}\nabla p + \nu \nabla^2 \vec{u} + \vec{g} \qquad (3.1)$$

and the continuity equation,

$$\nabla \bullet \vec{u} = 0 \qquad (3.2)$$

In equations (3.1) and (3.2), ν and ρ denote the kinematic viscosity and the density of the fluid respectively, $\vec{g}$ is the acceleration due to gravity and ∇ is a vector operator given by $\left[\frac{\partial}{\partial x}\vec{e}_x + \frac{\partial}{\partial y}\vec{e}_y + \frac{\partial}{\partial z}\vec{e}_z\right]$. To solve for a certain flow configuration, the equations above should be supplemented by the initial conditions,

$$\vec{u}(\vec{x},0) = \vec{u}_o(\vec{x}) \qquad (3.3)$$

and the boundary conditions which need to be enforced. On a rigid body $(\vec{x}_o)$, the velocity of the fluid $(\vec{u})$ should be equal to the velocity of the body $(\vec{u}_s)$ and at infinity, if the flow is unbounded

$$\vec{u}(\vec{x}) \to \vec{U}_\infty \quad as \quad |\vec{x}| \to \infty \qquad (3.4)$$

where $\vec{U}_\infty$ is the free stream velocity.

For the purpose of the present numerical scheme, equation (3.1) is recast in terms of vorticity $\vec{\omega}$. The vorticity $\vec{\omega}$ of a flow field with velocity distribution $\vec{u}$ is defined by

$$\vec{\omega} = \nabla \times \vec{u} \tag{3.5}$$

The vorticity in Cartesian tensor notation can also be expressed as

$$\omega_i = \varepsilon_{ijk} \frac{\partial u_k}{\partial x_j} \tag{3.6}$$

where ε_{ijk} is the alternating tensor. As the curl of a velocity vector, the vorticity is a vector too and its magnitude is twice the rate of solid body rotation of a small fluid element about its own axis.

To develop the general vorticity equation, recognizing that

$$(\vec{u} \bullet \nabla)\vec{u} = \nabla(\frac{1}{2}\vec{u} \bullet \vec{u}) - \vec{u} \times \vec{\omega} \tag{3.7}$$

equation (3.1) may be written as,

$$\frac{\partial \vec{u}}{\partial t} + \nabla\left(\frac{1}{2}\vec{u} \bullet \vec{u}\right) - \vec{u} \times \vec{\omega} = \frac{1}{\rho}\nabla p + \nu\nabla^2 \vec{u} + \vec{g} \tag{3.8}$$

taking the curl of the equation above and making use of the following vector identities; for any scalar field a and vector field $\vec{b}$, $\nabla \times \nabla a = 0$, $\nabla \bullet \nabla \times \vec{b} = 0$. Also assuming that the flow is barotropic; that is the density is a function of pressure only and assuming that the body force is conservative, i.e. can be written as a gradient of scalar potential, the vorticity equation is written as

$$\frac{\partial \vec{\omega}}{\partial t} + (\vec{u} \bullet \nabla)\vec{\omega} = (\vec{\omega} \bullet \nabla)\vec{u} + \nu\nabla^2 \vec{\omega} \tag{3.9}$$

It is helpful to explain the significance of the different terms in equation (3.9). The first term on the left hand side is the unsteady term. The second term on the left hand side represents the convective transport of vorticity. The first term on the right hand side represents the stretching and tilting of the vorticity lines which intensifies the vorticity. The diffusion of vorticity due to the action of viscosity is represented by the last term.

Equation (3.9) is a vector equation that has three separate component equations in six unknowns (three components of vorticity and three components of velocity). The definition of vorticity in equation (3.5) is another vector equation expressing the relation between $\vec{u}$ and $\vec{\omega}$. At first glance, it would appear that no additional equations to find $\vec{u}$ and $\vec{\omega}$ are needed and the continuity equation is redundant. This conclusion is not true,

because the vector definition of vorticity in equation (3.5) is actually two independent scalar equations. This can be easily shown by taking the divergence of equation (3.5).

$$\nabla \bullet \vec{\omega} = \nabla \bullet \nabla \times \vec{u} = 0 \tag{3.10}$$

Therefore the three components of vorticity are related by equation (3.10); i.e. once any two components of vorticity are known, the third may be deduced by integration of (3.5) and application of boundary conditions. The continuity equation is therefore necessary to close the set of equations. It is utilized by introducing the vector potential $\vec{\Phi}$ such that,

$$\vec{u} = \nabla \times \vec{\Phi} \tag{3.11}$$

because the divergence of the curl of any vector field is identically equal zero. Taking the curl of the equation (3.11) and without loss of generality select $\vec{\Phi}$ to be a solenoidal field (Marshall 2001), the vector potential is related to the vorticity via the following vector Poisson equation.

$$\nabla^2 \vec{\Phi} = -\vec{\omega} \tag{3.12}$$

The velocity components can be found from equation (3.11). Equations (3.9, 3.11 and 3.12) along with the boundary and initial conditions constitute a complete set of equations to solve for the vorticity and velocity fields. This formulation is widely used in two dimensional flow situations, mainly because The Poisson equation (3.12) is a scalar

equation in this case. This argument does not hold when three dimensional flow problems are to be investigated. In this case, Poisson equation (3.12) is a vector equation and additional numerical operation is necessary to calculate the velocity field. In addition, the entire solution of vorticity-vector potential formulation is dependent on the accurate calculation of the vorticity at the boundaries. In other words implementation of boundary conditions for the three dimensional case appears to be far more complicated than the vorticity-velocity formulation which is discussed in the next section.

3.3 Vorticity-Velocity Formulation

Alternative formulation of the governing equations can be obtained by taking the curl of vorticity definition given in equation (3.5),

$$\nabla \times \vec{\omega} = \nabla \times \nabla \times \vec{u} = \nabla(\nabla \bullet \vec{u}) - \nabla^2 \vec{u} \tag{3.13}$$

Utilizing the incompressibility constraint, equation (3.2) results in

$$\nabla^2 \vec{u} = -\nabla \times \vec{\omega} \tag{3.14}$$

Summarizing the above results, the mathematical model for the flow in domain D is expressed by the following set of equations,

$$\frac{\partial \vec{\omega}}{\partial t} + (\vec{u} \bullet \nabla)\vec{\omega} = (\vec{\omega} \bullet \nabla)\vec{u} + \nu \nabla^2 \vec{\omega} \qquad \text{in } D \qquad (3.9)$$

$$\nabla^2 \vec{u} = -\nabla \times \vec{\omega} \qquad \text{in } D \qquad (3.14)$$

$$\vec{\omega}(\vec{x},0) = \vec{\omega}_0(\vec{x}) \qquad \text{in } D$$

$$\vec{u} \to \vec{U}_\infty \qquad \vec{x} \to \infty$$

In the above equations $\vec{x} = (x, y, z)$ is the position vector, $\vec{u} = (u, v, w)$ is the velocity, t is time, $\vec{\omega} = (\omega_x, \omega_y, \omega_z)$ is the vorticity vector field, $\nabla = (\partial/\partial x, \ \partial/\partial y, \ \partial/\partial z)$ is the gradient operator, $(\nabla\times)$ is the curl operator, $\nabla^2 = \partial^2/\partial x^2 + \partial^2/\partial y^2 + \partial^2/\partial z^2$ is the Laplacian operator and $\vec{\omega}_0(\vec{x})$ is the initial vorticity distribution,

The above set of equations is well posed and is equivalent to the unsteady incompressible Newtonian Navier – Stokes equations in three dimensions. The vorticity-velocity formulation helps in eliminating the pressure from the unknowns of the equations. Our numerical method is based on the discretization of the above equations using a mixed Eulerian-Lagrangian Vortex-In-Cell method.

3.4 Vortex Particle Method

The starting point to solve equations (3.9 and 3.14) shown in the box by vortex particle method is to rewrite equation (3.9) in a coordinate frame following fluid particle (Cottet and Koumoutsakos, 2000)

$$\frac{d\vec{\omega}}{dt} = (\vec{\omega} \bullet \nabla)\vec{u} + \nu \nabla^2 \vec{\omega} \qquad (3.15)$$

In Lagrangian representation, the fluid volume is discretized into a finite set of material particles and equation (3.15) is used to describe the motion of each particle as it interacts with other particles. In other words, the left hand side of equation (3.15) represents the total derivative following a single particle and the flow problem is dealt with by solving equation (3.15) for each particle. The difference between equation (3.9) and equation (3.15) is the absence of the convection term $(\vec{u} \bullet \nabla)\vec{\omega}$ in equation (3.15). In the present vortex particle method, the vorticity is advected explicitly by the moving particles. Thus the explicit discretization of the convection term that causes smearing of the flow features in a purely grid based method can be avoided.

The vorticity field for the present numerical scheme is represented by a finite number of particles *N* and the vorticity at any point $\vec{x}$ is considered as the discrete sum of the vorticity field of the particles. The p^{th} Lagrangian particle is defined by a position vector $\vec{x}_p$ and a vector strength $\vec{\alpha}_p$ that have the unit of circulation times length,

$$\vec{\alpha}_p = \int_{V_p} \vec{\omega} dv \approx \vec{\omega}_p v_p \tag{3.16}$$

where v_p is a fluid volume associated with the particle *p*. Therefore the vorticity field can be retrieved from the discretized vortex particle field by

$$\vec{\omega}(\vec{x},t) = \sum_N \vec{\omega}_p(t) v_p \delta(\vec{x} - \vec{x}_p(t)) = \sum_N \vec{\alpha}_p(t) \delta\left(\vec{x} - \vec{x}_p(t)\right) \tag{3.17}$$

Where δ is the three dimensional Dirac delta function. Rigorous mathematical justification of this particle approximation along with its error estimates is given in Cottet and Koumoutsakos (2000), based on the weak solution of advection equation. The velocity field induced by the vorticity is obtained by solving Poisson equation (3.14) using the discretized vorticity field for the right hand side. However the singularity of this representation will result in unrealistically high velocities when the distance between two vortices tends to zero, i.e. when $(\vec{x}-\vec{x}_p)\to 0$. In fully Lagrangian approach a mollification function, usually with a circular symmetry is used to represent the distribution of vorticity within a finite predetermined core. This function has to satisfy certain moment conditions. Two and three dimensional Gaussian distributions are the most commonly used ones. In the mixed Eulerian-Lagrangian Vortex-In-Cell method adopted by this study, the grid system serves as mollification mechanism that removes the singularity of the vorticity representation in equation (3.17). Once the singularity is removed and the velocity is obtained by the solution of Poisson equation the convection step of the vorticity transport equation is accounted for by a set of ordinary differential equations following the motion of the material point as

$$\frac{d\vec{x}_p}{dt} = \vec{u}(\vec{x}_p, t) \tag{3.18}$$

The change of particle vorticity due to stretching and tilting are dealt with separately as

$$\frac{d\vec{\omega}_p}{dt} = \left(\vec{\omega}_p \bullet \nabla\right)\vec{u}_p \tag{3.19}$$

and in the case of viscous flow, the diffusion effects on vortices are computed by

$$\frac{d\vec{\omega}_p}{dt} = \nu\nabla^2\vec{\omega}_p \tag{3.20}$$

Equations (3.18-3.20) are the Lagrangian equivalent of the commonly used Eulerian vorticity transport equation (3.9).

3.5 Fractional Step Method

This work is concerned with the development and validation of a hybrid Lagrangian-Eulerian vortex method for numerical simulation of unsteady, incompressible and viscous flows. The solution proceeds by successively considering equations (3.18-3.20) using the fractional step method. The essence of fractional step method is to consider the different physical processes within the governing equations successively rather than simultaneously. Extensive description of this method may be found in Yanenko (1971).

Cottet and Koumoutsakos (2000) associated this method, which is sometimes called viscous splitting, to the division made by Prandtl in 1904 between viscous and inviscid effects. Convergence of fractional step method for Navier Stokes equation for unbounded flow was proved by Beale and Majda (1981). The analysis of fractional step method for the general linear convection-diffusion equation is also given in Cottet and Koumoutsakos (2000). It reveals that fractional step method is always first order accurate in time irrespective of the time stepping used. The algorithm consists of sub-time steps, where the effects of convection, stretching and diffusion are considered successively.

Algorithmically, for three dimensional viscous flows, the method consists of advancing the vortices with the convective velocity in the first sub-step and changing the strength of the vortices to account for stretching in the second sub-step. The viscous diffusion is accounted for in the third sub-step. For three dimensional viscous flows, the mathematical representation of the vorticity transport equation in the fractional step method is

$$\frac{\partial \vec{\omega}}{\partial t} + (\vec{\omega}.\nabla)\vec{u} = 0 \qquad \text{(a)} \qquad \begin{cases} \dfrac{d\vec{x}_p}{dt} = \vec{u}_p(\vec{x}_p, t) \\ \dfrac{d\vec{\omega}_p}{dt} = 0 \end{cases} \qquad \text{(b)} \qquad (3.21)$$

where equation (3.21 a) corresponds to the Eulerian formulation of the convection sub-step and equation (3.21 b) represents the Lagrangian formulation of the convective sub-step

$$\frac{\partial \vec{\omega}}{\partial t} = (\vec{\omega}.\nabla)\vec{u} \qquad \text{(a)} \qquad \begin{cases} \dfrac{d\vec{x}_p}{dt} = 0 \\ \dfrac{d\vec{\omega}_p}{dt} = (\vec{\omega}_p.\nabla)\vec{u}_p \end{cases} \qquad \text{(b)} \qquad (3.22)$$

where equation (3.22 a) corresponds to the Eulerian formulation of the stretching sub-step and equation (3.22 b) represents its Lagrangian counterpart, and

$$\frac{\partial \vec{\omega}}{\partial t} = \nu \nabla^2 \vec{\omega} \qquad \text{(a)} \qquad \begin{cases} \dfrac{d\vec{x}_p}{dt} = 0 \\ \dfrac{d\vec{\omega}_p}{dt} = \nu \nabla^2 \vec{\omega}_p \end{cases} \qquad \text{(b)} \qquad (3.23)$$

where equation (3.23 a) corresponds to the Eulerian formulation of the viscous sub-step and equation (3.23 b) represents its Lagrangian counterpart. In equations (3.21-3.23) subscript *p* corresponds to the values at the particle locations. In the following sections every sub-step of the solution procedure will be discussed explicitly

3.5.1 The Convection Substep

In the present Vortex-In-Cell (VIC) method, the initial vorticity field is discretized into a set of vortex particles same as in pure Lagrangian method. Upon initializing a vortex method calculation, one needs to obtain the identifying quantities of the vortex particles, i.e. their location and circulation strength. The strength of each particle is computed using equation (3.16). The resolution of the calculation is dictated by a grid system overlaid on the computational domain. Uniform grid of dimension *h* is used in this work. Therefore the volume associated with each particle is h^3 and the initial strength of each particle is given by $\vec{\omega} h^3$. The strength of each particle is therefore a vector parallel to $\vec{\omega}$. The strength of each particle is then projected onto the nodes of the fixed Eulerian grid using the appropriate interpolation formula. The contribution of each particle is summed to find the mesh vorticity. The velocity field is calculated by solving Poisson equation (3.14) on

the mesh instead of computing the velocity from Biot-Savart law which is applied directly to the set of vortex particles. Thus the present work combines the mesh based method with the particle formulation to form a hybrid method. Thus the present method combines the best feature of Lagrangian approach, which is free of dissipation errors and the best feature of the Eulerian approach, which has reasonable computation cost.

3.5.1.1 Interpolation Scheme

The two dimensional and three dimensional interpolation rules are built by Cartesian tensor products of their one dimensional kernels. These schemes have been constructed in increasing order with respect to the highest order of moment they conserve. Mathematically, the three dimensional interpolation schemes are expressed in terms of grid spacing *h*, as

$$\omega_i = \frac{1}{h^3}\sum \vec{\alpha}_p \varphi\left(\frac{x_p - x_i}{h}\right)\varphi\left(\frac{y_p - y_i}{h}\right)\varphi\left(\frac{z_p - z_i}{h}\right) \tag{3.24}$$

where φ is the interpolation kernel, subscripts p and i indicate the particle and grid locations respectively. As discussed in chapter 2, the M family of interpolation schemes are developed by successive convolution of the window function with itself. In this work the M'$_4$ scheme is used because it introduces minimum computational diffusion. For the M'$_4$ interpolation scheme, the effective hyperviscosity ν_{eff}, as indicated by Winckelmans (2004), is bounded by

$$(\nu_{eff}\Delta t)^2 = 3h^4/128 \tag{3.25}$$

Where Δt is the time step and h represents the grid size. The M'$_4$ one dimensional kernel is given by

$$\varphi(x) = \begin{cases} 1-\frac{5}{2}|x|^2+\frac{3}{2}|x|^3 & |x|<1 \\ \frac{1}{2}(2-|x|)^2(1-|x|) & 1<|x|<2 \\ 0 & |x|>2 \end{cases} \tag{3.26}$$

This interpolation kernel is of second order approximation, which means that the total circulation, the first and the second moments are conserved. As an example, let us assume a one dimensional frame in which a particle is located at a point x_p at a distance of 0.3 to the right of the grid point x_i as shown in figure (3.1). Using the M'$_4$ scheme, this particle will contribute to the vorticity of the grid points x_{i-1}, x_i, x_{i+1}, x_{i+2} , in the following proportions, -0.0735, 0.8155, 0.2895, -0.0315, respectively

In three dimensional coordinate system,the vorticity of a particle at point p within a cell, will be assigned to the closest 64 mesh points by the three dimensional filter built from the tensorial product of the one dimensional kernel. Equation (3.26) is used to find the particle contribution to the vorticity of the grid. Figure 3.2 (a) shows the one dimensional distribution of the M'$_4$ interpolation scheme. Figure 3.2 (b) represents its two dimensional counterpart and figure 3.2 (c) shows an isosurface plot with a section through the plane x=0; fifty equally distributed levels between -0.16 and 1 are used in the plot.

3.5.1.2 Calculation of Velocity

Instantaneous velocity of the flow is obtained by solving Poisson equation (3.14) along with the boundary conditions. In this work, Poisson equation is solved on the Eulerian grid covering the flow field. By this method, the computational cost is significantly reduced compared to the Biot-Savart law used in fully Lagrangian schemes. Applying the central differencing to left hand side term of equation (3.14) gives the seven-point approximation of the Laplacian. Successive Over Relaxation (SOR) with point by point solution is used, (Moin, 2001). The resulting finite difference approximation of the Poisson equation with successive over relaxation, for the streamwise component as an example, is given by,

$$u_{ijk}^{n+1} = (1-\kappa)u_{ijk}^{n} + \frac{\kappa}{2(1+\beta^2+\lambda^2)}[u_{i+1,j,k}^{n} + u_{i-1,j,k}^{n+1} + \beta^2(u_{i,j+1,k}^{n} + u_{i,j-1,k}^{n+1})$$

$$+ \lambda^2(u_{i,j,k+1}^{n} + u_{i,j,k-1}^{n+1}) + (h_x)^2 D] \qquad (3.27)$$

where h_x, h_y and h_z are the grid size in *x, y, z* directions, respectively, *n* indicates the iteration number, *i, j, k* are the indices of grid location in *x, y, z,* directions, respectively. $\beta = h_x/h_y$ and $\lambda = h_x/h_z$. The numerical value of the over-relaxation factor $\kappa = 1.8$ was adjusted by numerical trials such that fast convergence was obtained. *D* corresponds to the nodal values of the right hand side of equation (3.14), i.e. the curl of vorticity. Two methods are used to calculate latter term; namely fourth order finite difference method and the moving least squares method. These methods will be further elaborated and discussed in chapters 5 and 6, respectively. Once the velocities at the nodes are obtained,

the velocity of the particles is calculated using the M'$_4$ scheme by involving the velocity at the nearest 64 grid points according to

$$\vec{u}_p = \sum_{i=1}^{64} \vec{u}_i \varphi\left(\frac{x_p - x_i}{h}\right)\varphi\left(\frac{y_p - y_i}{h}\right)\varphi\left(\frac{z_p - z_i}{h}\right) \tag{3.28}$$

where $\varphi\left(\frac{x_p - x_i}{h}\right)\varphi\left(\frac{y_p - y_i}{h}\right)\varphi\left(\frac{z_p - z_i}{h}\right)$ represents the contribution of grid point *i* to the velocity of the particle *p*. The particles are then advected by integrating equation (3.21) using the modified Euler method.

3.5.1.3 Stretching and Tilting

The vorticity transport equation for three dimensional flows involves the stretching term $(\vec{\omega} \bullet \nabla)\vec{u}$. A direct method to determine the strength increment of a particle due to stretching is used. In this method, the velocity derivative at the node is computed and multiplied by the corresponding grid value of vorticity. Then the product is interpolated back to the particle location. Thus the change of the particle vorticity is obtained by explicitly solving the following equation (3.22 b)

$$\left(\Delta\vec{\omega}_i\right)_{st} = \left[(\vec{\omega} \bullet \nabla)\vec{u}\right]_d \Delta t \tag{3.29}$$

where the first term on the left hand side represents the change in the grid vorticity due to stretching and Δt is the time step. The subscript *d* indicates the discrete approximation of

the exact term inside the square brackets. The changes in vorticity computed by equation (3.29) are then interpolated back to the particle position to update their strength using the M'_4 interpolation scheme.

Two methods have been used to compute the velocity derivative on the grid, the fourth order finite difference and the moving least squares. Details of implementation of these methods will be discussed in chapters 5 and 6 respectively. In this work M'_4 interpolation scheme is used to transfer information between the grid and the surrounding particles. Consequently, vorticity increments computed from the solution of equation (3.29) will contribute to the strength change of particles located inside a cube of four mesh length in every direction.

3.5.2 The Diffusion Sub-step

In the present work, the diffusion term is calculated on the grid using two methods to compute the Laplacian of the vorticity field, namely a fourth order finite difference scheme and the moving least squares scheme. The vorticity increment due to the diffusion term is computed from the explicit solution of equation (3.23 b),

$$\left(\Delta\vec{\omega}_i\right)_{diff} = \left[\nu\nabla^2\vec{\omega}\right]_d \Delta \tag{3.30}$$

where the same notations as in equation (3.29) are used. The vorticity increment is then interpolated from the grid location to the neighboring Lagrangian particles using the M'_4 interpolation schemes outlined earlier. As a consequence of diffusion, during every time

step vorticity usually enters regions that were devoid of vorticity in the previous time step. This is manifested in a significant vorticity increment at the grid locations where there are no particles within one or two grid sizes, depending on the interpolation scheme, surrounding the corresponding grid. In that case new particles are created at the grid location if the vorticity increment is greater than a predetermined threshold.

3.6 The Vorticity Correction

Although vortex methods for two dimensional and three dimensional solutions are based on the same concept of weak solutions of the advection equation (Cottet and Koumoutsakos, 2000), the three dimensional implementation has specific difficulties related to the divergence free constraint on the vorticity field, i.e. equation (3.10) has to be satisfied. Vortex methods in general do not guarantee that the divergence of the vorticity field remains zero for long time simulations. Vortex filament methods are very particular in this respect, since the solenoidality constraint is specified implicitly. However the divergence free condition is crucial to ensure that the velocity is accurately computed by the solution of Poisson equation. Consequently, the question of the divergence of the vorticity is central in the three dimensional vortex methods not only from the physical point of view but also from the numerical point of view. One way of assuring that the vorticity field is solenoidal at all times was proposed by Cottet (1996). Cottet proposed to correct the vorticity field at every time step such that the divergence free condition is satisfied all the time. The method is based on the Helmholtz vector decomposition of the vorticity field (like any vector field) into a gradient and rotational (curl) parts as

$$\vec{\omega} = \nabla\gamma + \nabla \times \vec{A} \tag{3.31}$$

where γ is a scalar and $\vec{A}$ is a vector. Then by taking the divergence of the above equation and making use of the vector identity $\nabla \cdot \nabla \times \vec{A} = 0$ for any vector $\vec{A}$, the following Poisson equation is obtained,

$$\nabla^2 \gamma = \nabla \cdot \vec{\omega} \tag{3.32}$$

The divergence free condition can be maintained by subtracting the gradient part of the vorticity $\nabla\gamma$ from the vorticity field. For VIC implementation, the Poisson equation (3.32) along with the boundary conditions of the problem can be easily solved. The implementation of the vorticity correction method within the VIC frame work comprises the following steps starting from the vorticity values at the grid.

1. Compute the vorticity divergence $\nabla \cdot \vec{\omega}$ on the grid
2. Solve Poisson equation (3.32) on the grid along with the boundary conditions and find the gradient part γ. The same solution method for the velocity Poisson equation (3.14) is used
3. Compute the gradient of γ on the grid using fourth order central difference approximation.
4. Subtract the gradient $\nabla\gamma$ from the grid vorticity to obtain the corrected vorticity field, i.e. $\vec{\omega}_{corrected} = \vec{\omega} - \nabla\gamma$

This procedure allows exterminating the divergence of the grid vorticity resulting from the discretization scheme of the vorticity field. The solenoidality of the particle vorticity will follow if a robust and efficient interpolation and assignment scheme is used, i.e. the M'_4 interpolation scheme.

Chapter 4

Validation Tests for the Numerical Method

4.1 Introduction

Prior to considering the three dimensional vortex method, results of preliminary calculations to validate the various aspects of the numerical method which are pertinent to the problem to be considered are presented. The two dimensional spatially growing mixing layer will be used in this validation test. This flow has been chosen because it is one of the most extensively scrutinized flow problems both experimentally and numerically over the past half century and consequently a wealth of well established information and literature are available for comparison. The validation will comprise of velocity calculation from a given vorticity field, testing the interpolation and assignment scheme and study the effect of grid size and particle number on the accuracy of the method. Flow features to be considered are the mean flow, momentum thickness, velocity statistics, development of the vorticity field, turbulent energy spectrum and streak lines.

4.2 Initial and Boundary Conditions

The flow configuration used to validate the solution procedure is comprised of a smooth plate separating two streams of fluids at different velocities. Neglecting the effects of the boundary layer, the uniform velocities above and below the splitter plate, u_1 and u_2, respectively, will generate a vortex sheet at the interface of the two streams as shown in figure 4.1. The vortex sheet is inherently unstable and tends to rollup due to the shear instability or Kelvin-Helmholtz instability (Drazin, 2002). . The projection of the vortex sheet on a two dimensional plane is a line at the level of the splitter plate with a singular vorticity. The strength of this line, which has the dimension of circulation per unit length, is given by

$$\Delta u = u_1 - u_2 \tag{4.1}$$

In the vortex particle method the line vortex is initially discretized into a finite number of particles *N*, each of which is defined by its location and circulation. The circulation of each particle is given by

$$\alpha_p = \Delta u . d_x \tag{4.2}$$

where α_p is the particle circulation and d_x is the initial distance between two adjacent particles.

For the base run, the computational domain in this work consists of a square grid of uniform size h_x=h_y=0.125 cm and the number of grid points in two dimensions are M_x·M_y=289x129, where x and y refer to the stream-wise and cross-stream directions, respectively. Initially the vortex line at the splitter plate level is discretized into 14400 particles, with a number of particles per grid element equal to 50. The velocity difference between the two streams is taken to be 675 cm/s and the velocity ratio $r = \frac{u_2}{u_1} = 0.5$. The strength of the vorticity sheet is 675 cm/s and the circulation of each particle initially is 1.6875 cm^2/s. These conditions will be referred to as base run throughout this Chapter. Velocity boundary conditions are taken as follows; error function velocity profile at the inflow edge of the solution domain as given by Spencer and Jones (1971),

$$\frac{u-u_2}{u_1-u_2} = \frac{1}{2}(1-\sigma\, erf\,(\eta-\eta_o)) \tag{4.3}$$

where η is the similarity coordinate given by,

$$\eta = \frac{y}{x-x_o} \tag{4.4}$$

where y is the cross-stream distance measured from the level of the splitter plate, x is the stream-wise distance and x_o is the virtual origin of the mixing layer. The spreading parameter is σ and has been found by Spencer and Jones (1971) to be a function of the

velocity ratio *r*. The experimental data of this parameter are fitted by to the following curve,

$$\frac{\sigma}{\sigma_o} = \frac{1+r}{1-r} \tag{4.5}$$

where σ_o is the spreading parameter when *r=0*. The experimental data for η_o and x_o are also tabulated as a function of *r*, for $r = 0.5,\ \eta_o = 0.009$.

The outflow boundary conditions used in this work is the convective boundary condition, that is the velocity at the outer edge of the solution domain is computed from,

$$\frac{\partial u}{\partial t} + u_{av}\frac{\partial u}{\partial x} = 0 \tag{4.6}$$

where $u_{av} = (u_1 + u_2)/2$ is the average stream-wise velocity. Far field Neumann boundary conditions for the cross stream and streamwise components of velocity (i.e. $\frac{\partial u}{\partial y} = \frac{\partial v}{\partial x} = \frac{\partial v}{\partial y} = 0$) are implemented at the upper and lower edges of the computational domain

The time step is selected such that the initial array of vortex particles will be convected with the average velocity u_{av}, a distance $d_x = u_{av}\,\Delta t$ each time step. Therefore one vortex particle enters the computational domain each time step. The strength of this particle is given by equation (4.2) and the rate of vorticity production at the edge of the splitter plate

is $\frac{\alpha_p}{\Delta t} = u_{av}(u_1 - u_2)$. In the present code, at every time step the particle that leaves the solution domain is discarded while a fresh particle is introduced to the solution domain at the level of the splitter plate. The Kelvin-Helmholtz instability is simulated by perturbing vertically the vortex elements closest to the splitter plate by a small distance $y_d(t)$ around the splitter plate level according to

$$y_d(t) = A\varepsilon \sin(2\pi f t) \tag{4.7}$$

where $A=0.5u_c\Delta t$ is the amplitude and ε represents an arbitrarily small percentage of A (taken as 0.03) in the present study. The frequency f is calculated using $f\theta_o / 2u_{av} = 0.02$,(Milane, 2004) where θ_o=0.56cm is the initial momentum thickness. The flow Reynolds number based on the velocity difference and θ_o is 2500.

4.3 Development of Mean Flow

Despite the extensive studies for understanding the structure and development of self similar plane mixing layers, there exists considerable scatter in the published data leading to many areas of confusion. The main reason for confusion and lack of agreement is that mixing layers are inherently very sensitive to small changes in their operating and initial conditions, the effects of which can persist for relatively long distance downstream. This can be observed even in experiments of nominally similar conditions. Among the parameters that are known to affect the mixing layer behaviour are: state of the initial boundary layer (Mehta, 1991), trailing edge thickness (Dziomba and Fiedler, 1985),

presence of trip wire (Bell and Mehta,1990), periodic oscillation force (Oster and Wygnanski, 1982). Hence it is very difficult to set up comparable experimental results. In this study all these factors are neutralized in order to study the effects numerical parameters on the solution stability, accuracy and convergence.

Self similarity of a single stream mixing layer is shown by Bradshaw (1966) to be attained at a distance equivalent to $1000\theta_o$. No such criterion has been established for two stream mixing layers. However Bell and Mehta (1990) has shown that two stream mixing layers develop self similarity in much smaller distance. In this study figure 4.2 shows the mean flow velocity profiles plotted in similarity coordinate at five downstream locations. The mean stream-wise velocity $[(u-u_2)/\Delta u]$ at every grid points is computed by averaging the instantaneous velocity, obtained from the solution of Poisson equation, over four residence times, that is 57600 time steps. Residence time is defined as the time required for a vortex particle to travel along the solution domain at the convective (average) velocity. Collection of mean velocity data starts after two residence time allowance for flow development. The normalized mean stream-wise velocity is plotted in figure 4.2 against the similarity parameter ξ, where;

$$\xi = \frac{y - y_{0.5}}{\theta(x)} \tag{4.8}$$

The momentum thickness $\theta(x)$ was selected as a length scale parameter because it is an integral parameter and shows less sensitivity to noise in data. As shown in figure 4.2, similarity of velocity profiles was attained at 1/6 of the length of the computation

domain. The inflection point of the mean velocity profile is apparently shifting toward the lower speed stream as the computation moves down stream. In experimental results, self similarity took longer distance downstream to be established due to the wake effects of the splitter plate. Results of experiment of Bell and Mehta (1990) are also plotted on the same figure. The agreement is adequate.

To study the effect of grid size and number of particles on the accuracy of the mean flow, same code was run with the same computational domain and Reynolds number. The grid size in both directions is twice that of the base run i.e. $M_x \cdot M_y = 145 \cdot 65$ and the vortex line at the level of the splitter plate was discretized into 7200 particles. That means that the number of particles per grid is maintained similar to the base run. Results of averaging over four residence time, i.e. 28800 time steps in this case, for the same x locations are shown in figure 4.3 for both the base run and the coarse grid size run.

The lateral position at which the streamwise velocity equal to the mean velocity $(u_1+u_2)/2$ is denoted by $y_{0.5}$. Figure 4.4 shows the $y_{0.5}$ line growing linearly in the streamwise direction with a negative slope. This shows that the spatial mixing layer is not symmetric and spreads preferentially toward the low speed stream to entrain fluid into the shear layer. Similarity of the velocity profiles entails that $y_{0.5}$ grows linearly in the downstream direction. The slope of $y_{0.5}$ is calculated to be 2^o, while 2.2^o was obtained by Champagne et al (1976) experiment. Also shown on the same figure, $y_{0.5}$ for the case of coarse grid $M_x \cdot M_y = 145 \cdot 65$, which indicates that grid size below that of the base run did not provide any noticeable differences, i.e. at this level of resolution, the simulation is insensitive to the grid size.

Figure 4.5 shows the growth of momentum thickness for both the base run and the coarser grid case. For both cases, the data cover the region where similarity of mean velocity profiles was developed. The difference between the two can hardly be identified. Both cases show effectively linear growth of momentum thickness.

4.4 Velocity Statistics

Intensities of velocity fluctuations are computed through out the computational domain. Root mean square of streamwise velocity, cross stream velocity and cross correlation are then obtained by averaging the instantaneous values over four residence times following the calculation of the mean velocity. These statistics are normalized by the velocity difference across the mixing layer. Profiles of the root mean square of the streamwise fluctuations $RMSu'/\Delta u$ for four stations in the streamwise direction are shown in figure 4.6 for the base run data. Compared to the mean velocity profile, similarity of $RMSu'/\Delta u$ profiles take longer distance to be established further downstream starting at 1/3 of the computational domain length. Although similarity is developed quite well for $1/3<x/L_x<5/6$, minor scatter in $RMSu'/\Delta u$ can be observed around the $y_{0.5}$ line. However the average value of the maximum $RMSu'/\Delta u$ over the similarity domain i.e $1/3<x/L_x<5/6$ is 0.175, which is in line with many published experimental data, such as Bell and Mehta (1990) shown as solid points on figure 4.6 for two streamwise locations, namely x=108.1 cm and x=128.4 cm. Figure 4.7 shows same data when coarse grid was used superposed on the results of the base run at the two streamwise locations, namely x/L_x =1/3 and 2/3. The data of the two runs in good agreement and therefore the simulation is insensitive to the grid size.

The normalized root mean square of cross stream velocity fluctuation $RMSv'/\Delta u$ is presented in figure 4.8. Fully developed profiles of the base run are observed at $x/L_x \geq 1/3$ and beyond. Data from experiment of Bell and Mehta (1990) are also plotted on the same graph. The peak value of $RMSv'/\Delta u$ for the present method averaged over the similarity region was 0.256 while a peak value of 0.13 was reported by Bell and Mehta (1990) . A peak value of $RMSv'/\Delta u$ of 0.25 was also obtained by Inoue and Leonard (1987) in their vortex method simulation of forced and unforced mixing layer. The discrepancy between numerical and experimental results of this parameter can be explained as follows: the strain rate of the shear layer du/dy contributes to the generation of streamwise turbulent kinetic energy. This energy transfers to the cross-stream and spanwise directions due to the effects of pressure velocity correlations (Tennekes and Lumley, 1972). In two dimensional flows, spanwise component of velocity fluctuations disappears and the energy transfers solely to the cross-stream direction. Therefore the cross-stream component is expected to be higher than that of the experiment. This explanation will be confirmed in Chapters 5 and 6 when the three dimensionality effects are considered. $RMSv'/\Delta u$ results for coarse grid superposed on that of the base run are shown in figure 4.9 to explore the grid sensitivity to this parameter. No significant effect can be deducted from the two plots.

A more sensitive indicator of self similarity is the cross correlation function $\langle u'v' \rangle$. Figure 4.10 shows the cross correlation function normalized by velocity difference across the splitter plate squared for the base run conditions. Four streamwise locations in the range $1/3 < x/L_x < 5/6$ were tested for evidence of similarity. Experimental results of Bell and Mehta (1990) were also plotted on the same figure. The maximum value of cross

correlation function obtained in this simulation was 0.013 at x/L_x=5/6, while Bell and Mehta (1990) reported a maximum of 0.01. However the difference is attributed to the three dimensionality effects on the experimental results as discussed above. Figure 4.11 shows the same data for a computational domain of $M_x \cdot M_y$=145·65 superposed on the base run data.

4.5 Energy Spectra

The contribution of different spatial scales to the total energy is estimated by performing spectral analysis on the velocity field obtained from Poisson solver. Spectral analysis was carried out after 6 residence times i.e. after calculating the mean velocity. It was performed along the streamwise *(x)* direction and the resulting energy is integrated over the cross-stream *(y)* direction. The first step in obtaining the energy spectrum is to compute the autocovariance (*AC*) of each velocity component separately. For the evenly distributed M_x samples of velocity field obtained from Poisson solver and assuming that the flow is statistically stationary, the autocovariance of the streamwise velocity component as a function of spatial separation is given by

$$AC(ih_x) = \frac{1}{M_x - i} \sum_{l=1}^{M_x - i} (u_l - u_{mean})(u_{l+i} - u_{mean}), \qquad i = 1, \quad 2, ..., M_x - 1 \qquad (4.9)$$

AC function was computed by using ACF subroutine of the IMSL statistical library of FORTRAN. Same function is used to calculate the autocovariance function for the cross stream components of the velocity. The resulting autocovariance function is then Fourier

transformed using the Fast Fourier Transform subroutine (FFTRF) provided by IMSL mathematical library. FFTRF uses the following formulas to determine the transform coefficients of the discrete autocovariance function.

$$c_{2i-2} = \frac{1}{M_x}\sum_{l=1}^{M_x} AC(lh_x)\cos\left(\frac{(i-1)(l-1)2\pi}{M_x}\right)$$

$$i = 2, 3, ...(M_x - 1)/2$$

$$c_{2i-1} = -\frac{1}{M_x}\sum_{l=1}^{M_x} AC(lh_x)\sin\left(\frac{(i-1)(l-1)2\pi}{M_x}\right)$$

$$c_1 = \frac{1}{M_x}\sum_{l=1}^{M_x} AC(lh_x) \qquad (4.10)$$

The energy E of each component of velocity is computed separately. For example the energy of the streamwise velocity component u is computed by the following formula:

$$E_1^u = |c_1|$$

$$E_l^u = \sqrt{\left(c_{2l-2}^2 + c_{2l-1}^2\right)} \qquad l = 2,3,....,\frac{N}{2}+1 \qquad (4.11)$$

The wave number k corresponding to Energy E_l is given by $k = \frac{l}{M_x h_x}$, the number of resolved modes are *(N/2)+1*. The total energy as a function of wave number in the streamwise direction x is obtained by integrating the total energy along the cross stream direction,

$$E(k) = \int_{y_{min}}^{y_{max}} (E^u + E^v) dy \qquad (4.12)$$

The one dimensional modal energy for the base run is shown in figure 4.12. Power spectra were calculated at two times, namely after 6 and 8 residence times. For both times, the second mode is shown to be the most energetic. Figure 4.13 shows the same data for the case of $M_x \cdot M_y = 145 \cdot 65$ superposed on the base run data, both sampled after six residence time. In both cases the maximum energy occurs at the second mode and no significant grid size effect can be recognized between the two aside from the numbers of resolved modes.

4.6 Development of Vortical Structures

Development of vortical structures of a mixing layer downstream of a splitter plate will be discussed in this section. Similar sequence of events has been observed when the code was run with coarse mesh and base run. Therefore only results for the base run will be discussed in this section. The early stages of growth of mixing layer can be explained through tracking the augmentation of the sinusoidal perturbation (y_d) imparted to the vorticity layer, along with its manifestation in terms of changes in the vorticity distribution and its consequential effect on the induced velocity distribution. Following Inoue (1989), an initial perturbation was given to the particle location as

$$y_d = \frac{A}{2}\{1 + \cos[2\pi x / \chi]\} \qquad (4.13)$$

with $A=0.1d_x$ and $\chi_{=}30$. It should be mentioned however that according to the instability analysis by Pierrhumbert and Widnall (1982), a broad range of wavelengths has approximately the same amplification rates. Figure 4.14 shows the initial sinusoidal perturbation (y_d) of the vorticity layer. As a result, vorticity in part of the sheet will be displaced downwards and displaced upwards in others. At point B for instance, where $y_d=0$, $dy_d/dx<0$ and since the vorticity moves as a material, the vorticity from $y_d>0$ will move faster toward point B. Hence vorticity will be enhanced and accumulated at point B. At points like A, the reverse will occur. Since $y_d=0$, $dy_d/dx>0$ for the frame and flow configuration shown in figure 4.14, the net effect of vorticity movement above and below $y_d=0$ will be that vorticity swept away from point A. When vorticity does accumulate close to point B and diminish at point A, there will be a net subsequent induced velocity which tends to move fluid in the clockwise sense and therefore increase the amplitude of the sinusoidal perturbation. These processes of building up of vorticity at points like B and wear off vorticity at A will go on together leading to the exponential growth of perturbation amplitude. This growth is governed by the linear Kelvin-Helmholtz instability mechanism.

Figure 4.15 presents the particle field for different regions in the computation domain tracking the development of instabilities and the vortical structures. Figure 4.15 (a) zooms into the region close to the splitter plate x/L_x (0 - 0.04). In this region the mixing layer is dominated by exponential growth of the initial perturbation as a result of linear Kelvin-Helmholtz instability.

Beyond the region of exponential growth, Kelvin-Helmholtz instability saturates and develops the first roll up of the vorticity layer. This is clearly identified at $x/L_x=0.08$ in

figure 4.15 (b). Further down stream the linear instability theory is no longer applicable and mixing layer evolves into a periodic array of coherent vortices. These vortices are moving with the average velocity of the two streams and connected by thin vorticity layer, or braids. This is shown in figure 4.15 (c). Further downstream, as shown in figure 4.15 (d), these well organized periodic vortices interact with each other leading to the pairing of neighbouring vortices. Hence, the vorticity initially contained in one vortex, is constantly distributed into larger and larger vortices with roughly double the strength and half the wave number. It has been established by Winant and Browand (1974) that successive merging of vortices is the principal mechanism controlling the streamwise growth of the mixing layer.

Figure 4.16 shows two snapshots of the vorticity contours within the computational domain. Fifty contour levels with 0.02 increment of the difference between the minimum and maximum vorticity. Figure 4.16 (a) represents the vorticity field after 14450 time steps and figure 4.16 (b) represents the vorticity fields after 15450 time steps. Same sequence of events as depicted by the particle field , namely, initial linear growth, roll up, compact periodic vortices and pairing, can be observed.

Chapter 5

Finite Difference Approximation with Remeshing

5.1 Introduction

In chapter 4 of this work the two dimensional mixing layer has been simulated. This computation confirmed the existence of well organized spanwise vortical structures (rollers). Sequential merging of these rollers provides the primary mechanism that controls the entrainment and growth of mixing layer. Previous experimental work due to Lasheras et al (1986) has revealed that the spanwise rollers are unstable to three dimensional disturbances. This instability results in the flow departing its two dimensionality and forming three dimensional structures. In this chapter, the implementation of Vortex-In-Cell (VIC) method with remeshing to solve the three dimensional vorticity equation as applied to temporally developing mixing layer will be discussed. The capability of the Vortex-In-Cell method to predict the flow features associated with this flow will also be explored.

5.2 Temporally Developing Mixing Layer

In contrast to spatially developing mixing layer in the laboratory coordinates, when a frame of reference moving in x direction with the convective velocity $(u_1+u_2)/2$, the two streams will appear, to an observer travelling with this frame, moving to the right and left with a velocity of $(u_1-u_2)/2$ and $-(u_1-u_2)/2$, respectively. According to this frame of reference the flow becomes statistically one dimensional and time dependent. Such a flow configuration is called temporal mixing layer, (Pope, 2000). Temporal mixing layers loose their asymmetry which is usually observed in the spatially developing mixing layers. As a result the free streams are parallel and $y_{0.5}$ (the locus of the points where the average streamwise velocity is $(u_1+u_2)/2$) is a horizontal line with no preferential spread towards any of the two streams. For computational efficiency and to realize adequate resolution of the simulation, a temporally evolving mixing layer was simulated in this work, rather than the spatially evolving layer which is typical in experimental studies. Published comparison of direct numerical simulation showed that temporally and spatially evolving mixing layers are at least qualitatively (some times quantitatively) similar (Rogers et al, 1990).

5.3 Remeshing

The particle formulation of a flow problem entertains an automatic adaptation of the computational elements (particles) to the physical features of the flow. That is the distribution of the elements is strongly dependent on the flow conditions. Local strain generates substantial clustering of particles in one location associated with expansion in

others. Therefore an initially uniformly distributed set of overlapping particles may become totally distorted as the particles respond to the flow conditions. When particles loose overlap, information can not be exchanged between them and the simulation accuracy deteriorates. This has been realized during this simulation, where the solution blew up within less than 100 time steps. In particular, unrealistic results have been observed during computation of derivatives needed to determine stretching, diffusion and velocity.

As a remedy within the frame work of vortex methods, spatial adaptation techniques have been developed. In this simulation a remeshing (regridding) technique has been implemented in which, a new set of particles is initiated at a regular lattice within the computational domain while the older set is discarded every few time steps. Strengths of the new set are calculated using an interpolation scheme. Fidelity of the new particle field to the old is categorized by the highest order of moment preserved during interpolation. In this simulation, the widely recognized M'_4 scheme, where the total circulation, the linear and angular moments of vorticity field in three dimensional domain are conserved, has been implemented. Using M'_4 scheme, every particle contributes to the strength of the closest 64 particles of the new set. Figure 5.1 depicts the two dimensional application of M'_4 scheme where every particle affects 16 particles of the new set. The three dimensional interpolation scheme was built from the one dimensional kernel by tensorial product in three dimensions. At the boundaries of the computation domain in stream wise and spanwise directions, it is obvious that new particles will be outside the computation domain. Periodic conditions were devised in these locations. That is new particles will be reflected onto the opposite side of the domain.

5.4 Evaluation of Derivatives

Within the frame work of the present VIC method implementation to the temporal three dimensional mixing layer, evaluation of spatial partial derivatives of velocity and vorticity are encountered in three instances, namely, velocity derivatives in the stretching term, vorticity derivatives in the right hand side of the Poisson equation and the second order derivatives in diffusion term. Knowing the velocity and vorticity on the grid points the stretching term for every spatial dimension is computed using fourth order central difference approximation for the velocity derivatives. For instance the spatial derivative of the streamwise component of velocity u with respect to cross stream direction y at the grid point (i,j,k) is approximated by

$$\left(\frac{\partial u}{\partial y}\right)_{i,j,k} \approx \frac{u_{i,j-2,k} - 8u_{i,j-1,k} + 8u_{i,j+1,k} - u_{i,j+2,k}}{12h_y} \tag{5.1}$$

Similarly, the second order derivatives of the Laplacian of vorticity encountered in the diffusion term is approximated by fourth order central difference. For example, the second order derivative of cross-stream vorticity with respect to the streamwise direction is approximated by

$$\left(\frac{\partial^2 \omega_y}{\partial x^2}\right)_{i,j,k} \approx \frac{-(\omega_y)_{i-2,j,k} + 16(\omega_y)_{i-1,j,k} - 30(\omega_y)_{i,j,k} + 16(\omega_y)_{i+1,j,k} - (\omega_y)_{i+2,j,k}}{12h_x^2} \tag{5.2}$$

Once computed on the grid, the vorticity increments due to stretching and diffusion effect are back projected to the particle location using the M'_4 scheme to update its strength. Fourth order central difference approximation was also used in the calculation of the curl of vorticity term at the right hand side of the Poisson equation that was used to calculate velocity.

5.5 Initial and Boundary Conditions

Based on the linear instability analysis of the mixing layer, the most amplified wave number k_a is calculated by Michalke (1964) as

$$k_a = 0.8\delta_{\omega o}^{-1} \tag{5.3}$$

where $\delta_{\omega o}$ is the initial vorticity thickness of the shear layer. The initial vorticity thickness of the shear layer computed using equation (5.17) for the error function velocity profile (Equation 4.3) was found to be approximately equal to three grid element sizes. i.e. $\delta_{\omega o} \approx 3h_y$. The spatial wave length $\lambda_a = 2\pi/k_a$ of the most amplified wave for this flow can be written as,

$$\lambda_a = 7.5\pi h_y \tag{5.4}$$

The computation box for the present simulation was chosen to span six wave lengths of the most amplified wave in the streamwise (x) and spanwise (z) directions. The number

of grid points used are $M_x=M_z=145$ and $M_y=259$ points was used. A uniform grid size with $h_x=h_y=h_z=0.125$ cm was used in this simulation. The Reynolds number based on strength of the vorticity sheet α is equal to 1800.

The initial vorticity in the computational domain must also be specified. Initially, the velocity difference across the splitter plate is simulated as a vortex sheet**.** The total strength of the vortex sheet is discretized into a set of particles, each of the particles carries a strength of $\Delta u \cdot d_x \cdot d_z$, where the velocity difference across the splitter plate is $\Delta u = u_2 - u_1$, d_x is the initial distance between two adjacent particles in the streamwise direction and d_z represents the initial distance between any two adjacent vortex particles in the spanwise direction. In the present simulation, *dx* is chosen to be half the grid size in the streamwise direction ($d_x=h_x/2$), i.e. there are two rows of particles in the streamwise direction in every cell. Similarly d_z is chosen to be half the grid size in the spanwise direction ($d_z=h_z/2$), i.e. there are two rows of particles in the spanwise direction in every cell. Consequently the initial number of particles in the computational domain is 82944. It is important to mention here that, in contrast to the two dimensional case where particle strength is a scalar, particle strength in three dimensions is a vector parallel to the direction of the vorticity vector. The time step Δt is taken to be the initial distance between two adjacent rows of particles in the streamwise direction, i.e. d_x, divided by the average velocity of the flow.

In order to initiate the flow, localized three dimensional disturbances, i.e. instabilities, are imposed. The location of every particle is initially perturbed in a sinusoidal form following Inoue (1989) as

$$y_p = \frac{A}{2}\{1 + \cos[2\pi(z - z_o)/\chi]\}$$
$$x_p = \frac{A}{2}\{1 + \cos[2\pi(z - z_o)/\chi]\} \tag{5.5}$$

where A and χ are arbitrarily chosen to be $0.1d_x$ and 30, respectively. In this method the particles that are initially located on the same row in spanwise direction are viewed as markers on a vortex filament. When disturbed the strength vector will have three components, each with strength equals to the initial strength of the particles times the cosine of the angle between the vorticity vector and the respective direction. By this method, vorticity in the streamwise and cross-stream direction is initiated. Figure 5.2 shows an initial layout of the particles along with the initial perturbation.

Since this simulation is dealing with a temporally evolving mixing layer, periodic boundary conditions were used in the streamwise (x) and spanwise (z) directions. Periodic boundary conditions are achieved by equating the values of each variables at the nodes just upstream and downstream of the inlet plane to the nodal values just upstream and downstream of the outlet plane. For any variable q we have

$$q_{1,j,k} = q_{Mx-1,j,k} \quad , \quad q_{Mx,j,k} = q_{2,j,k} \quad , \quad q_{i,j,1} = q_{i,j,Mz-1}, \; and \quad q_{i,j,Mz} = q_{i,j,2} \tag{5.6}$$

As stated in section 5.1, in temporal mixing layers, the local spatial evolution is neglected and the preferential spreading of the layer towards the lower velocity stream is lost. Therefore the two streams become parallel at y=-∞ and at y=∞ and Neumann type boundary conditions is used for the streamwise velocity and spanwise velocity, that is

$$\frac{\partial u}{\partial y} = \frac{\partial w}{\partial y} = 0 \qquad at\ y = -\infty\ and\ at\ y = \infty \qquad (5.7)$$

The cross stream component of velocity v vanishes at these two planes. The initial velocity profile used in this simulation was error function distribution similar to the one used in equation (4.3).

5.6 Sequence of Computations over a Time Step

Integration over one time step is done using second order predictor-corrector scheme. Particles are advanced and their strengths are updated in every time step according to second order modified Euler predictor corrector method. Such time step is as follows:

Euler predictor step: in this step the Euler first order method is used to update the particle location according to

$$\vec{x}_p^{\,n+\frac{1}{2}} = \vec{x}_p^{\,n} + \Delta t\left[\vec{u}_p\left(\vec{x}_p^{\,n}, \vec{\alpha}_p^{\,n}\right)\right] \qquad (5.8)$$

where $\vec{x}_p$ represents the particle location, the superscript n represents the time step, $\vec{u}_p$ represent the particle velocity obtained from the solution of Poisson equation on the grid and interpolated back to the particle location by M'_4 scheme. Then the nodal vorticity change due to stretching and diffusion is calculated according to

$$\Delta\vec{\omega}_i^{*,n+\frac{1}{2}} = \Delta t\left[L_S\left(\vec{\omega}_i^n\right) + L_D\left(\vec{\omega}_i^n\right)\right] \tag{5.9}$$

where L_S and L_D represent the discrete operator of stretching term $(\vec{\omega}\cdot\nabla)\vec{u}$ and the diffusion term $\nabla^2\vec{\omega}$, respectively, applied to the nodes using the fourth order finite difference approximation. The subscript *i* indicates nodal values. The nodal vorticity change is then interpolated back to the particle location to update its strength using M'$_4$ scheme as

$$\vec{\alpha}_p^{*,n+\frac{1}{2}} = \vec{\alpha}_p^n + \sum_{i=1}^{64}\left(\Delta\vec{\omega}_i\right)^{*,n+\frac{1}{2}} \frac{\varphi\left(\frac{x_p - x_i}{h}\right)\varphi\left(\frac{y_p - y_i}{h}\right)\varphi\left(\frac{z_p - z_i}{h}\right)}{\left[\varphi\left(\frac{x_p - x_j}{h}\right)\varphi\left(\frac{y_p - y_j}{h}\right)\varphi\left(\frac{z_p - z_j}{h}\right)\right]_{it}} h^3 \tag{5.10}$$

where *h* is the grid size and $\left[\varphi\left(\frac{x_p - x_j}{h}\right)\varphi\left(\frac{y_p - y_j}{h}\right)\varphi\left(\frac{z_p - z_j}{h}\right)\right]_{it}$ is the sum of the three dimensional contributions $\varphi\left(\frac{x_p - x_i}{h}\right)\varphi\left(\frac{y_p - y_i}{h}\right)\varphi\left(\frac{z_p - z_i}{h}\right)$ from all particles that contribute to the vorticity at the node**.** The updated particle strength $\vec{\alpha}_p^{*,n+\frac{1}{2}}$ is used to generate new and modified nodal vorticity field $\vec{\omega}_i^*$ by assigning vorticity to the nodes from the particles. The velocity field $\vec{u}^*$ is then calculated using equation (3.14) and interpolated to the particle location using M'$_4$ scheme. This will end the predictor step.

The corrector step: in this step the location of the particles is updated according to

$$\vec{x}_p^{n+1} = \vec{x}_p^{n} + \frac{\Delta t}{2}\left[\vec{u}_p + \vec{u}_p^{*}\right] \tag{5.11}$$

Then the vorticity increment due to stretching is computed on the grid as

$$\Delta\vec{\omega}_i^{n+1} = \frac{\Delta t}{2}\left[L_S\left(\vec{\omega}_i^{n}\right) + L_S\left(\vec{\omega}_i^{*}\right) + L_D\left(\vec{\omega}_i^{n}\right) + L_D\left(\vec{\omega}_i^{*}\right)\right] \tag{5.12}$$

The vorticity increment resulting from stretching and diffusion effect and computed from the equation above is used to update the particle strength by employing the M'$_4$ scheme as

$$\vec{\alpha}_p^{n+1} = \vec{\alpha}_p^{n} + \sum_{i=1}^{64}\left(\Delta\vec{\omega}_i\right)^{n+1}\frac{\varphi\left(\frac{x_p - x_i}{h}\right)\varphi\left(\frac{y_p - y_i}{h}\right)\varphi\left(\frac{z_p - z_i}{h}\right)}{\left[\varphi\left(\frac{x_p - x_j}{h}\right)\varphi\left(\frac{y_p - y_j}{h}\right)\varphi\left(\frac{z_p - z_j}{h}\right)\right]_{it}}.h^3 \tag{5.13}$$

As a result of diffusion and stretching, vorticity occupies new regions which were irrotational in the previous steps. Therefore, new particles are created at the nodes where the computed vorticity increment is greater than a predetermined threshold and there is no particle within the support of the interpolation scheme. The threshold is set to 1% of the initial grid vorticity.

The solution procedure outlined above does not guarantee that the outcome discrete vorticity field is divergence free. The spurious divergence is managed by projection method as described in section 3.5. This method is applied every time step.

Also, a remeshing scheme is applied every few (seven) time steps to maintain spatial uniformity of the particle distribution as outlined in section 5.2.

5.7 Results

Results of the momentum thickness, vorticity thickness, similarity of mean flow, flow statistics, power spectrum and the development of three dimensional instabilities to form the streamwise vorticity structure will be presented in the following sections.

5.7.1 Mixing Layer Evolution Parameters

The momentum thickness $\theta(t)$ in a temporal mixing layer is defined by

$$\theta(t) = \int_{-\infty}^{\infty} \frac{\bar{u}(y,t) - u_2}{u_1 - u_2} \left(1 - \frac{\bar{u}(y,t) - u_2}{u_1 - u_2} \right) dy \qquad (5.14)$$

Where $\bar{u}(y,t)$ represents the streamwise velocity averaged over *x*-*z* plane. The integral in equation (5.14) above is computed using Simpson's 1/3 rule with 258 intervals in the cross stream direction. Growth of the momentum thickness with time constitutes an indicator of the spreading rate of the mixing layer. In a numerical simulation of spatially developing three dimensional mixing layers due to Inoue (1987), Results of momentum thickness showed linear development when the flow was not forced and nonlinear

development when the flow was forced. Figure 5.4 shows the evolution of momentum thickness, normalized by its initial value θ_o, as a function of dimensionless time. Linear growth is attained after the non-dimensional time $t\Delta u/\theta_o$=50. Neglecting the viscous dissipation and the production in the mean motion, the rate of change of the momentum thickness can be shown to be equal to the integral of turbulence production as (Smits and Dussauge, 1996),

$$\frac{d\theta}{dt} = \frac{2}{(\Delta u)^2}\int -\langle u'v' \rangle \frac{\partial \bar{u}}{\partial y} dy \tag{5.15}$$

From the physical view point, self preservation implies that the flow has reached through its evolution to a kind of equilibrium among all its turbulence parameters, i.e. all turbulence parameters evolve together in a self preserved flow. The equation above indicates that constant rate of momentum thickness growth means constant turbulence production and consequently the mixing layer is evolving self-similarly. From figure 5.4 the dimensionless mixing layer growth rate based on momentum thickness evolution given by,

$$r_\theta = \frac{1}{\Delta u}\frac{d\theta}{dt} = \frac{d(\theta/\theta_o)}{d(t\Delta u/\theta_o)} \tag{5.16}$$

can be calculated to be 0.015 during the self similarity period. The DNS simulation of Rogers and Moser (1994) produced a value of 0.014 for r_θ. The range for r_θ for experiments quoted by Rogers and Moser (1994) is from 0.014 to 0.022.

Figure 5.5 shows the development of vorticity thickness. The vorticity thickness is defined as

$$\delta_\omega = \frac{\Delta u}{\left(\frac{\partial \bar{u}}{\partial y}\right)_{\max}} \tag{5.17}$$

It is nondimensionlized by its initial value. A slight non linearity in the development of the vorticity thickness, even over the similarity period, can be attributed to the fact that the definition of the vorticity thickness involves the calculation of derivatives which is known to be very sensitive to numerical noise. In contrast the calculation of momentum thickness involves an integral that is less sensitive to the numerical noise. That may be the reason, the momentum thickness growth shows better linear behavior. If θ is replaced by δ_ω in equation (5.17), an average value of 0.064 will result for the nondimensional growth rate of the vorticity thickness r_ω, the ratio of the vorticity thickness growth rate to the momentum thickness growth rate (r_ω/r_θ) is 4.5. Rogers and Moser (1994) predicted a value of 4.27 for this ratio in their DNS simulation.

If one takes a reference frame moving with the mean velocity and the lateral spreading of the layer is neglected, the temporal mixing layer will be established. The distance downstream of the splitter plate in the spatial mixing layer will correspond to $t = 2x/(u_1 + u_2)$ in the temporal mixing layer. The vorticity thickness measures the

spread of the mixing layer. Similarity solution requires linear development of the vorticity thickness, i.e. the rate of development of the vorticity thickness is constant. The commonly acceptable experimental value for the normalized growth rate $\frac{u_1+u_2}{u_1-u_2}\frac{d\delta_\omega}{dx}$ for spatially developing mixing layer is 0.17. However, values ranging from 0.15 to 0.27 can be found in the literature (Lesieur, 1997). For the present simulation an average normalized rate of growth of the vorticity thickness, in terms of streamwise distance is calculated to be approximately 0.15.

5.7.2 Mean Flow and Velocity Statistics

Temporally developing mixing layers forget the initial conditions after certain time and attain a state of self-preservation that is the evolution of the mixing layers becomes totally determined by the local scales of velocity and length. The length scale used in this simulation is the momentum thickness $\theta(t)$ and the velocity scale is the velocity difference of the streamwise component across the layer Δu. In this simulation the mixing layer attains self similarity at a dimensionless time $t\Delta u/\theta_o$=42.8. Figure 5.6 shows the normalized average streamwise velocity $\frac{u-u_2}{\Delta u}$ against the normalized cross-stream distance $y/\theta(t)$ at five different times. Sampling of velocity started after allowing two residence times for the flow to develop. Similarity of mean velocity is achieved for the period $t\Delta u/\theta_o$ between 42.8 and 123.8. Every point on this figure represents the streamwise velocity averaged over the two periodic directions, i.e. x-z plane at certain point of time. Mean streamwise velocity data at two streamwise locations obtained from Bell and Mehta (1990) experiment are superposed on the figure. Agreement between the

present simulation and the experiment are very good except for a small discrepancy at the outer edge of the layer probably due to the intermittency of turbulence at the edge. In Rogers and Moser (1994) DNS simulation, the mixing layer took more time to attain self similarity at $t\Delta u/\theta_o$=105. This discrepancy is attributed to the fact that boundary layer effect has been considered in their simulation.

A more sensitive indication of self similarity is the fall down of the statistics of velocity components profiles on a single curve when scaled appropriately. The velocity scale of self similarity scale the root mean square is (Δu). In figures 5.7-5.9, the similarity of the root mean square of the three components of velocity is demonstrated over the similarity period. However, self preservation of velocity statistics have taken longer times to be established. Similarity of root mean square of velocity fluctuations was attained at $t\Delta u/\theta_o$=63.7. In figures 5.7-5.9, the root mean square of the velocity is compared to the experimental data of Bell and Mehta (1990) at two streamwise locations; namely (x=108.1 cm and x=128.4 cm). In order to make the comparison plausible, the preferential spreading of the spatial mixing layer is eliminated by considering a coordinate parallel to its line of symmetry. The average of the maximum root mean square value of the streamwise velocity component over the similarity period in figure 5.7 was 0.18 which corresponds to less than 10% difference from the experimental data of 0.17 obtained by Bell and Mehta (1990). Furthermore, in the simulation, velocity fluctuations are asymptotically assimilating into the undisturbed flow as compared to the clearer boundary between turbulent and undisturbed fluid of the experiment. Similar trend can also be noted for the cross stream velocity component in figure 5.8. That is probably the manifestation of remeshing process considered in this simulation. Figure 5.9 shows the root mean square of the spanwise component of velocity compared to that of

Bell and Mehta (1990) experimental data. The two sets are almost indistinguishable. The cross correlation of the streamwise and cross stream components of velocity normalized by the square of the velocity difference is shown in figure 5.10. The maximum value of the scaled primary component of Reynolds stresses was - 0.011. Experimental results due to Bell and Mehta (1990) showed a maximum of -0.01.

5.7.3 Mixing Layer Three Dimensionality

As stated in section 5.1, temporal mixing layers are effectively one dimensional when neglecting its local lateral spreading. However, one of the main objectives of the present study is to show the capability of the Vortex-In-Cell method to capture three dimensional features of mixing layer flow. Figure 5.11 presents the mean streamwise velocity $u/\Delta u$ contour lines at four non-dimensional times ($t\Delta u/\theta_{o=}$ 42.8, 63.7, 84.4 and 105.2*)*. Velocity results for this figure were obtained by averaging instantaneous values over the streamwise direction. Several features can immediately be drawn from these plots. The contours for all cases are distorted in the spanwise direction and clearly exhibit a spanwise-varying thickness, thus implying that the mixing layer is three dimensional over the time period within which it is investigated.

The evolution of the total streamwise and cross-stream vorticity which can be used as a measure of three dimensional effects is plotted in figure 5.12. In this figure the volumetric integral defined by

$$\int_v \left[\omega_x^2 + \omega_y^2\right]^{1/2} dv$$

is plotted against the non-dimensional time $t\Delta u/\theta_o$. Figure 5.12 indicates that three dimensional effects are small during the early stage of the instability development; that is the two dimensional linear stage. The three dimensionality of the shear layer grows rapidly after the roll up of the vorticity sheet. The rate of growth of the integral parameter tends to slow down toward the end of computation time, $t\Delta u/\theta_o$>120, due to maturity of the fluid structures.

By definition, the vorticity field is a divergent free (solenoidal) field. This condition is implicitly satisfied in two dimensional flows since the vorticity is directed normal to the flow plane. However in three dimensional flows this condition has to be explicitly fulfilled. In this study, the vorticity divergence $\left(\frac{\partial \omega_x}{\partial x}+\frac{\partial \omega_y}{\partial y}+\frac{\partial \omega_z}{\partial z}\right)$ is computed globally every time step through out the computational domain. Fourth order central difference approximation is used, for example

$$\left(\frac{\partial \omega_y}{\partial y}\right)_{i,j,k} \approx \frac{(\omega_y)_{i,j-2,k}-8(\omega_y)_{i,j-1,k}+8(\omega_y)_{i,j+1,k}-(\omega_y)_{i,j+2,k}}{12h_y} \qquad (5.18)$$

Figure 5.13 presents the evolution of the vorticity divergence in time. Higher peak to peak fluctuation is observed before $t\Delta u/\theta_o$=50. After that, the value of the vorticity divergence almost converges to zero. Given the fact that the global vorticity divergence reported in Fig 5 .13 is the result of summation of local divergence computed at more than $5.4\text{x}10^6$ grid points, the computed vorticity field can be described as divergence

free. The slight fluctuations in figures 5.12 and 5.13 are attributed to the changes in the number of particles within the computational domain, as will be seen in Chapter 7.

5.7.4 Evolution of Instabilities in Three Dimensional Mixing Layers

It is well established now that instabilities in three dimensional mixing layers are first developed into spanwise vortical structures followed by secondary instabilities which evolve into streamwise vortices bridging the spanwise rollers. In the following these two physical processes will be discussed in details.

5.7.4.1 Formation of Spanwise Vortices

As discussed in Chapter 4, mixing layers are subjected to Kelvin-Helmholtz instability. According to linear stability theory and under parallel flow assumption disturbances will grow exponentially and the vorticity is gradually accumulated and concentrated through the instability mechanism. Figure 5.14 shows the temporal evolution of instability which leads to the formation of the spanwise rollers in terms of development of spanwise vorticity contours at the mid spanwise plane (z/L_z=0.5). This is presented in a frame of reference moving with the average velocity. Figure 5.14 (a) shows the vorticity contours during the exponential growth at $t\Delta u/\theta_o$=12.1. After the exponential growth, the instability waves evolved into non linear regime and reached its saturation, after which the instability waves lead to the first roll up as shown in figure 5.14 (b) ($t\Delta u/\theta_o$=27.5). At later times the vorticity in the mixing layer is gradually accumulated and concentrated through the instability mechanism as shown in figure 5.14 (c) ($t\Delta u/\theta_o$=57.3). The

fundamental vortices are not stable structures. These vortices exist in the background of the mean shear field and therefore are subjected to pairing as shown in figure 5.14 (d) and (e) ($t\Delta u/\theta_o$=87.4 and $t\Delta u/\theta_o$=123.8, respectively).

Same progression of events can also be deduced from the velocity components computed on the grid points by solving Poisson equations. Figures 5.15 (a-e) show instantaneous velocity vector of the streamwise and cross-stream components, i.e. the two components that contribute to the spanwise vorticity, plotted at the mid spanwise plane (z/L_z=0.5) and at the same corresponding times as in figure 5.14. After the first roll up illustrated in figure 15 (b), Kelvin-Helmholtz instability evolved to form two regions of concentrated vorticity (rollers), as shown in figure 5.15 (d) and (e). For a frame of reference moving with the mean velocity the evolution of the two rollers is associated with formation of a local saddle point. At this point, the flow appears stagnant in the *x*-*y* plane and the spanwise vorticity is thinning between the two rollers. The stagnation point forms because the undisturbed fluid which is entrained into the mixing layer by the rollers induced velocity has to separate into two streams: one winds around the first roller and the other around the second roller. Figure 5.16 presents a schematic description of this phenomenon as suggested by Ashurst and Mieberg (1988). As depicted in figure 5.16 saddle (stagnation) points are subjected to maximum stretching and compression, therefore there is more chance for a stream line passing through these points to be disturbed by three dimensional instabilities and forming three dimensional (streamwise) structures as will be discussed in the next section.

One of the merits of vortex methods is that particles exist where the vorticity is significant; therefore particle positions provide a pictorial view of the flow structures. Figures 5.17 (a-e) indicate the evolution of Kelvin-Helmholtz instability from the particle

field at a slice of one grid size thickness around *(z/L_z=0.5)* plane. The successive steps toward the formation of the main spanwise rollers at different times can be observed as described in figure 5.14.

5.7.4.2 Secondary Instability and the Formation of Streamwise Vorticity

As discussed in the previous section inflection point in the mean flow profile and Helmholtz instability lead to roll up of the vortex sheet and the formation of spanwise vortices. However, the formation of spanwise rollers is not solely a two dimensional process. These rollers are constantly subjected to secondary (translative) instability along their axis in the spanwise direction resulting from three dimensional disturbances. The evolution of translative instabilities is captured by Pierrehumbert and Widnall (1982) in their spectral simulation. In due course, if these secondary instabilities are subjected to sufficiently strong shear, they will grow into streamwise pairs of counter-rotating vortices (Lin and Corcos, 1984), as will be explained in the next paragraph and as shown in figures 5.18-5.20. These three figures demonstrate the formation and evolution of streamwise vorticity. In each figure the streamwise vorticity contours are presented at four different planes in the streamwise direction; x/L_x= 0.2, 0.4, 0.6 and 0.8. which is reproduced at three different times, namely $t\Delta u/\theta_o$=42.8, 84.4 and 123.8 for figures 5.18, 5.19 *and* 5.20, respectively. The contour levels are explained in the caption.

When a long spanwise roller that includes many vortex filaments is deformed by three dimensional disturbances, small ripples in the cross stream direction along the roller will result. The bump up part of the spanwise vortex will be advected at higher velocity than the rest. As a consequence, the strain field in the mixing layer will initiate a streamwise

vortex pair as shown in figure 5.18. Thus what is started effectively as two dimensional spanwise vortices, transfer into complicated three dimensional flow. This sequence of events is captured experimentally by Bernal and Roshko (1986) and numerically by Ashurst and Meiberg (1988), Inoue (1989) and Knio and Ghoniem (1992). The schematic description of the formation of spanwise rollers presented in figure 5.16 shows also stagnation points between these rollers where the strongest stretching and compression exert on a streamline passing through such point. It is, therefore, more likely for the stretching mechanism to work at these points. Consequently the already formed streamwise vorticity will be further stretched and accentuated into well defined pairs of large streamwise counter-rotating vortices as shown in figure 5.19. At this time the braid vortices appear as long thin structures span the rollers, that suggests strain dominance in this region. The induced velocity of the counter rotating vortices on each other will bring these vortices closer as shown in figures 5.20 (a-d) and as the two vortices move closer, the effect of vorticity will outweigh the strain influence and the streamwise vortices become more rounded. Opposite movement occurs at a second row of smaller vortices generated under the main counter rotating vortices, where the two vortices are pushed away by the induced velocity as shown in figure 5.20 (a)

Figure 5.21 shows a three dimensional perspective view of the streamwise vorticity iso-surfaces. The initial momentum thickness and the velocity difference are used to non-dimensionalize the vorticity. This figure illustrates the stretching of streamwise vorticity into elongated thin vortices that wrap around spanwise rollers. Figure 5.22 presents one surface of constant streamwise vorticity that is, $\omega_x\theta_o/\Delta u$=0.004. The elongated thin vortices are evident

In figures 5.23-5.25, the growth of instability which resulted in strong and complicated three dimensional flow features is presented in terms of velocity vectors. Cross stream and spanwise velocity components are used to present these vectors at four planes across the streamwise direction corresponding to those presented in figures 5.18 to 5.20 and at the same times as those figures. Instantaneous velocity computed by the solution of Poisson equations are used to follow the evolution of the three dimensional instabilities. In figure 5.23, streamwise vorticity appears as organized row of counter rotating vortices. Their location is determined by the initial sine wave perturbation. At later times, the vorticity intensifies and develops in phase with the initial perturbation as shown in figures 5.24 and 5.25.

5.7.5 Energy Spectra

Energy spectrum provides a pictorial view of the distribution of turbulent kinetic energy among the wave numbers. In practice it is more convenient to present these spectra as one dimensional energy spectra. For the temporal three dimensional mixing layer the flow is periodic in the streamwise and spanwise directions and aperiodic in the cross stream direction. The one dimensional energy spectra is computed for both the streamwise and spanwise directions. The first step to compute the one dimensional spectrum is to compute the two dimensional autocovariance function *(AC)* for every velocity fluctuation components for every x-z plane in the computation domain in terms of space separation (lag) (ih_x, jh_z). For N and M grid points in the x and z directions respectively, the autocovariance function is given by

$$AC(ih_x, jh_y) = \frac{1}{(N-i)(M-j)} \sum_{l=1}^{N-i} \sum_{k=1}^{M-j} \left(u - u_{mean}\right)_{l+i,k+j} \left(u - u_{mean}\right)_{l,k}$$

$$i = 1, \quad 2, \ldots\ldots, N-1 \qquad \text{and} \quad j = 1, \quad 2, \ldots\ldots, M-1 \tag{5.19}$$

The modal energy at every x-z plane is obtained by the two dimensional Fourier transform of the autocovariance function for each component separately. The IMSL FORTRAN library subroutine FFT2D was used to obtain the modal energy. The total modal energy is computed by integrating over the cross stream direction

$$E(k_x, k_z, t) = \int_{y_{\min}}^{y_{\max}} \left[F(AC)_u + F(AC)_v + F(AC)_w \right]_{k_x, k_z} dy \tag{5.20}$$

where k_x and k_z are the wave numbers in the x and z directions respectively. $F(AC)_u$ represents the Fourier transform of the autocovariance function for the streamwise component of the velocity. Similar notations are used for v and w components. The one dimensional energy spectrum in the streamwise direction is defined by

$$E(k_x, t) = \sum_{k_z} E(k_x, k_z, t) \tag{5.21}$$

where the summation is over all spanwise wave numbers. Similarly the one dimensional energy spectrum in the spanwise direction is given by,

$$E(k_z,t)=\sum_{k_x}E(k_x,k_z,t) \tag{5.22}$$

where the summation is over all streamwise wave numbers.

The one-dimensional energy spectra using the method described above are shown in figures 5.26 and 5.27. Figure 5.26 presents the energy spectrum in the streamwise direction at four times through out the computation ($t\Delta u/\theta_o$= 63.7, 84.4, 105.2 and 123.8*)*. It is observed that at all the four times the maximum energy occurred in the fifth mode suggesting that rolling is occurring at this mode. Also, superposed on the figure is the Kolmogorov -5/3 spectrum. Comparing the present simulation results to Kolmogorov spectrum inertial subrange extending over half a decade of the wave numbers can be noticed. At early stages ($t\Delta u/\theta_o$< 84.4), energy spectrum appears to be evolving with time, however a saturation state is attained at $t\Delta u/\theta_o \approx 105$, with a slight drop at $t\Delta u/\theta_o$= 123.8 at almost all wave numbers.

Figure 5.27 presents the one dimensional energy spectrum in the spanwise direction at the same four times as in Figure 5.26. Same general trend can be observed with the maximum energy at the fifth mode except for $t\Delta u/\theta_o$= 123.8 where the maximum energy occurs at the fourth mode.

5.7.6 Effect of Numerical Parameters

Simulation results compiled and discussed so far in this chapter are for what will be called as the base run. In the base run, the grid size was $h_x=h_y=h_z=0.125$ cm and the number of grid points M_xxM_yxM_z=145x145x289 where M_x, M_y *and* M_z represent the number of grid points in the streamwise, cross-stream and spanwise directions

respectively. Four uniformly distributed vortex particles per cell box are used initially, that is two in the streamwise directions and two in the spanwise direction, making the total number of particles 82944 at the level of the splitter plate.

As discussed in Sarpkaya (1994), the accuracy of Vortex-In-Cell method is sensitive to numerical parameters. Sensitivity of the results to the grid size and number of particles are investigated by doubling the grid size in the three dimensions and preserving the initial number of particles in grid box and the computational domain size. That is the number of grid points in this case is M_xxM_yxM_z=73x73x145 and the initial number of particles is 20736.

5.7.6.1 Mean Streamwise Velocity

The normalized streamwise mean $\frac{u-u_2}{\Delta u}$ velocity for both cases, namely the base run and the double grid size run are presented in figure 5.28. The two profiles are plotted against the normalized cross stream direction y/θ(t). Every point represents the average of the streamwise velocity at a particular x-z plane. The two profiles are sampled at effectively the same nondimensional time $t\Delta u/\theta_o \approx 84.4$. As shown in the figure, the two velocity profiles are hardly distinguishable which demonstrates that at this grid size and initial particle number the simulation, on the mean, effectively converges to the same solution.

5.7.6.2 Velocity Statistics

Sensitivity of velocity statistics of this simulation to the numerical parameters is presented in Figs. 5.29 through 5.32. In these figures the base run values are compared to the values obtained by doubling the grid size and keeping the initial number of particles per cell unchanged. The comparison is conducted at $t\Delta u/\theta_o \approx 84.4$ within the similarity period.

Figure 5.29 shows the root mean square of streamwise velocity fluctuations normalized by the velocity difference. The two profiles are obtained after allowing two residence times for the flow to develop. Every point is calculated by averaging the sum of squares of velocity fluctuation over a *x-z* plane. The two plots are generally close enough to each other to show that the simulation is insensitive to grid size and number of vortex particles. Identical behavior can be observed in figures. 5.30 and 5.31 where the root mean square of the cross stream velocity fluctuation and spanwise velocity fluctuation are presented, respectively.

The cross correlation of the streamwise and cross stream components of velocity fluctuations normalized by the square of the velocity difference is shown in figure 5.32. Negative correlation between the two components can be shown for both the base run and the double grid size run, with a minimum normalized correlation of -0.012, in line with the experimental results of Bell and Mehta (1991). The agreement between the two cases demonstrates grid size insensitivity of the base run. However a slightly positive values at $-4 < y/\theta < -3$ can be observed that for the case of double grid size run. This can be attributed to the fact that the correlation between the two components of velocity fluctuation at a certain location in the computation domain is depending on the

inclination of the streamwise vorticity. And because of the random nature of the vorticity tilt, positive values for the cross correlation can be resulted.

5.7.6.3 Power Spectra

Figures 5.33 and 5.34 show the effects of numerical parameters, grid size and number of particles on the one dimensional energy spectra. Figure 5.33 represents the turbulent kinetic energy distribution among the wave numbers in the streamwise direction. It is obtained by integrating the modal energy in the cross stream direction and performs summation in the spanwise direction. The number of harmonics that can be analyzed for the base run is 72, twice as many as the case of double the grid size. These harmonics appear at the higher end of the wave number spectrum. For both cases of figure 5.33 maximum energy appear at the fourth harmonics. The two cases explored in this figure are close enough to be considered insensitive to the grid size.

Figure 5.34 represents the one dimensional energy as a function of the wave number in the spanwise direction. It is obtained in a similar method as that of figure 5.33 with the exception that summation is performed in the streamwise direction. In general figure 5.34 shows similar behavior to that of figure 5.33.

5.7.7 Inviscid Run

To explore the evolution of the temporal problem treated in this work under inviscid conditions, the simulation code is run with the diffusion calculation switched off. Since the effects of numerical diffusion are not significant as will be shown in Chapter 7, the equations being solved are effectively the Euler's equations. Without diffusion,

calculations terminated at $t\Delta u/\theta_o$=92.6, because unrealistically high velocity is predicted. It is noted that this termination time is well beyond the development of spanwise rollers. In the following, the implication of the absence of dissipation mechanism and its significance to the numerical method will be discussed.

It is imperative to demonstrate that the synthetic diffusion associated with the numerical scheme is not the main means by which the turbulent energy is dissipated. Figures 5.35 and 5.36 present the temporal evolution of momentum thickness and vorticity thickness, respectively. These two parameters are measures of lateral thickness evolution of the shear layer. Except for the earlier termination time at $t\Delta u/\theta_o$=92.6, no significant differences can be noted between the inviscid and viscous treatment of the problem. Similar behavior is observed for the similarity of the mean velocity profiles presented in figure 5.37. Therefore we can conclude that the interactions of large scale structures are essentially governed by inviscid flow dynamics.

Nonetheless, noticeable differences are observed in the evolution of velocity statistics and power spectra between the inviscid and viscous simulation. Figures 5.38-5.41, respectively, show the evolution of the root mean square of streamwise velocity, cross-stream velocity, spanwise velocity and cross-correlation of streamwise and cross stream velocity fluctuations. In these figures velocity statistics are presented at four times, namely, $t\Delta u/\theta_o$=42.8, 57.1, 71.3 and 84.4. It is obvious that similarity of velocity statistics could not be attained within the computational time. This trend is attributed to the fact that the numerical diffusion associated with the numerical scheme does not provide sufficient damping to alleviate the turbulent activities. Consequently, viscous effects play significant role in predicting these parameters. This can be better demonstrated with the one dimensional energy spectra plotted in figures 5.42 and 5.43,

plotted as a function of streamwise wave number (k_x) and spanwise wave number (k_z) at the same times as the velocity statistics. In both figures the energy spectrum continues to develop through out the computation time and there is accumulation of energy toward the high wave numbers since there is no dissipation mechanism to absorb the turbulence energy. The figures also show larger growth rates and hence more energetic fluctuations toward the end of the computational time.

Chapter 6

The Moving Least Square Method

6.1 Introduction

In Chapter five, Vortex-In-Cell (VIC) method has been utilized to simulate temporally developing mixing layer. Accuracy deterioration, when particles become irregularly distributed, was alleviated by remeshing. This is achieved by initiating new set of vortex particles on a regular lattice every few time steps. Remeshing introduces some numerical diffusion as discussed by Barba et al (2005). Therefore an alternative to remeshing, the moving least squares method is investigated in this chapter. In this method, derivatives in the governing equations, namely, the stretching and diffusion terms in the vorticity equations and the source term in Poisson equations, are obtained on the grid by locally fitting a second order polynomial to a small box surrounding the grid point where derivatives are sought using the least squares criterion. The moving least squares method maintained good accuracy even when the particles were highly irregularly distributed. The focus of this chapter was on the capability of this three dimensional VIC method to capture the amplification and interaction of the three dimensional instability which leads

to the generation and intensification of streamwise vorticity in the highly strained regions connecting the spanwise rollers as shown in Chapter 5. Also, the objective is to explore the ability of this method to identify the sequence of events that have been demonstrated in the previous Chapter. These events comprise progression of Kelvin-Helmholtz instability, which encompasses amplification of the initial perturbation followed by the first rollup and the formation of the spanwise (two dimensional) rollers. The flow then departs its two dimensionality and generates three dimensional structures in the form of streamwise vortices spanning the flow domain and wrapping around the main rollers. Quantitative results for the mean velocity, second moment of velocity fluctuations and power spectrum are also explored and compared to the published experimental results.

6.2 Description of the Solution Method

In order for vortex methods to converge to the solution of vorticity transport equation, the particles support should overlap at all times. Computations involving non-overlapping particles tend to deteriorate very fast. The cause of the problem is the flow strain that clusters particles in one region and spread them in others. This will result in a non-smooth vorticity field and consequently a non-smooth velocity field. That is why the calculation of derivatives encountered in the stretching and diffusion terms of the vorticity equation (Equation 3.9) and in the source term of Poisson equation (Equation 3.8), i.e. the curl of the vorticity, represents a challenging task in vortex methods. Traditionally this difficulty is alleviated by remeshing as shown in Chapter 5. It proceeds by replacing the irregularly spaced vortex particles with a new set of particles located on a regularized lattice (mesh). In the present study, several numerical approximations

based on finite difference for calculating the spatial derivatives of vorticity and velocity were investigated, among them the robust fourth order scheme used by Verman et al (1997) but all of them have diverged after less than 100 time steps. Therefore an approach based on calculating the spatial derivatives of vorticity and velocity by the moving least squares method, which is used by Marshall and Grant (1997) for fully Lagrangian vortex method, is proposed in this study. This approach yielded a scheme that converged to a physically realistic result with no remeshing step being used throughout the computation. In this method, a polynomial is fit to the discrete values of the velocity and vorticity in the region around each grid point $\vec{x}_i$ where the derivatives are desired. This is accomplished by minimizing the sum of squares of errors. To this end, let us suppose that the derivative of a function $f(\vec{x}_i, t)$ is to be computed at a grid point $\vec{x}_i$ and the values of f is known at a finite number of discrete points (m) in the neighbourhood of $\vec{x}_i$. In the moving least squares method, a quadratic polynomial $p_2(\vec{x})$ is locally fit to the m data points in terms of the components of position difference as

$$p_2(\vec{x}) = a_o + a_1(x-x_o) + a_2(y-y_o) + a_3(z-z_o) + a_4(x-x_o)(y-y_o) + a_5(x-x_o)(z-z_o) + a_6(y-y_o)(z-z_o) + a_7(x-x_o)^2 + a_8(y-y_o)^2 + a_9(z-z_o)^2 \qquad (6.1)$$

where a_o , a_1 , ….., a_9 are unknowns to be found by minimizing the sum of squares of errors introduced by this approximation. The sum of squares of error E^2 is given by

$$E^2 = \sum_{j=1}^{m} \left[f(\vec{x}_j, t) - p_2(\vec{x}_j) \right]^2 \qquad (6.2)$$

The error is minimized by setting the partial derivatives of E^2 with respect to a_k to zero which result in a system of ten linear algebraic equations of this form.

$$\frac{\partial E^2}{\partial a_k} = \sum_{j=1}^{m} \left[f(\vec{x}_j, t) - p_2(x_j) \right] \left[\frac{\partial p_2}{\partial a_k} \right] = 0 \qquad k = 0,1,2,.....,9 \qquad (6.3)$$

The resulting linear system has to be solved for every grid point at every time step. In the present three dimensional work, seven points in every direction, that is 7^3 points are contributing to the calculation of coefficients in the three dimensional polynomial (Equation 6.4). Subroutine DLSLRG of FORTRAN numerical library IMSL is used to solve the linear system. This double precision subroutine solves real general system of linear equations with high accuracy. The solution is based on computing LU factorization of the coefficient matrix using Gauss elimination with partial pivoting. This polynomial is used to calculate the partial derivative of the velocity/vorticity at the node in the centre of a cubic box. The length of each side of the box is seven grid points. Implementation of this method to calculate derivatives is discussed in sections 6.2.1 and 6.2.2

6.2.1 Implementation of the Moving Least Squares Method

The moving least squares method is utilized to compute the derivatives encountered in the stretching term in the vorticity transport equation (Equation 3.9) and the source term Poisson equation (Equation 3.14). As an example, the vorticity increment due to stretching at point *i,j,k* in streamwise direction $(\Delta\omega_x)_{i,j,k}$ is given by

$$(\Delta\omega_x)_{i,j,k} \approx \left[\omega_x \frac{\partial u}{\partial x} + \omega_y \frac{\partial u}{\partial y} + \omega_z \frac{\partial u}{\partial z} \right]_{i,j,k} \Delta t \tag{6.4}$$

For simplicity, the time index is removed from equation 6.4. The spatial partial derivatives in equation 6.4 are computed by analytically differentiating the second order polynomial obtained from the moving least squares method (Equation 6.1) for velocity components. For example, the spatial derivative of *u* with respect to *x* is approximated by:

$$\left[\frac{\partial u}{\partial x}\right]_{i,j,k} \approx a_1 + a_4\left(y_{i,j,k} - y_o\right) + a_5\left(z_{i,j,k} - z_o\right) + 2a_7\left(x_{i,j,k} - x_o\right) \tag{6.5}$$

Coefficients a_1, a_4, a_5 and a_7 in equation 6.5 can be interpreted as weights to account for variation of u in the three directions within the small cube surrounding point *i,j,k* used in the calculation of the least squares polynomial. Similar expressions are used for the rest of the spatial derivatives terms in equation 6.4. Same approach is used to compute spatial derivatives of other components of stretching term. The least squares method is also used to fit a second order polynomial for the vorticity field with in a small computational box surrounding point of interest. This polynomial is used to compute derivatives occuring in the right hand side of Poisson equation. For instance, the streamwise velocity field is computed by solving Poisson equation,

$$\frac{\partial^2 u}{\partial x^2} + \frac{\partial^2 u}{\partial y^2} + \frac{\partial^2 u}{\partial z^2} = -\left(\frac{\partial \omega_z}{\partial y} - \frac{\partial \omega_y}{\partial z} \right) \tag{6.6}$$

The first term in the right hand side of equation 6.6 is approximated by analytically differentiating the least squares polynomial obtained for the vorticity in the neighbourhood of point *i,j,k* as,

$$\left[\frac{\partial \omega_z}{\partial y}\right]_{i,j,k} \approx a_2 + a_4\left(x_{i,j,k} - x_o\right) + a_6\left(z_{i,j,k} - z_o\right) + 2a_8\left(y_{i,j,k} - y_o\right) \qquad (6.7)$$

Similarly the second term on the right hand side of equation 6.6 is given by

$$\left[\frac{\partial \omega_y}{\partial z}\right]_{i,j,k} \approx a_3 + a_5\left(x_{i,j,k} - x_o\right) + a_6\left(y_{i,j,k} - y_o\right) + 2a_{10}\left(z_{i,j,k} - z_o\right) \qquad (6.8)$$

It should be noted at this point that a second order polynomial is computed for every internal point in the computational domain for every component of velocity and vorticity at every time step.

6.2.2 Diffusion Computation

In the present work, the diffusion effect is accounted for by modifying the particle strength ($\vec{\alpha}_p$) using the moving least squares method. Particle strength is updated every time step according to

$$\frac{d\vec{\alpha}}{dt} \approx \nu\nabla^2\vec{\omega}\left(\vec{x}_p\right)v_p \qquad (6.9)$$

The vorticity increment due to the diffusion term is computed on the grid by first calculating the Laplacian of the vorticity $\nabla^2 \vec{\omega}$ using the moving least squares method. As an example, the second order partial derivative of the vorticity with respect to x is approximated using equation 6.1 by

$$\frac{\partial^2 \omega_x}{\partial x^2} \approx 2a_7 \tag{6.10}$$

The vorticity increment is then interpolated from the grid location to the neighboring Lagrangian particles using M'_4 interpolation scheme as described in Chapter 3. As a consequence of diffusion, vorticity usually enters new regions every time step. This is manifested in a significant vorticity increment at the grid locations where there are no particles within the support of the interpolation scheme, surrounding the corresponding grid. In that case new particles are created at the grid location if the vorticity increment is greater than a predetermined threshold. In this work, a threshold value of 1% of the initial particle vorticity is considered.

6.2.3 Initial and Boundary Conditions

In order to perform meaningful comparison between the classical vortex in cell method which includes the remeshing step and the proposed moving least squares method which is used to compute the stretching term and to solve Poisson equations, the initial and boundary conditions used in this chapter are chosen to be same as those used in Chapter 5. Periodic boundary conditions are used for the streamwise and spanwise directions and

far field conditions are used for cross stream directions. Number of grid points are M_x=M_z=145, and M_y=259 similar to the base run in the remeshing case. A uniform grid size with h_x=h_y=h_z=0.125 cm was used in this simulation. Error function initial velocity profile for the streamwise component is utilized. All other conditions including initial perturbation, initial number of particles, initial particle strength and particle distribution are similar to those implemented in simulation of Chapter 5 of this study.

6.3 Outline of Algorithm

The sequence of steps followed in the program is as follows:

1. The initial vorticity sheet is discretized into a set of particles, each of which is identified by six parameters, namely particle strength vector $(\vec{\alpha}_p)$ and position vector $(\vec{x}_p)$.
2. The vorticity strength of each particle is projected to the mesh using M'_4 scheme.
3. The velocity components on the mesh are found from the solution of Poisson equations (Equation 3.9). The right hand side of equation 3.9 (curl of vorticity) is computed by the moving least square method.
4. The sequence of steps outlined in section (5.4.1) are followed to update the strength and position of each particle except that,
    - First and second spatial derivatives in the stretching and diffusion terms of the vorticity equation (Equation 3.14) are computed using the moving least square method.

- No remeshing step; that is no reinitialization of the particles on a regular lattice.

5. New particles are created on the nodes if the vorticity is greater than a threshold of 0.01 of the initial node vorticity.
6. Every time step, the vorticity is corrected to according to the methodology described in section 3.5 to satisfy the divergence free condition of the vorticity.
7. Repeat the algorithm from step 3

6.4 Results

The computational domain is similar to the one shown in figure 5.3. Results of the momentum thickness, vorticity thickness, similarity of the mean flow, velocity statistics, power spectra and the development of three dimensional instabilities to form the streamwise vorticity structure will be presented in the following sections.

6.4.1 Particle and Filament Presentation

In practical implementation of vortex filament method, every filament is identified by a finite set of points along it. These points are advected by the local velocity computed from solving Poisson equation every time step. Each filament is then reconstructed by reconnecting these points using an interpolation scheme. It is, therefore, natural to associate any points along a filament with a vector directing to the next point on that filament, which represent to a first order approximation the tangent to the filament at that point. Locations of these points and their associated tangents are used to find the velocity field induced by the filament. In vortex particle method, the vorticity field is

represented by a set of discrete, independent particles. A particle is defined by a vector of length proportional to the strength of the element and direction parallel to the vorticity vector at that point. As such, it can be easily shown that the strength of a particle is developing by the same rules as that of the filament, Cottet and Koumoutsakos (2000).

In the present three dimensional implementation of the Vortex-In-Cell method, the particles preserve their identity during their residence within the computational domain. Therefore, every particle is viewed as a marker on a vortex filament. For presentation purpose only, a vortex filament is reconstructed by linear interpolation of the particle location and tracked in time. In figures 1(a-i), a set of particles that belongs initially (i.e. at $t\Delta u/\theta_o = 0$) to the same filament are connected and the time evolution of this filament is tracked. The perspective views indicate that with the passing of time, the initial perturbation is amplified and leads to considerable waviness of the filament along the spanwise direction. Basically the number of waves is the same as the number of waves of the initial perturbations as illustrated in section 5.4. The filament is stretched and rotated starting approximately at $t\Delta u/\theta_o = 28.3$, showing noticeable stretching effects. The filament shape further evolves from the initial pattern given by the perturbations to a more pronounced square-wave pattern with legs in the streamwise direction, i.e. streamwise vorticity is being formed. In figure 1 (h and i) for $t\Delta u/\theta_o \geq 128$, no significant difference in the filament configuration is observed. Results and discussion will be limited to $t\Delta u/\theta_o \leq 128$**.** This time span is long enough to show the full process of Kelvin-Helmholtz instability, formation of large scale structures and development of secondary instability.

6.4.2 Growth Rates

The temporal development of the momentum thickness is calculated using equation (5.14) and shown in figure. 6.2. Momentum thickness data from the direct numerical simulation of Rogers and Moser (1994) is superposed in figure 6.2. At early stages the rate of growth of the momentum thickness is slow. This trend continues until the roll up where the vorticity developed into discrete structures. At later times the growth rate becomes faster when these structures start to entrain fluid from the irrotational flow. Figure 6.2 shows reasonable agreement between the current study and the direct numerical simulation of Rogers and Moser (1994).

Figure 6.3 shows the time evolution of the vorticity thickness defined by equation 5.17. The derivative is calculated for the streamwise velocity averaged over *x*-*z* plane. Fourth order central difference approximation was used to calculate the derivatives. From figure 6.3, during the self similarity period, the development of the vorticity thickness is almost linear. The ratio of average growth rate of the vorticity thickness to that of momentum thickness (i.e. ratio of slope of figure 6.3 to that of figure 6.2 ($\frac{d(\theta/\theta_o)}{d(\delta_\omega/\delta_{\omega o})}$)) is found to be equal to 3.92. Rogers and Moser (1994) computed this ratio to be 4.8. For comparison, this ratio would be 4.44 for an error function mean velocity profile and 4.00 for hyperbolic tangent profile. This variation shows that this ratio is very sensitive to the detailed shape of the mean velocity profile.

6.4.3 Mean Flow and Velocity Statistics

Average streamwise velocity profiles are shown in figure 6.4 at five times, namely at $t\Delta u/\theta_{o=}$ 43.1, 63.2, 89.4, 103.8 and 121.6. The figure shows that self similarity is attained and preserved within the specified time span when the temporal momentum thickness is used to normalize the cross stream coordinate. Data from experiment of Bell and Mehta at two streamwise locations within the similarity zone (namely *at* x=108.1 *and* x=128.4 *cm*) is also presented on figure 6.4, suggesting that self similarity is achieved and in agreement with the experimental data.

Figure 6.5 shows the root mean square for the streamwise velocity fluctuations at four times within the simulation time, namely $t\Delta u/\theta_{o=}$ 63.2, 89.4, 103.8 and 121.6. The root mean square values are normalized by the velocity difference across the mixing layer. Because the root mean square represents the second moment, it took the flow longer time to attain similarity than that for the mean (first moment). However, the conventional bell shaped profile of the root mean square can be observed within the similarity period. Experimental results due to Bell and Mehta (1990) are also presented on the plot. Reasonable agreement can be observed between the experimental results and the current simulation. The average maximum value for the root mean square of the current simulation was 0.174 compared to 0.17 for Bell and Mehta experimental results.

The bell shape of the root mean square of cross stream velocity fluctuation is also preserved within the similarity period mentioned above as demonstrated by figure 6.6. Good agreement can be observed between the present simulation and the experimental data of Bell and Mehta (1990). The average maximum value for the root mean square for

the experiment and the present simulation are almost equal (0.12 for the experimental results and 0.123 for the present simulation).

Similarity of root mean square of spanwise component of velocity profile is shown in figure 6.7. In this figure, experimental data of Bell and Mehta (1990) are superposed on four profiles for the same times considered above. The average maximum of experimental data is 0.14, while the average maximum of the present simulation is 0.132. Cross correlation of streamwise and cross stream components of velocity fluctuations is presented in figure. 6.8 for the same times considered in figures. (6.5-6.7). The values of cross correlation are normalized by the square of streamwise velocity across the shear layer. Similarity of profiles is well established over that period. Also the data is in good agreement with the experimental data of Bell and Mehta (1990). On average, the maximum value for the cross correlation is -0.107 for the present simulation and -0.01 for the experimental data of Bell and Mehta (1990).

It is observed that velocity statistics of the present simulation show, in figures 6.5-6.8, better congruence to the experimental data than that of figures (5.7-5.10) when remeshing is used. In particular, the present data shows better agreement at the tails of bell shaped profiles.

6.4.4 Mixing Layer Three Dimensionality

To demonstrate mixing layer three dimensionality, the streamwise velocity contours across *y-z* plane are presented in figure 6.9. In this figure the streamwise velocity values are obtained by averaging over the streamwise direction. Thirty (30) uniformly

distributed contour levels are shown for the interval $u/\Delta u$ [-0.5, 0.5]. Figure 6.9 shows the streamwise velocity contours at four points in time, namely $t\Delta u/\theta_{o=}$ 43.1, 63.2, 89.4 and 103.8. These four contour snapshots started after the vorticity sheet roll up and saturation of two dimensional Kelvin-Helmholtz instability. Measured by the variation of streamwise velocity across spanwise direction, figure 6.9 shows that three dimensionality accentuates with the passing of time, however no noticeable changes occurred after $t\Delta u/\theta_o$=103.8.

Three dimensionality of the flow can also be demonstrated by generation and evolution of spanwise and cross stream vorticity. This simulation started with streamwise and cross-stream vorticity comprising 0.01% of the total vorticity in the computational domain. Figure 6.10 illustrates the evolution of the vector modulus of streamwise and cross stream particle strength as a measure of three dimensionality. This parameter is calculated as,

$$\int_v \left[\omega_x^2 + \omega_y^2\right]^{1/2} dv$$

where v corresponds to the volume of the computational domain. Development of three dimensionality, as determined by the parameter above, passes through three regions as shown in figure 6.10. Initially, slow rate of evolution can be identified when $t\Delta u/\theta_o$<10. At the end when $t\Delta u/\theta_o$>120 the graph reaches a plateau where the growth of this parameter is insignificant. In between the above two time limits, linear temporal three dimensionality growth rate can be observed. The oscillations in this figure are thought to

be due to the change in the number of particles within the computational domain and the effects of interpolation scheme.

As stated in Chapter 5, the divergence free vorticity field criterion is implicitly satisfied in two dimensional flows. But that is not the case for three dimensional flows. In order to ensure the vorticity field solenoidality, the vorticity correction technique due to Cottet (1996) was used as outlined in Chapter 3. The result of this methodology as reflected in the calculation of vorticity divergence is presented in figure 6.11. As shown in the figure the vorticity divergence is preserved, hovering around zero through out the computation.

6.4.5 Evolution of Instabilities in Three Dimensional Mixing Layers

In this section, evolution of both the two dimensional Kelvin-Helmholtz instability and three dimensional secondary instability, as pertinent to the present moving least squares are examined. Vorticity field, velocity field and particle location are used to investigate the development of these instabilities and to show the potentials of this method to capture different three dimensional flow characteristics.

6.4.5.1 Formation of Spanwise Vortices

Figure 6.12 shows the evolution of spanwise vorticity contours at mid-plane in z direction (i.e. z/L_z=0.5), at four times through out the computation, namely $t\Delta u/\theta_o$=15.0, 43.1, 89.4 and 121.6. Initially, the shear layer is dominated by the influence of Kelvin-Helmholtz instability until the first roll-up occurring at the edges of the computational domain, as shown in figure 6.12 (a). After that, the flow is mainly two dimensional where the first

roll-up is followed by few others to generate the rollers as can be observed in figure 6.12 (b). The formation of ribs connecting these rollers is presented in figure 6.12 (c). At the rib regions, spanwise vorticity is thinning and eventually becomes devoid of spanwise vorticity as evident from figure 6.12 (d).

Figure 6.13 presents the velocity vector at the same location and times as in figure 6.12. The velocity vector in figure 6.13 is comprised of the streamwise and cross stream components, the two components that produce the spanwise vorticity. Kelvin-Helmholtz instability amplifications and the formation of the two dimensional rollers can be observed in figures 13 (a) and (b), respectively. In a reference frame moving with the average velocity**,** i.e. a temporal mixing layer, the rotation of the two rollers leads to the formation of a local stagnation point at the rib (braid) region between the rollers as shown in figure 6.13 (c) and (d). The stagnation point is formed because the fluid entrained by the vorticity is split into two streams, one stream orbits around the upstream roller while the other orbits around the downstream roller. As indicated by the velocity vector field around the stagnation point, the braid region is characterized by high strain rate, this is the reason the particles passing through the stagnation point are subjected to large amount of stretching. Similar results were obtained by Ashurst and Meiberg (1988).

6.4.5.2 Formation of Streamwise Vorticity-The Onset of Three Dimensionality

Figures 6.14 (a-d) present a three dimensional view of all the particles in the computational domain at four different times, $t\Delta u/\theta_o$=12.1, 43.1, 63.2 and 103.8. Since the vortex particles are advected with the flow field, their relative positions give a clear

picture of the main flow features, i.e. the large to moderate structures. Initially for $t\Delta u/\theta_o$ =12.1 in figure 6.14 (a), the vortex particles are concentrated around the plane $y/L_y \approx 0.5$. As the flow develops due to the rollup of the mixing layer, figure 6.14 (b) shows that vortex particles accumulate, form tube like structure along the spanwise direction and in particular a concentration of particles appears along the centre line of the tube. For $t\Delta u/\theta_o \geq 63.2$, the originally small perturbation of the vortex particle location in the spanwise direction magnifies significantly at the plane z/L_z =0.5**,** leading the flow to departing from its two dimensionality. Figure 6.14 (c) and (d) shows that the growth of the spanwise rollers continue and at the same time their spanwise undulations increase, which demonstrate the onset of new instability mechanism, i.e. the secondary (translative), instability as presented in section 5.5.4.2 and discussed in the simulation of Knio and Ghoniem (1992). The evolution of the translative instability is better demonstrated in figure 6.15 (a-d) where a magnified view of the particle field is presented for $0.3 \leq x/L_x \leq 0.7$, at the same times as in figure 6.14 with different orientation of the coordinate system. The translative instability shown in figure 6.15 (a-d) appears initially as a slight undulation in the spanwise direction which intensifies with time and evolves into a significant deformation of the spanwise rollers. The slight perturbation of the vortex sheet in figure 6.15 (a) becomes quite noticeable as time evolves in figure 6.15 (b). The onset of the formation of well defined streamwise structure is shown in figure 6.15 (c) (dark regions along x direction). The translative instability and the high strain rate of the braid region lay the ground to the evolution of the streamwise structures shown in figure 6.15 (d).

6.4.5.3 Three Dimensional Large Scale Structures

Development of the flow in the braid region is illustrated in figures 6.16(a-d), where the isosurfaces of the streamwise vorticity (ω_x) is presented at four different times, namely $t\Delta u/\theta_o$=12.1,43.1, 63.2 and 103.8, where the streamwise vorticity is nondimensionalized by the initial momentum thickness θ_o and the velocity difference across the mixing layer. At $t\Delta u/\theta_o$=12.1, the streamwise vorticity starts to organize as sticks spanning the computational domain in the spanwise direction as shown in figure 6.16 (a). Figures 16 (b) and (c) show that the vorticity in the braid region, as a result of stretching and secondary instability effects, intensifies and grows into ribs like undulated vortex patches of opposite sense spanning the distance between rollers. These patches further grow by the action of the translative instability and eventually, extend through the braid region and wrap around the spanwise rollers as shown in figure 16 (d).

Growth of streamwise vorticity is also shown in figures 6.17-6.19, in each of which the grid vorticity contours are plotted at four *y-z* planes through out the computational domain, namely x/L_x=0.2, 0.4, 0.6 and 0.8. The three figures represent snapshots of streamwise vorticity at three times during computation, $t\Delta u/\theta_o$=43.1, 63.2 and 103.8 *r*espectively. Ten contour levels of the streamwise vorticity ($\omega_x\theta_o/\Delta u$) are shown in each of these figures. Dashed lines in these figures represent negative vorticity and continuous lines represent the positive vorticity. In figure 6.17 the ten contour levels are chosen such that $\omega_x\theta_o/\Delta u$ is in the range [-0.0005, 0.0005*]* with uniform increment of 0.00001. At $t\Delta u/\theta_o$=43.1 the undulation due to initial perturbation is not obvious, however two pairs of elliptical counter-rotating vortices are emerging with their major axes coincide with

the level of splitter plate. No differences in these structures can be discerned along the streamwise direction.

Figure 6.18 (a-d) is plotted with the same characteristics as Figure. 6.17 except that the streamwise vorticity range $\omega_x\theta_o/\Delta u$ is *[-0.002, 0.002]* and the increment is *0.0004.* This figure shows the streamwise velocity at $t\Delta u/\theta_o$=89.4. At this time the magnification of the initial perturbation is clearly revealed and is in phase with the perturbations. Vortex structures appear as pairs of opposite sense. The evolution of streamwise vorticity at the same four locations at later time ($t\Delta u/\theta_o$=103.8*)* is shown in figure 6.19, where augmentation in thickness of the rib vortices is detected.

Figures 6.20-6.22 show velocity vectors constructed using spanwise and cross stream components of velocity. The time and streamwise locations used in these figures correspond to those used in figures 6.17-6.19. The evolution of the counter-rotating streamwise structure is attributed to the streamwise vortex rods that develop, stretch and wrap around the upper stream and lower stream of the spanwise rollers as shown in the experiment of Lasheras and Choi (1988) and captured by the numerical simulations of Ashurst and Meiberg (1988) and Inoue (1989)

The existence of the counter-rotating streamwise structure can also be demonstrated using the particle velocity shown in figure 6.23. In this figure the evolution of spanwise and cross stream components of particle velocity is shown at x/L_x=0.6 at four times, $t\Delta u/\theta_o$=12.1, 43.1, 63.2 and 103.8. Particles are located within a slice with a thickness of one grid size. Particle velocity is obtained by interpolating the grid value to the particle location. These figures indicate that these pairs of counter-rotating vortices forms and

persists at fixed spanwise locations. The locations of the streamwise rollers are in phase with the initial perturbation given to the particle location. This suggests that translative instability is evolving as proposed by Pierrehumbert and Widnall (1982). Figures 6.24 (a-d) show a section through the plane x/L_x=0.6 for the particle field at the same times as the previous figure. The small perturbation in figure 6.24 (a) is amplified in (b) and (c) while staying in phase with the initial perturbation. The rollup of the braid region in figure 6.15 and the stretching of the streamwise vortices which wrap around the spanwise rollers generate a mushroom like structure as shown in figure 6.24 (d). This structure was identified experimentally by Bernal and Roshko (1986) and numerically by Knio and Ghoniem (1992).

6.4.6 Energy Spectra

Turbulent kinetic energy scattered through the wave number space is collected as a function of one dimensional wave number in figures 6.25 and 6.26. These figures are produced following the same method used in section 5.5.5. Temporal evolution of energy spectra are shown at four times, namely at $t\Delta u/\theta_o$=43.1, 63.2, 89.4 and 103.8. In these figures a -5/3 spectrum is also plotted for comparison. Figure 6.25 shows the energy spectrum as a function of streamwise wave number. During the development stage at $t\Delta u/\theta_o$=43.1 and 63.2, maximum energy is contained in the fifth mode and the spectra at these times do not decrease monotonically. Whereas for $t\Delta u/\theta_o$>89 energy spectra become saturated and decrease monotonically, it is also observed that at these times, maximum energy is contained at the second mode. The distribution of turbulence energy among wave numbers in the spanwise direction is shown in figure 6.26. For all the times

presented in the figure maximum energy is contained in second mode of the spectra. The exception was the energy spectrum at $t\Delta u/\theta_o$=63.2, where the maximum energy occurred at the third mode.

6.4.7 Effect of Numerical Parameters

The Lagrangian nature of the vortex methods, which is maintained during this simulation by advection the vortex particles with the local velocity, liberates these methods from the advection stability constraints (Cottet et al, 2002) and (Chetalain et al, 2008). Therefore, time step in particle methods is not explicitly linked to the grid resolution. However, as discussed in Sarpkaya (1994), the accuracy of Vortex-In-Cell method is sensitive to numerical parameters. In this simulation, the sensitivity of the numerical solution to the spatial resolution of the computational box and the initial number of particles was investigated by maintaining the vorticity sheet strength and doubling the grid size in each direction of the computational domain. Therefore an additional run is made in which the grid size is doubled and the initial number of particles per grid is kept unchanged, that is M_xxM_yxM_z=73x73x129 and the initial number of particles is 20736 to investigate the influence of the numerical parameters.

6.4.7.1 Mean Streamwise Velocity

The normalized streamwise mean $\frac{u-u_2}{\Delta u}$ velocity for both cases, namely the base run and the double grid size run are presented in figure 6.27. The two profiles are plotted against the normalized cross stream direction $y/\theta(t)$. Every point represents the average of

the streamwise velocity at a particular x-z plane. The two profiles are sampled at effectively the same nondimensional time $t\Delta u/\theta_o$=89.4 within the similarity period of the flow. As shown in the figure, the two velocity profiles are hardly distinguishable which demonstrates that at this grid size and initial particle number the simulation, on the mean, effectively converges to the same solution.

6.4.7.2 Velocity Statistics

Sensitivity of velocity statistics to the numerical parameters is presented in figures 6.28 through 6.31. The comparison is conducted at $t\Delta u/\theta_o \approx 89.4$ within the similarity period.

Figure 6.28 shows the root mean square of streamwise velocity fluctuations normalized by the velocity difference. The two profiles are obtained by the same method used in the Chapter 5. Every point is calculated by averaging the sum of squares of velocity fluctuation over an *x-z* plane. The two plots are generally close enough to each other to demonstrate that the simulation is insensitive to grid size and number of vortex particles.

Identical behaviour can be observed in figures 6.29, 6.30 and 6.31 where the root mean square of the cross stream velocity fluctuation, spanwise velocity fluctuation and the cross correlation of the streamwise and cross stream components of velocity fluctuations are presented, respectively.

6.4.7.3 Energy Spectra

Figures 6.32 and 6.33 show the effects of doubling the grid size on the one dimensional energy spectra. Figure 6.32 represents the turbulent kinetic energy distribution among the

wave numbers in the streamwise direction at $t\Delta u/\theta_o \approx 89.4$. It is obtained by integrating the modal energy in the cross stream direction and performing summation in the spanwise direction. For the base run, 72 Fourier modes are considered in the Fourier space, twice as many as the case of doubling the grid size. The wave numbers range in both runs is

$$k_{\min} = \frac{2\pi}{M_x h_x} \quad to \quad k_{\max} = \frac{2\pi}{h_x}$$

When doubled the grid size, only half the Fourier modes can be resolved, i.e. 36 modes. The base run harmonics appear at the higher wave numbers toward the dissipative end of the spectrum. For both runs in figure 6.32, maximum energy appears at the fourth harmonics. The two runs explored exhibit well defined inertial subrange; however the two plots tends to diverge toward the higher end of the spectrum.

Figure 6.33 represents the one dimensional energy as a function of the wave number in the spanwise direction. It is obtained in a similar method as that of figure 6.32 with the exception that summation is performed in the streamwise direction. In general figure 6.33 exhibits similar trend as that of figure 6.32.

6.4.8 Inviscid Run

In practical implementation of vortex methods some numerical dissipation is inevitable due to Lagrangian discretization of the vorticity field and the use of Eulerian mesh to compute velocity. However it is important to ensure that numerical diffusion introduced by vortex method implementation does not significantly contaminate the role of physical

viscosity in flow dynamics. Therefore and to investigate these effects, the diffusion computation is shut off in this run. Due to unrealistic high velocity the run is terminated at $t\Delta u/\theta o$=95.4 The consequences of inviscid simulation on the evolution of momentum thickness, vorticity thickness, mean velocity, velocity statistics and energy spectra will be discussed in the following.

Results of simulation of inviscid temporal mixing layer are shown in figures 6.34-6.42. Temporal growth of momentum thickness and vorticity thickness are shown in figures 6.34 and 6.35, respectively. In general, these two parameters are developing linearly and no significant influence of disregarding viscosity can be deduced from these figures, except for the momentum thickness exhibits a slightly higher rate of growth than that of the viscous run.

Figure 6.36 shows the mean velocity plotted at four different times; namely $t\Delta u/\theta_o$=57.6, 66.3, 73.8, 82.5. Similarity of mean velocity profiles for the inviscid run is observed over the reported time period and in agreement with the experimental results, an indication that the interaction of large scale structures is essentially governed by inviscid flow dynamics.

Figures 6.37-6.40, respectively, show the root mean square of streamwise velocity, cross stream velocity, spanwise velocity and cross-correlation of streamwise and cross stream velocity fluctuations, at times corresponding to that of figure 6.36. Similarity of velocity statistics could not be established in these figures due to the omission of diffusion effects in this run. Energy spectra presented in figures 6.41 and 6.42 show incremental increase in turbulent energy levels and accumulation of energy at high wave numbers.

Chapter 7

Numerical Performance of the Two Methods

7.1 Introduction

The two vortex methods used in Chapters 5 and 6 were able to satisfactorily predict the evolution of three dimensional temporal mixing layer, including mean flow, velocity statistics and three dimensional flow structures. For the applications of high Reynolds number flows, vortex methods, in general, offer the advantage of being free of numerical dissipation errors. However, in practice, they introduce some numerical dissipation as a result of operator splitting (fractional step) and remeshing process. Therefore, the first fundamental question one may pose in regards to the practical use of the vortex (blob) method refers to the accuracy that one can expect from the spatial discretization of the vorticity field. Therefore an objective comparison between these two methods will be presented. The comparison focuses on the results of Chapters 5 and 6 in relation to momentum and vorticity thicknesses, mean velocity, velocity statistics, power spectra, and, vorticity structures. Also, the numerical diffusion associated with the two solution

methods and the performance of each method regarding the computational time will be presented.

7.2 Comparison of Growth Parameters and Mean Velocity

Figure 7.1 presents the results of momentum thickness evolution of the remeshing scheme and the moving least squares scheme presented in Chapters 5 and 6, respectively. The growth rates of both methods are effectively the same and the two graphs are hardly distinguishable.

Figure 7.2 shows the vorticity thickness growth of two schemes used in this work. It can be observed that the two graphs are coinciding up until $t\Delta u/\theta_o$=50, after which they tend to slightly divert from each other. Later, around $t\Delta u/\theta_o$=120, the two graphs begins to converge toward each other. The reason for this discrepancy is that; unlike momentum thickness which is computed from an integration formula, the vorticity thickness is calculated from a differentiation formula which makes it more sensitive to the numerical noise.

In figure 7.3, the mean velocity of the two schemes is compared. Results for remeshing scheme are presented at $t\Delta u/\theta_o$=84.4, 105.2 and results for the moving least squares are presented at $t\Delta u/\theta_o$=89.4, 103.8. In general, the two schemes show good similarity characteristics. However, the remeshing scheme shows smoother convergence toward the upper end of the computational domain where $(u-u_1)/\Delta u$=1.

7.3 Comparison of Velocity Statistics

The results of the second moment of velocity for the two schemes are compared in figures 7.4-7.7. Velocity statistics of the remeshing scheme are plotted at $t\Delta u/\theta_o$=84.4, 105.2 and velocity statistics for the moving least squares method are plotted at $t\Delta u/\theta_o$=89.4 and 103.8.

Figure 7.4 shows the comparison of the root mean square of the streamwise velocity for the two schemes. The figure shows that the two schemes provide close predictions of the root mean square values, however faster convergence toward the undisturbed flow can be observed in the remeshing scheme results. Figure 7.5 compares the root mean square of the cross-stream velocity. Slightly better similarity characteristics are presented by the moving least squares scheme as shown in the figure. Similar trend is noted in figure 6 where the root mean square of the spanwise velocity is compared. Figure 7 presents a comparison of the results of cross correlation of streamwise velocity and cross-stream velocity. In contrast to the moving least squares results where the cross correlation is negative through out the computational domain, remeshing scheme results show slightly positive values around y/θ= -3.

7.4 Comparison of Power Spectra

Figures 7.8 and 7.9 show a comparison between the energy spectra results of the two schemes used in this work. Energy spectra of the remeshing scheme are plotted at $t\Delta u/\theta_o$=84.4, 105.2 for both the streamwise and spanwise wavenumbers. Energy spectra of the moving least square method scheme are plotted at $t\Delta u/\theta_o$=89.4 and 103.8.for both the streamwise and spanwise wavenumbers. Figure 7.8, in which the energy spectra are

plotted against the streamwise wave number, shows that remeshing result are developing as compared to the moving least squares results. This behaviour is also observed in figure 7.9 where the energy spectra are plotted against the spanwise wavenumber. It is also observed that maximum energy occurs at the fifth harmonics in the case of remeshing simulation while it occurs in the second harmonics in the case of moving least squares method.

7.5 Comparison of Vorticity Structures

Figures 7.10 and 7.11 prersent a comparison of the vortical structures resulted from the two schemes used in this work. Figures 7.10 (a-d) show the development of the vorticity contours of the spanwise vortices of the remeshing scheme while (e-h) show that of the moving least squares method. As discussed in Chapter 5, temporal mixing layers are made by a frame of reference moving at the average velocity of the two streams. Thus for an observer moving with this frame, the two streams will appear to move toward each other with a velocity equal to half the velocity difference of the two streams. That means, spanwise vortices generated in this flow are living in the background of high shear field and subject to mutual interactions. Therefore they continue to evolve and in the mean time they will be deformed and subjected to pairing; the dominant mechanism of the growth of mixing layers. In temporal mixing layers, there are two competing phenomena affecting the development of spanwise vortices. While the induced velocity is trying to push the two rollers apart, the strong shear field is trying to pull them together. Pairing of spanwise vortices occurs due to the dominance of shearing effects over the vorticity induced velocity. This sequence of events is qualitatively well captured by both schemes.

Figures 7.11 (a-d) shows the streamwise vorticity contours results of the remeshing scheme and figures 7.11 (e-h) show that of the moving least squares method. The two schemes produced two pairs of counter-rotating vortices structures. However it can be noted that the vortices produced by the moving least squares method are rounded compared to that produced by the remeshing scheme which shows deformation in the spanwise direction. Also, it observed that the remeshing scheme produced clear two rows of vortices quite similar to the LES results of Rajab (1995). This feature is less obvious in the moving least squares scheme results.

7.6 Accuracy

Extensive theoretical work has been done on the convergence analysis of both viscous and inviscid vortex methods. Among many others, most notably work of Beale and Majda (1982), Cottet et al (1991) and Hald (1983). In this work the initial vorticity distribution is approximated by a finite set of particles, the voricity distribution within each particle is three dimensional Dirac delta function (Equation 3.17). Difficulties associated with the singularity of delta function are alleviated by the Eulerian grid system and interpolation scheme. These measures introduce some errors due to their dissipative effects on the numerical method. Accuracy of the discretization and effects of the Eulerian grid smoothing manifested as numerical diffusion will be investigated by the actual numerical experiment.

The enstrophy ς, a flow parameter measuring the amplification of vorticity due to stretching, is defined by

$$\varsigma = \left\langle \omega_x'^2 \right\rangle + \left\langle \omega_y'^2 \right\rangle + \left\langle \omega_z'^2 \right\rangle \tag{7.1}$$

It has a relationship to the vorticity similar to that of the kinetic energy E to the velocity. For a free shear flow where there is no wall effects and under the assumption of homogenous turbulent flow, the turbulence kinetic energy is related to the enstrophy ς by, (Bernard and Wallace 2002)

$$\frac{dE\ (t)}{dt} = -\nu_{eff}\varsigma(t) \tag{7.2}$$

This equation abstracts one of the most basic phenomena and distinctive feature of the three dimensional turbulence. That is the predominance of vortex stretching which is manifested by enstrophy production and balanced by viscous dissipation. Therefore equation (7.2) is used as a measure of the effective viscosity of the numerical algorithm used in this work. Fourth order central difference method is used in temporal derivative of equation (7.2) during the post processing step for the obtained data,

$$\frac{dE(t)}{dt} \approx \frac{E_k(t-2\Delta t) - 8E_k(t-\Delta t) + 8E_k(t+\Delta t) - E_k(t+2\Delta t)}{12\Delta t} \tag{7.3}$$

Figure 7.12 shows a comparison between the turbulence energy history of the two vortex methods used in this work, namely the Vortex-In-Cell with remeshing (dotted line) and

the Vortex-In-Cell with moving least square (continuous line). Computation of total energy began after computing the mean velocity and after introducing remeshing step within the computation scheme.

In temporal mixing layers, the production of turbulent kinetic energy exceeds the dissipation, (Rogers and Moser, 1994). However this excess of energy is transported outward due to the inhomogeneity in the cross-stream direction. Thus, the turbulent kinetic energy tends to a value that does not significantly change with time as shown in figure (7.12).

It is generally acceptable to use the term $v_{eff}\ \varsigma$ interchangeably with the energy dissipation even in the presence of significant mean shear as in the case of mixing layer (Bernard and Wallace 2002).The time variation of the enstrophy for the two schemes is shown in figure 7.13).

Fig 7.14 shows the temporal development of the relative diffusion error $[(v_{eff}-v)/ v]$ for the two methods. This figure essentially provides a comparison of the cumulative dissipative effect of interpolation on the least square method and the effect of remeshing and interpolation on the remeshing method. In other words this figure offers a quantitative measure of the artificial viscosity introduced by each of the two numerical algorithms used in this work. The maximum absolute relative diffusion error is 13.6% for the remeshing method and 13.0% for the least squares method. However the average diffusion error for the remeshing method is 11.2% and that for the moving least squares is 9.4%.

7.7 Resolved Scales

By its nature, turbulence is a multiscale phenomenon. The well known Kolmogorov scaling law (Pope, 2000) revealed that turbulence consists of a continuum of scales, from the largest scales determined by the flow geometry to the smallest ones at Kolmogorov dissipation scale. Thus there is no clear and distinct scale separation in turbulent flows. The scale separation can only be regarded as a hypothetical concept by which different physical processes can be recognized. Scale separation is also beneficial to identify the extent of resolution attained by a particular grid size in a numerical simulation.

Based on the universal equilibrium concept due to Kolmogorov (Pope, 2000), the dissipation scale η is related to the viscosity ν and the dissipation ε by

$$\eta = \frac{\nu^{\frac{3}{4}}}{\varepsilon^{\frac{1}{4}}} \tag{7.4}$$

But as stated earlier the dissipation is directly related to the enstrophy by $\varepsilon=\nu\ \varsigma$, therefore,

$$\eta = \frac{\nu^{\frac{1}{2}}}{\varsigma^{\frac{1}{4}}} \tag{7.5}$$

Figure 7.15 shows the time variation of the dissipation scale during the simulation time of the two schemes. It can be observed that the dissipation scale for the remeshing scheme and the moving least squares scheme asymptotically approaches 0.68mm and

0.72 mm, respectively. In comparison to the grid size used in this study, the simulation in both cases was under-resolved.

7.8 CPU Time Comparison

In fully Lagrangian vortex methods when Biot-Savart solution of Poisson equations is used, the operation count is of order of N^2 if N vortex particles exist within the computational domain. The Vortex-In-Cell method is devised mainly to reduce the execution time without sacrificing the accuracy. Figure 7.16 shows a comparison of the CPU time for every time step as a function of the number of vortex particles. Both methods effectively exhibit linear relationship between the CPU time and the number of particles. However at the early stages of the execution, particularly prior to remeshing commencement, remeshing method shows lower time requirements as the number of particles increases. Significant step change in the time requirements can be observed as a consequence of the remeshing step. After initiation of remeshing, the least squares method shows better performance. For example, at 120000 particles, the least squares method outperformed the remeshing method by 10.7% reduction in CPU time. As the number of particles within the computational domain increases the two lines diverges in favor of the least squares method.

Figure 7.17 shows the total (accumulative) execution time against the number of particles for the two methods used. Starting with 82944 particles, the number is roughly doubled by the end of simulation for both methods (160415 particles for the least squared method and 155511 for the remeshing method). The remeshing method shows steep increase in the number of particles at the beginning of the simulation particularly after introduction

of remeshing step. Then it reaches a plateau where there are no significant changes in the flow features. Slower rate of increase of particles number can be observed for the least squares method until it reaches a plateau. It can also be observed that at the beginning of the simulation the time requirement for the remeshing method is significantly less than that of the least squares method for the same number of particles. However, towards the end the trend is reversed.

Chapter 8

Summary, Conclusions and Recommendations

8.1 Closing Remarks

A hybrid Eulerian-Lagrangian numerical method, based on the Vortex-In-Cell method has been developed and implemented to simulate three dimensional temporally evolving mixing layer flows. This scheme has demonstrated proper account for diffusion and stretching effects. The main contribution of this work was the utilization of the moving least squares method within the framework of Vortex-In-Cell method and the implementation of this approach to a three dimensional temporal mixing layer.

A two dimensional code was first developed to test and validate the major building blocks of a successful VIC method. That includes, among other details, a Poisson solver to compute velocity, an interpolation scheme for exchanging information between Eulerian and Lagrangian grids, and a time integration technique to advance the flow. The two dimensional code was used to simulate two dimensional spatially evolving mixing layer flow. The two dimensional code is then significantly developed to simulate three dimensional vorticity equation using VIC method. Within the context of three

dimensional VIC method, two schemes were used to compute the stretching and diffusion operators. In the first, the Lagrangian mesh (particles) are replaced by a new set of well overlapped and organized particles every few time steps to best approximate the current vorticity field. Stretching and diffusion are computed using fourth order finite difference approximation. The M'_4 interpolation scheme is used to identify the locations and strengths of the new set of particles. Without this remeshing scheme the computation of derivatives that occur in the stretching and diffusion terms of the vorticity equations would have deteriorated at early stages of the simulation. Second numerical scheme is developed where the remeshing step is alleviated and the derivatives are approximated using the least squares method. Both methods were implemented to three dimensional temporal mixing layer. The two schemes were able to reasonably reproduce the mean flow, velocity statistics, energy spectra, and most importantly the evolution of secondary instability and the formation of streamwise structures. The performance of these two schemes and the flow features they produced will be summarized in the following sections. The merits and improvement opportunities of the two schemes used in this work within the context of VIC method are put in perspective.

8.2 Two Dimensional Mixing Layer

The VIC method is used to simulate two dimensional spatially developing mixing layer. This flow is used to validate the main code elements. Results of mean flow and the root mean square of streamwise velocity fluctuations demonstrated good agreement with the experimental results of Bell and Mehta (1990). The higher values of the root mean square of the cross stream components is attributed to the fact that kinetic energy from the

streamwise transfers only to the cross stream direction while in three dimensional flows it is distributed among cross stream and spanwise directions. The simulation was also able to predict evolution of flow instabilities including the linear stage, the first roll up, and vortex pairing.

8.3 Three Dimensional Mixing Layer

Three dimensional VIC computer code was developed to simulate three dimensional temporal mixing layer. Two schemes were used to calculate the derivatives encountered in the stretching and diffusion terms. Both schemes were able to satisfactorily predict the mean flow, velocity statistics, energy spectra, development of two dimensional Kelvin-Helmholtz instability, and evolution of secondary (translative) three dimensional instabilities that leads to the formation of streamwise structures.

8.3.1 Mean Flow and Velocity Statistics

Linear Growth rate of the temporal mixing layer as described by the momentum thickness and vorticity thickness are computed for both schemes with reasonable accuracy. Mean velocity profiles are well predicted by both schemes compared to the experimental results of Bell and Mehta (1990). Similarity of mean velocity profiles is established for $t\Delta u/\theta_o$=42.8 to 123.*1* for the remeshing scheme and for $t\Delta u/\theta o$=43.1 *to* 121.6 for the least squares scheme. However least squares results shows slightly improved congruence to the experimental data.

For the velocity statistics, both schemes took longer time to establish similarity than that for the mean flow. Root mean square of streamwise velocity fluctuations results shows, to some extent, less scatter than that of the remeshing scheme at the maximum value. On average, the maximum value of root mean square of streamwise velocity fluctuations is 0.18 for the remeshing scheme, 0.174 for the least squares scheme, and 0.17 for the experimental results of Bell and Mehta (1990). For the root mean square of the cross stream velocity fluctuations, both schemes attain similarity and same average maximum value, which is in good agreement with the experimental data, however remeshing scheme produced somewhat narrower profile compared to that of the experiment and the least square scheme. Root mean square profiles of spanwise velocity fluctuations are generally in good agreement with the experimental data for both schemes. Results of the remeshing scheme show some positive values of the cross correlation. This is attributed to the fact that the long time average of the cross correlation depends on the tilt angle of spanwise vorticity structure and the strain rate of the flow field. Certain tilt angles could result in positive values of cross correlation.

8.3.2 Energy Spectra

Both schemes resolved the temporal mixing layer flow well. Qualitatively, significant flow scales are captured by these schemes. Energy spectra are also used as a diagnostic tool for the accuracy of both schemes. When viscous substep is shut off, accumulation of energy at the higher end of the spectrum is observed for both schemes. Since the reverse cascading of energy from smaller to larger eddies could not be noticed in figures 5.33, 5.34, 6.32, and 6.33 and the calculation of the effective viscosity as shown in figure 7.3

did not show any global negative value (backscatter), the accumulation of energy is most likely due to the absence of dissipation mechanisms, and consequently the minimal effect of numerical diffusion in these methods.

8.3.3 Spanwise Vortices

As suggested by many numerical and experimental studies, development of mixing layer results from the amplification of small instabilities that exist naturally in the experimental device or artificially introduced in numerical simulation. These mechanisms trigger Kelvin-Helmholtz instability which starts as a linear amplification of these small disturbances. In their non linear stage, Kelvin-Helmholtz instabilities lead to the first rollup which later grow into large spanwise vortical structures. Such progression of events is captured by both schemes. Evidences from particle field and mesh values are presented. That includes particle locations, velocity vectors, and vorticity contours.

8.3.4 Streamwise Vortices

As discussed in the previous section, the primary Kelvin-Helmholtz instability develops first leading to the formation of almost two dimensional vortex rollers. Under the influence of the strain field generated by the growing spanwise vortices, the small initial sinusoidal perturbations amplify and undergo axial stretching resulting in the formation of pairs of counter rotating vortex pairs. Both schemes captured these developments and showed that the characteristic time for growth of three dimensional secondary instabilities is longer than that of the Kelvin-Helmholtz instability.

8.4 Recommendations for Future Work

In summary, the vortex method developed in this work has shown promising prospects for its application in the fields of vortex dynamics. The potential for a hybrid Eulerian-Lagrangian method to perform high-accuracy computations is quite positive, as CFD has been constantly burdened by the computation of non-linear convection in Eulerian methods. Therefore, the author strongly believes that contributing to the progress of VIC method is a meaningful research effort. In this regard it is recommended that the following aspects of the VIC method be further investigated:

1. In order to produce significant calculations of problems of physical, aeronautical or industrial relevance for VIC to become accepted by the mainstream CFD community, it is necessary to introduce the capability of computing three dimensional bounded flows. The standard way to introduce solid boundaries in vortex method is the use of boundary element at the surface, i.e. panel method, in conjunction with a model for vorticity generation. The use of flat panels to approximate a complex geometry may introduce some error since the boundary conditions are only satisfied at the control points of the panels. An alternative formulation of the boundary geometry that takes into consideration the boundary surface contour could be imagined.
2. Another avenue for future research which appears very promising is the development of an adaptive remeshing scheme, that is, providing the spatial adaptation in a scheme that is local, applied only where needed, and based on some error estimates or measurements (values of derivative is a possible measure for the Lagrangian distortion). This is probably a challenging project. It would,

however, offer great potential in some applications with varying degrees of dynamics in different regions of the domain.

3. It is also worthwhile to explore the feasibility of implementing the derivative limiters used to control instability of Eulerian techniques. The suggestion is to use limiters in the calculation of stretching and diffusion terms when the Lagrangian distortion of particles starts deteriorating the solution accuracy.

References

1. Anderson, C. R. and Greengrad, C. (1985) “On Vortex Methods” J. Numer. Anal., **v. 22**, pp. 413-440.

2. Aref, H and Siggia, E. D. (1980) “ Vortex Dynamics of Two-Dimensional Turbulent Shear Layer”. J. Fluid Mech., **v. 100**, pp. 705-737.

3. Aris, R. (1989) ” Vectors, Tensors and Basic Equations of Fluid Mechanics”, Dover Publications, New York.

4. Ashurst, W. T. and Meiburg, E. (1988) “Three-Dimensional Shear Layers Via Vortex Dynamics”, J. Fluid Mech., **v. 189, pp**. 87-116.

5. Barba, L. A., Leonard, A. and Allen, C. B (2005) ”Advances in Viscous Vortex Methods - Meshless Spatial Adaption Based on Radial Basis Function Interpolation” Int. J. Num. Meth. Fluids, **v. 47** , pp 387 – 421

6. Batchelor, G. K. (1979) “An Introduction to Fluid Dynamics” Cambridge University Press.

7. Beale, J. T. and Majda, A. (1982) “Vortex methods I: Convergence in three dimensions.”, Math. Comp., **v. 39**, pp1-27.

8. Beale, J. T. (1986) “A Convergent 3-D Vortex Method with Grid-Free Stretching”, Math. Comp., **v.** 46, pp 401-424.

9. Beale, T. J. and Majda, A. (1982) “Vortex Methods II: High Order Accuracy in 2 and 3 Dimensions”, Math. Comput., **v. 32**, pp 29-52.

10. Bell, J. H. and Mehta, R. D. (1990) “Development of Two-Stream Mixing Layer from Tripped and Untripped Boundary Layers”, AIAA J., **v. 28,** pp 2034-2042.

11. Bernal, L. P. and Roshko, A. (1986) “Streamwise Vortex Structure in Plane Mixing Layers”, J. Fluid Mech., **v. 170,** pp 499-525.

12. Bernard, P. S. and Wallace J. M. (2002) “Turbulent Flow Analysis, Measurements and Prediction”, John Wiley & Sons, Inc.

13. Bradshaw, P. (1966) “The Effect of Initial Conditions on the Development of Free Shear Layer”, J. Fluid Mech., **v. 26**, pp 225-236.

14. Brecht, S. H. and Ferrante, J. R. (1990) “Vortex-in-Cell Calculations in Three Dimensions”. Comp. Phys. Comm., **v. 58**, pp. 25-54.

15. Champagne, F. H., Pao, Y. H. and Wygnanski, I. J. (1976) "On the Two-Dimensional Mixing Region.", J. Fluid Mech. **v.74**, pp 209-250.

16. Chang, C. C. and Chern, R. L. (1991) "A Numerical Study of Flow around an Impulsively Started Circular Cylinder". J. Fluid Mech., **v. 233**, pp. 243-263.

17. Chatelain, P., Curioni, A., Bergdorf, M, Rossinelli, D. Andreoni, W. and Koumoutsakos, P. (2008) "Billion vortex particle direct numerical simulations of aircraft wakes" Comput. Methods Appl. Mech. Engrg., **v. 197,** pp1296–1304.

18. Chen, H. and Marshall J. S. (1999) " A Lagrangian Vorticity Method for Two-Phase Particulate Flows with Two-Way Phase Coupling" J Comp. Phys., **v. 148**, pp 169-198.

19. Chorin, A. J. (1973) "Numerical Study of Slightly Viscous Flow", J. Fluid. Mech., **v. 57**, pp 785-796.

20. Chorin, A. J. (1982) "The Evolution of a Turbulent vortex", Commun. Math. Phys. **v. 35**, pp. 517-535.

21. Chorin, A. J. (1996) "Vortex Methods", In Computational Fluid Dynamics, Lesieur, M., Comte, P. and Zinn-Justin J. Elsevier Science.

22. Christiansen, J. P. (1973) "Numerical Solution of Hydrodynamics by the Method of Point Vortices", J. Comput. Phys., **v. 13**, pp 363-379.

23. Cottet G. H., Koumoutsakos, P. D. (2000) "Vortex methods: theory and practice." Cambridge university press, Cambridge.

24. Cottet, G. H. and Poncet, P. (2003) "Advances in Direct Numerical Simulations of 3D Wall-Bounded Flows by Vortex-in-Cell Methods", J. Comp. Phys., **v**. **193**, pp136–158.

25. Cottet, G. H., Goodman, J. and Hou, T. Y. (1991) "Convergence of the grid-free point vortex method for the three-dimensional Euler equations." SIAM J. Num. Anal., **v. 28**, pp291-307.

26. Cottet, G., Michaux, B., Ossia, S. and VandeLinden, G., (2002) "A Comparison of Spectral and Vortex Methods in Three-Dimensional Incompressible Flows", J. Comp. Phys. **v. 175**, pp 702-712.

27. Couet, B., Buneman, O. and Leonard, A. (1981) "Simulation of Three-Dimensional Incompressible Flows with Vortex-in-Cell method". J. Comp. Phys., **v. 39**, pp. 305-328.

28. Degond, P. and Mas-Gallic, S. (1989) "The Weighted Particle Method for the Convection-Diffusion Equations. Part 1. The Case of an Isotropic Viscosity" Math. Comp., **v. 53**, pp 485-507.

29. Degond, P. and Mas-Gallic, S. (1989) "The Weighted Particle Method for the Convection-Diffusion Equations. Part 2. The Anisotropic Case" Math. Comp., **v.** 53, pp 509-525.

30. Drazin, P. G. (2002) "Introduction to Hydrodynamic Stability", Cambridge University Press.

31. Dziomba, B. and Fiedler, H.E. (1985)"Effect of Initial Conditions on Two-Dimensional Free Shear Layer", J. Fluid Mech., **v. 152**, pp 419-442.

32. Fishelov, D. (1990) "A New Vortex Scheme for Viscous Flow", J. Comp. Phys., **v. 86**, pp 211-224.

33. Fishelov, D. (1994) "Simulation of three-dimensional turbulent flow in non-cartesian geometry." J. Comp. Phys., **v. 115**, pp 249-266.

34. G. Winckelmans, Vortex methods, in: E. Stein, R. De Borst, T.J. Hughes (Eds.), Encyclopedia of Computational Mechanics, vol. 3, John Wiley and Sons, 2004.

35. Gharakhani, A. and Ghoniem, A. F. (1997) "Three-Dimensional Vortex Simulation of Time Dependent Incompressible Internal Viscous Flows", J. Comp. Phys.**, v. 134**, pp 75-95.

36. Giovannini, A. and Gagnon, Y. (2006)" Validation of a Three-Dimensional Vortex Particle Method for Fluid Flows" AMRX Applied Mathematics Research eXpress Volume 2006, Article ID 17027, 1–31.

37. Grant, J. R. and Marshall J. S. (2005) "Diffusion Velocity for a Three-Dimensional Vorticity Field". Theor. Cmput. Fluid Dyn. **v.19**, pp 377-390.

38. Green, S. I. (1995) "Fluid Vortices" Kluwer Academic Press

39. Greengrad, C. (1985) "The Core Spreading Method Approximates the Wrong Equation", J Comp. Phys., **v. 61**, pp 345-348.

40. Greengrad, C. and Rokhlin, V. (1987) "A Fast Algorithm for Particle Simulation". J Comp. Phys., **v.** 73, pp 325-348.

41. Hald, O. (1987) "Convergence of vortex methods for Euler's equations." SIAM J. Num. Anal., **v.24**, pp 538-582.

42. Ho, C. and Heurre, P. (1984) "Perturbed Free Shear Layers", Ann. Rev. Fluid Mech., **v. 16**, pp 365-424.

43. Hockney, R. W. and Eastwood, J. W. (1981) “Computer Simulation Using Particles”, McGraw-Hill, New york.

44. Inoue, O., Leonard A., (1987), “ Vortex simulation of forced/unforced mixing layers”, AIAA. J., **v. 26,** pp**.** 1417-1418.

45. Inoue, O. (1989), “Vortex Simulation of Spatially Growing Three-Dimensional Mixing Layers” AIAA Journal, **v. 27**, , pp.1517-1539.

46. Kempka S. N. and Strickland, J. H. (1993) “A Method to Simulate Viscous Diffusion of Vorticity by Convective Transport of Vorticesat a Non-Solenoidal velocity” Sandia Laboratory Report SAND93-1763.

47. Knio, O. M.and Ghoniem, A. F. (1992) “ The Three- Dimensional Structure of Periodic Vorticity Layers Under Non-Symmetric Conditions”, J. Fluid. Mech., **v. 243,** pp 353.

48. Knio, O. M. and Ghoniem, A. F.(1989) ”Three dimensional Vortex Simulation of Entrainment Augmentation Due to Streamwise structures ” AIAA-89-0574, 27th Aerospace Sciences Meeting.

49. Knio, O. M. and Ghoniem, A. F. (1990) ”Vortex Simulation of Three Dimensional Reacting Shear Layers” AIAA-90-0150, 28th Aerospace Sciences Meeting.

50. Kundu, P.K. and Cohen, I. M. (2002) “Fluid Mechanics”, Second Edition, Academic Press.

51. Lakkis, I. and Ghoniem, A. F. (2003) “Axisymmetric Vortex Method for Low-Mach Number Diffusion-Controlled Combustion”, J. Comp. Phys., **v. 184**, pp 435-475.

52. Lasheras, J. C. and Choi, H. (1988) “Three Dimensional Instability of a Plane Free Shear Layer: an Experimental Study of the Formation and Evolution of Streamwise Vortices”, J. Fluid Mech., **v**. **189**, pp 53-86.

53. Lasheras, J.C., Cho, J.S. and Maxworthy, T. (1986) “On the Origin and Evolution of Streamwise Vortical Structures in a Plane, Free Shear Layer”. J. Fluid Mech**. v. 172**, pp 231–258.

54. Leonard, A., (1980) “Vortex Methods for Flow Simulation”, J. comp. phys., **v. 37,** pp. 289-335**.**

55. Leonard, A., (1985) “Computing Three-Dimensional Incompressible Flows with Vortex Elements”. Ann. Rev. Fluid Mech., **v. 17**, 523-559.

56. Lesieur, M. (1997) “Turbulence in fluids” Third Edition, Kluwer Academic Publisher.

57. Lin, S.J. and Corcos, G.M. (1984) "The Mixing Layer: Deterministic Models of a Turbulent Flow. Part 3, The Effect of Plain Strain on the Dynamics of Streamwise Vortices." J. Fluid Mech. **v. 141**, pp 139–178.

58. Liu, H. C. and Doorly, D. J. (2000) "Vortex Particle-in-Cell Method for Three-Dimensional Viscous Unbounded Flow Computations", Int. J. Numer. Meth. Fluids.

59. Lui, C. H. (2001) "A Three-Dimensional Vortex Particle- in-Cell Method in The vicinity of a Wall", Int. J. Numer. Meth. Fluids., **v. 37**, pp. 501-523.

60. Lui, C. H. (2002) "Vortex Simulation of Unsteady Shear Flow Induced by a Vortex Ring", Computers and fluids, **v. 31**, pp. 183-207.

61. Marshall, J. S. (2001) "Inviscid Incompressible Flow" John Wiley & Sons, Inc.

62. Marshall, J. S. and Grant, J. R. (1995) "A Lagrangian Collocation Method for Vorticity Transport in Viscous Fluid Flows". Proceedings of the Forum on Vortex Methods for Engineering Applications. Sandia National Labs. Albuquerque, NM.

63. Marshall, J. S. and Grant, J. R. (1997) "A Lagrangian Vorticity Collocation Method for Viscous, Axisymmetric Flows with and without Swirl", J Comp. Phys., **v. 138**, pp 302-330.

64. Marshall, J. S., Grant, J. R. , Gossler, A. A. and Huyer, S. A. (2000), "Vorticity Transport on a Lagrangian Tetrahedral Mesh", J Comp. Phys., **v. 161**, pp 85-113.

65. Mathieu, J. and Scott, J. (2000) "An Introduction to Turbulent Flow", Cambridge University Press.

66. Mehta, R. D. (1991) "Effects of Velocity Ratio on Plane Mixing Layer Development: Influence of the Splitter Plate Wake." Exp. Fluids, **v. 10**, pp 194-204.

67. Micheal, J., Graham, R. and Arkell, R. H. (2000) "A Hybrid Vortex Method", in Vortex Methods , Editors: Kamemoto, K and Tsutahara, M., Word Scientific, pp. 16-25.

68. Milane, R. E. (2004) "Large eddy simulation (2D) using diffusion–velocity method and vortex-in-cell", Int. J. Numer. Meth. Fluids, **v. 44**, pp 837–860

69. Milane, R. E. and Abdolhoseini, R. (2004) "Development of Three_Dimensional Vortex-in-Cell Method for a Spatially Growing Uniformly Sheared Flow " Int. J. Comp. Fluid Dyn., **v. 18.** pp. 47-69.

70. Monaghan, J. J. (1985), "Extrapolating B-Splines for Interpolation", J. Comput. Phys., **v. 60**, pp. 253-262.

71. Ogami, Y. and Akamatsu, T. (1991) "Viscous Flow Simulation Using the Discrete Vortex Model-The Diffusion Velocity Method", Computer and Fluids, **v. 19**, pp 433-441.

72. Ogami, Y. and Ayano, Y. (1995) "Flows around a Circular Cylinder Simulated by The Viscous Vortex Model- The Diffusion Velocity Method" CFD J., **v. 4**, pp 383-399.

73. Oster D. , Wygnanski I. (1982) "The forced mixing layer between parallel streams", J. Fluid Mech., **v. 123**, pp. 91-130.

74. Pierrehumbert, R. T. and Widnall, S. E. (1982) "The Two and Three Dimensional Instabilities of a Spatially Periodic Shear Layer", J. Fluid Mech., **v**. **114**, pp 59-82.

75. Plouhans, P., Winckelmans, G. S., Salmon, J. K., Leonard, A. and Warren, M. S. (2002) "Vortex Methods for Direct Numerical Simulation of Three-Dimensional Bluff Body Flows: Application to Sphere at Re=300, 500 and 1000", J. Comp. Phys. **v. 78**, pp 427-463

76. Ploumhans, P. and Winckelmans, G. S. (2000) "Vortex methods for high-resolution simulations of viscous flow past bluff bodies of general geometry." J. Comp. Phys., **v. 165**, pp354-406.

77. Pope, S. B.,(2000) "Turbulent Flows", Cambridge University Press.

78. Puckett, E. G., (1993) "vortex methods: An Introduction and Survey of Selected Research Topics". In Incompressible Fluid Dynamics: Trends and Advances, Gunzburger, M.D., Nicolaides, R.A. (eds). Cambridge University Press , pp 335-408.

79. Rivoalen, E., Huberson, S. and Hauville, F. (1997) "Simulation Numérique des Equation de Navier-Stokes 3D par une Méthode Particulaire " C. R. Acad. Sci. Paris, t. 324, série 2, pp 543-549.

80. Rivoalen, E. and Huberson, S. (1999) "Numerical Simulation of Axisymmetric Viscous Flows by Means of a Particle Method", J. Comp. Phys., **v. 152**, pp 1-31.

81. Rogers, M. M., Moser, R. D (1994) "Direct Simulation of Self-Similar Turbulent Mixing Layer", Phys. Fluids, **v. 6**, pp 903-923

82. Rogers, M. M., Moser, R. D. and Buell, J. C. (1990). "A Direct Comparison of Spatially and Temporally Evolving Mixing Layers," Bull. Am. Phys. Soc., **v. 35**, pp 2294-2309.

83. Rosenhead, L. (1932) "The Point Vortex Approximation of a Vortex Sheet" Proc. R. Soc. London, Ser. A, **v. 134**, pp170-181.

84. Rossi, L. F. (1996) "Resurrecting core spreading vortex methods: A new scheme that is both deterministic and convergent" SIAM J. Sci. Comput., **v.**17, pp 370-397.

85. Sadek, N. and Milane, R.E. (2007) "Viscous Vortex Particle Simulation of Three Dimensional Mixing Layer", 15th Annual Conference of the CFD Society of Canada, Toronto-Canada

86. Saffman, P. G. (1992) "Vortex Dynamics", Cambridge University Press.

87. Sarpkaya, T., (1994), "Vortex Element Methods for Flow Simulation," In Advances in Applied Mechanics, (Ed. Th. Wu and A Hutchinson), Vol. 31, pp. 113-247, Academic Press, London.

88. Smith, P. A. and Stansby, P. K. (1988) "Impulsively started fow around a circular-cylinder by the vortex method". J. Fluid Mech., **v. 194**, pp 45-77.

89. Smits, A. J. and Dussauge, J. P. (1996) "Turbulent Shear Layers in Supersonic Flows" Woodbury N.Y. American Institute of Physics.

90. Spencer, B. W. and Jones, B. G. (1971) "Statistical Investigation of Pressure and Velocity Fields in the Turbulent Two-Stream Mixing Layer", AIAA paper No. 71-613, AIAA 4th Fluid and Plasma Dynamics Conference, Palo Alto CA, June 21-23, 1971.

91. Strickland, J. H, Kempka, S. Nand W. P. Wolfe (1996) "Viscous diffusion of vorticity using the diffusion velocity concept" ESAIM Proceedings, II International Workshop on Vortex Flows and Related Numerical Methods. Montreal, Canada, **v.1**, pp 135-151.

92. Strickland, J. H., Kempka, S. Nand Wolfe, W. P. (1995) "Viscous diffusion of vorticity in unsteady wall layers using the diffusion velocity concept. In Proceedings of the Forum on Vortex Methods for Engineering Applications." Sandia National Labs., .Albuquerque, NM.

93. Tennekes, H. and Lumley, J. L. (1972) "A First Course in Turbulence" The MIT Press.

94. Van Rees, W. M.; Leonard, A., Pullin, D.I.; Koumoutsakos, P. (2011) "A comparison of vortex and pseudo-spectral methods for the simulation of periodic vortical flows at high Reynolds numbers." J. Comp. Phys., **v. 230**, pp 2794–2805.

95. Verman, B., Geurts, B. and Kuerten, H. (1997) "Large-Eddy Simulation of Turbulent Mixing Layer", J. Fluid Mech., **v. 339**, pp 357-390.

96. Walther J. H. and Koumoutsakos, P. (2001) "Three-Dimensional Vortex Methods for Particle –Laden flows with Two-Way Coupling", J. Comp. Phys., **v. 167**, pp. 39-71.

97. Winant, C. D. and Browand, F. K. (1974) "Vortex Pairing: The Mechanism of Turbulent Mixing Layer Growth at Moderate Reynolds Number." J. Fluid Mech., **v. 63**, pp 237-255.

98. Winckelmans, G. S. and Leonard, A. (1988) "Weak Solution of the Vorticity Equation with Vortex Singularities", Phys. Fluids, **v. 31**, pp. 1838-1839.

99. Winckelmans, G. S. and Leonard, A. (1993) "Contributions to Vortex Particle Methods for the Computation of Three-Dimensional Incompressible Unsteady Flows", J. Comp. Phys., **v. 109**, pp. 247-273.

100. Yanenko, N. N. (1971) "The Method of Fractional Steps", Springer Verlag.

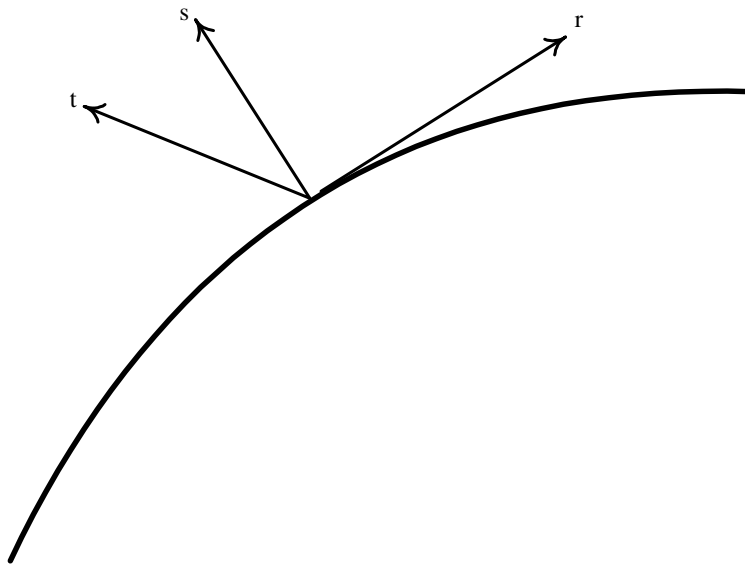

Fig. 2.1. Explanation of vorticity stretching.

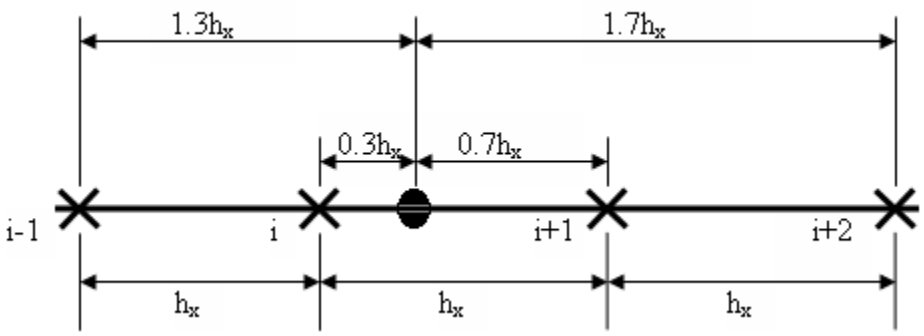

Fig. 3.1 One dimensional Example of M'_4 interpolation scheme.

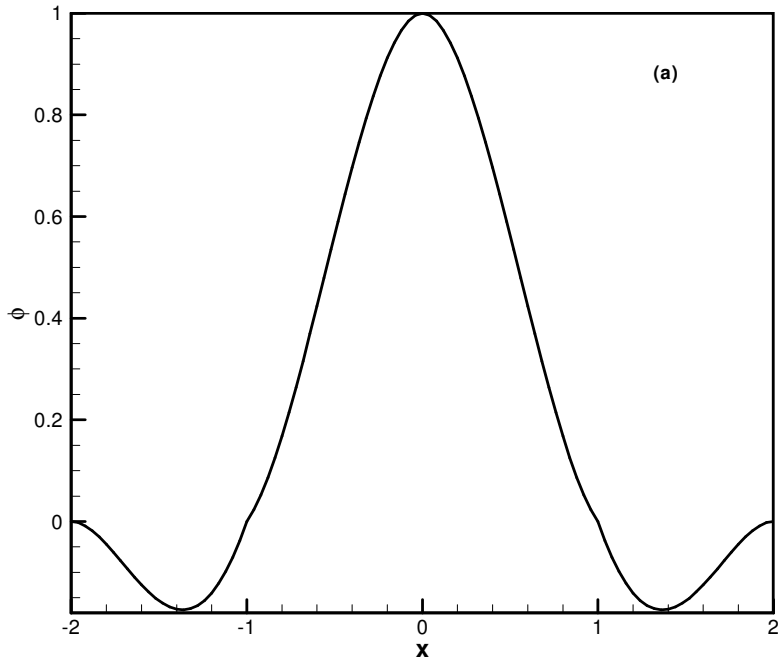

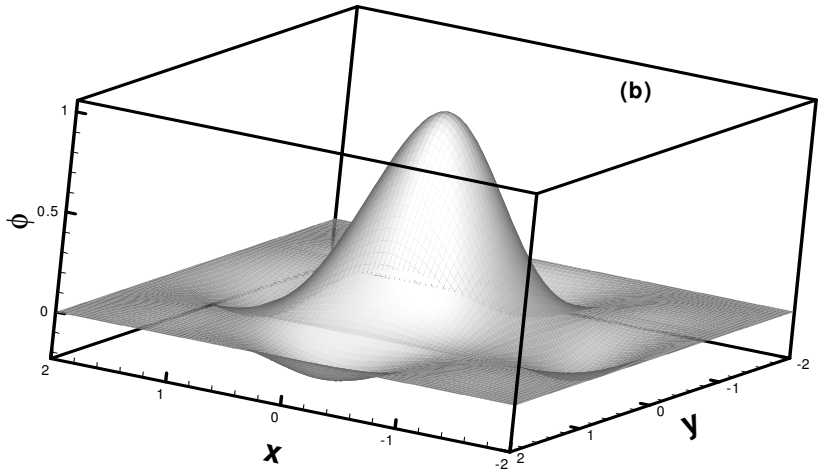

Fig. 3.2.
One dimensional kernel of M'_4 interpolation scheme.
Distribution of M'_4 scheme in two dimensions.
Isosurfaces of three dimensional M'_4 interpolation scheme. Fifty equally spaced levels are used.

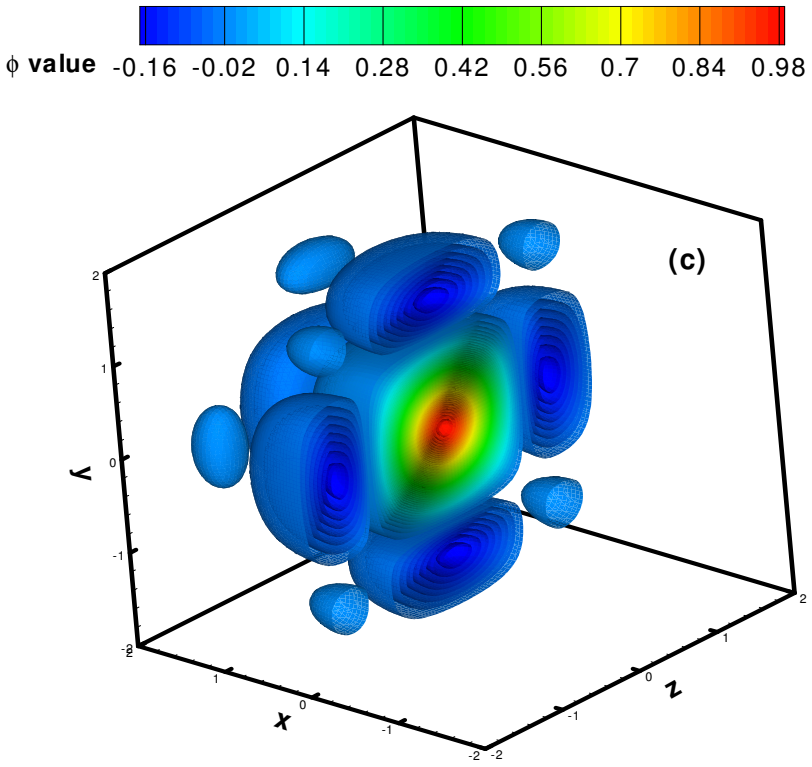

Fig. 3.1. (c) See previous page for caption.

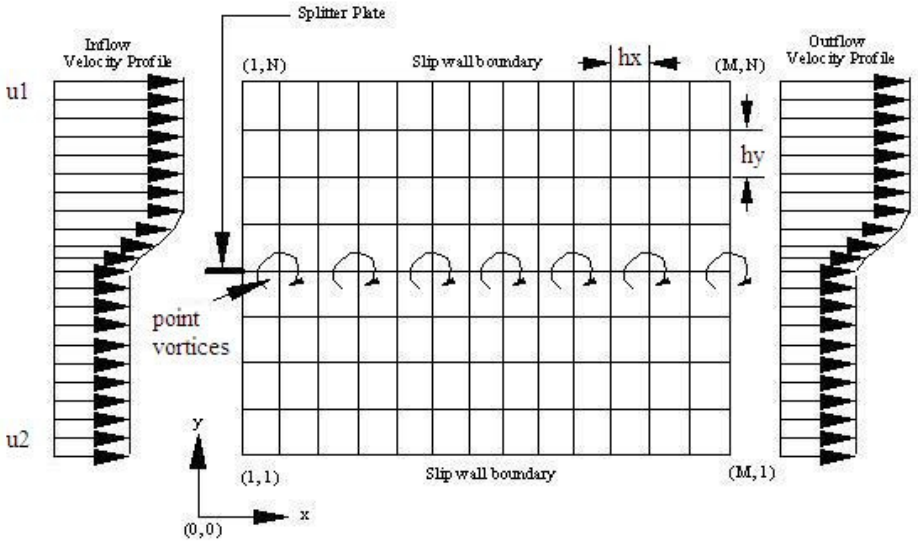

Fig.4.1. Computational domain.

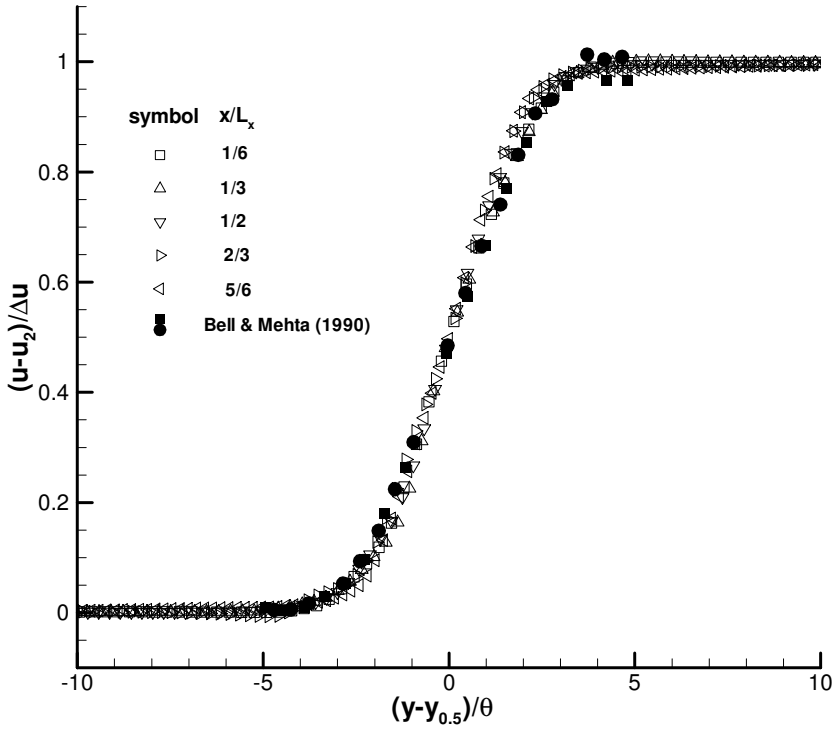

Fig.4.2. Profile of mean streamwise velocity.

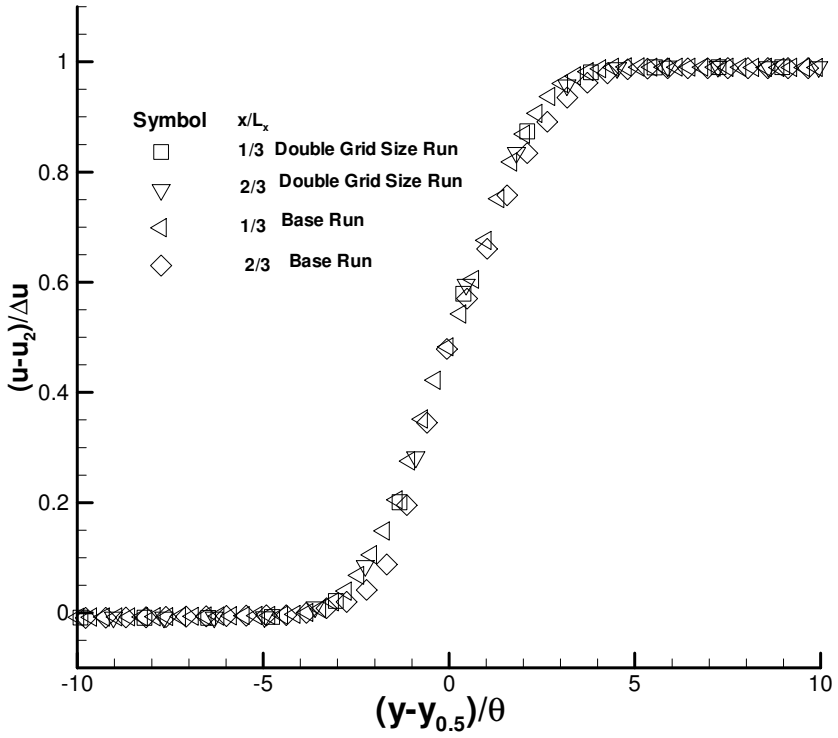

Fig. 4.3. Grid size effect on mean velocity within similarity region.

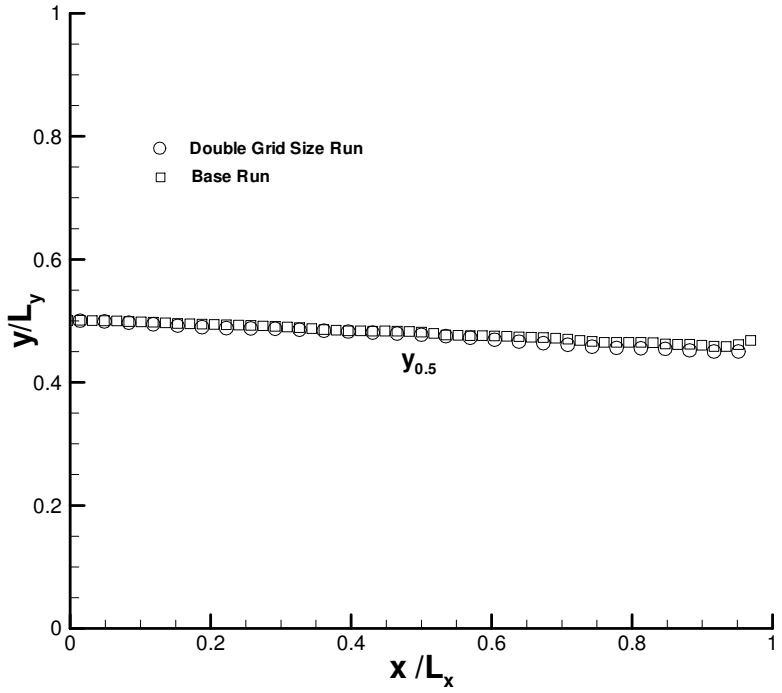

Fig. 4.4. Grid size effect on $y_{0.5}$.

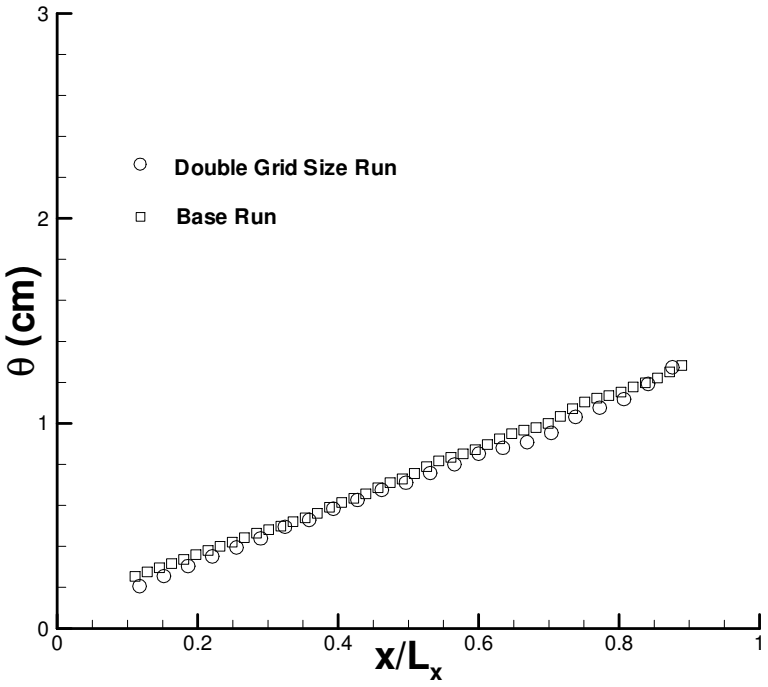

Fig. 4.5. Momentum thickness growth and its grid size sensitivity.

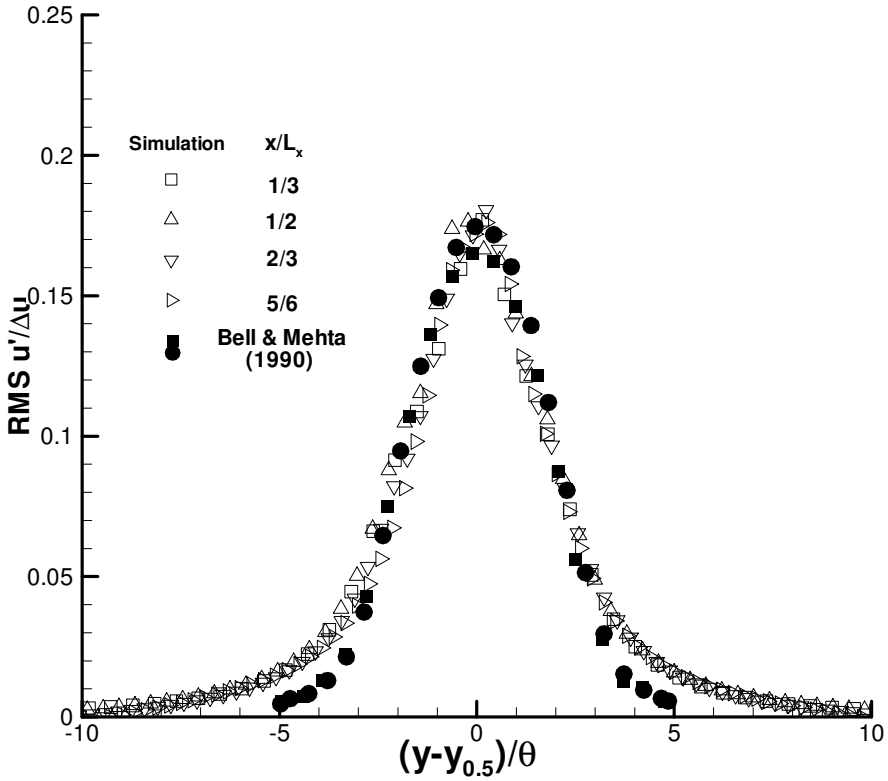

Fig. 4.6. Profiles of root mean square streamwise velocity fluctuations.

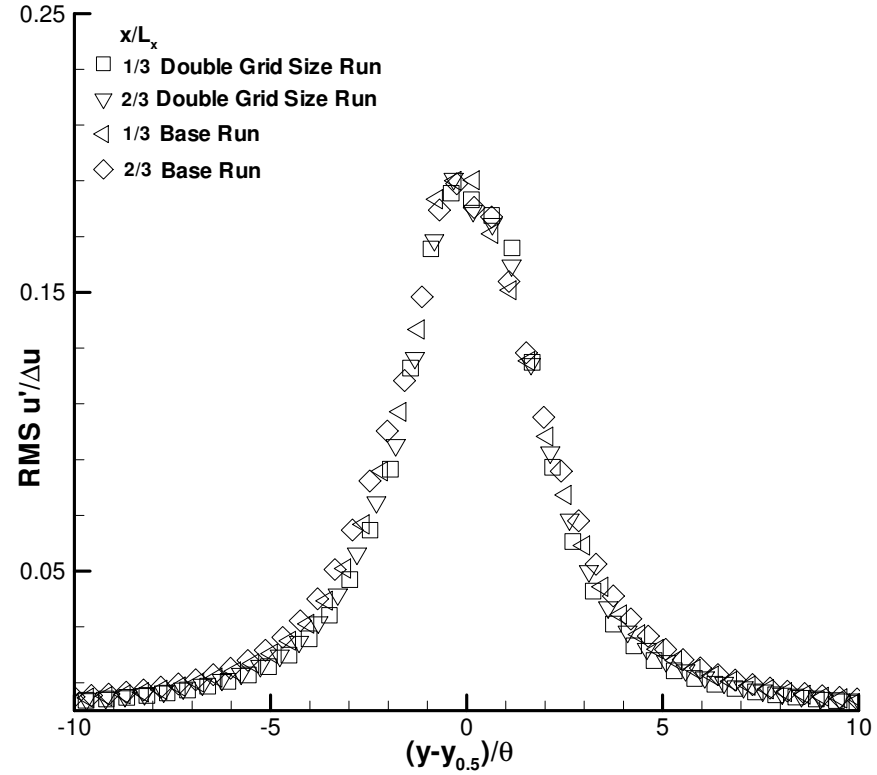

Fig. 4.7. Sensitivity of root mean square streamwise velocity fluctuations to grid size.

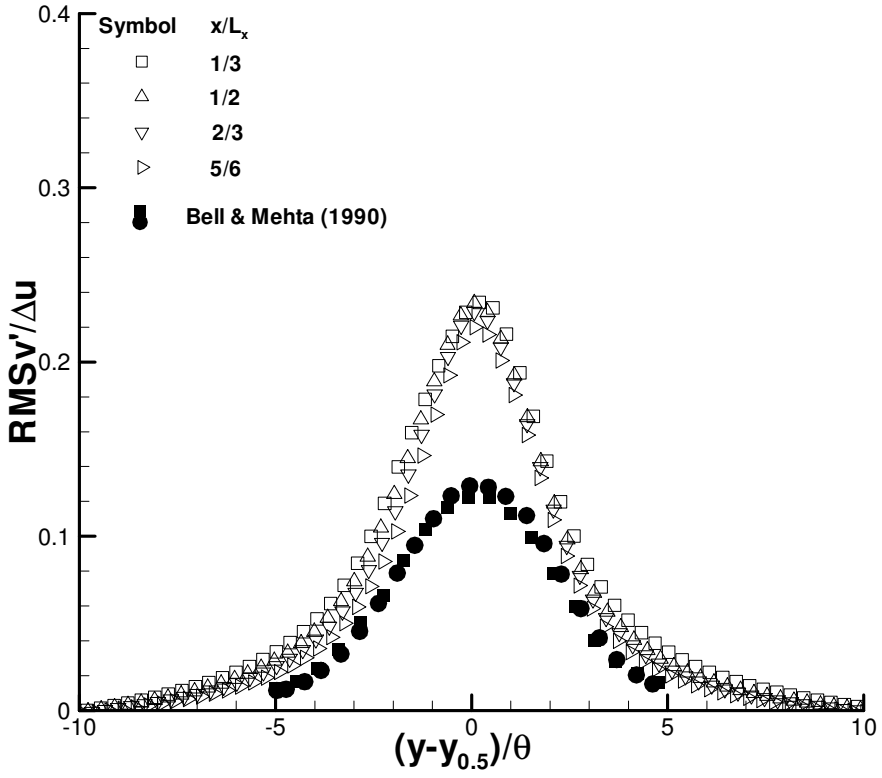

Fig. 4.8. Profiles of root mean square of cross-stream velocity fluctuations.

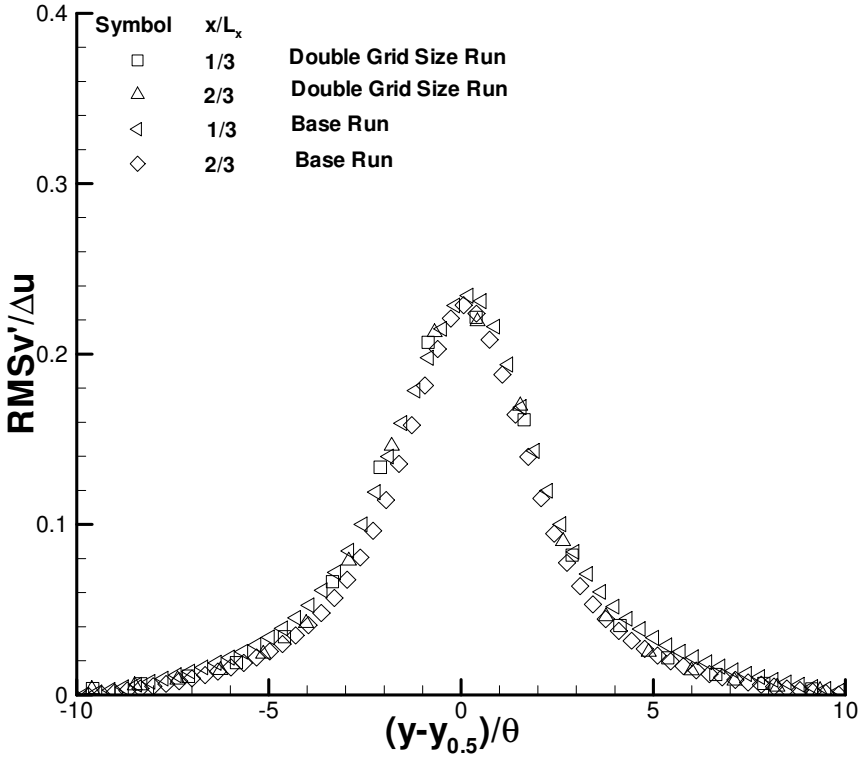

Fig. 4.9. Sensitivity of root mean square of cross stream velocity fluctuations to grid size.

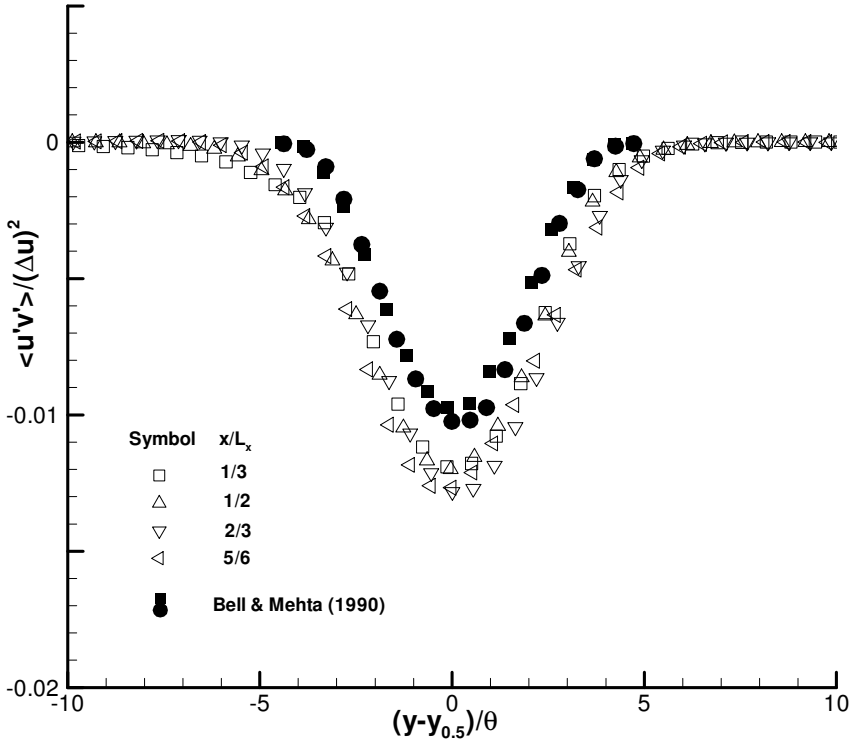

Fig. 4.10. Profiles of *u'v'* cross-correlation.

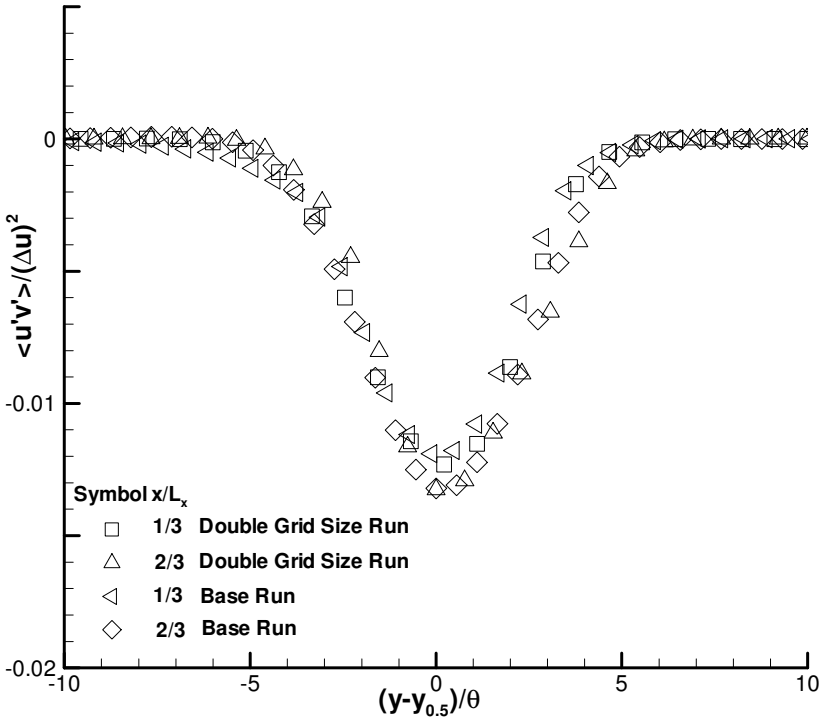

Fig. 4.11. Sensitivity of *u'v'* cross-correlation to grid size.

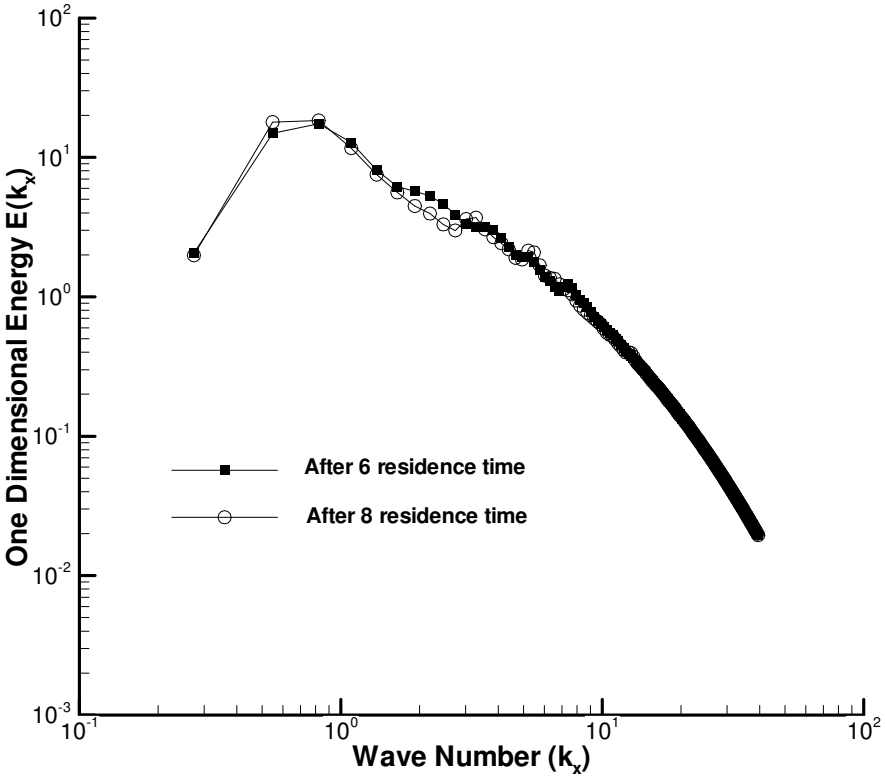

Fig. 4.12. Energy spectrum of fully developed two dimensional mixing layer.

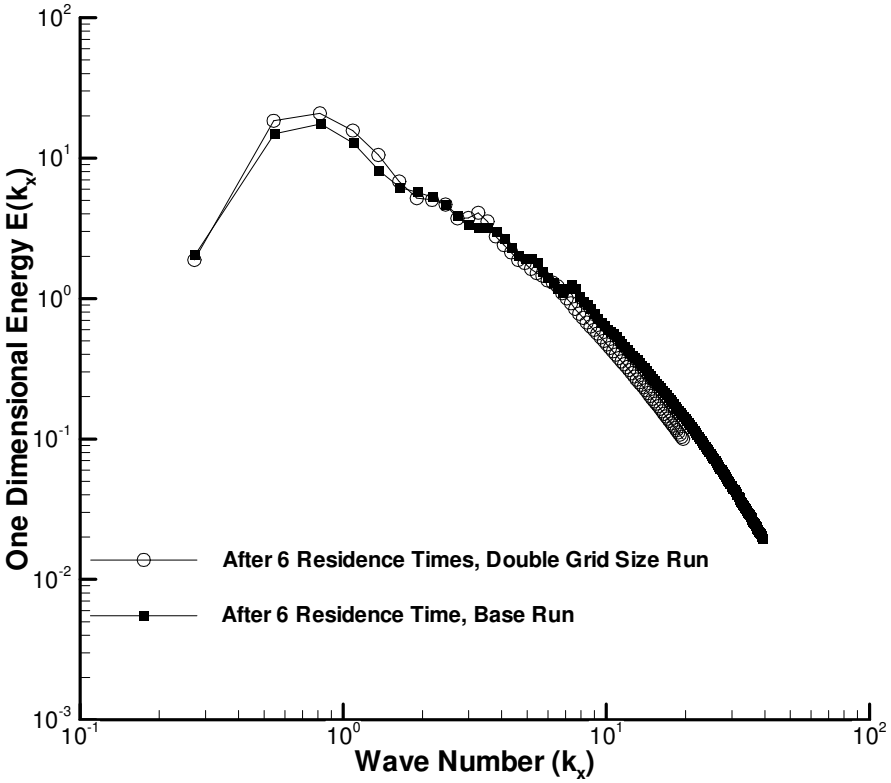

Fig. 4.13. Sensitivity of energy spectrum to grid size.

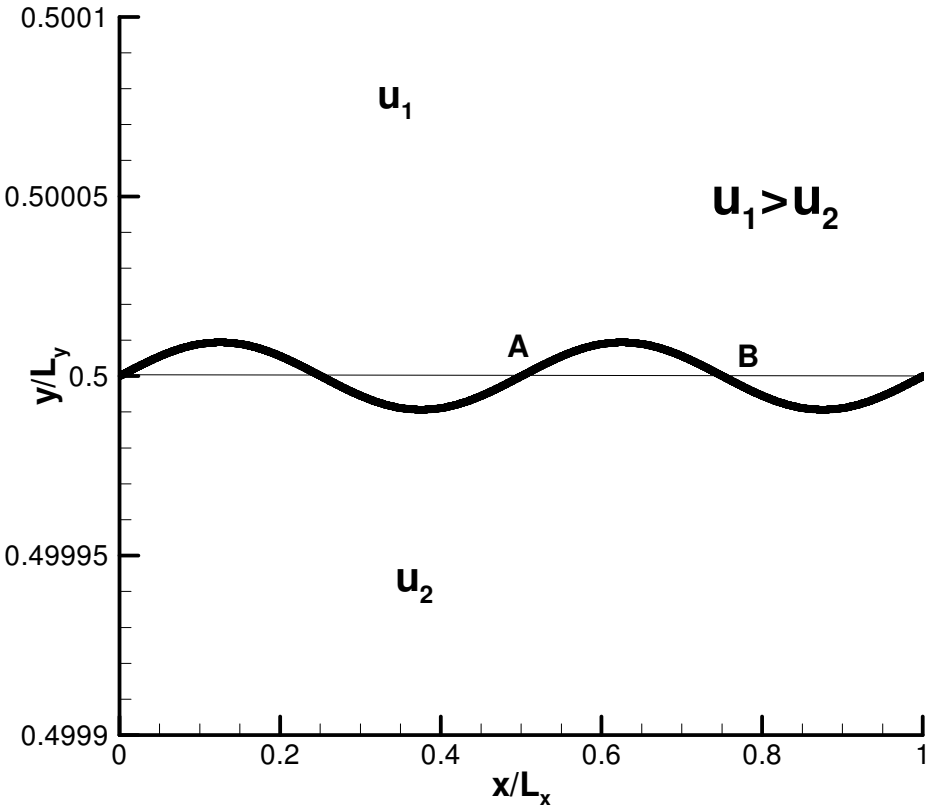

Fig. 4.14. Initial perturbation of the vortex sheet.

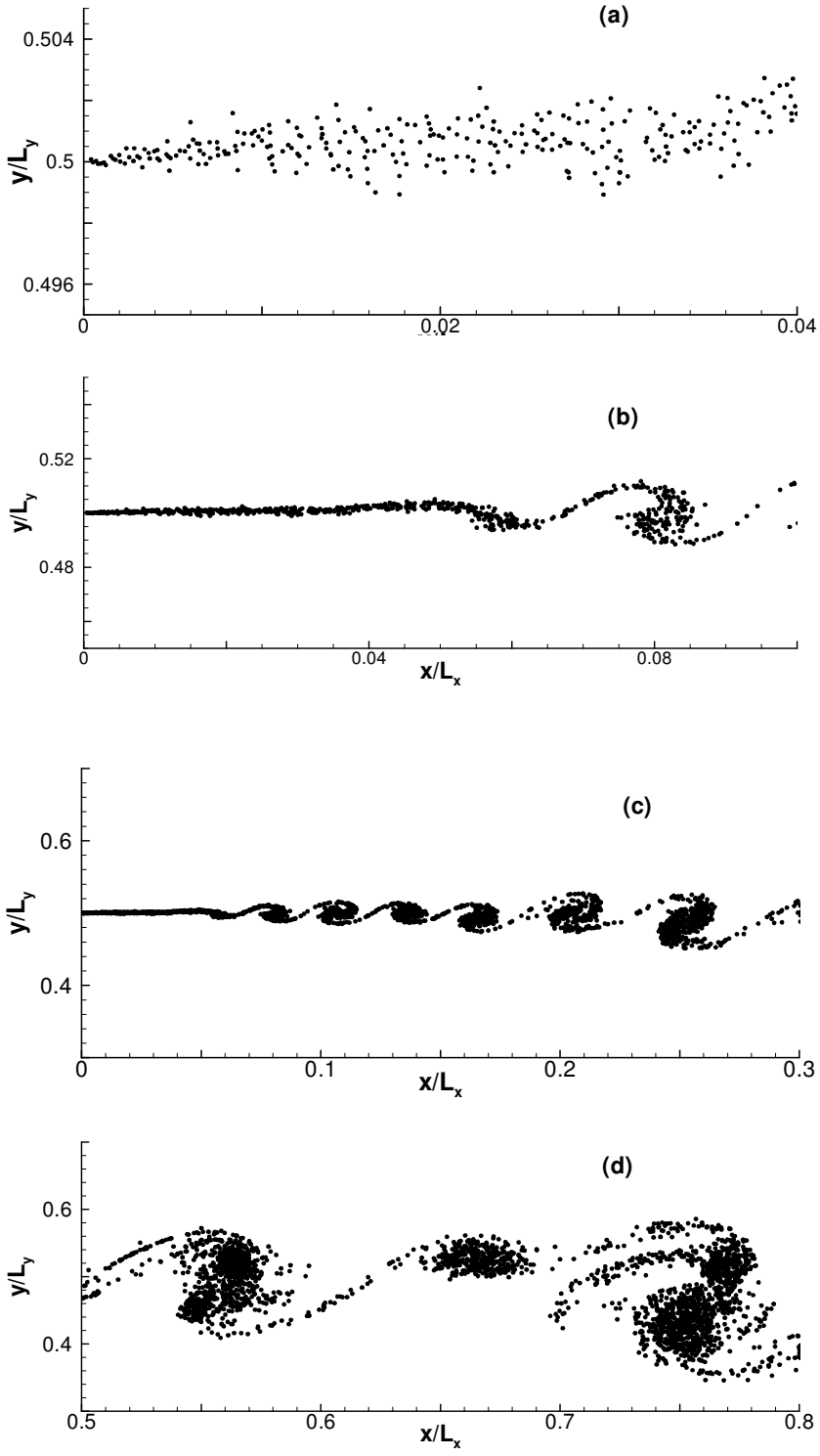

Fig. 4.15. Development of instabilities described by particle location.

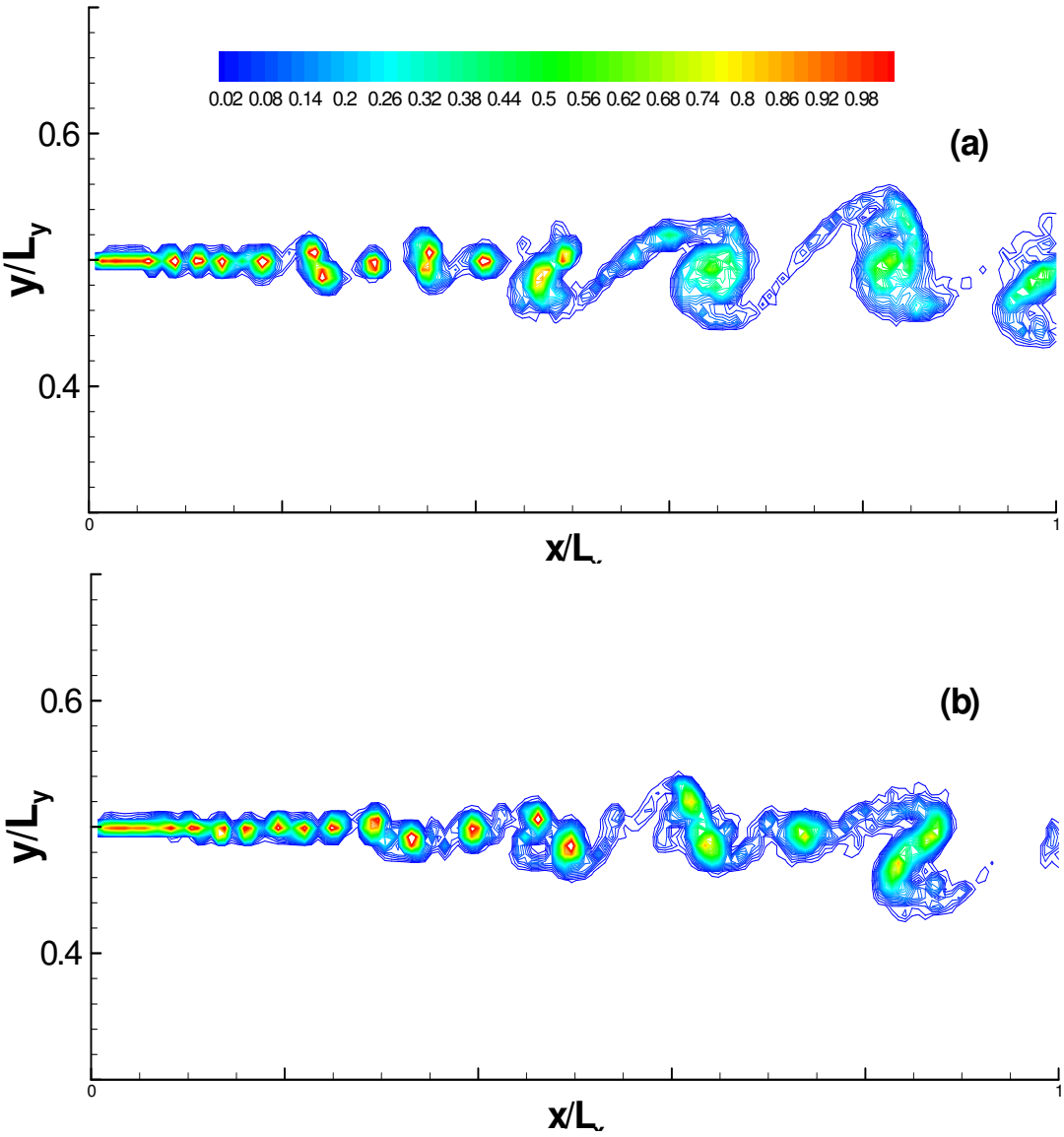

Fig. 4.16. Contour plot of spanwise vorticity, fifty contour levels are used with increment of 0.02, (a) at 14450 time steps, (b) at 15450 time steps.

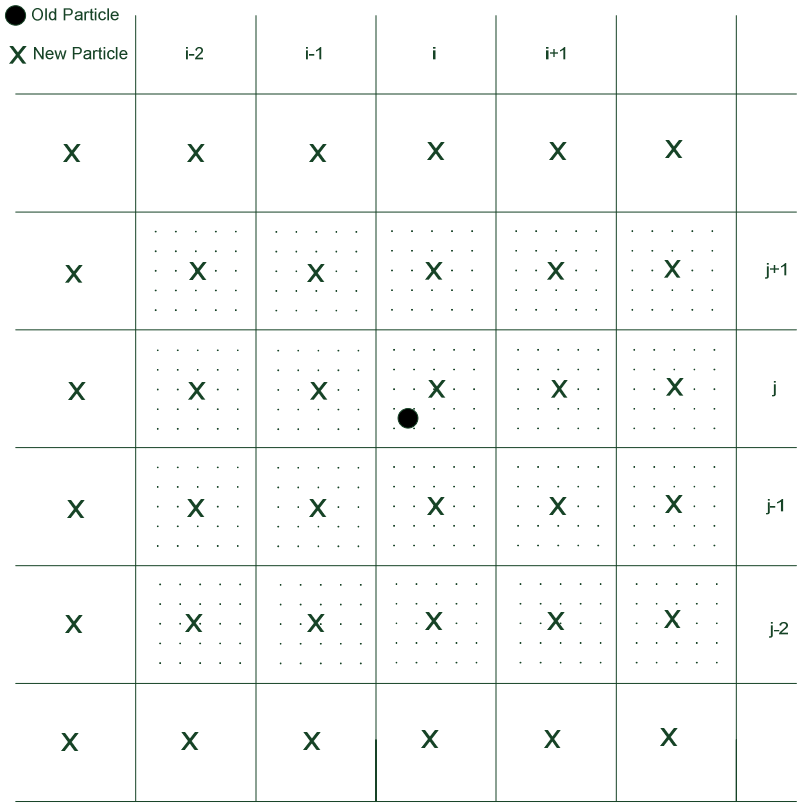

Fig. 5.1. Particles affected by M'$_4$ remeshing scheme.

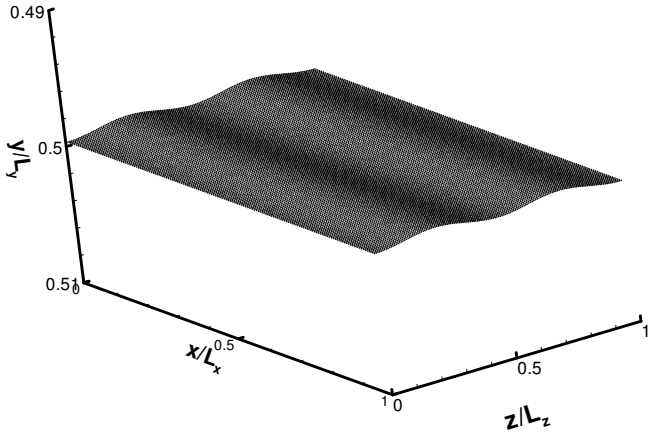

Fig. 5.2. Initial perturbation of particles.

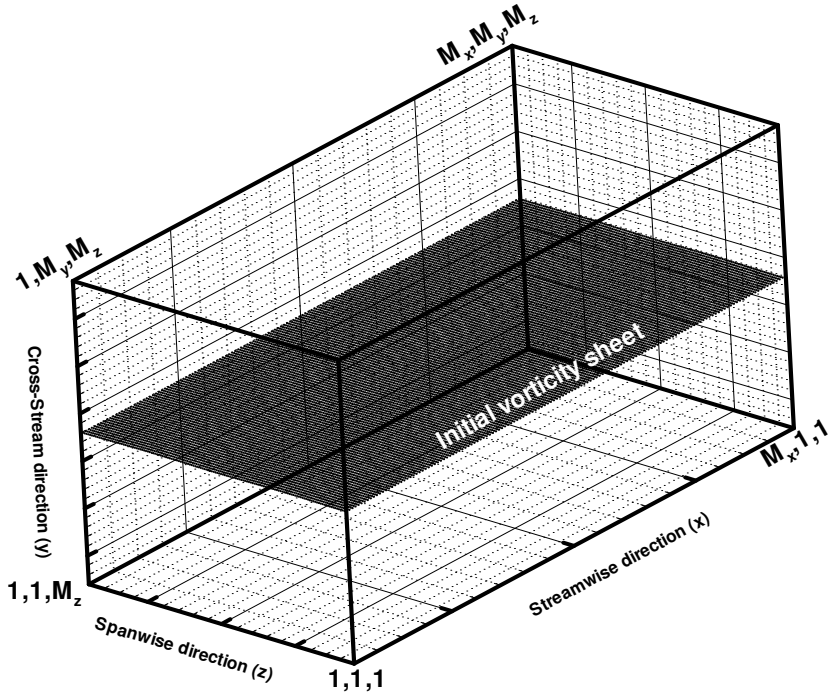

Fig. 5.3. Computational domain of three dimensional temporal mixing layer.

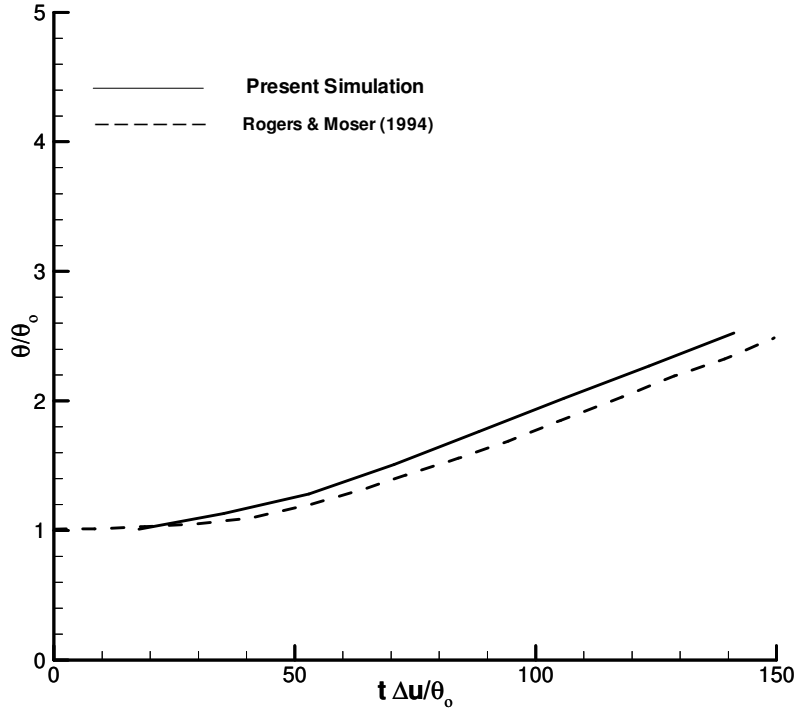

Fig. 5.4. Temporal development of momentum thickness.

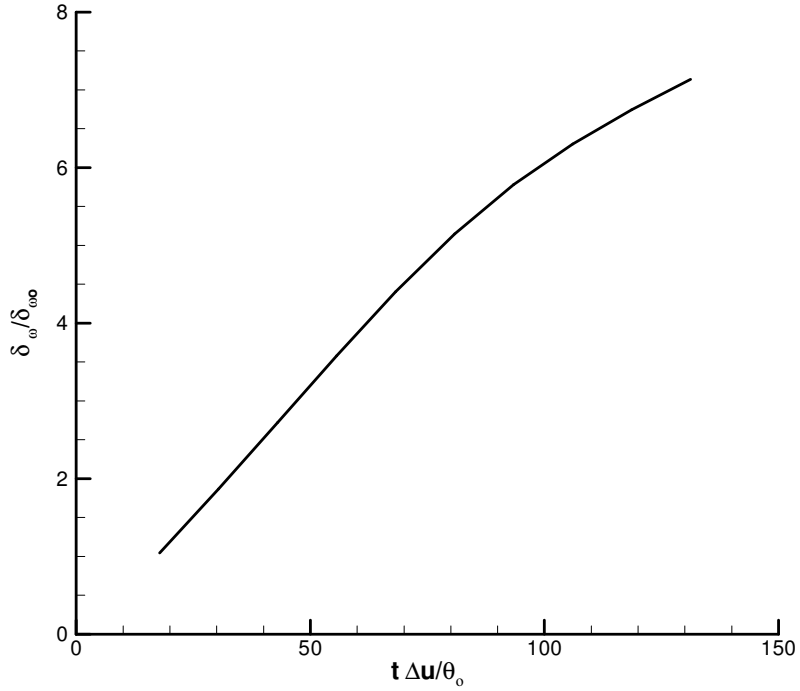

Fig. 5.5. Temporal development of vorticity thickness.

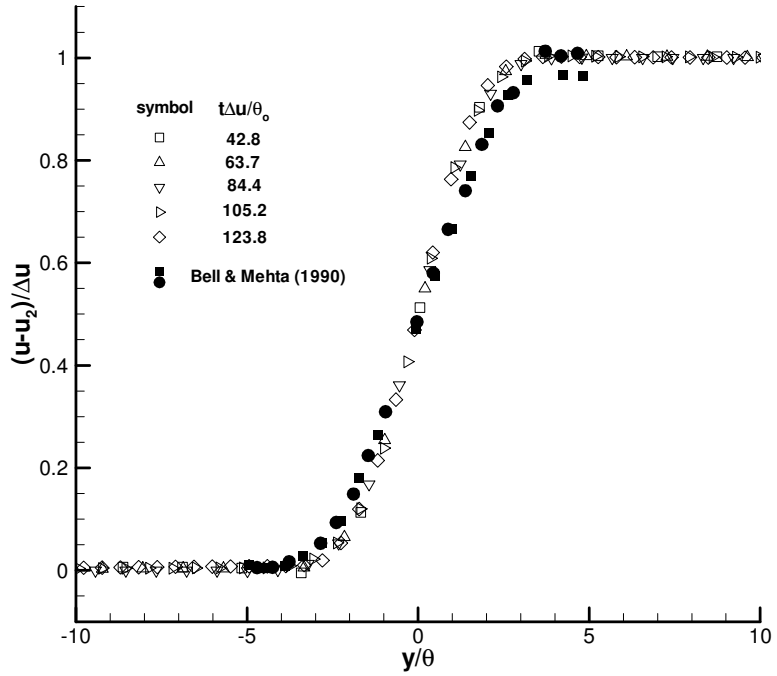

Fig 5.6. Profiles of mean streamwise velocity.

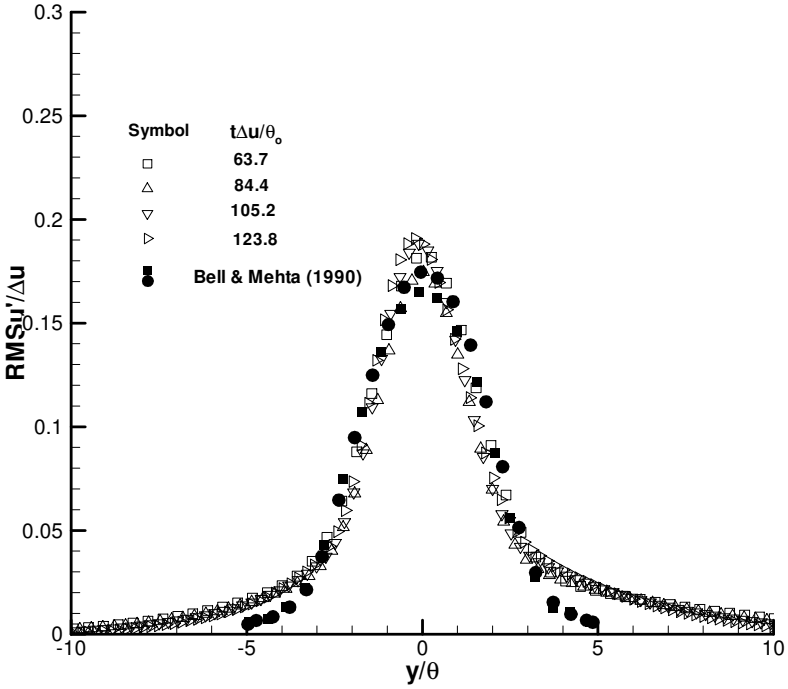

Fig 5.7. Profiles of root mean square streamwise velocity fluctuations.

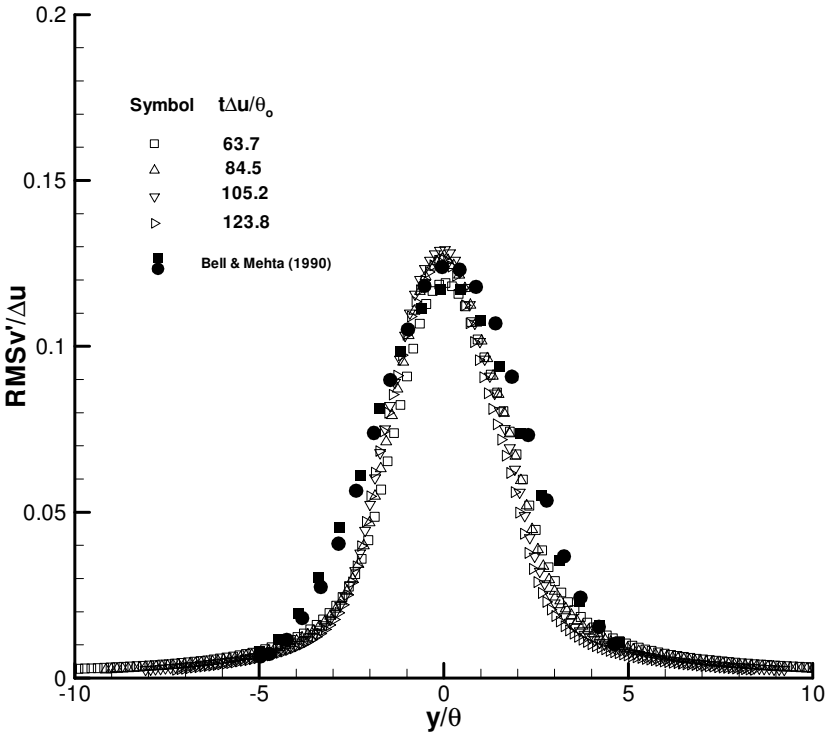

Fig. 5.8. Profiles of root mean square cross stream velocity fluctuations.

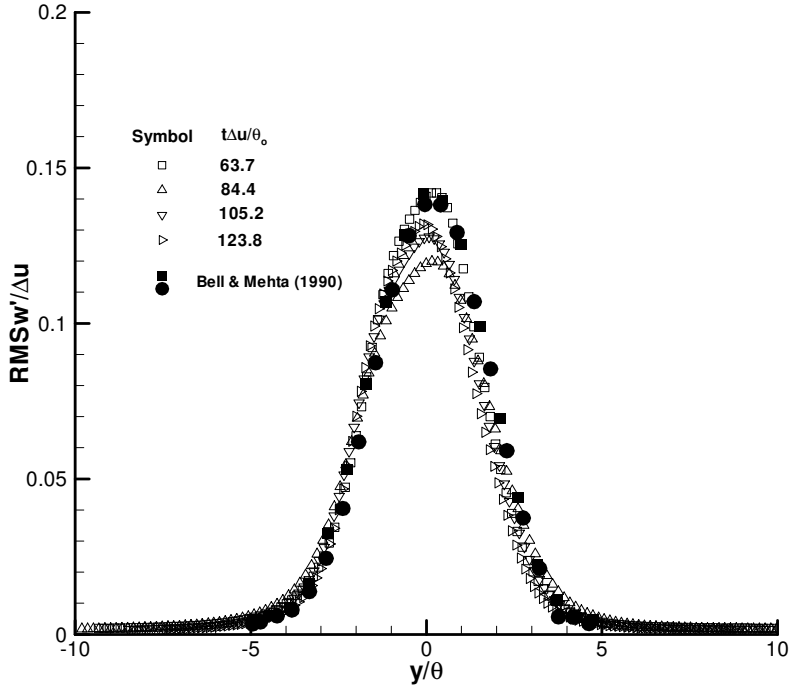

Fig. 5.9. Profiles of root mean square spanwise velocity fluctuations.

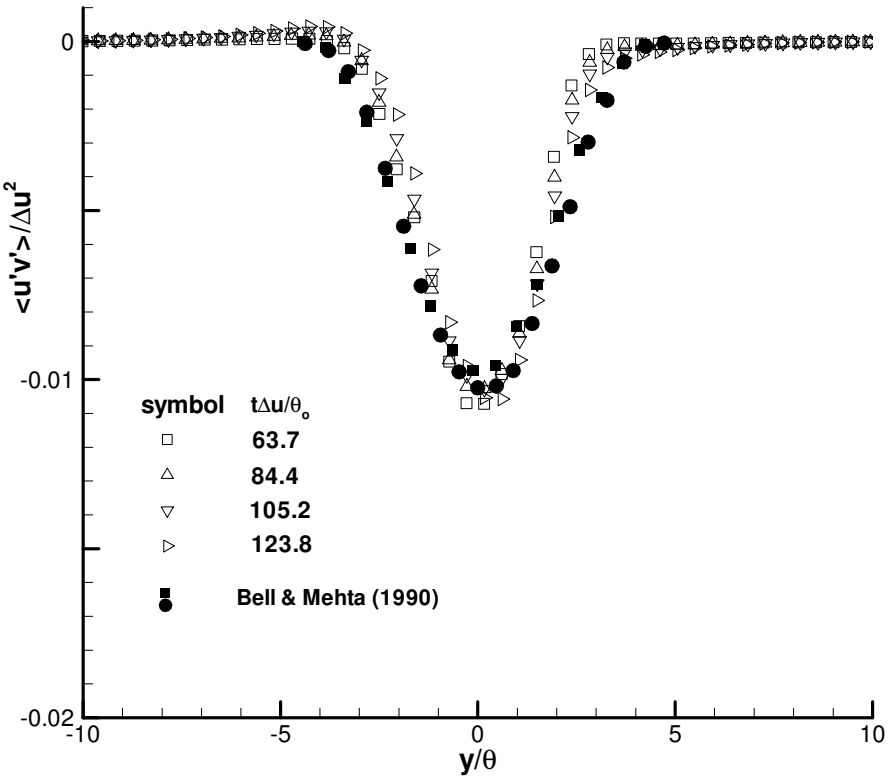

Fig. 5.10. Profiles of cross-correlation *u'v'*.

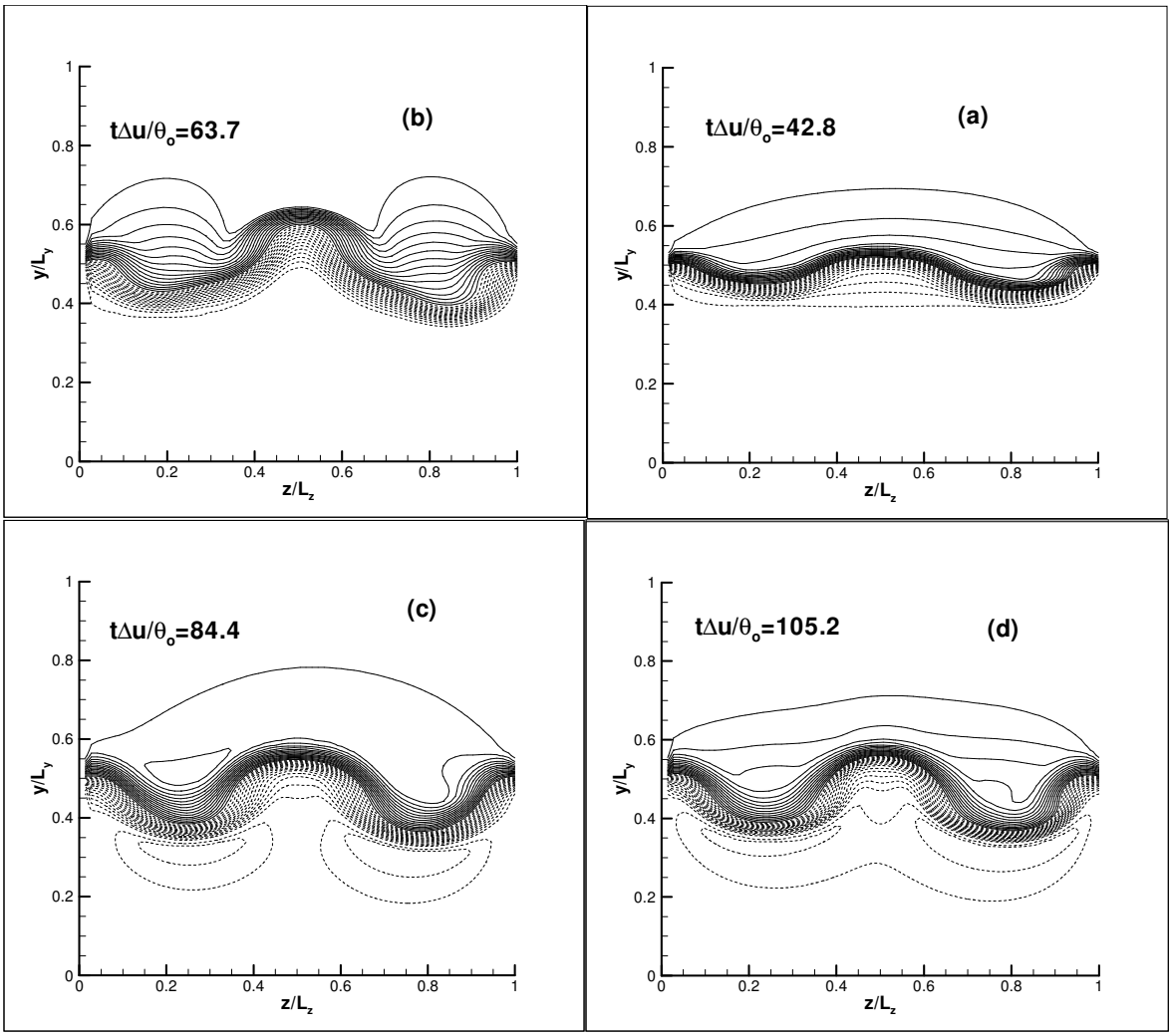

Fig. 5.11. Streamwise velocity contours showing flow three dimensionality at four times (a) $t\Delta u/\theta_o$=42.8, (b) $t\Delta u/\theta_o$=63.7, (c) $t\Delta u/\theta_o$=84.4 *and* (d) $t\Delta u/\theta_o$=105.2. Thirty equally distributed contour levels are used between u_{min} and u_{max}. Dotted lines represent negative velocity and continuous lines represent positive velocity.

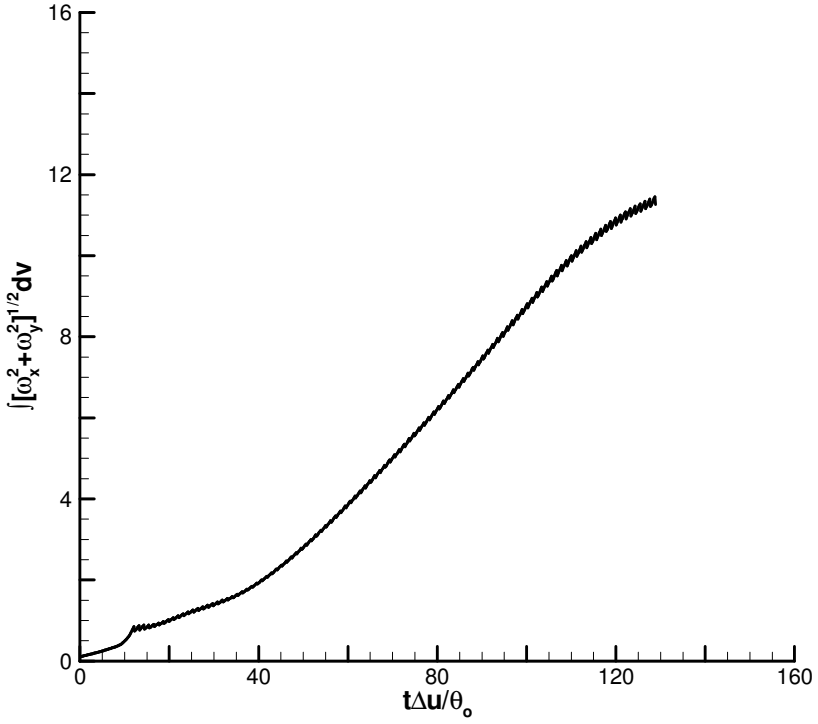

Fig. 5.12. Temporal growth of streamwise and spanwise vorticity.

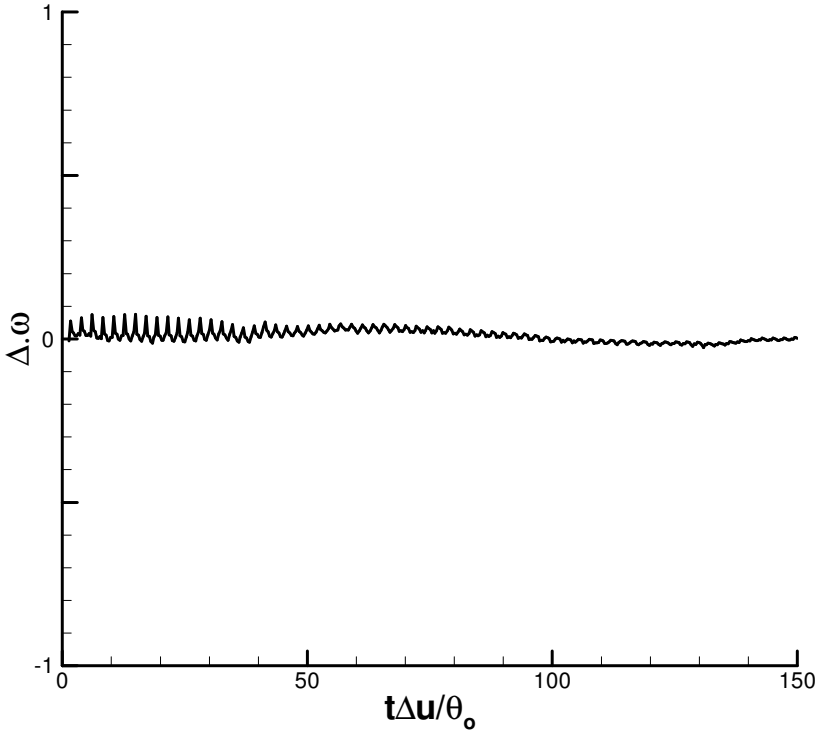

Fig. 5.13. Temporal evolution of vorticity divergence.

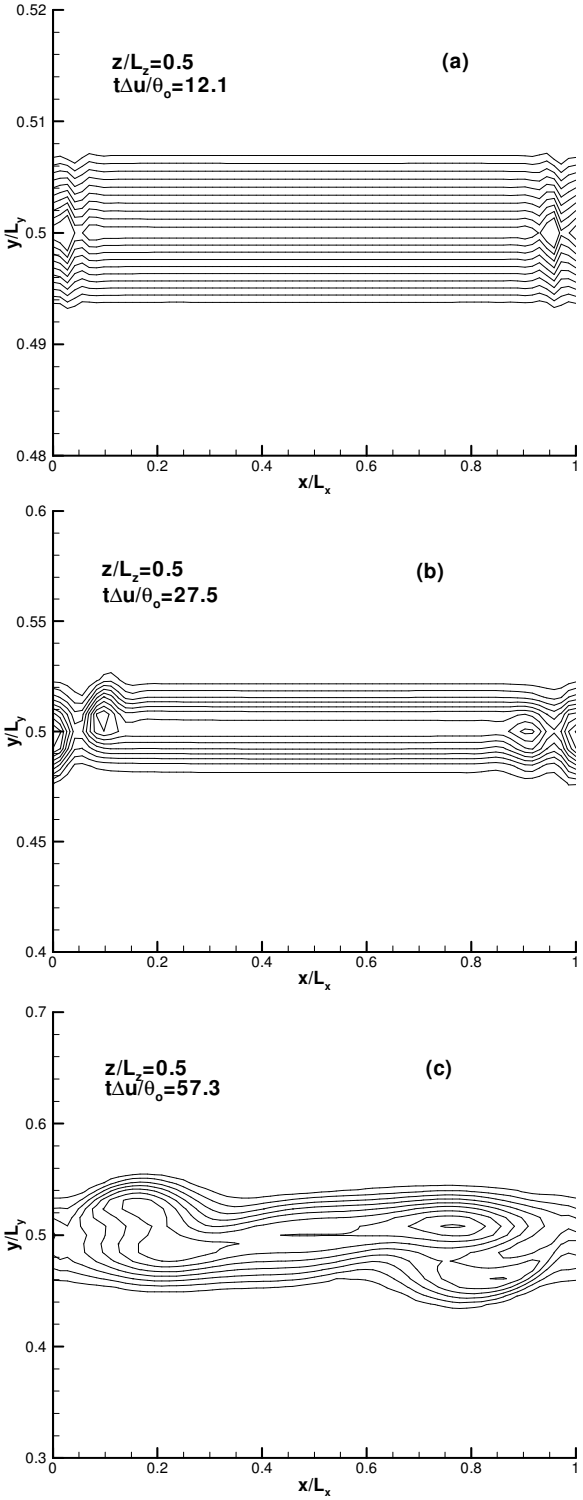

Fig. 5.14. Development of spanwise vorticity contours at the mid spanwise plane z/L_z=0.5 and at five times $t\Delta u/\theta_o$=12.1, (b) $t\Delta u/\theta_o$=27.5, (c) $t\Delta u/\theta_o$=57.3, (d) $t\Delta u/\theta_o$=87.4, *and* (e) $t\Delta u/\theta_o$=123.8. Ten equally spaced contour levels are used with $0.1\omega_{max}$ increment.

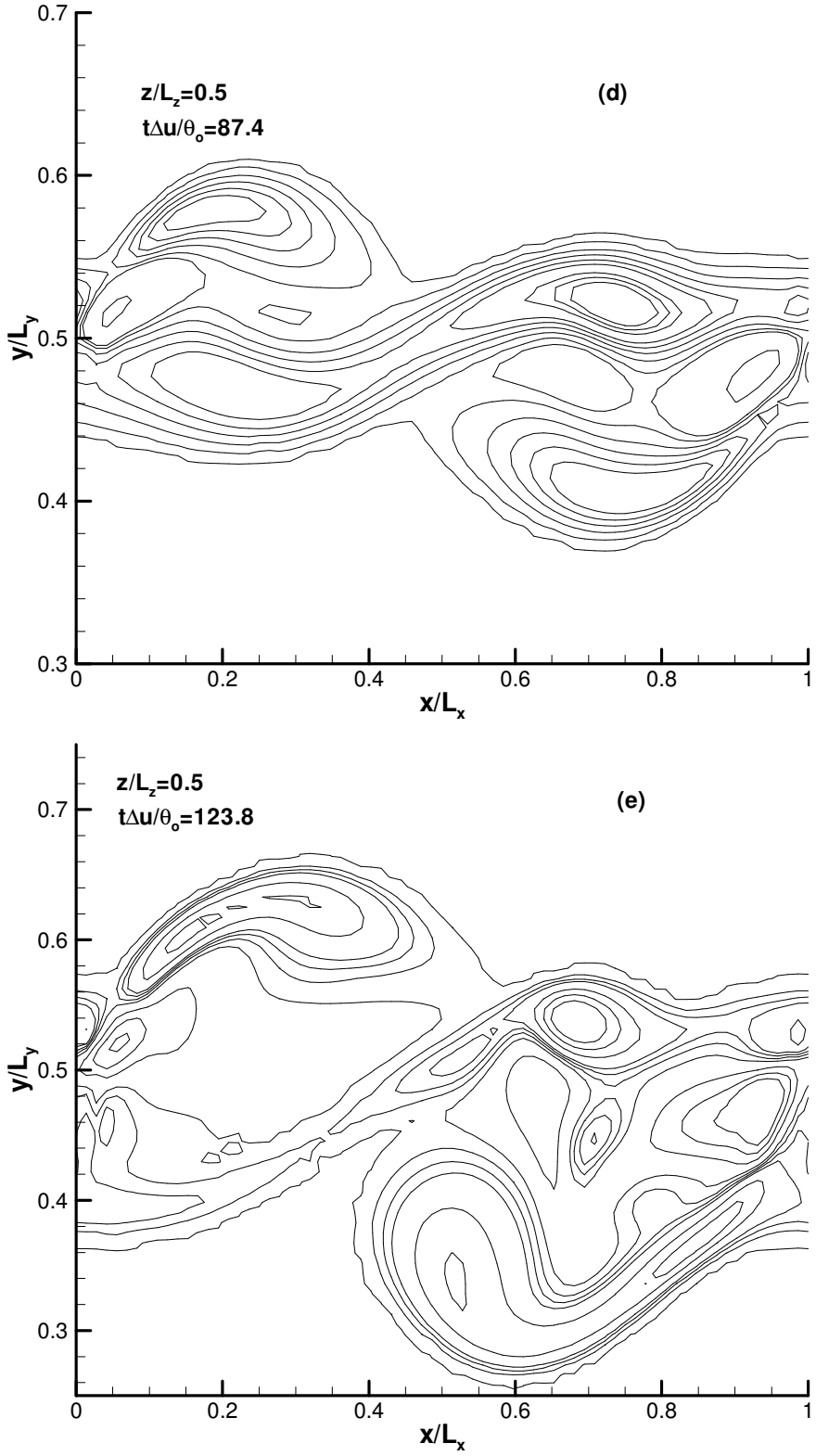

Fig. 5.14. For caption see previous page.

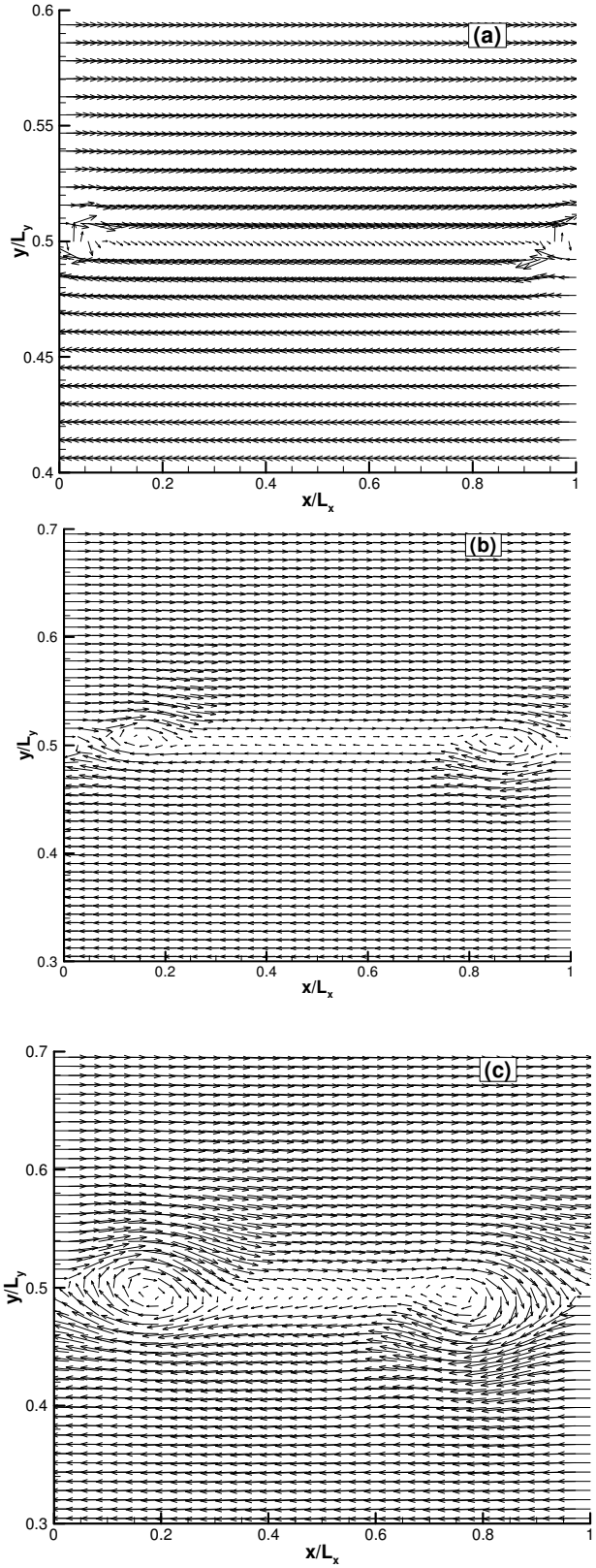

Fig. 5.15. Projection of velocity vector on x-y plane. Times and locations correspond to that of figure 5.14.

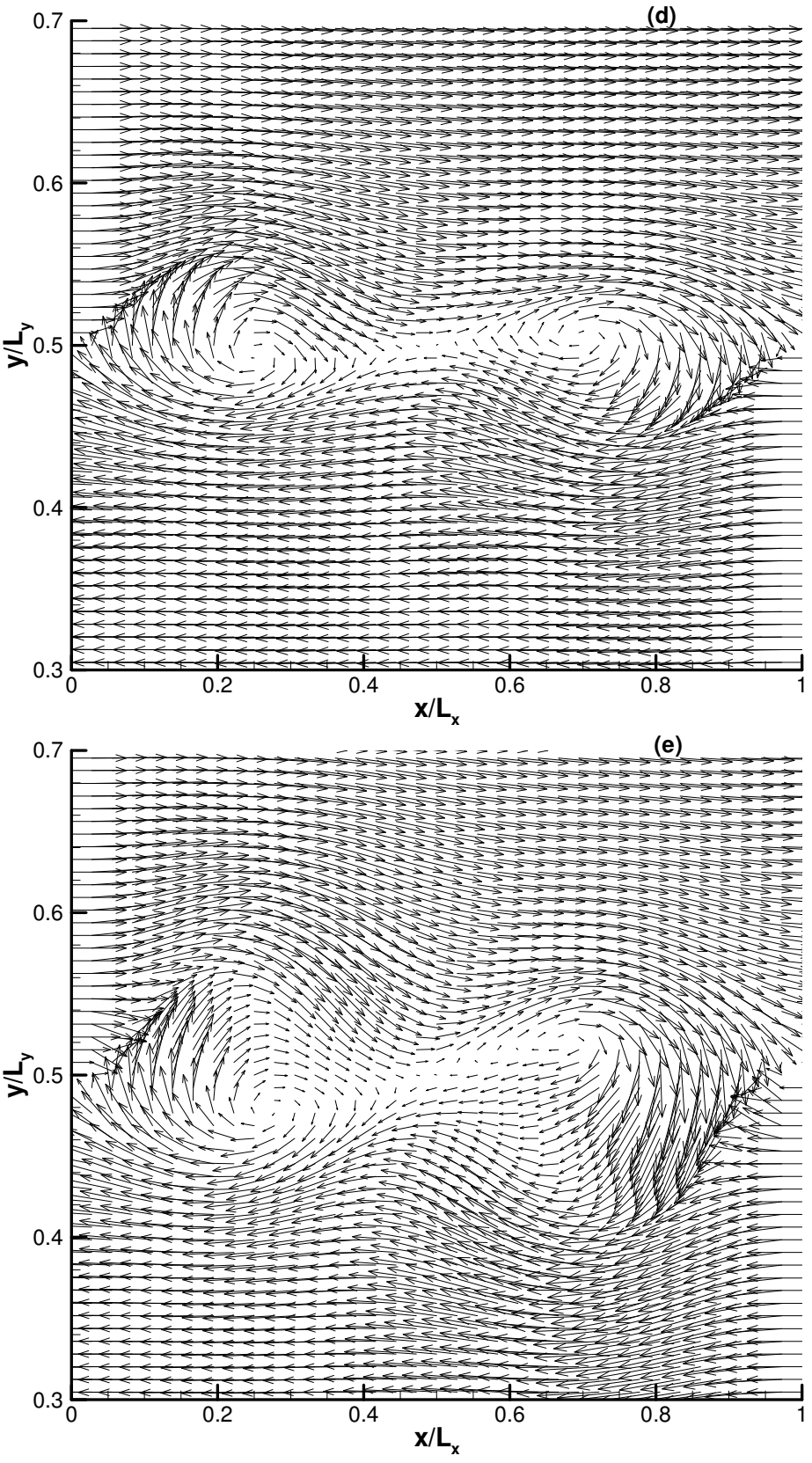

Fig. 5.15. For caption see previous page.

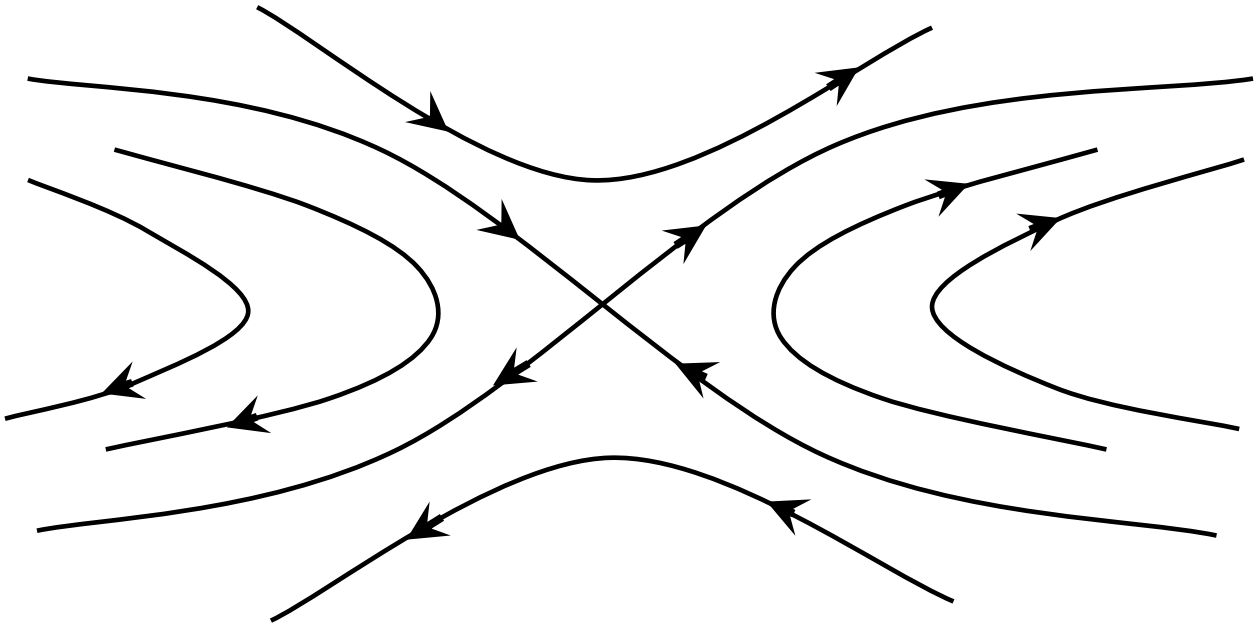

Fig. 5.16 Streamlines model for the onset of secondary (translative) instability in temporal mixing layer.

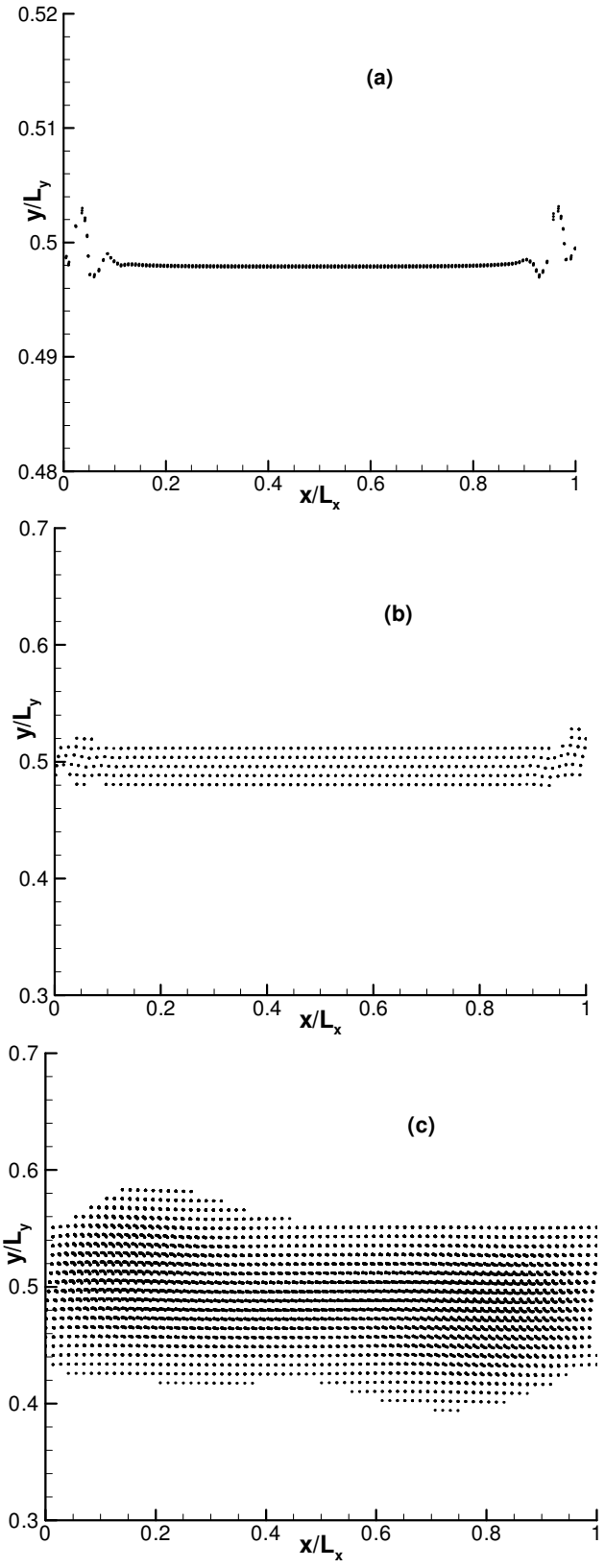

Fig. 5.17. Particles location at the same time and z plane as in figure 5.14.

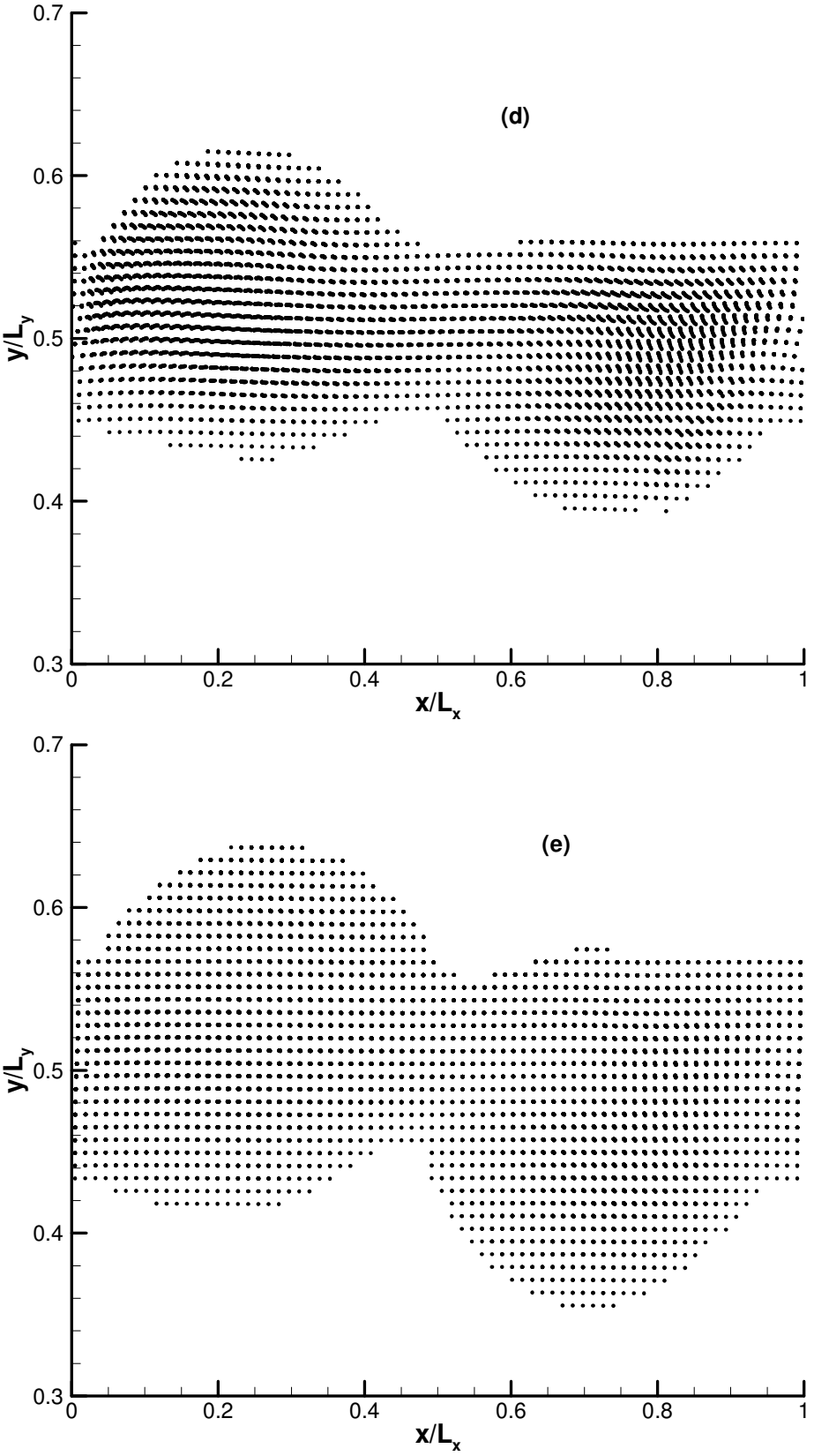

Fig. 5.17. For caption see previous page.

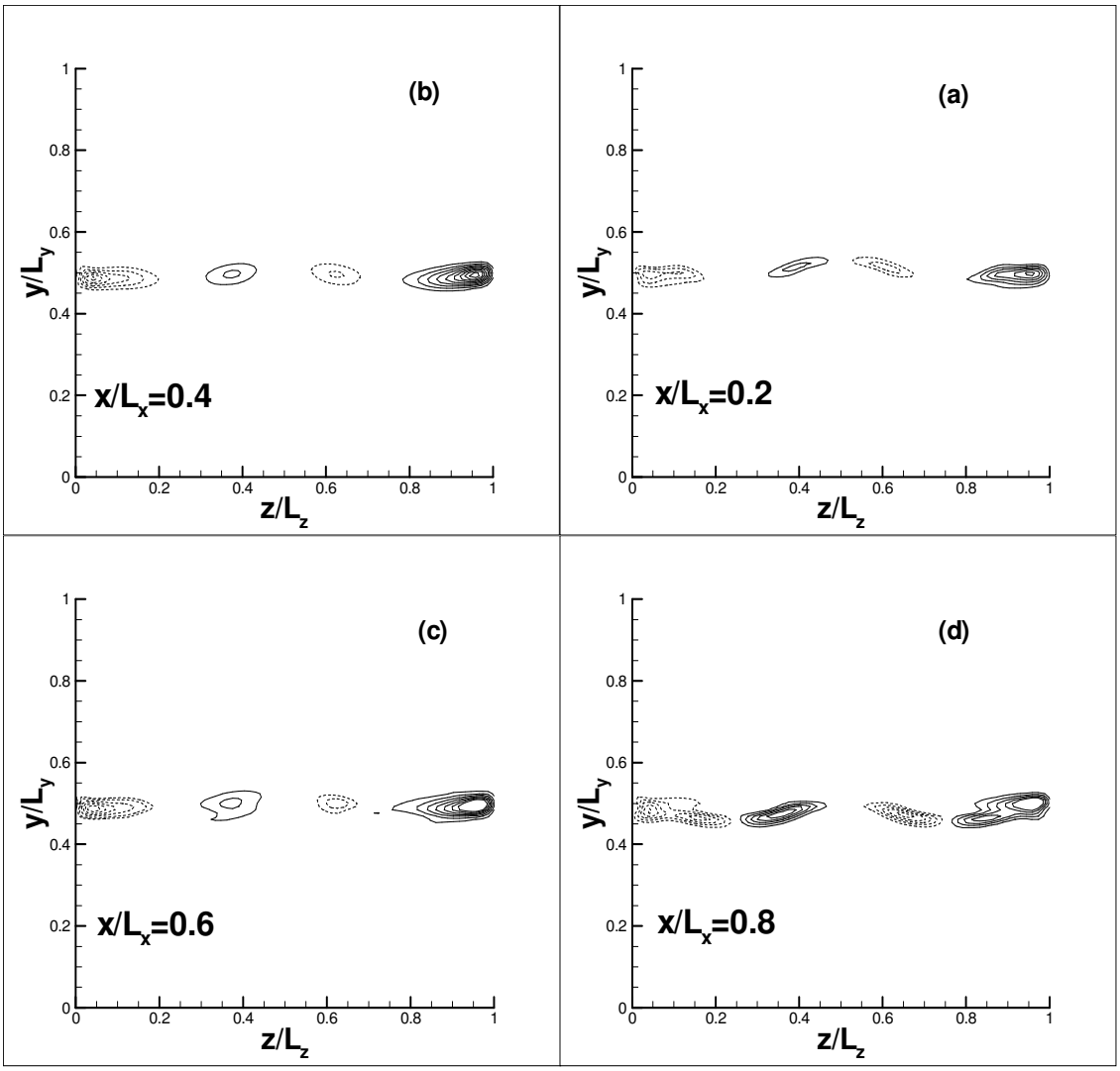

Fig. 5.18 Streamwise vorticity contours at $t\Delta u/\theta_o$=42.8 and four streamwise locations (a)x/L_x=0.2, (b)x/L_x=0.4 , (c)x/L_x=0.6 , (d)x/L_x=0.8. Twenty equally distributed contour levels with 0.05 $(\omega_{max}- \omega_{min})$ increments are used. Dotted lines represent negative vorticity and continuous lines represent positive vorticity.

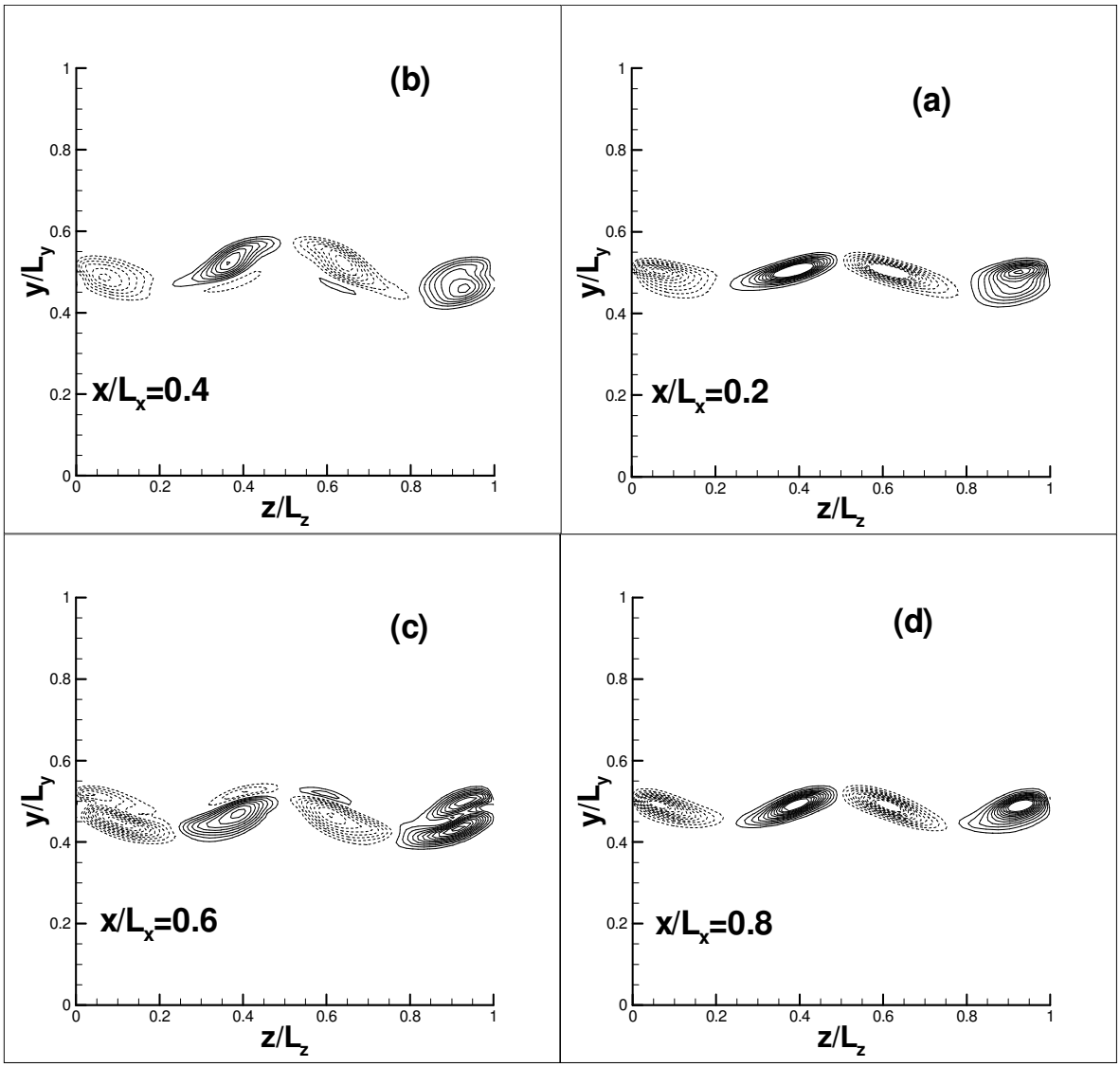

Fig. 5.19 Streamwise vorticity contours at $t\Delta u/\theta_o$=84.4 and four streamwise locations (a)x/L_x=0.2, (b)x/L_x=0.4 , (c)x/L_x=0.6 , (d)x/L_x=0.8. Twenty equally distributed contour levels with 0.05 $(\omega_{max}- \omega_{min})$ increments are used. Dotted lines represent negative vorticity and continuous lines represent positive vorticity.

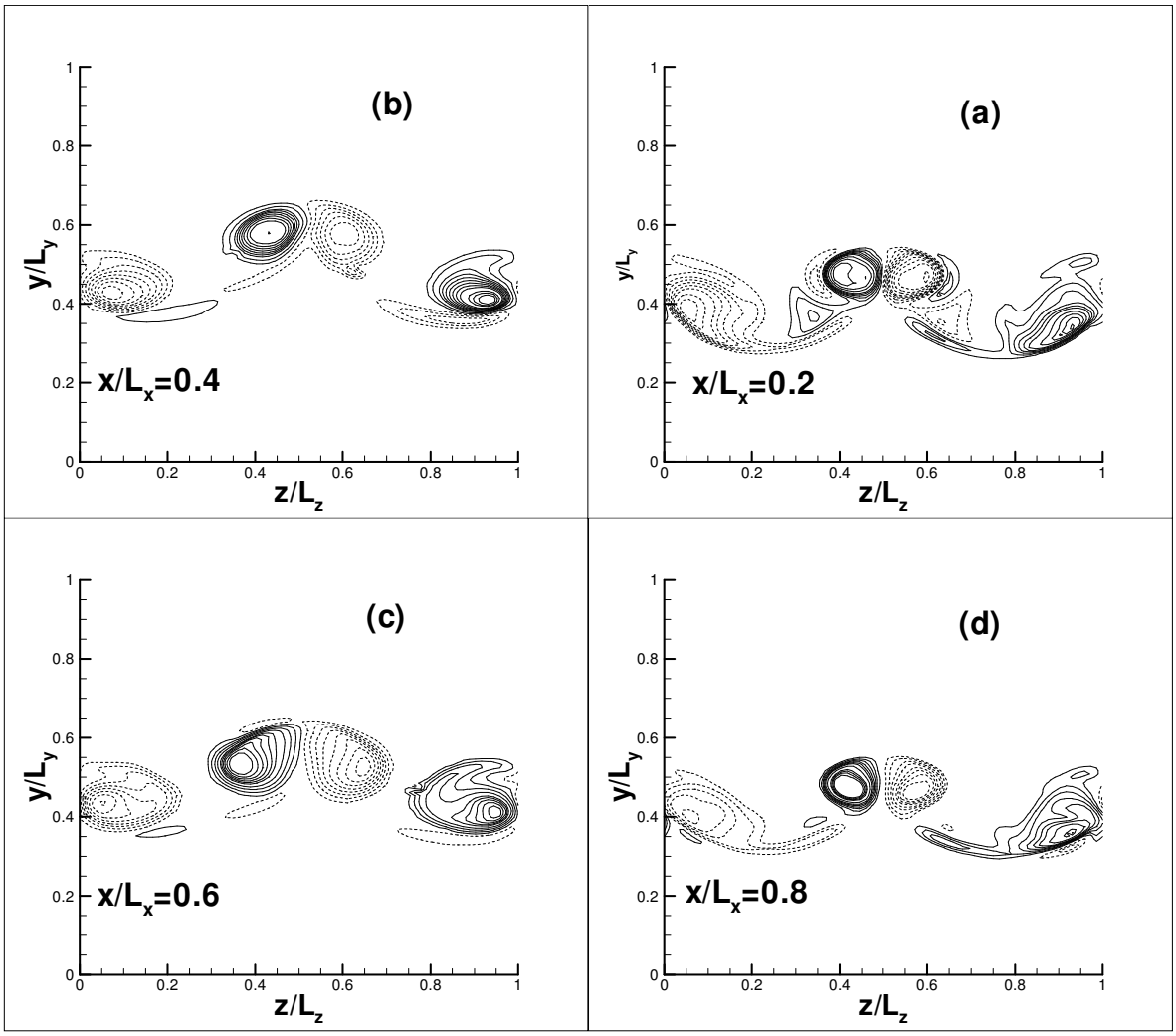

Fig. 5.20 Streamwise vorticity contours at $t\Delta u/\theta_o$=123.8 and four streamwise locations (a)x/L_x=0.2, (b)x/L_x=0.4 , (c)x/L_x=0.6 , (d)x/L_x=0.8. Twenty equally distributed contour levels with 0.05 $(\omega_{max}- \omega_{min})$ increments are used. Dotted lines represent negative vorticity and continuous lines represent positive vorticity.

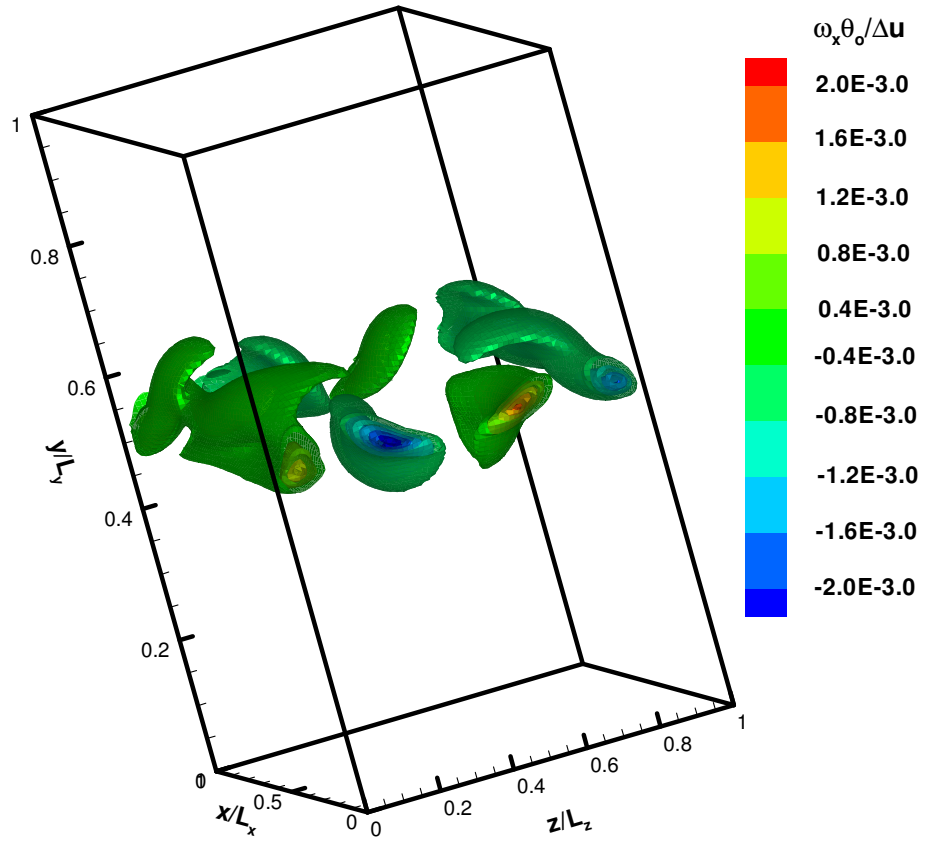

Fig. 5.21. Isosurfaces of streamwise vorticity at $t\Delta u/\theta_o$=84.4.

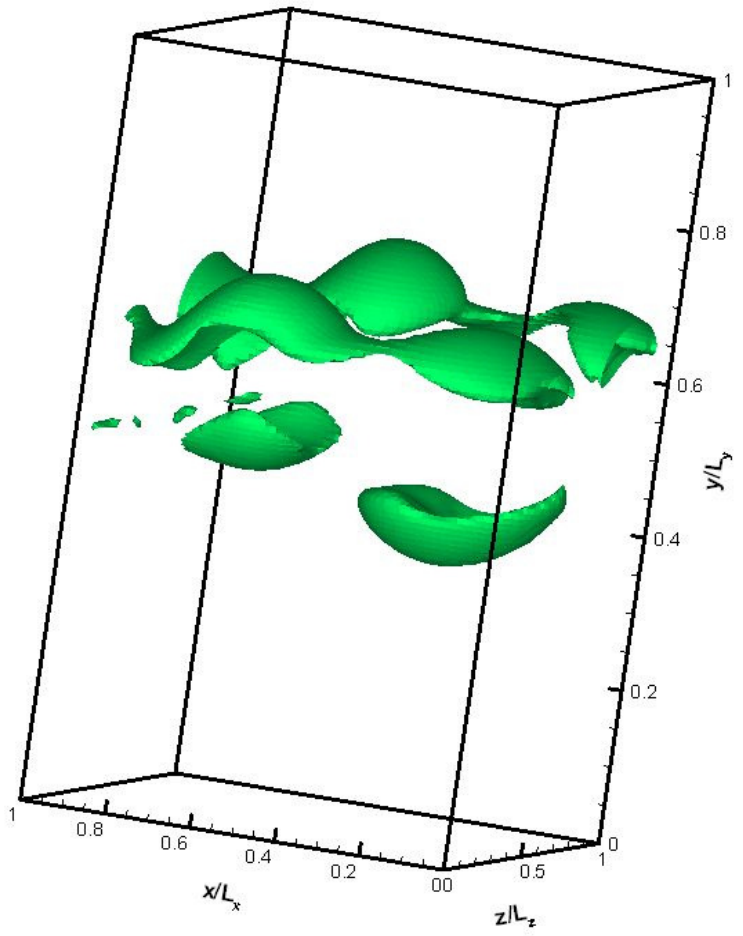

Fig. 5.22. Vorticity isosurface $\omega_x\theta_o/\Delta u$=0.004 at $t\Delta u/\theta_o$=84.4.

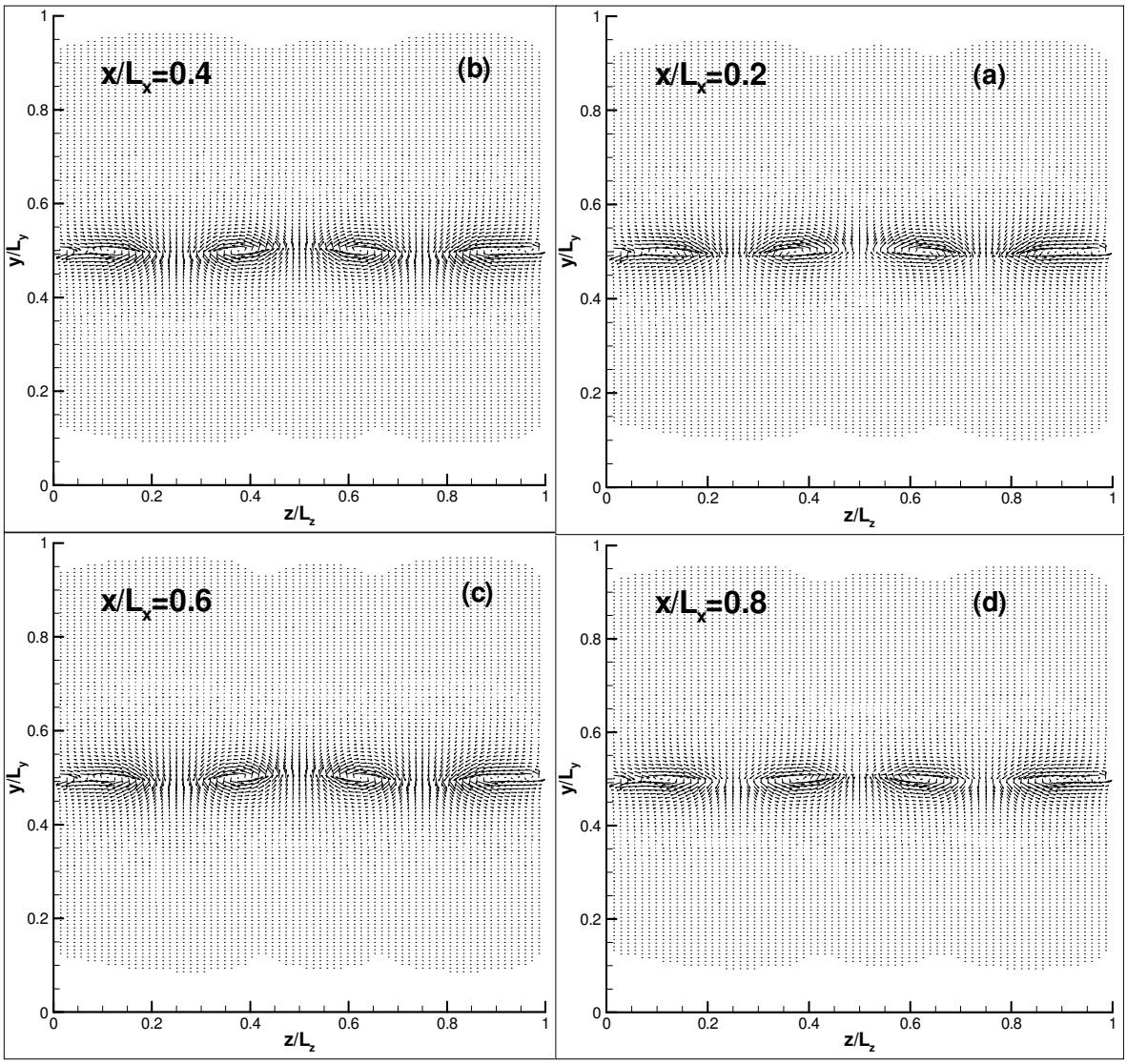

Fig. 5.23. velocity vector field (v,w) at $t\Delta u/\theta_o$=42.8 at four streamwise locations (a)x/L_x=0.2, (b)x/L_x=0.4 , (c)x/L_x=0.6 , (d)x/L_x=0.8

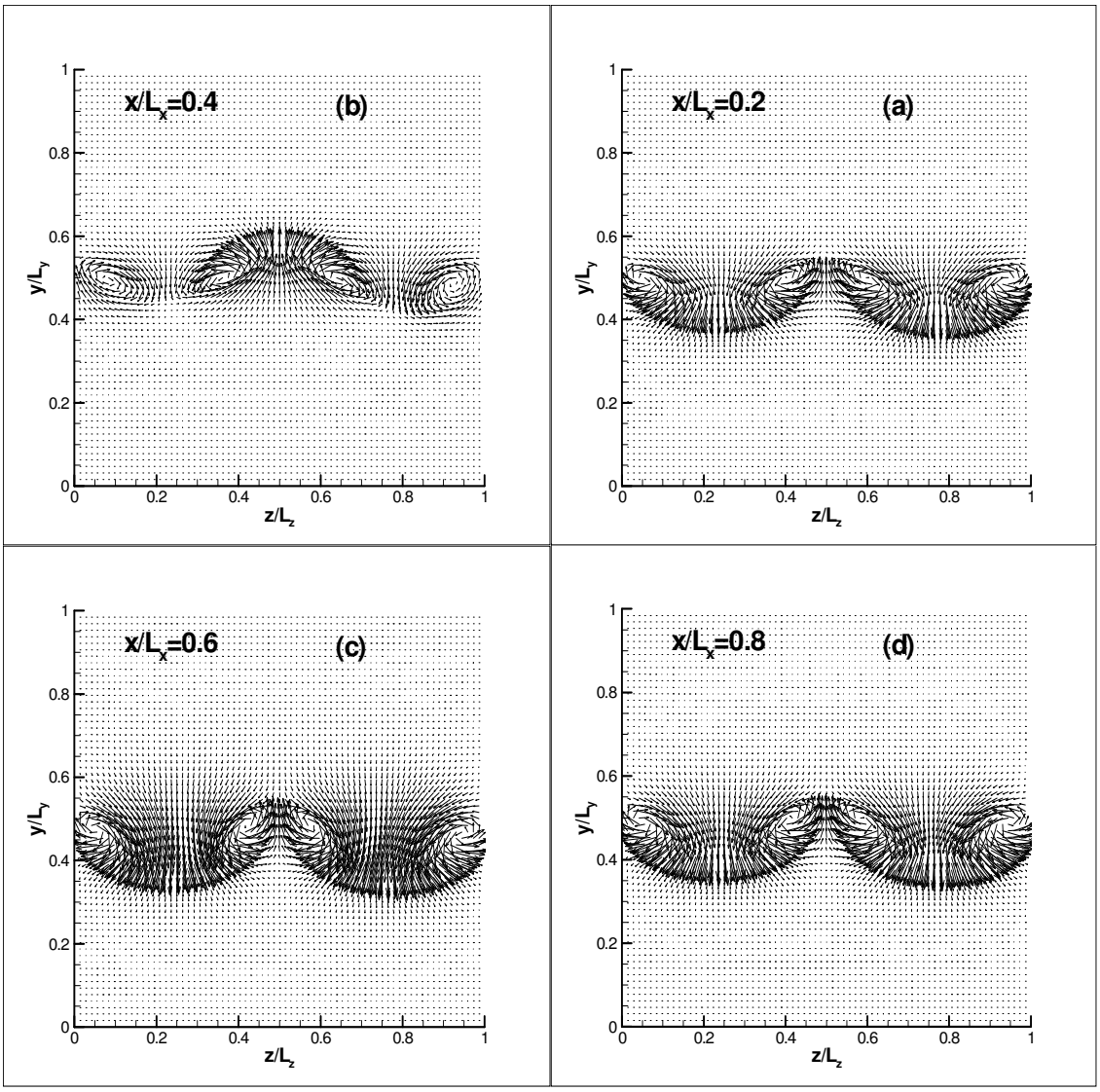

Fig. 5.24. velocity vector field (v,w) at $t\Delta u/\theta_o$=84.4 at four streamwise locations (a)x/L_x=0.2, (b)x/L_x=0.4 , (c)x/L_x=0.6 , (d)x/L_x=0.8

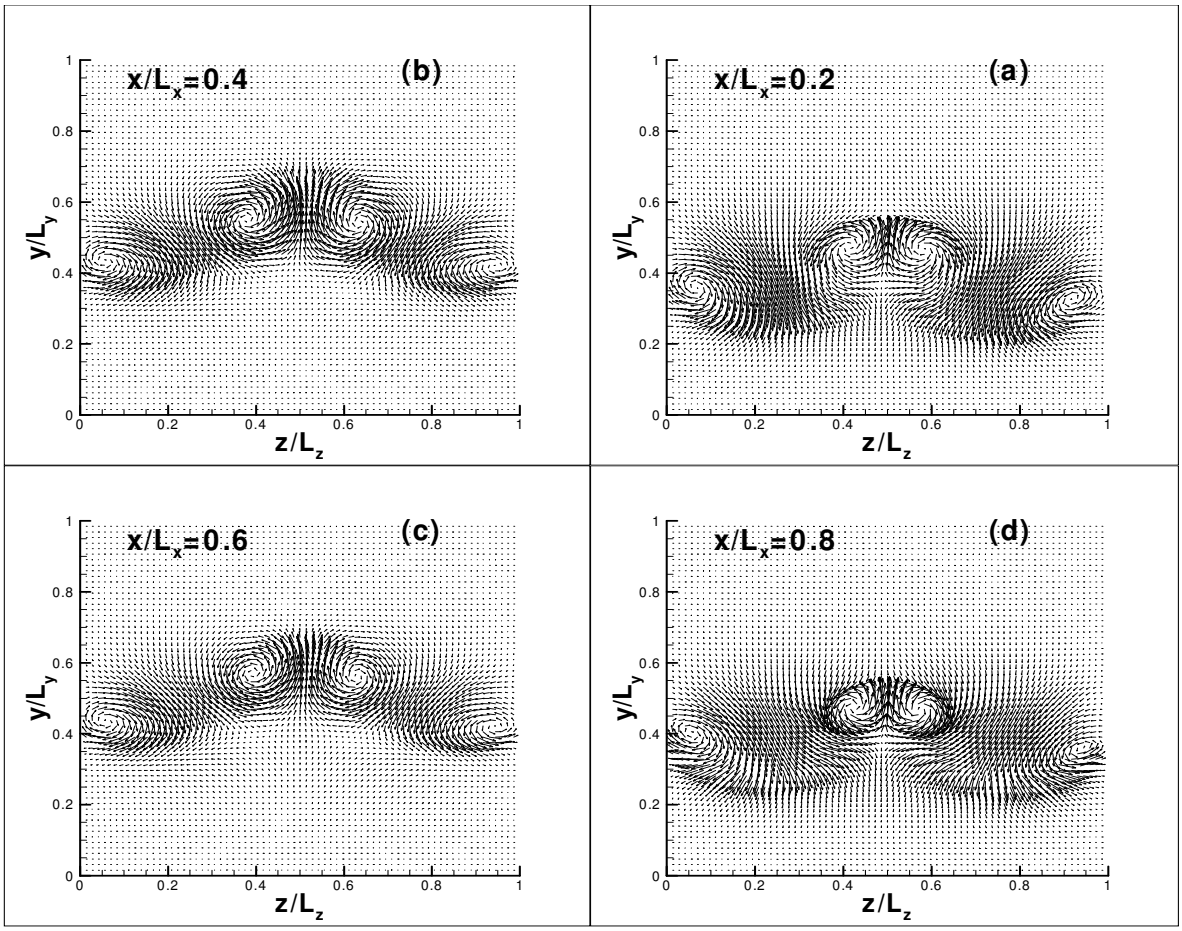

Fig. 5.25. velocity vector field (v,w) at $t\Delta u/\theta_o$=123.8 at four streamwise locations (a)x/L_x=0.2, (b)x/L_x=0.4 , (c)x/L_x=0.6 , (d)x/L_x=0.8

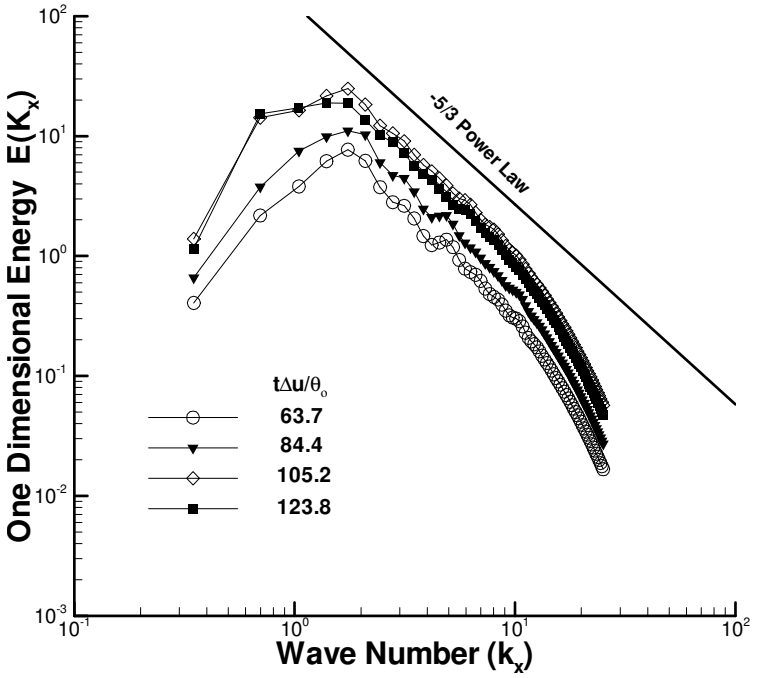

Fig. 5.26. Temporal Development of one dimensional streamwise energy spectrum at four times (a) $t\Delta u/\theta_o$=63.7, (b) $t\Delta u/\theta_o$=84.4, (c) $t\Delta u/\theta_o$=105.2, and (d) $t\Delta u/\theta_o$=123.8. Continuous line represents the -5/3 power law.

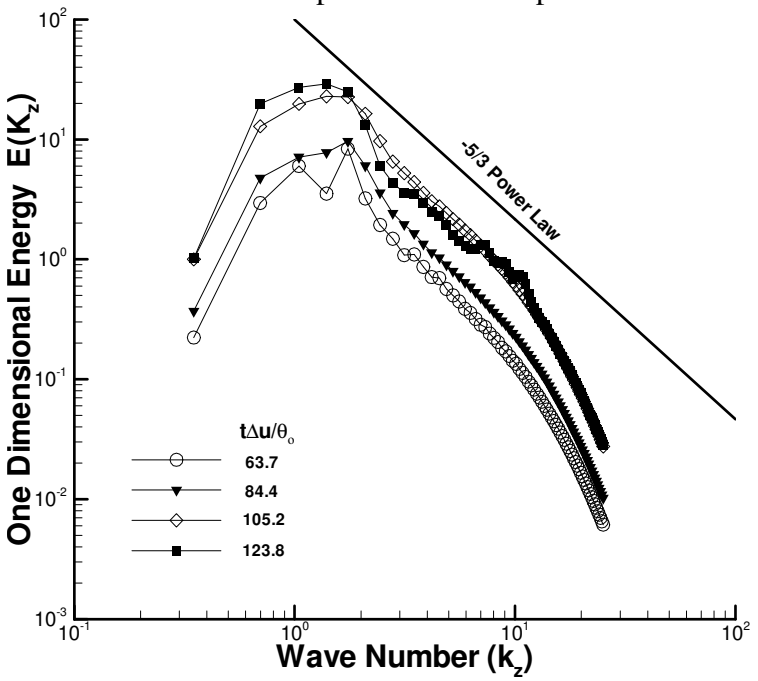

Fig. 5.27. Temporal Development of one dimensional spanwise energy spectrum at four times (a) $t\Delta u/\theta_o$=63.7, (b) $t\Delta u/\theta_o$=84.4, (c) $t\Delta u/\theta_o$=105.2, and (d) $t\Delta u/\theta_o$=123.8.. Continuous line represents the -5/3 power law.

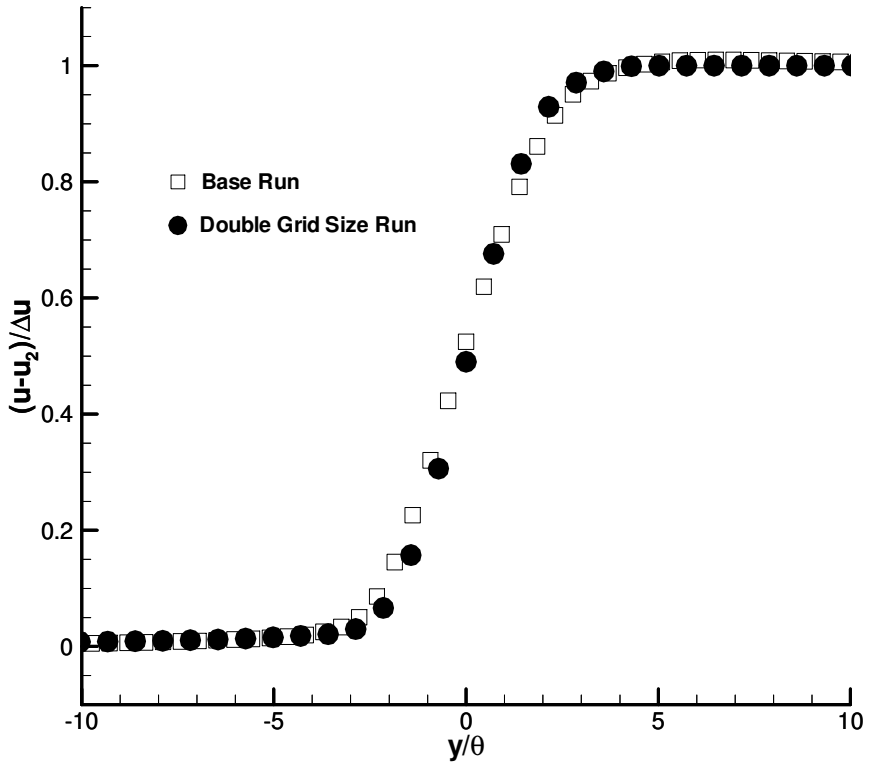

Fig. 5.28. Sensitivity of mean velocity profile to grid size at $t\Delta u/\theta_o=84.4$.

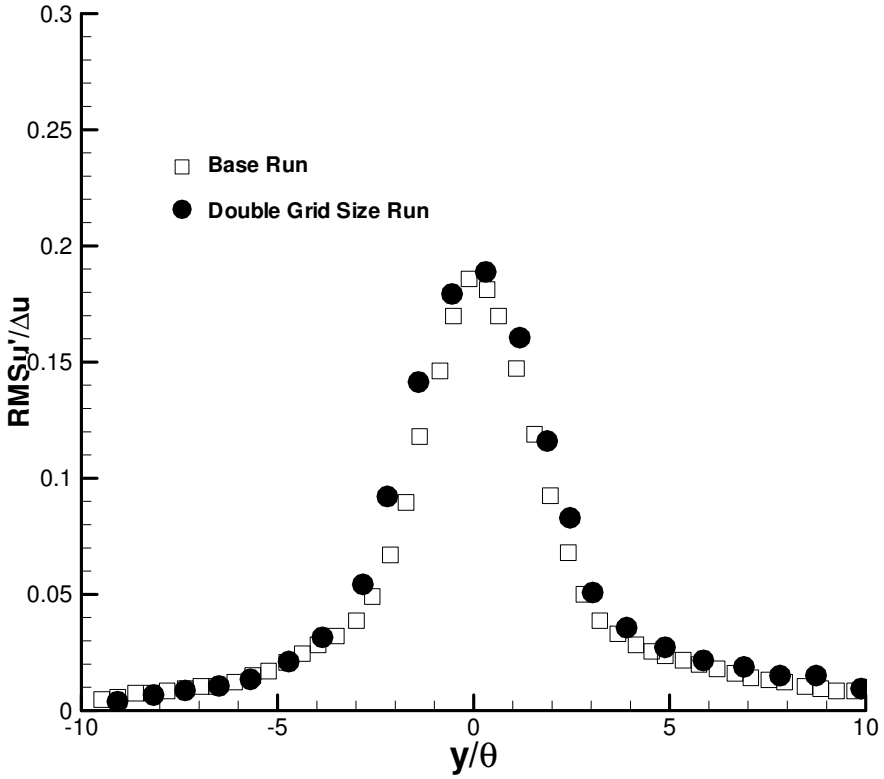

Fig. 5.29. Sensitivity of root mean square streamwise velocity fluctuations to grid size at $t\Delta u/\theta_o$=84.4.

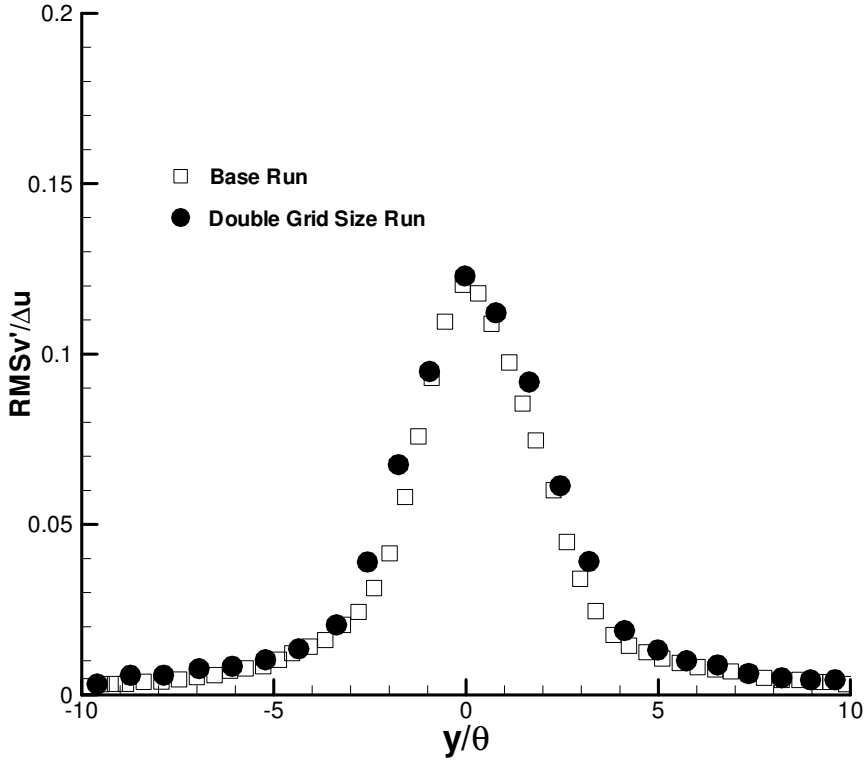

Fig. 5.30. Sensitivity of root mean square cross-stream velocity fluctuations to grid size at $t\Delta u/\theta_o$=84.4.

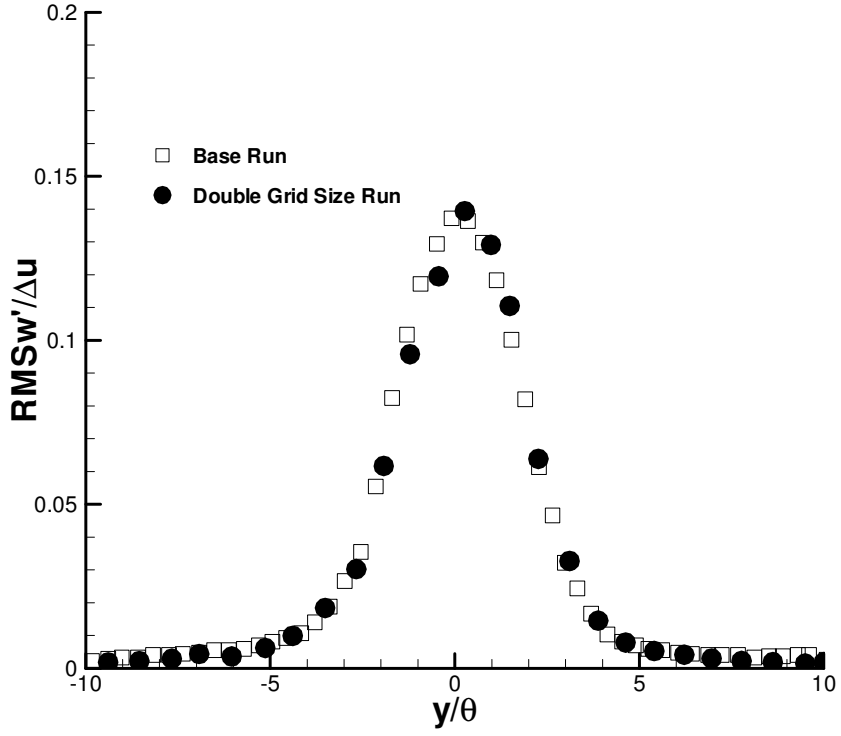

Fig. 5.31. Sensitivity of root mean square spanwise velocity fluctuations to grid size at $t\Delta u/\theta_o$=84.4.

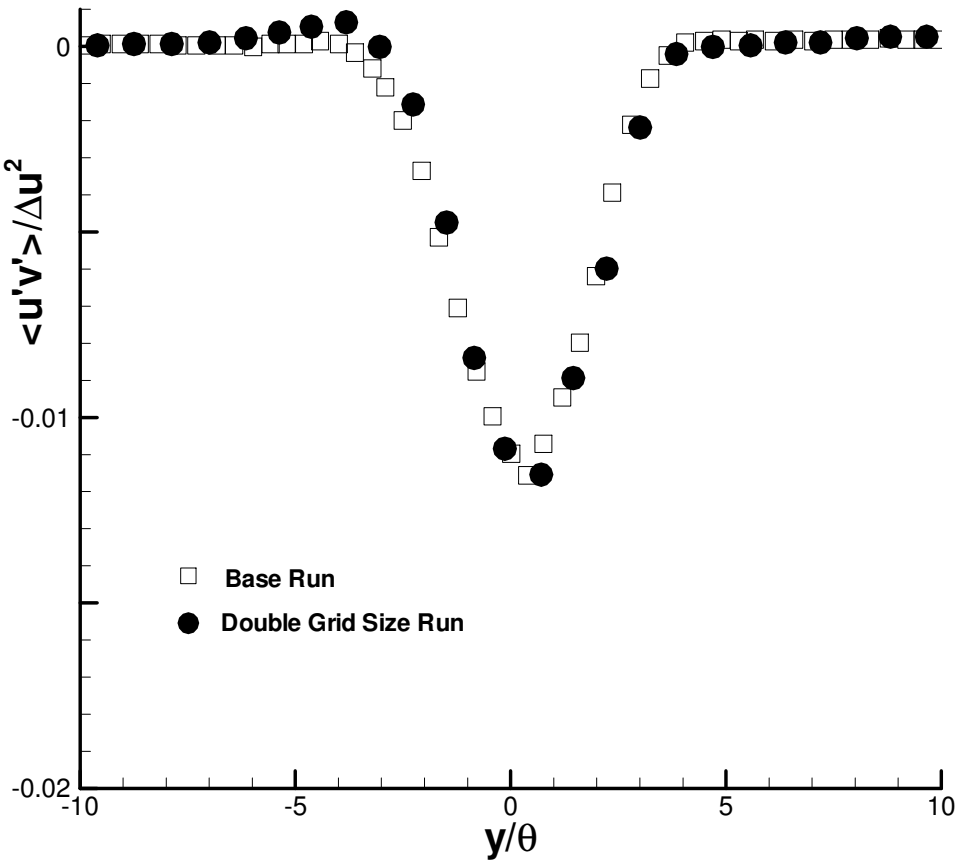

Fig. 5.32. Sensitivity of cross correlation $u'v'$ to grid size at $t\Delta u/\theta_o$=84.4.

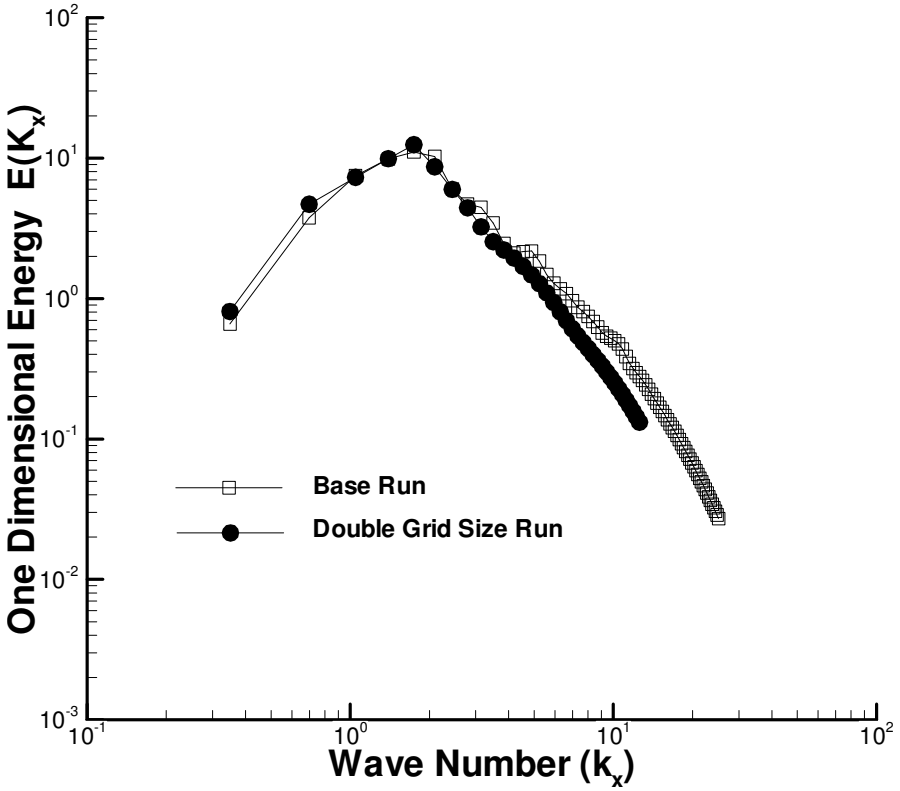

Fig. 5.33. Sensitivity of streamwise energy spectrum to grid size at $t\Delta u/\theta_o$=84.4.

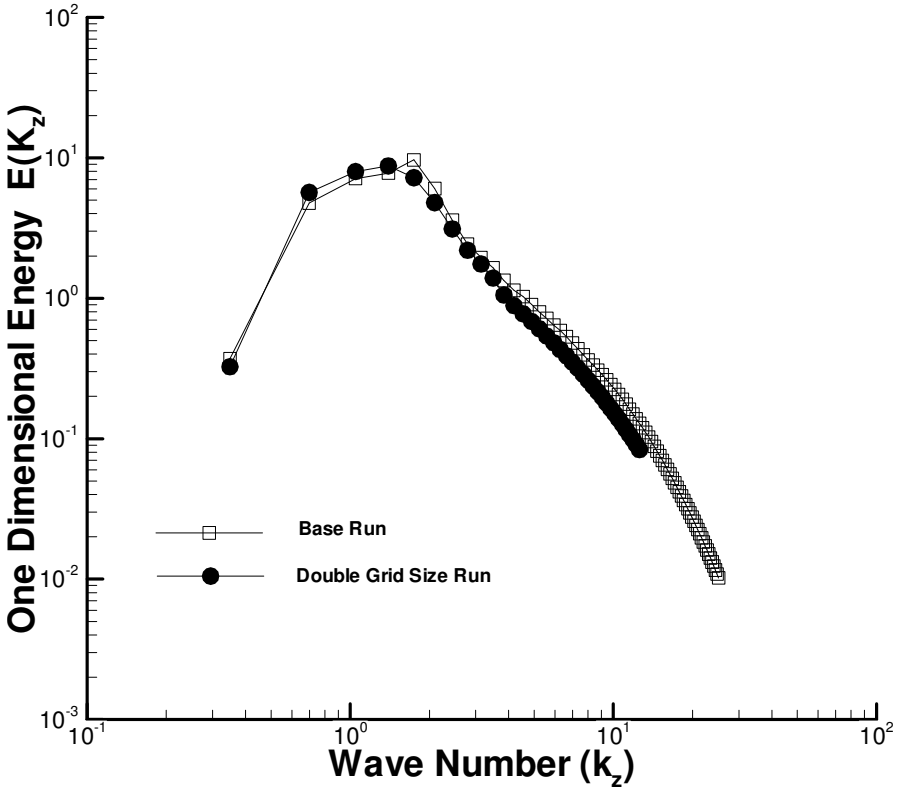

Fig. 5.34. Sensitivity of spanwise energy spectrum to grid size at $t\Delta u/\theta_o$=84.4.

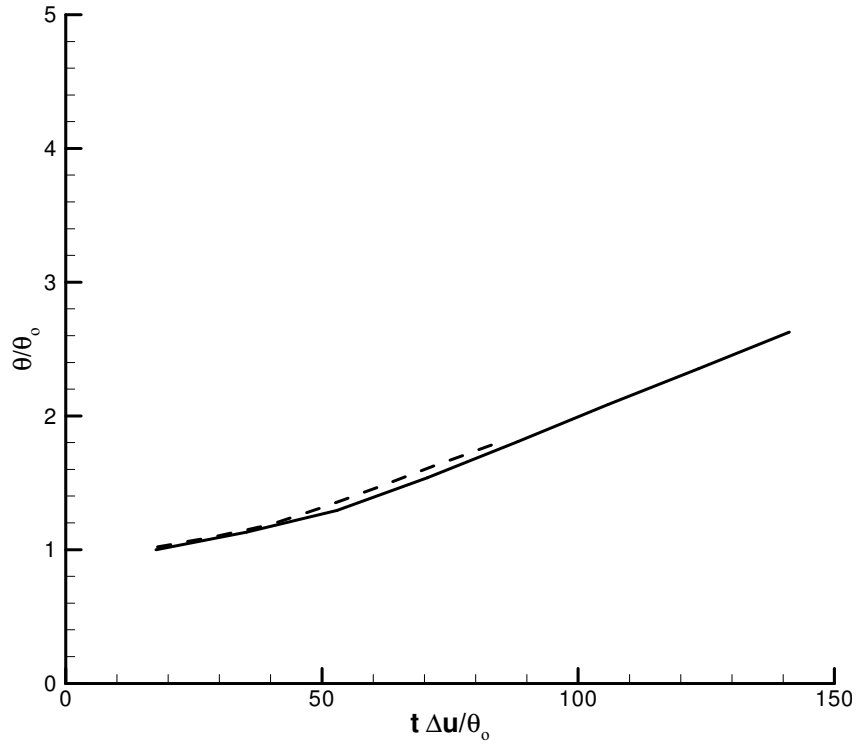

Fig. 5.35. Temporal growth of momentum thickness. ----- (invisid run), _____ (viscous run).

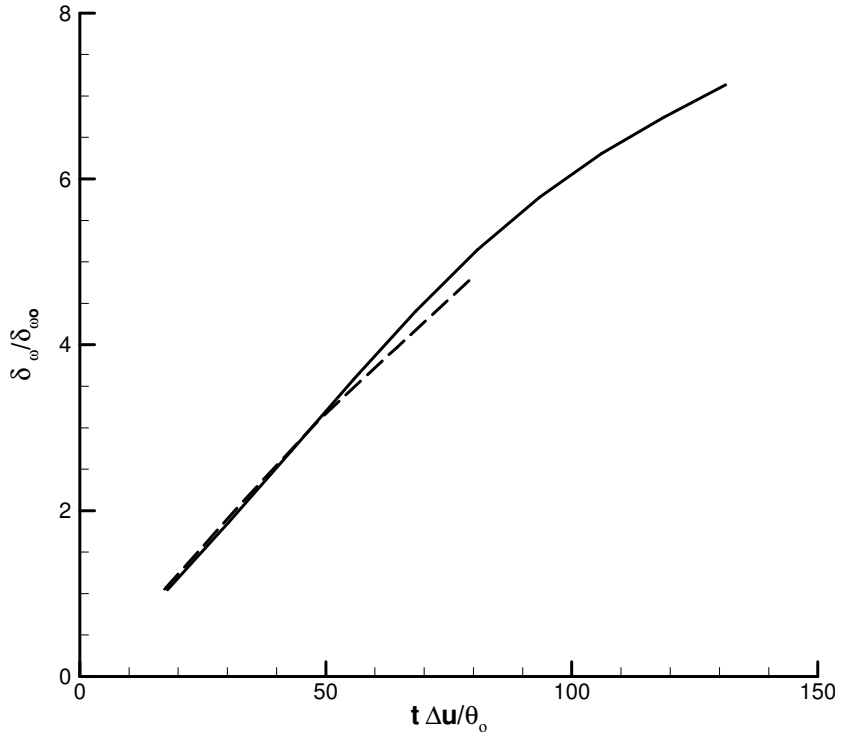

Fig. 5.36. Temporal growth of vorticity thickness. ----- (invisid run), _____ (viscous run)

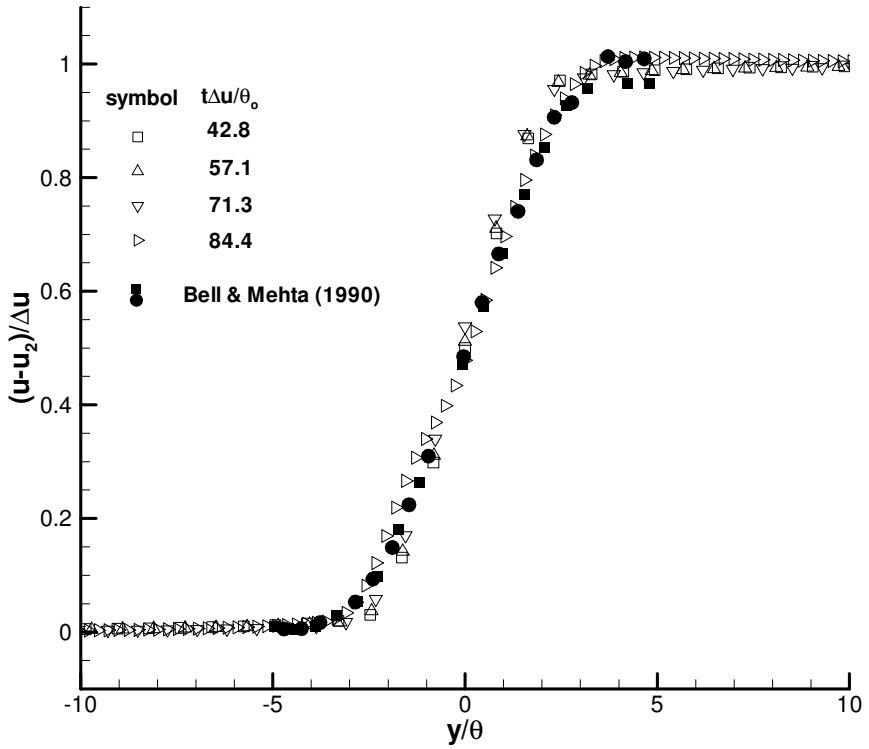

Fig. 5.37. Profiles of mean streamwise velocity in inviscid run at four times.

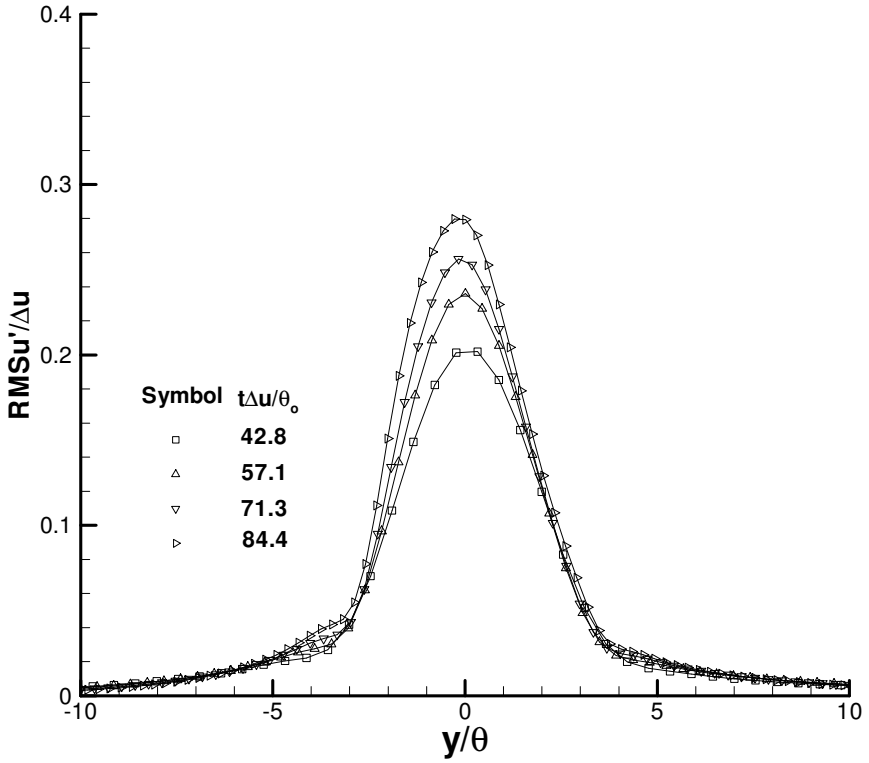

Fig. 5.38. Temporal evolution of root mean square streamwise velocity fluctuations in inviscid run at four times.

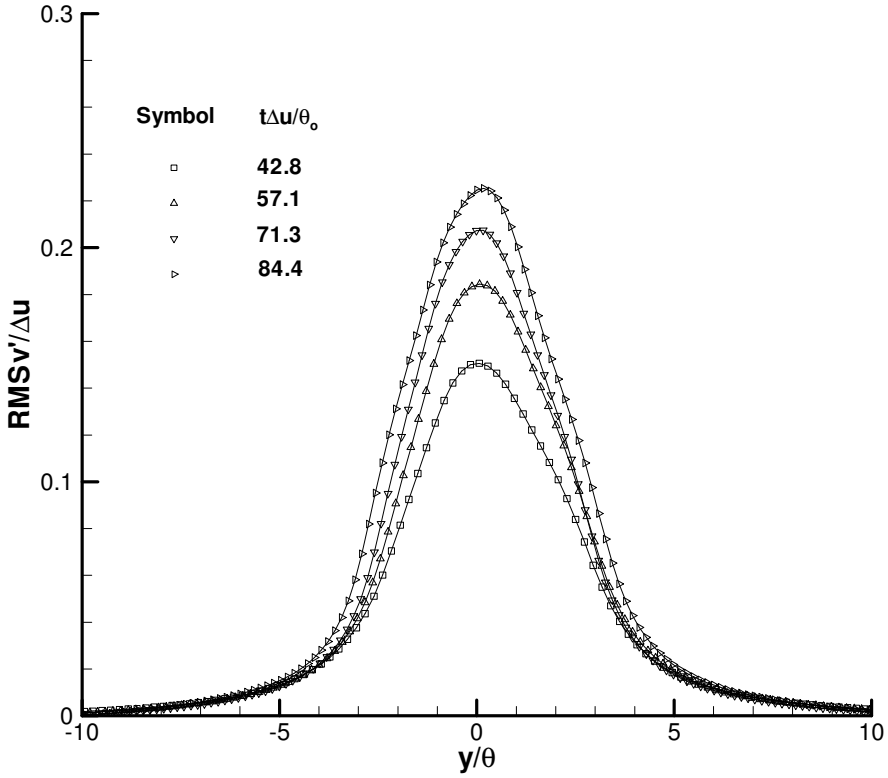

Fig. 5.39. Temporal evolution of root mean square cross-stream velocity fluctuations in inviscid run at four times.

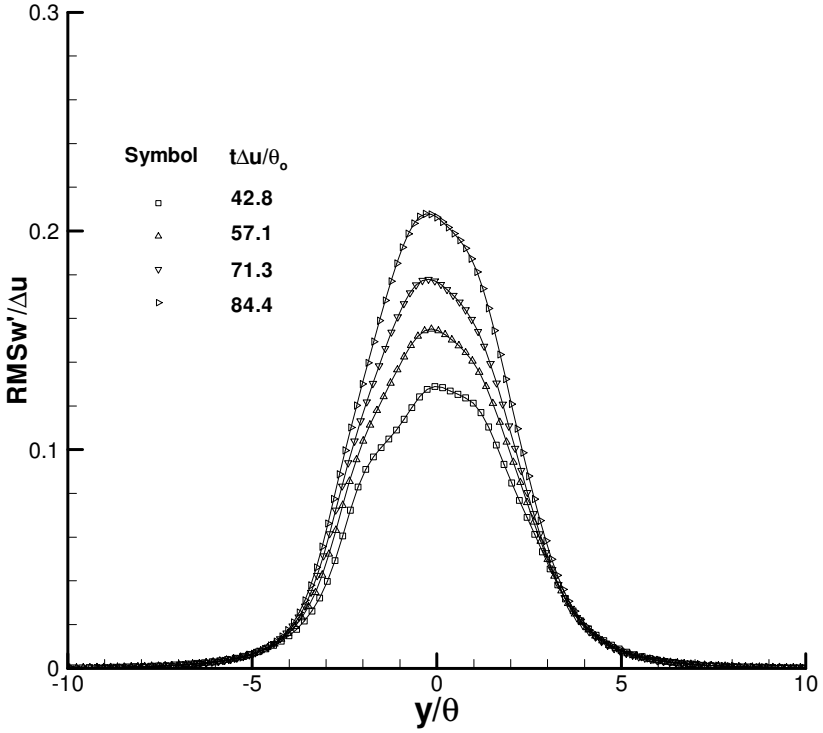

Fig. 5.40 Temporal evolution of root mean square streamwise velocity fluctuations in inviscid run at four times.

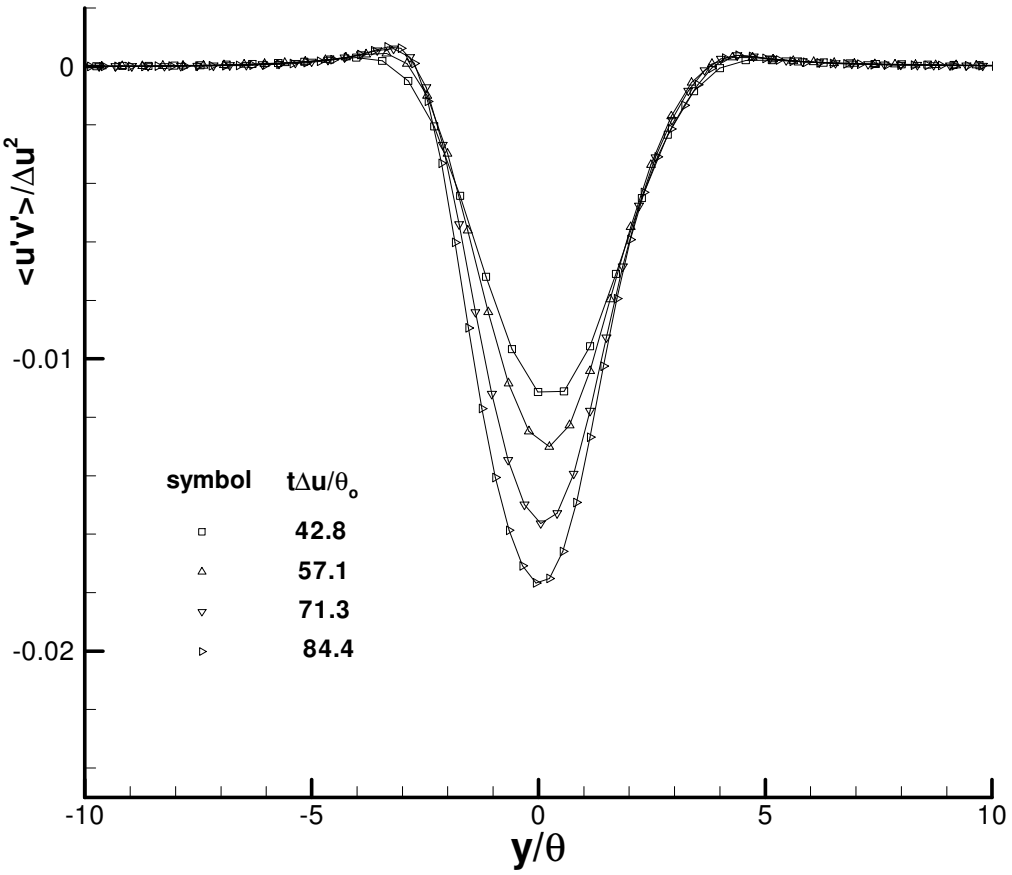

Fig. 5.41. Temporal evolution of cross correlation *u'v'* in inviscid run at four times.

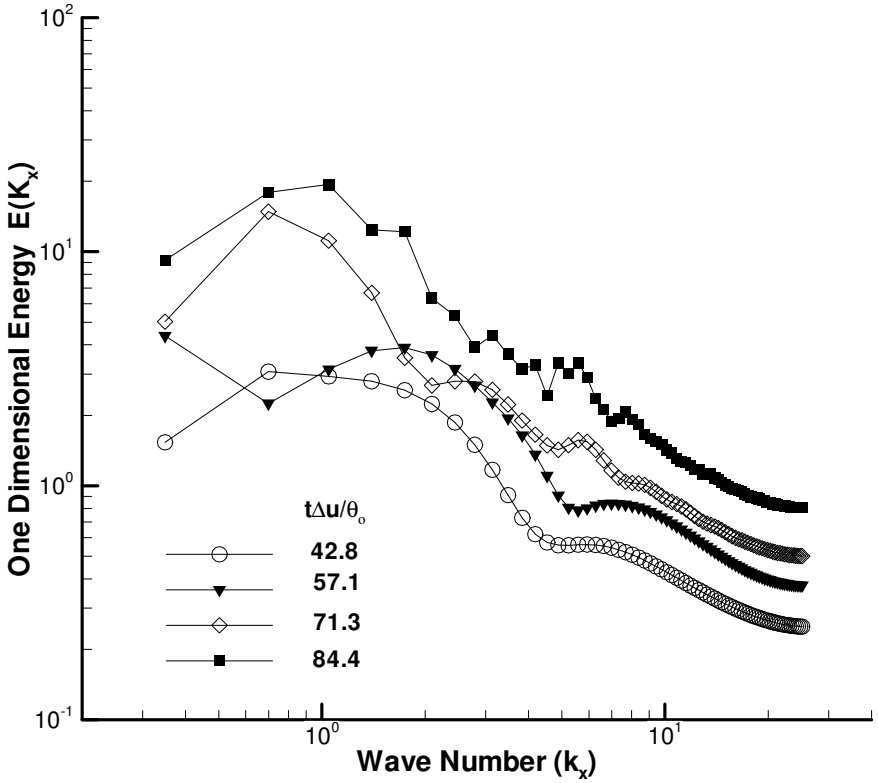

Fig. 5.42. Temporal evolution of streamwise energy spectrum in inviscid run at four times.

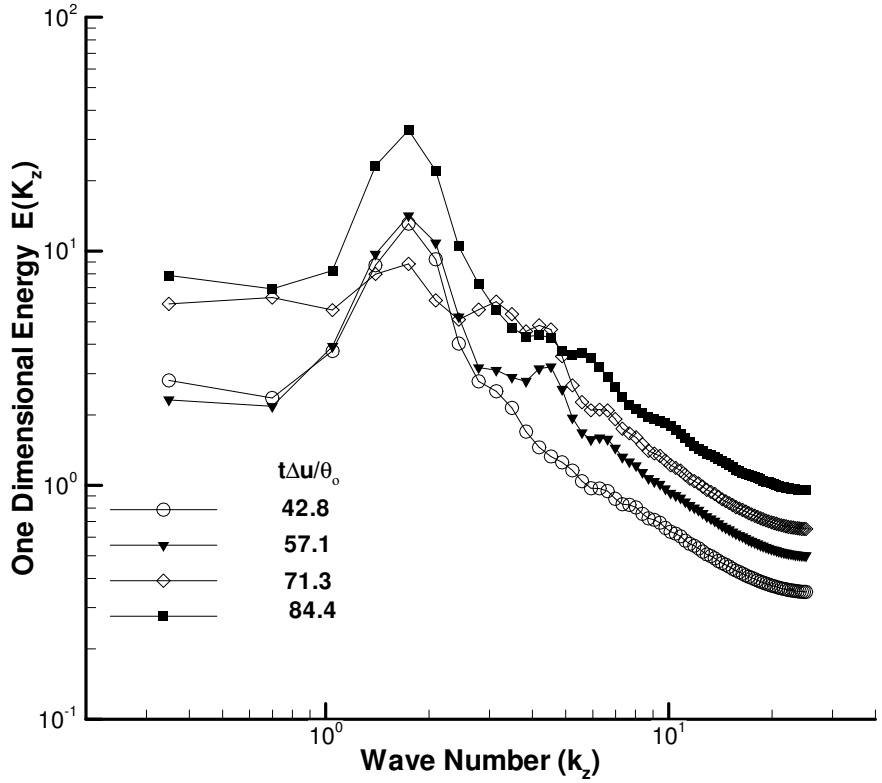

Fig. 5.43. Temporal evolution of spanwise energy spectrum in inviscid run at four times.

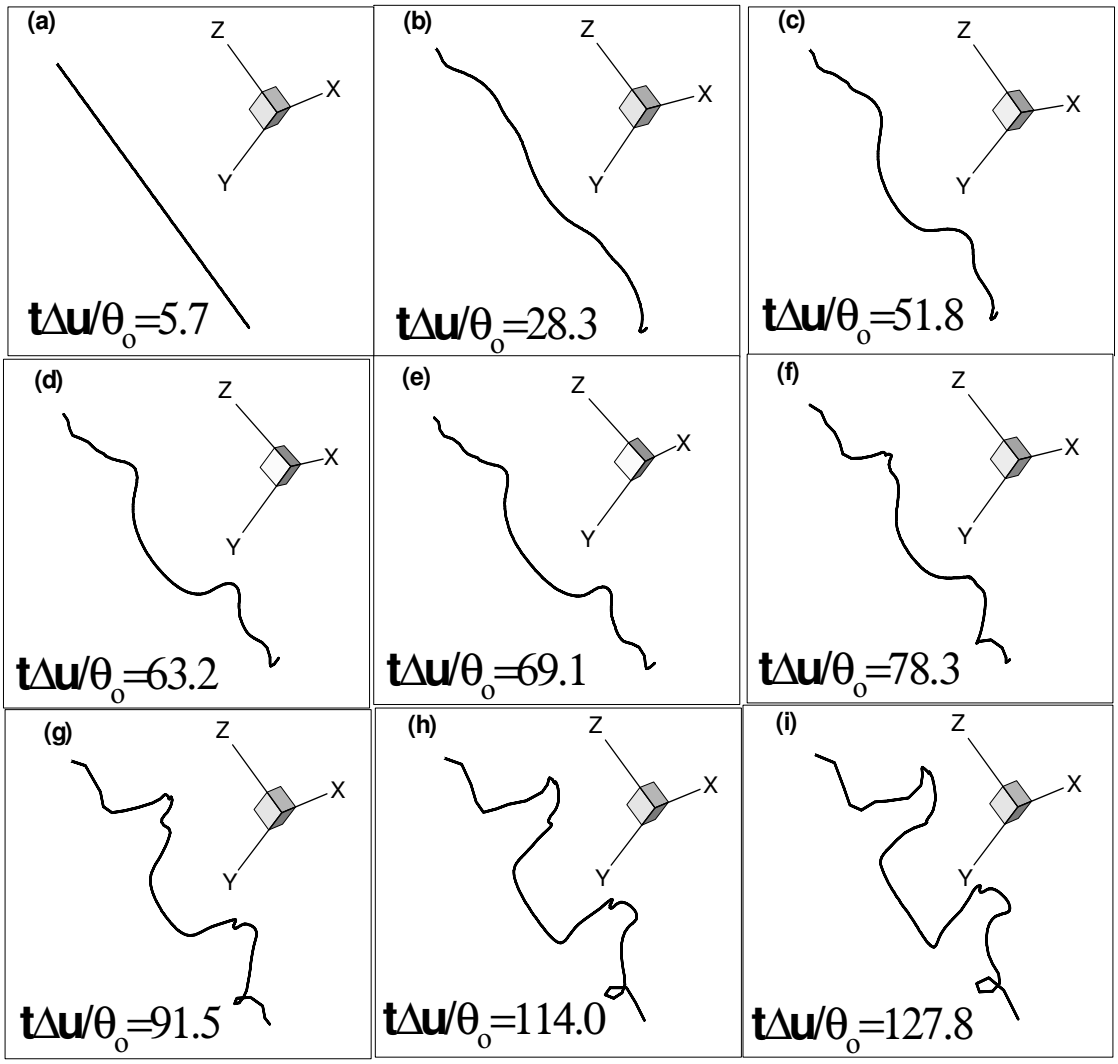

Fig. 6.1 Temporal development of a vorticity filament.

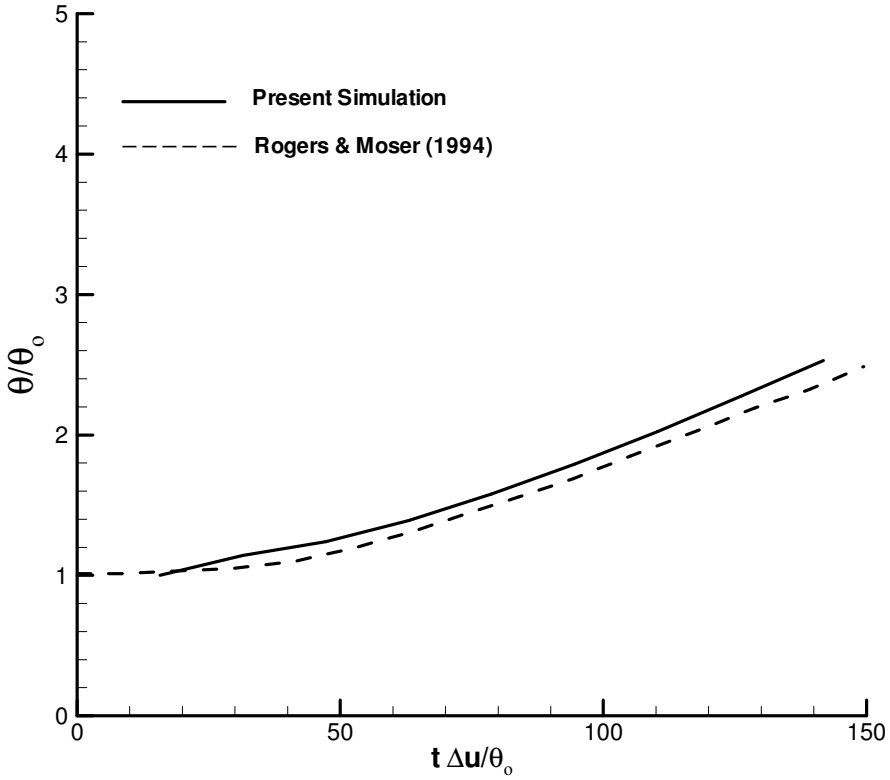

Fig. 6.2 Temporal development of momentum thickness.

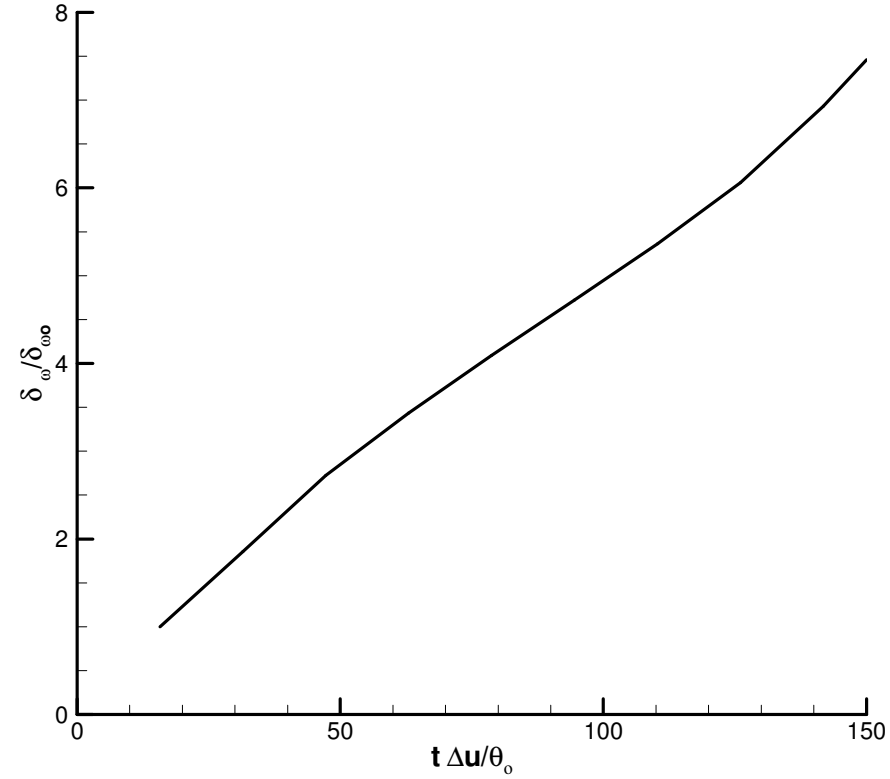

Fig. 6.3 Temporal development of vorticity thickness.

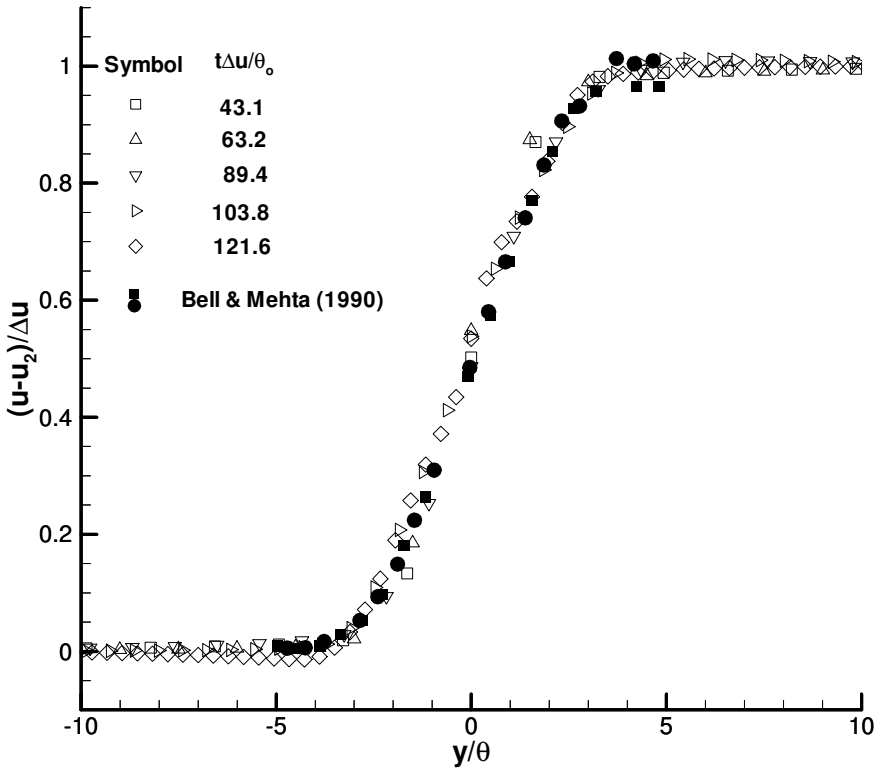

Fig. 6.4. Profiles of mean streamwise velocity.

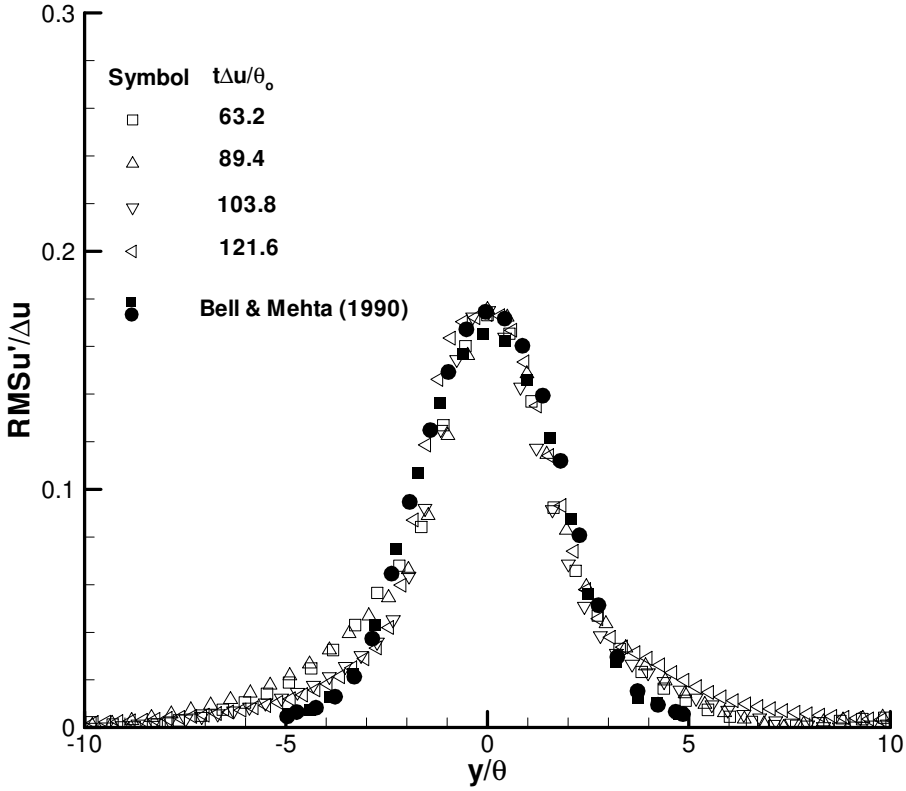

Fig. 6.5. Profiles of root mean square streamwise velocity fluctuations.

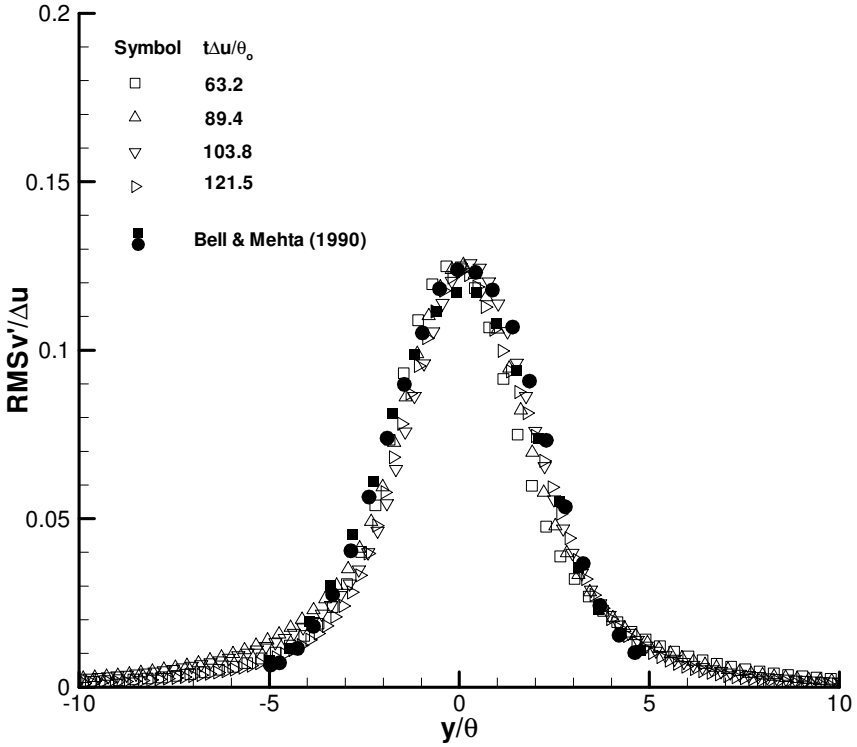

Fig. 6.6. Profiles of root mean square cross-stream velocity fluctuations.

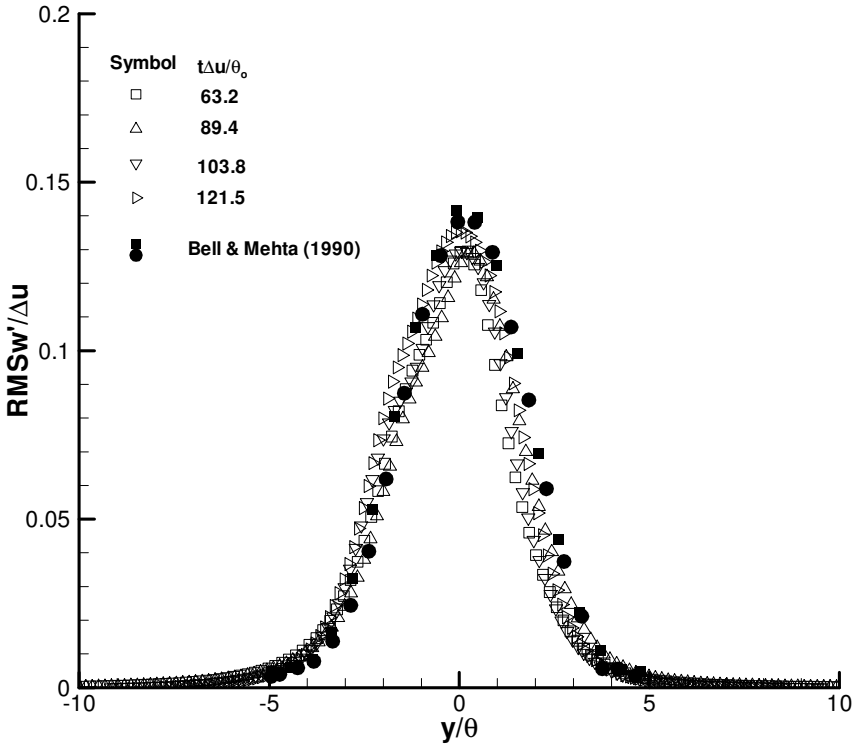

Fig. 6.7. Profiles of root mean square spanwise velocity fluctuations.

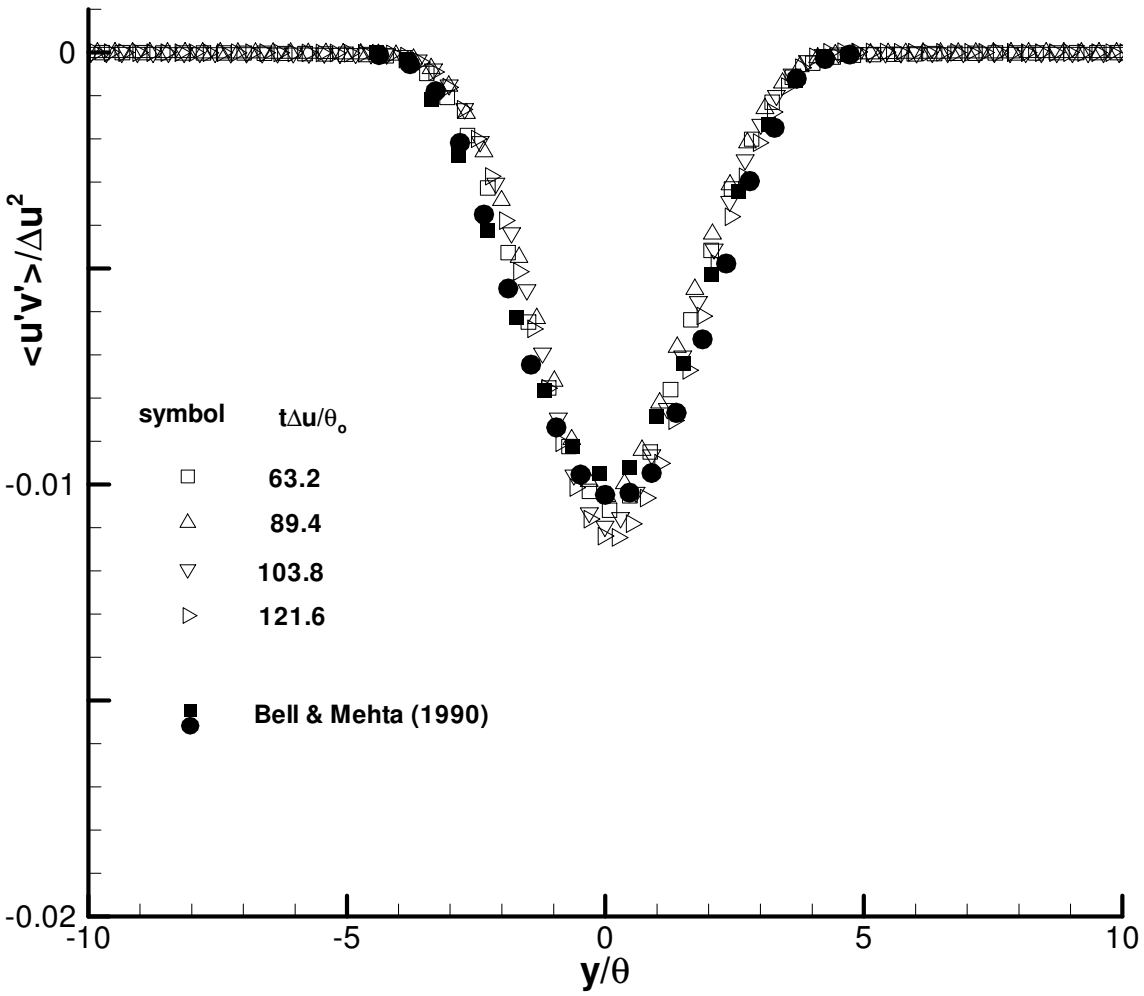

Fig. 6.8. Profiles of cross-correlation *u'v'*.

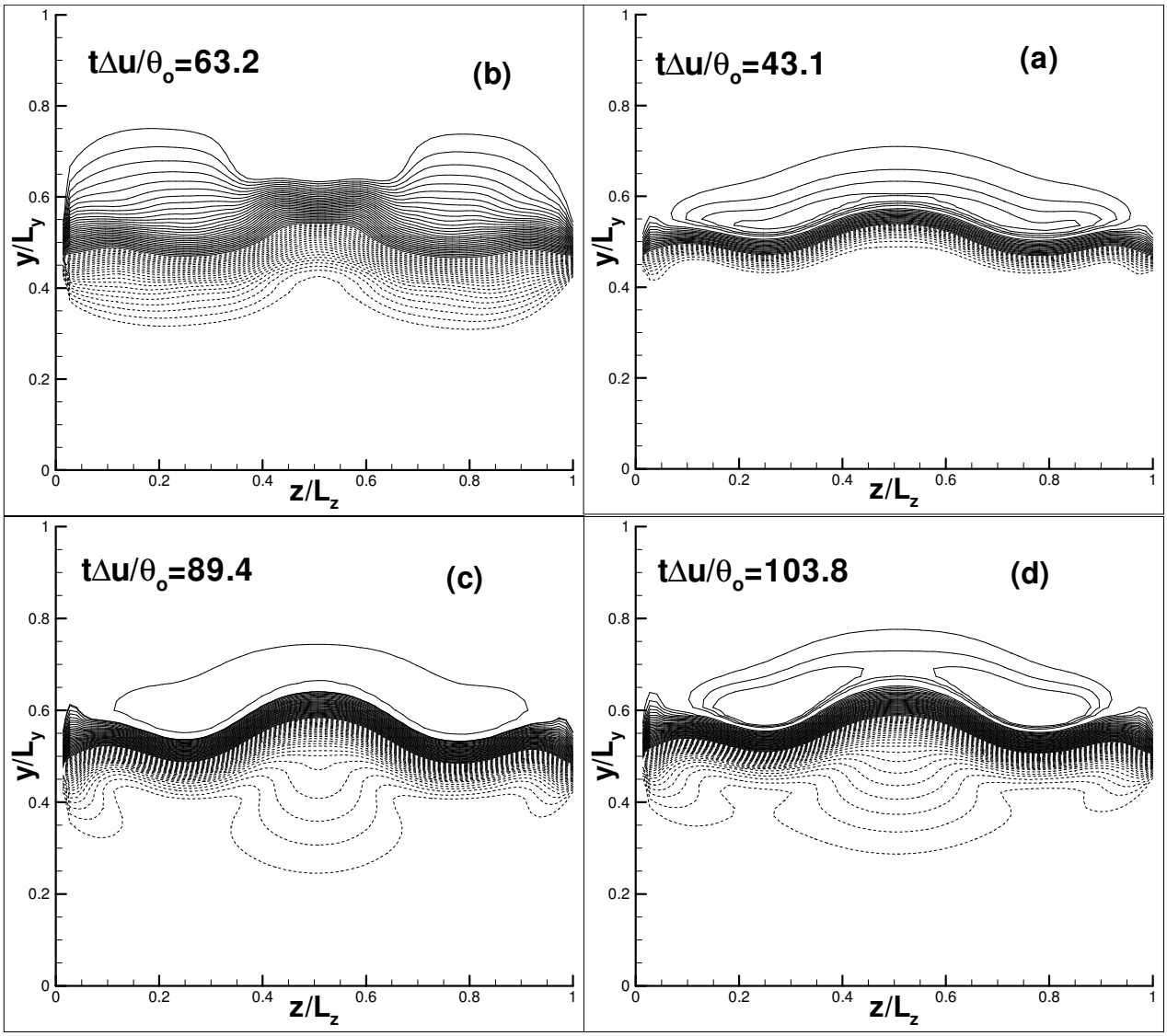

Fig. 6.9. Streamwise velocity contours showing flow three dimensionality at four times (a) $t\Delta u/\theta_o$=43.1, (b) $t\Delta u/\theta_o$=63.2, (c) $t\Delta u/\theta_o$=89.4 *and* (d) $t\Delta u/\theta_o$=103.8. Thirty equally distributed contour levels are used between u_{min} and u_{max}. Dotted lines represent negative velocity and continuous lines represent positive velocity.

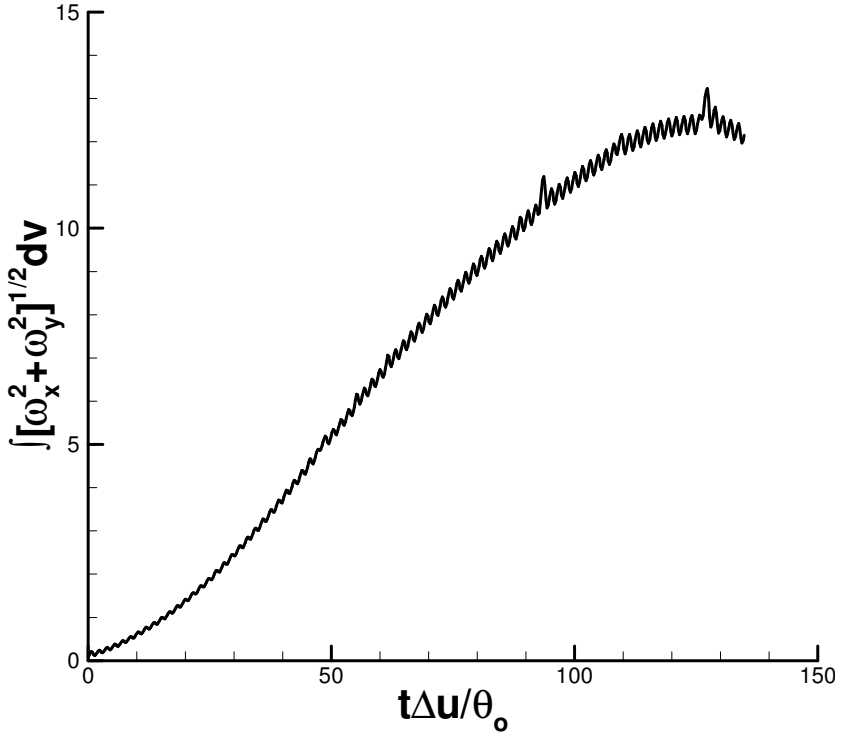

Fig. 6.10 Temporal growth of streamwise and spanwise vorticity.

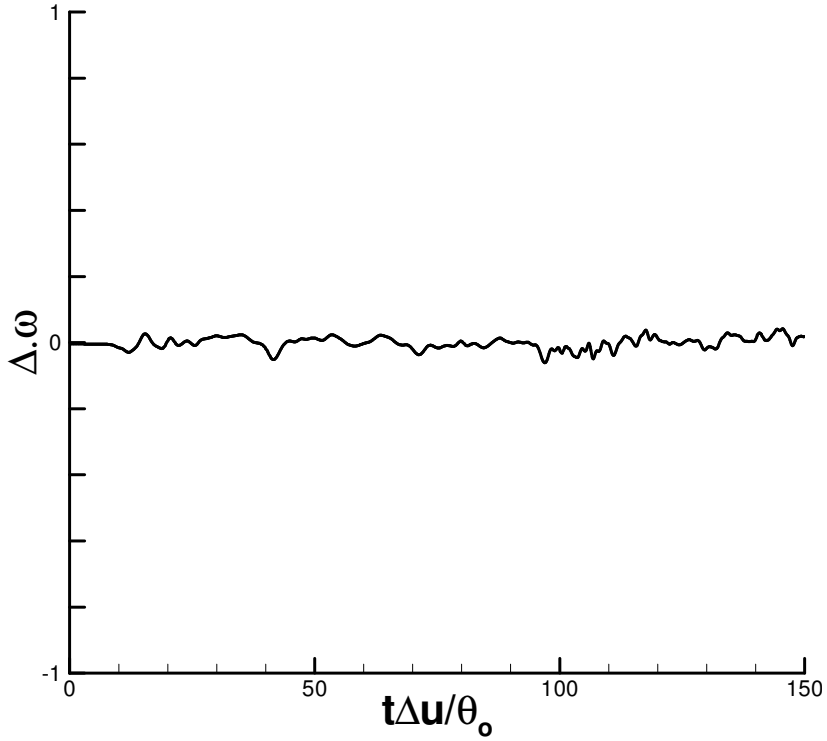

Fig. 6.11. Temporal evolution of vorticity divergence.

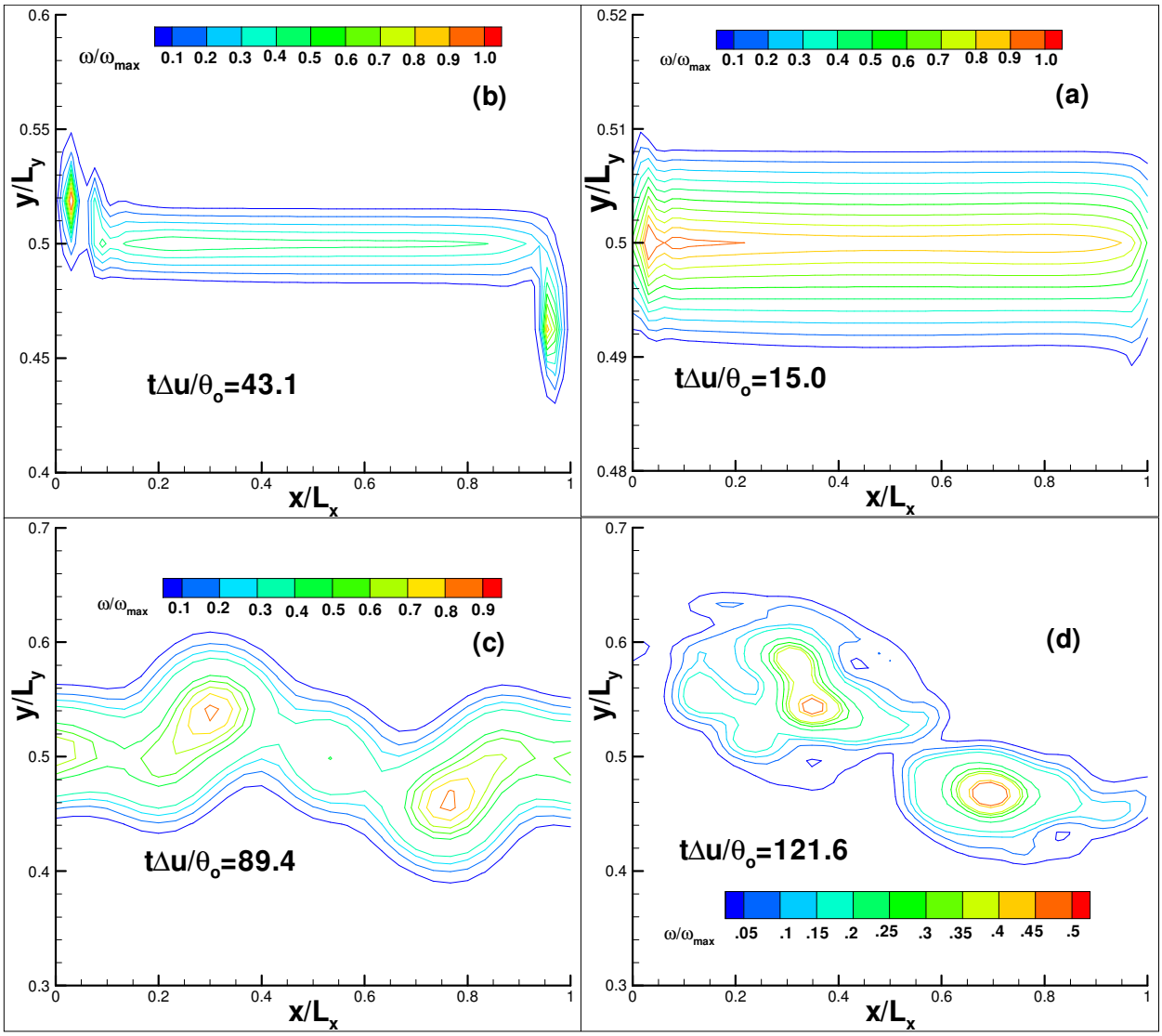

Fig. 6.12. Development of spanwise vorticity contours at the mid plane (z/L_z=0.5) at four times (a) $t\Delta u/\theta_o$=15.0, (b) $t\Delta u/\theta_o$=43.1, (c) $t\Delta u/\theta_o$=89.4 *and* (d) $t\Delta u/\theta_o$=121.6.

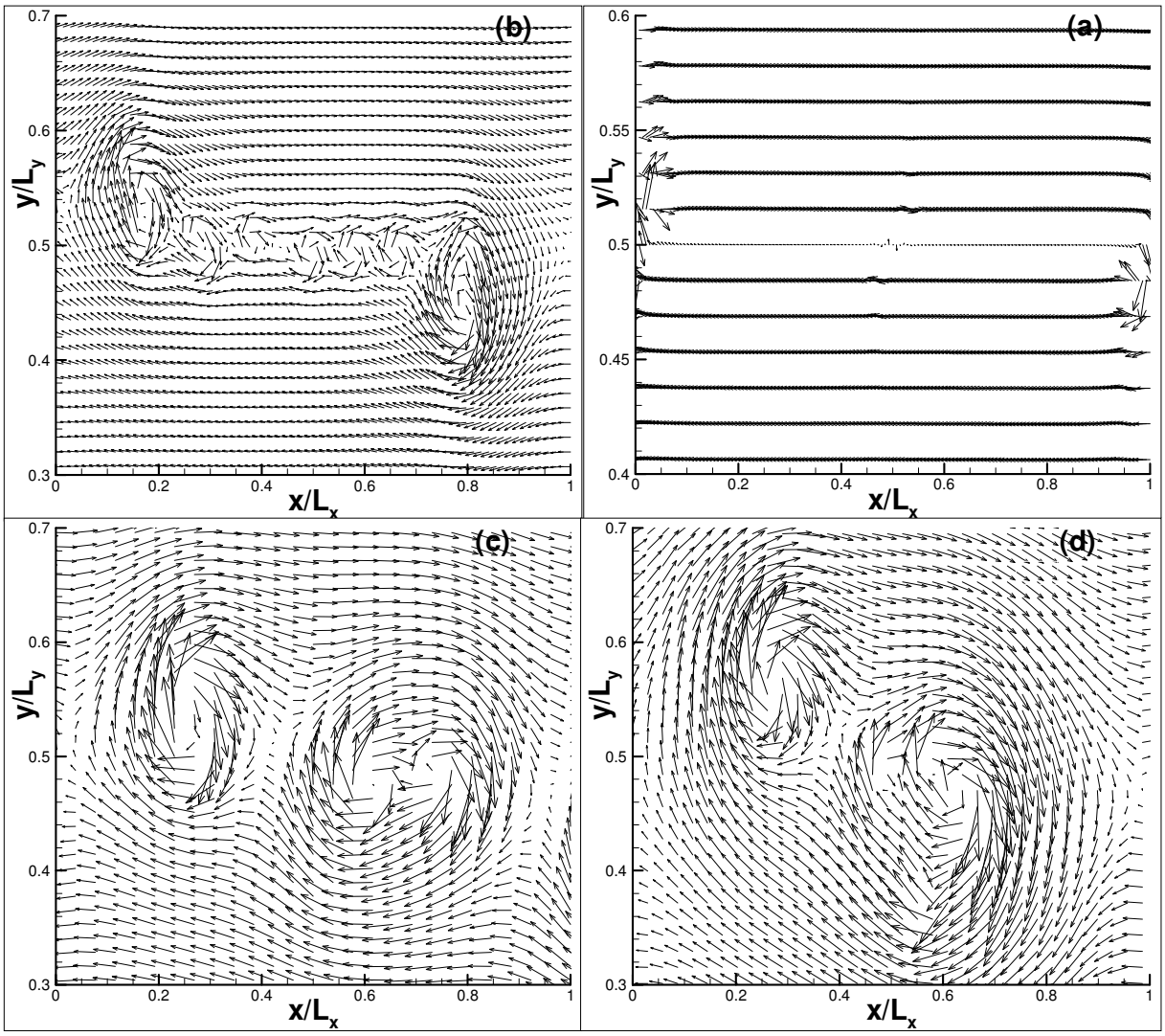

Fig 6.13. Projection of velocity vector field (u,v) on x-y plane. Times and locations correspond to that of figure 6.12

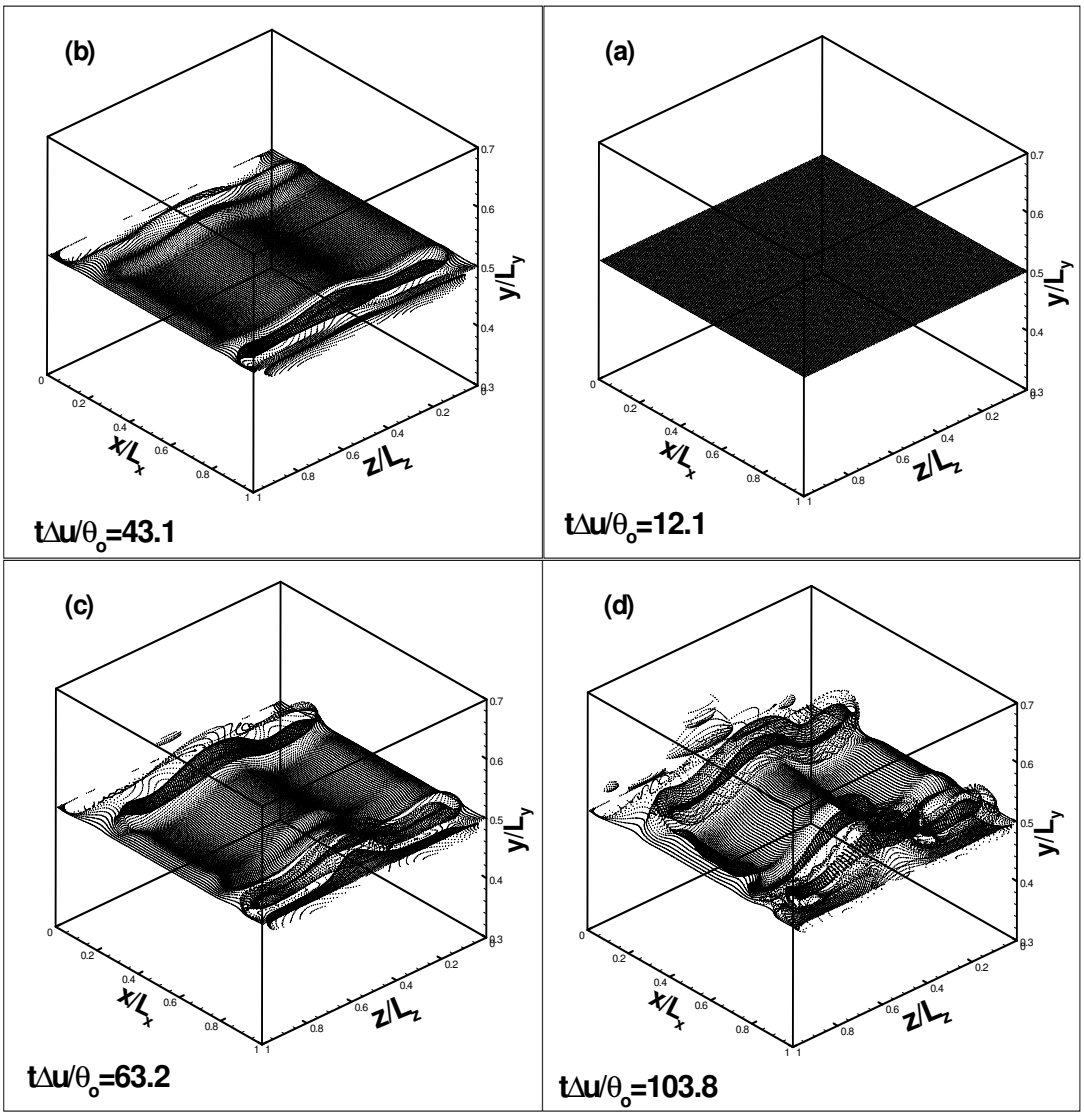

Fig. 6.14. Three dimensional perspectives of the particle field at four times (a) $t\Delta u/\theta_o$=43.1, (b) $t\Delta u/\theta_o$=63.2, (c) $t\Delta u/\theta_o$=89.4 *and* (d) $t\Delta u/\theta_o$=103.8

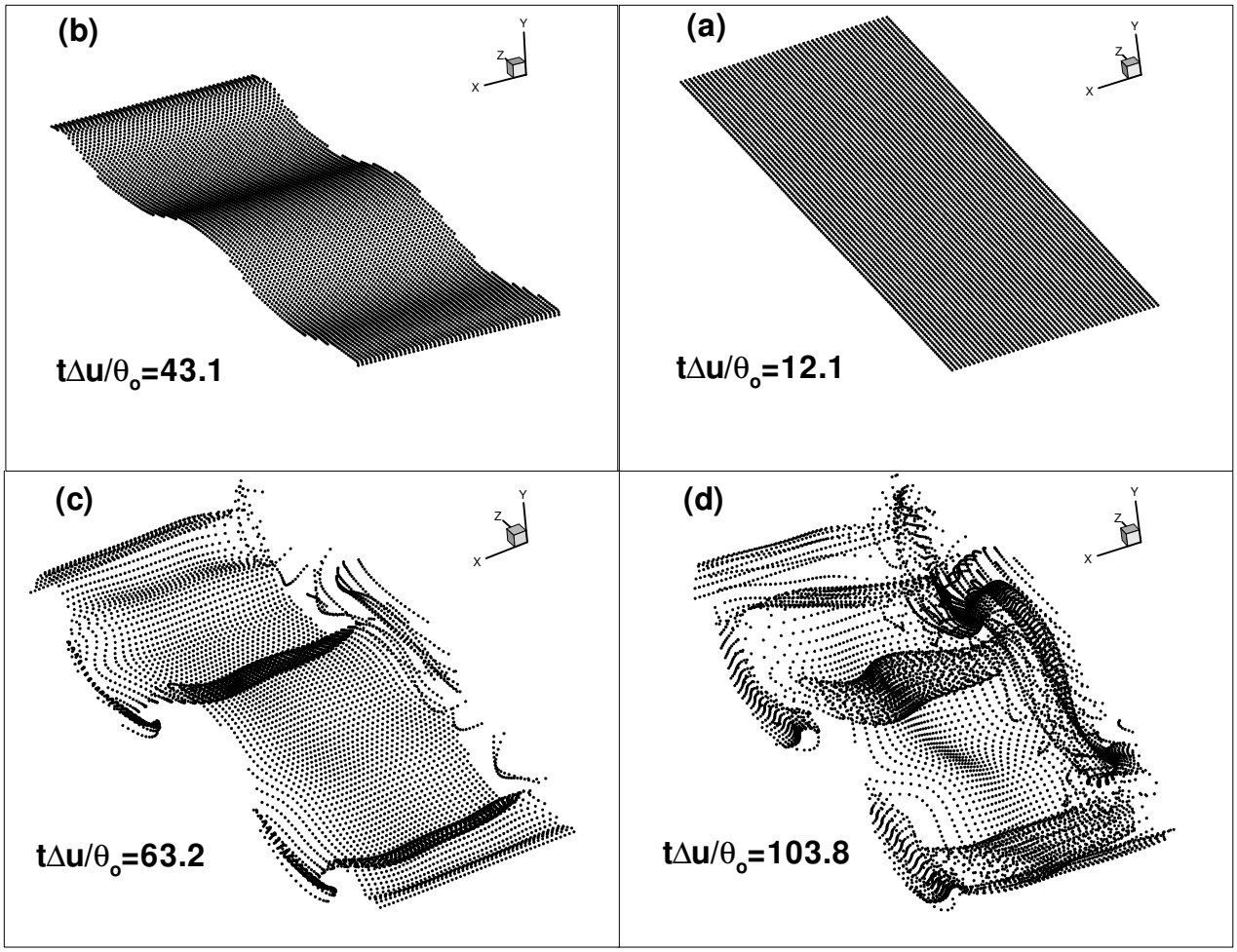

Fig. 6.15. Magnified view of the particle field for $0.3 \leq x/L_x \leq 0.7$ at the same times of figure 6.14.

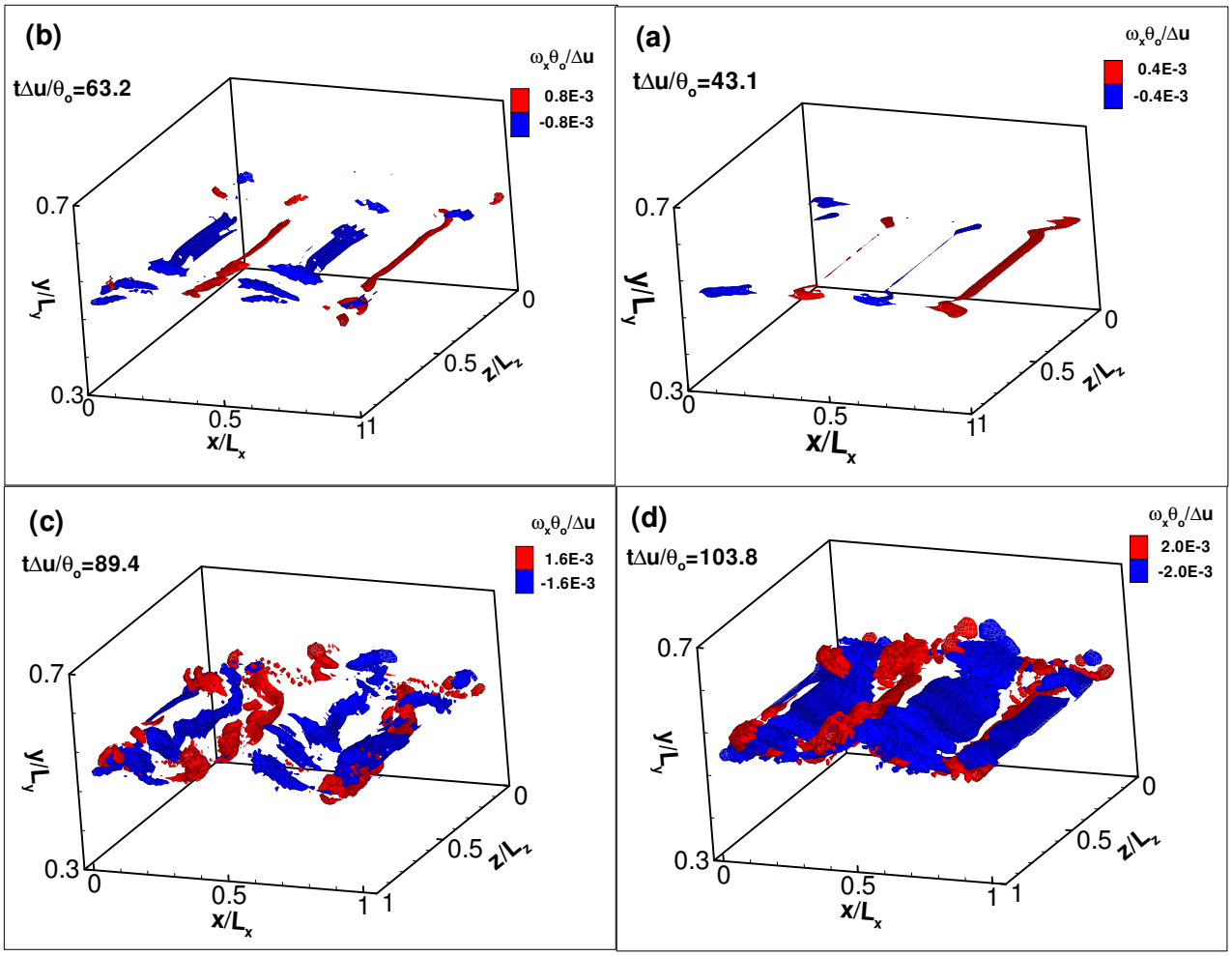

Fig. 6.16. Growth of streamwise vorticity at four times (a) $t\Delta u/\theta_o$=43.1, (b) $t\Delta u/\theta_o$=63.2, (c) $t\Delta u/\theta_o$=89.4 *and* (d) $t\Delta u/\theta_o$=103.8.

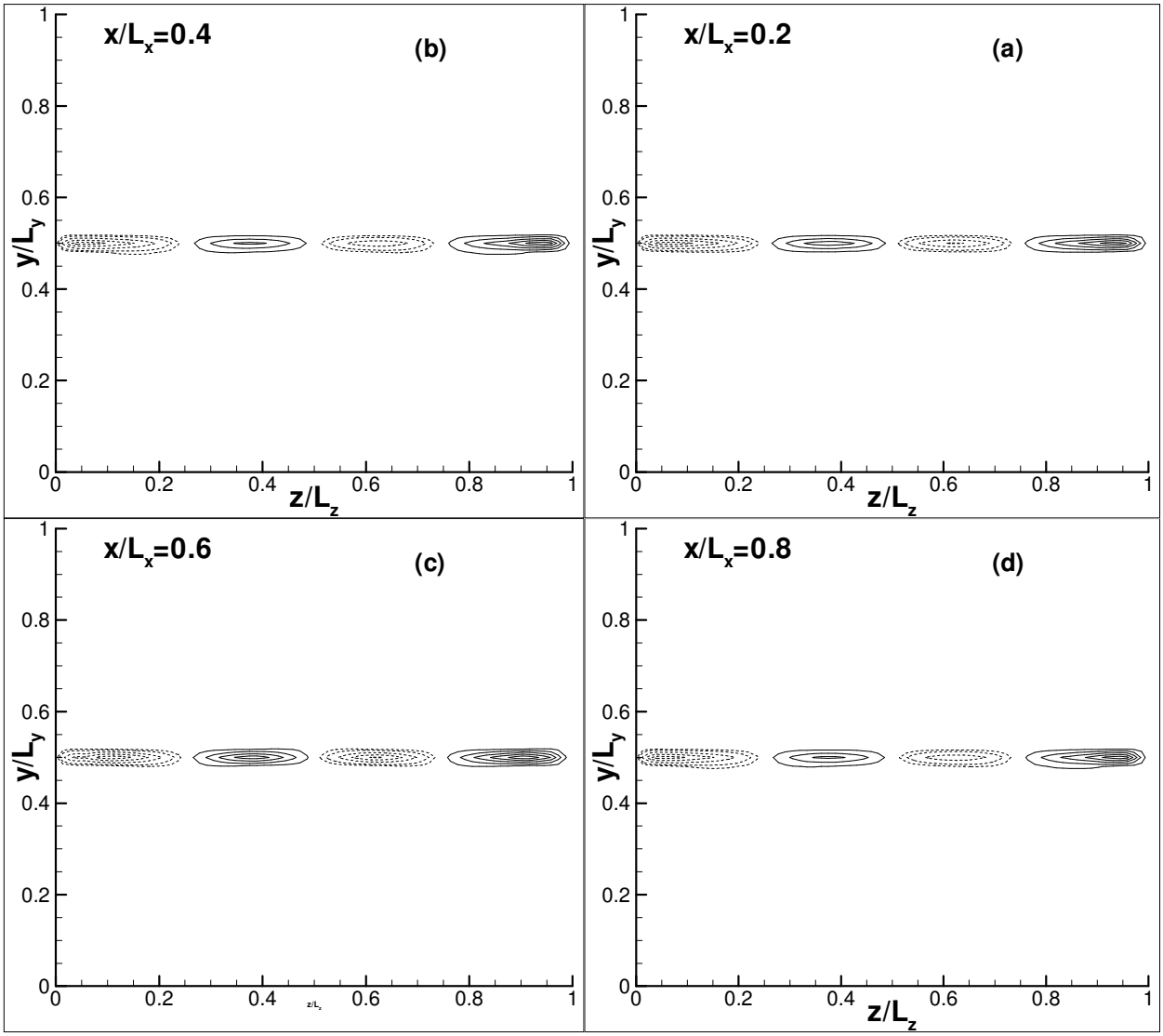

Fig. 6.17. Streamwise vorticity contours at $t\Delta u/\theta_o$=43. 8 and four streamwise locations (a)x/L_x=0.2, (b)x/L_x=0.4 , (c)x/L_x=0.6 , (d)x/L_x=0.8. Twenty equally distributed contour levels with 0.05 $(\omega_{max}- \omega_{min})$ increments are used. Dotted lines represent negative vorticity and continuous lines represent positive vorticity.

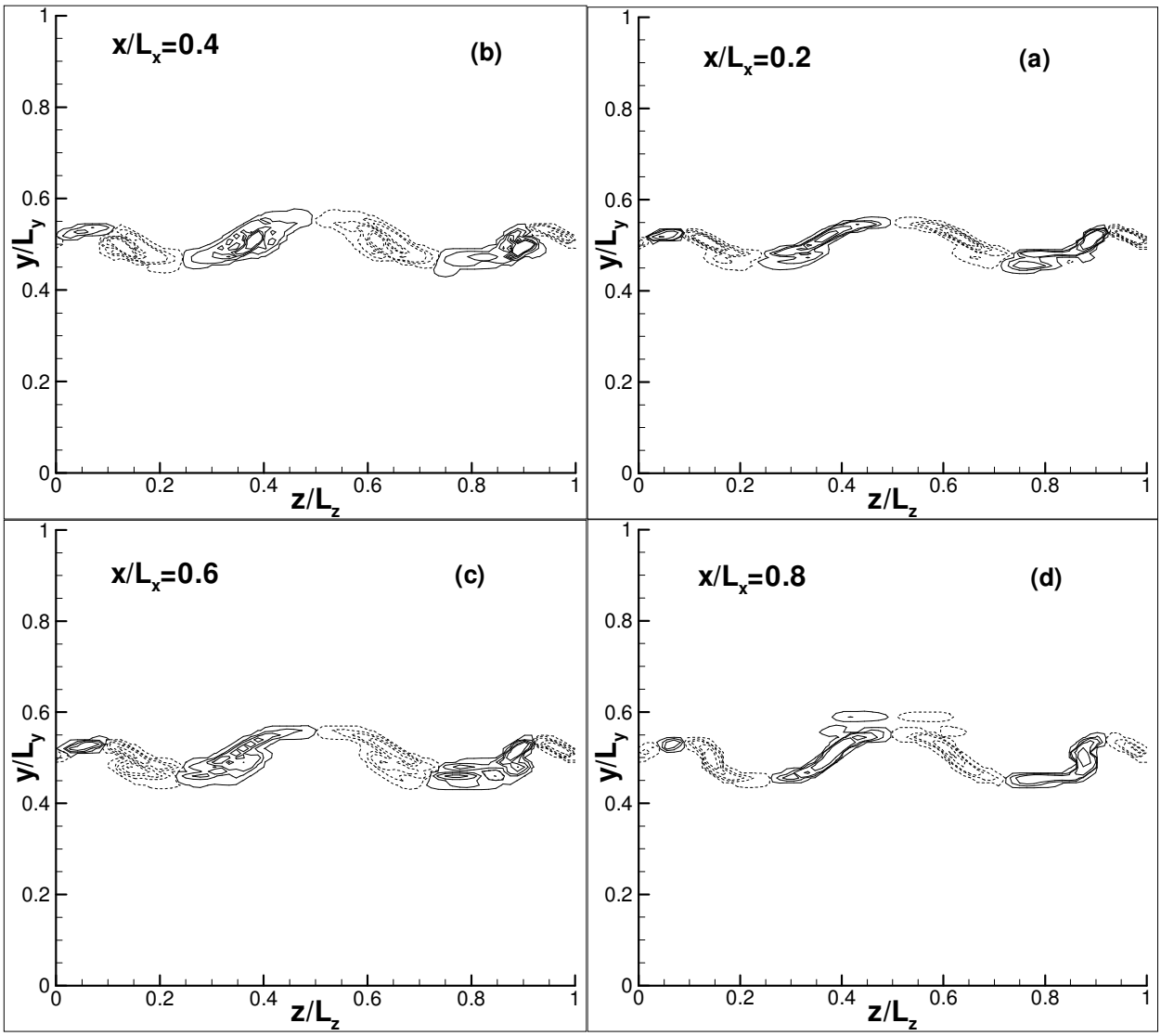

Fig. 6.18. Streamwise vorticity contours at $t\Delta u/\theta_o$=63.28 and four streamwise locations (a)x/L_x=0.2, (b)x/L_x=0.4 , (c)x/L_x=0.6 , (d)x/L_x=0.8. Twenty equally distributed contour levels with 0.05 $(\omega_{max}- \omega_{min})$ increments are used. Dotted lines represent negative vorticity and continuous lines represent positive vorticity.

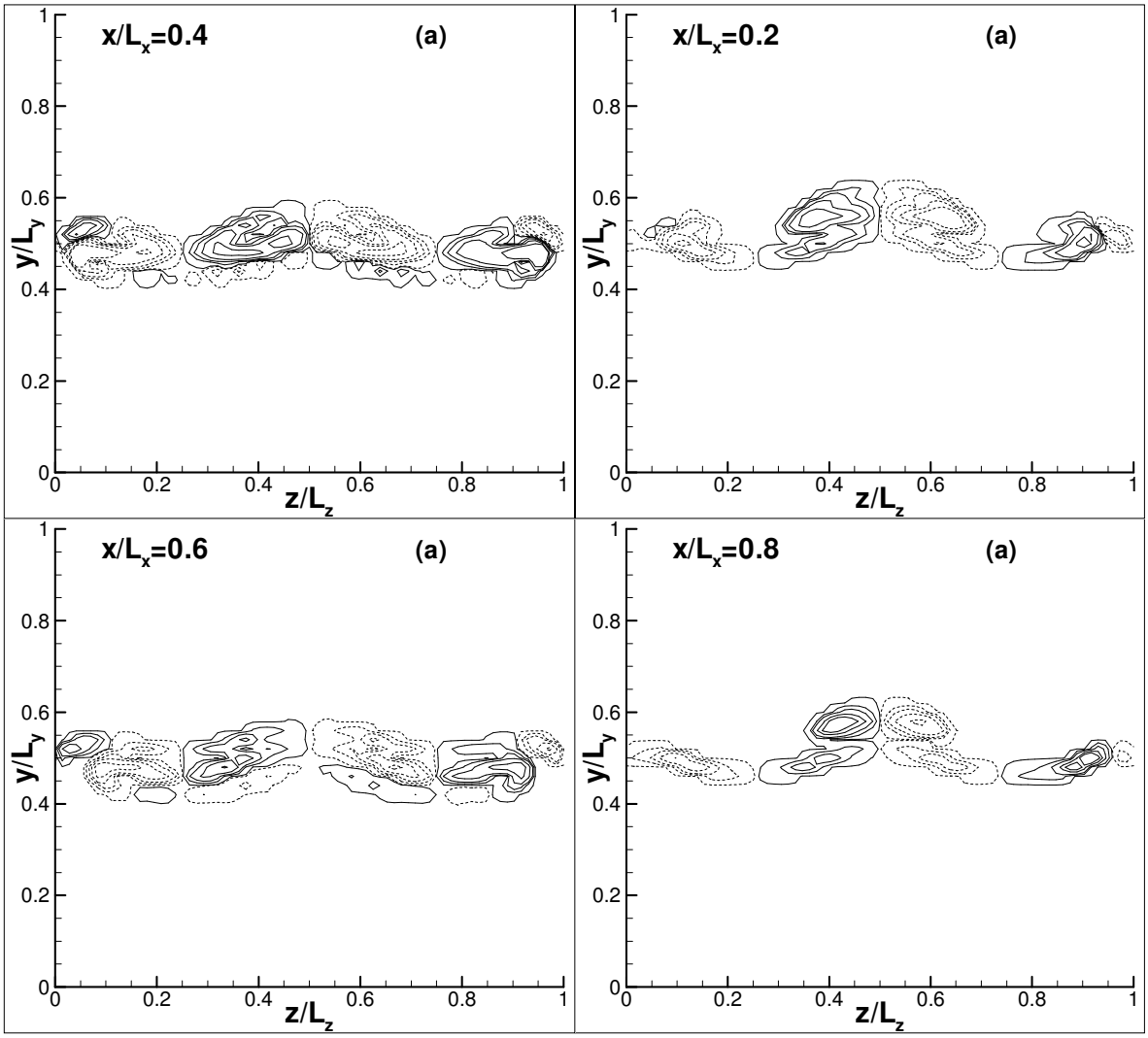

Fig. 6.19. Streamwise vorticity contours at $t\Delta u/\theta_o$=103.8 and four streamwise locations (a)x/L_x=0.2, (b)x/L_x=0.4 , (c)x/L_x=0.6 , (d)x/L_x=0.8. Twenty equally distributed contour levels with 0.05 $(\omega_{max}- \omega_{min})$ increments are used. Dotted lines represent negative vorticity and continuous lines represent positive vorticity.

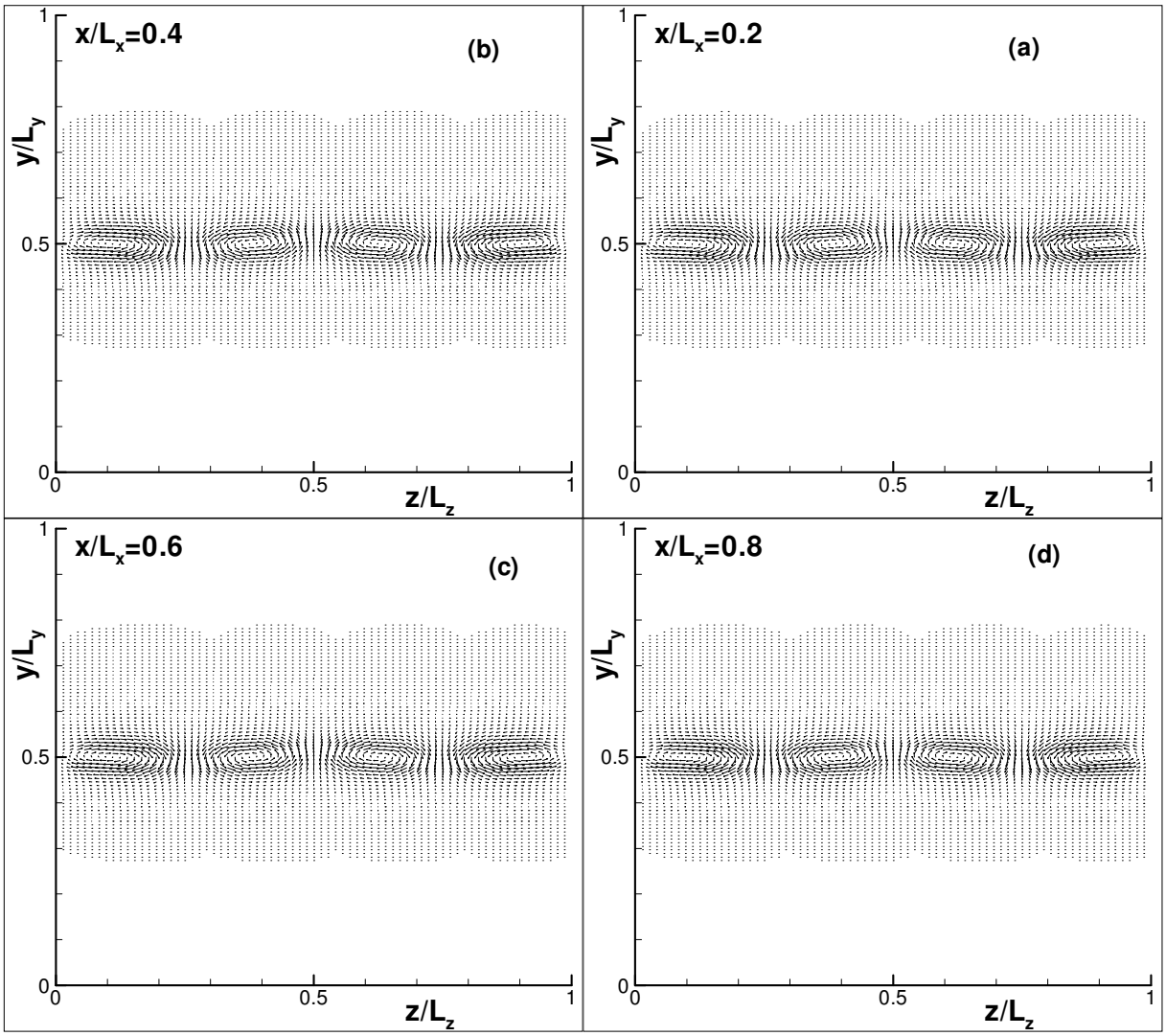

Fig. 6.20. Projection of velocity vector field (v,w) on y-z plane at $t\Delta u/\theta_o$=43.1 *8* and four streamwise locations (a)x/L_x=0.2, (b)x/L_x=0.4 , (c)x/L_x=0.6 , (d)x/L_x=0.8.

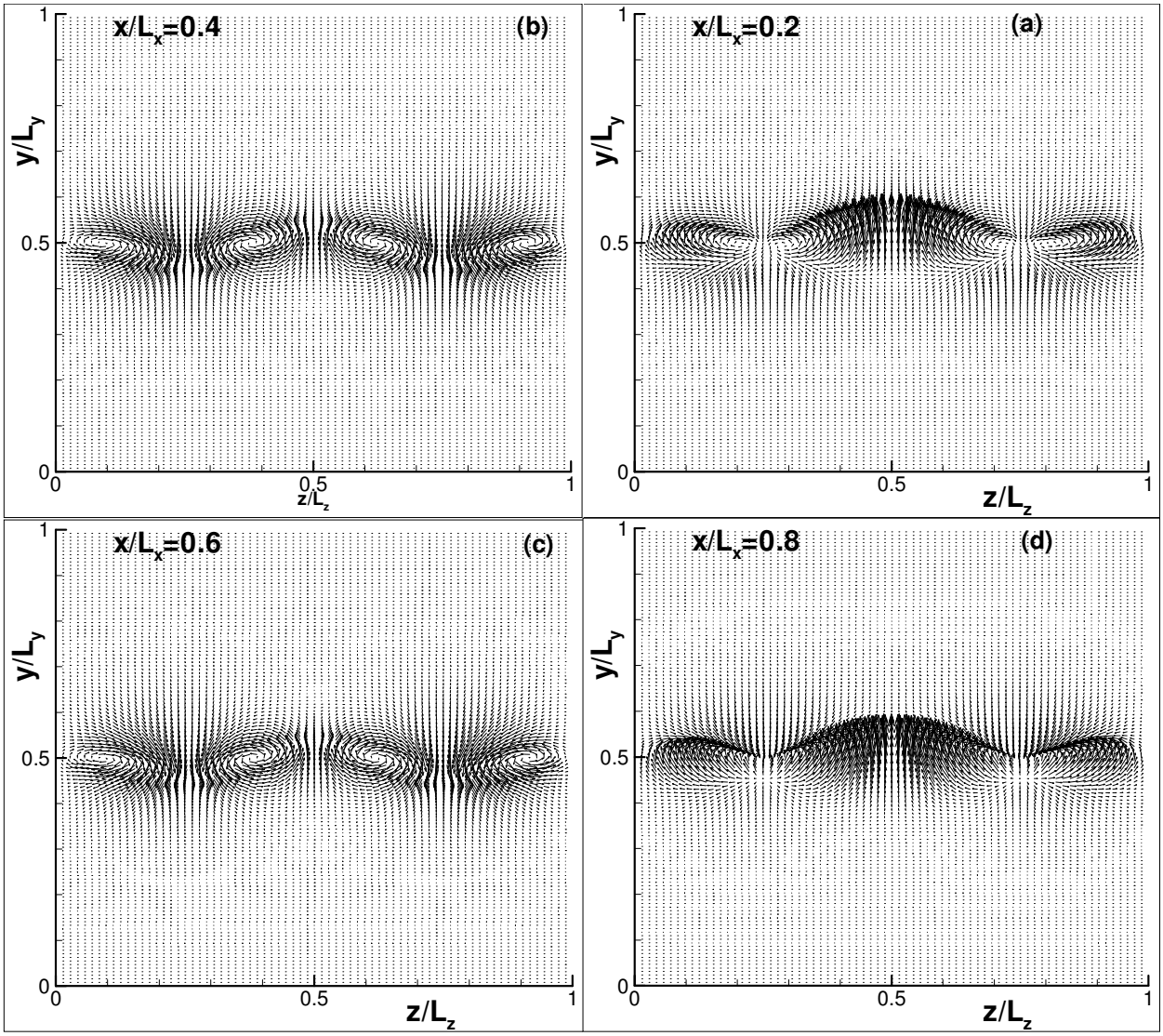

Fig. 6.21. Projection of velocity vector field (v,w) on y-z plane at $t\Delta u/\theta_o$=63.1 and four streamwise locations (a)x/L_x=0.2, (b)x/L_x=0.4 , (c)x/L_x=0.6 , (d)x/L_x=0.8.

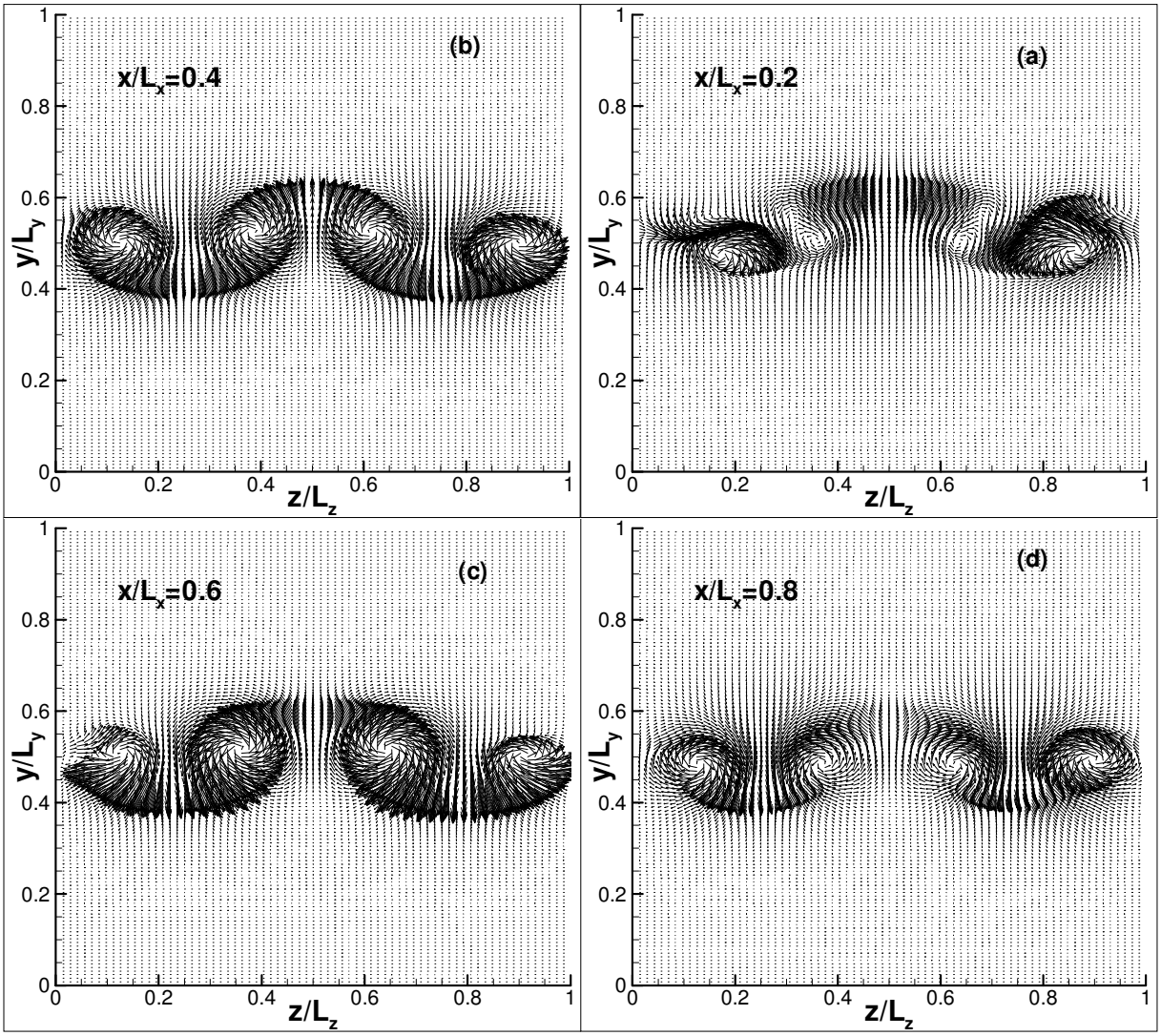

Fig. 6.22. Projection of velocity vector field (v,w) on y-z plane at $t\Delta u/\theta_o$=103.8 and four streamwise locations (a)x/L_x=0.2, (b)x/L_x=0.4 , (c)x/L_x=0.6 , (d)x/L_x=0.8.

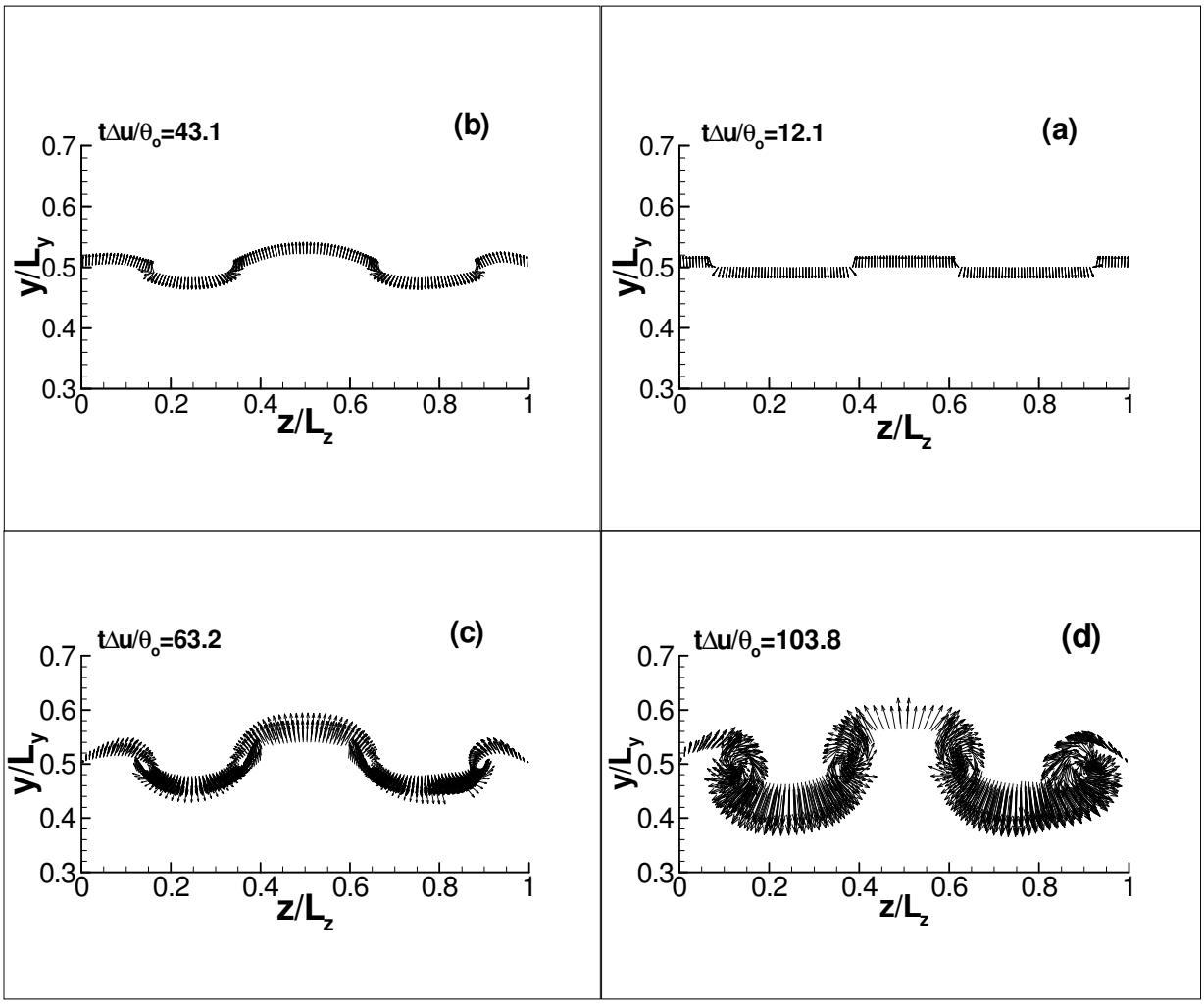

Fig. 6.23. Projection of particle velocity field (v,w) on y-z plane of one grid size thick slice at x/L_x=0.6 at four times (a) $t\Delta u/\theta_o$=12.1, (b) $t\Delta u/\theta_o$=43.1, (c) $t\Delta u/\theta_o$=63.2 and (d) $t\Delta u/\theta_o$=103.8.

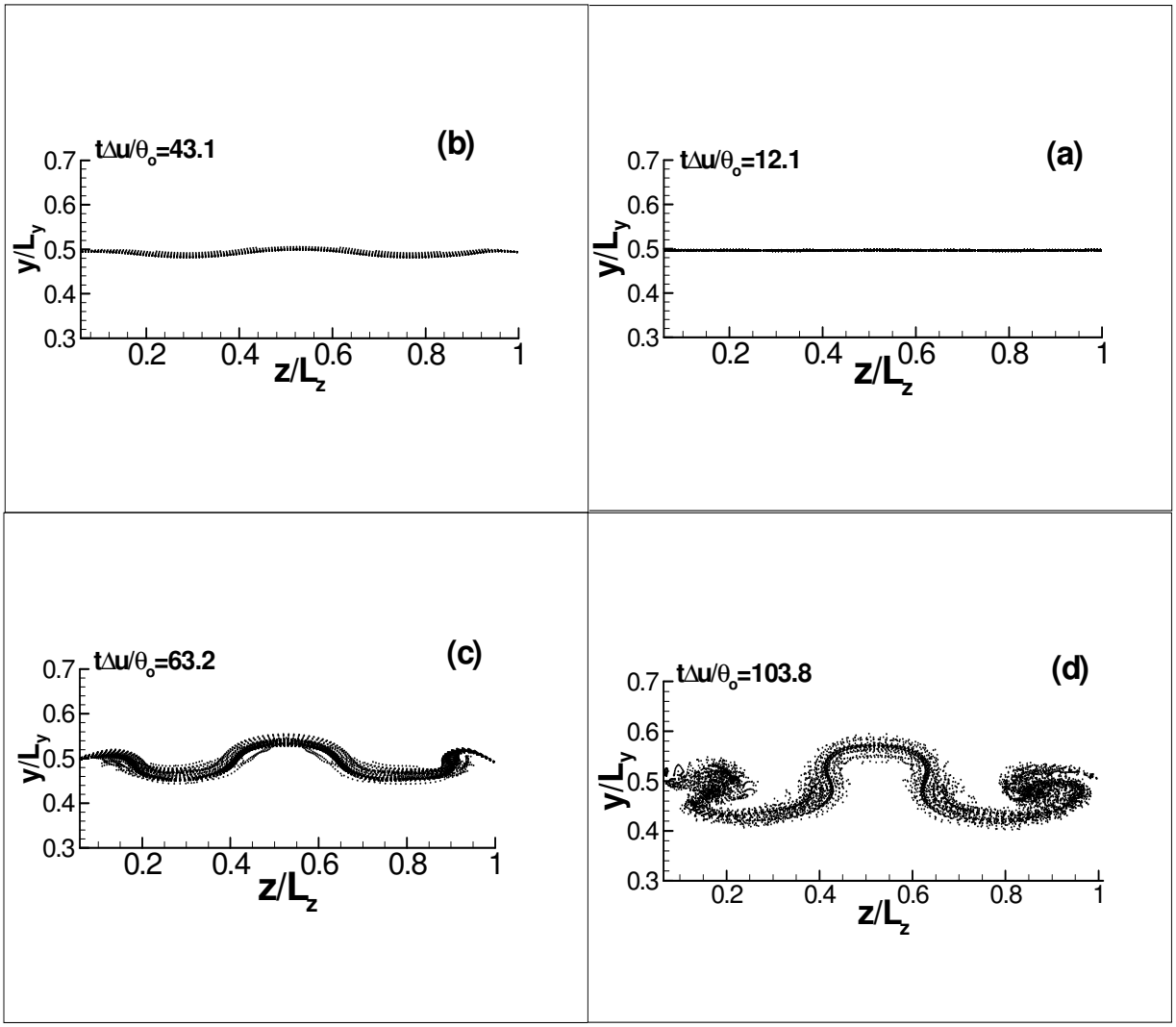

Fig. 6.24. Projection of particle location on y-z plane of one grid size thick slice at x/L_x=0.6 at four times (a) $t\Delta u/\theta_o$=12.1, (b) $t\Delta u/\theta_o$=43.1, (c) $t\Delta u/\theta_o$=63.2 *and* (d) $t\Delta u/\theta_o$=103.8.

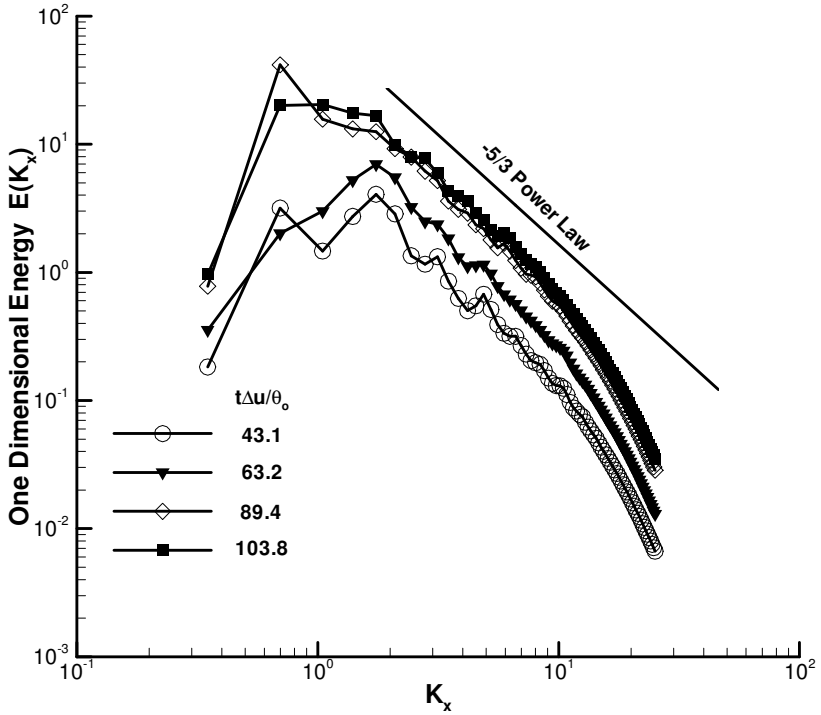

Fig. 6.25. Temporal Development of one dimensional streamwise energy spectrum at four times (a) $t\Delta u/\theta_o$=43.1, (b) $t\Delta u/\theta_o$=63.2, (c) $t\Delta u/\theta_o$=89.4, and (d) $t\Delta u/\theta_o$=103.8. Continuous line represents the -5/3 power law.

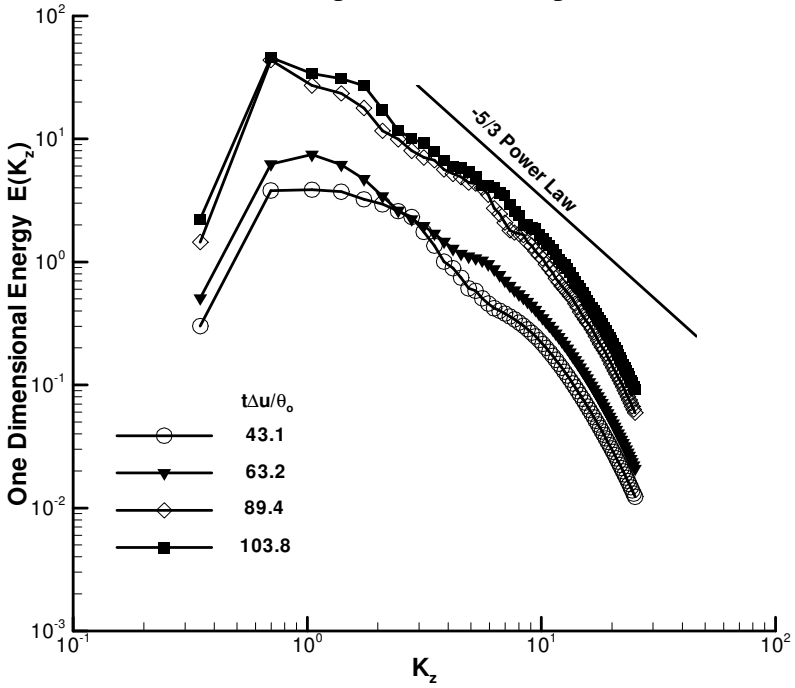

Fig. 6.26 Temporal Development of one dimensional spanwise energy spectrum at four times (a) $t\Delta u/\theta_o$=43.1, (b) $t\Delta u/\theta_o$=63.2, (c) $t\Delta u/\theta_o$=89.4, and (d) $t\Delta u/\theta_o$=103.8. Continuous line represents the -5/3 power law.

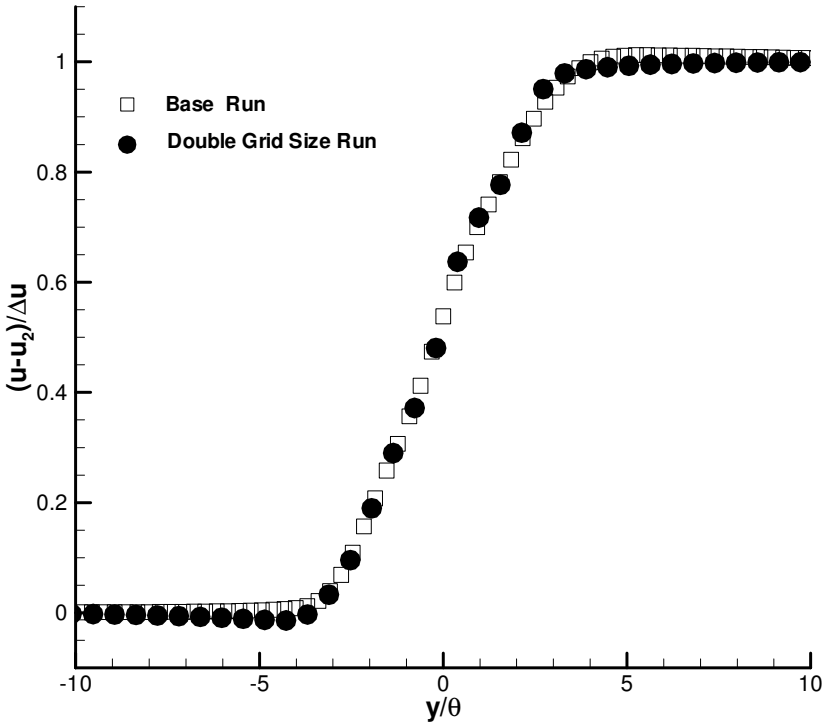

Fig. 6.27. Sensitivity of mean velocity profile to grid size at $t\Delta u/\theta_o$=89.4.

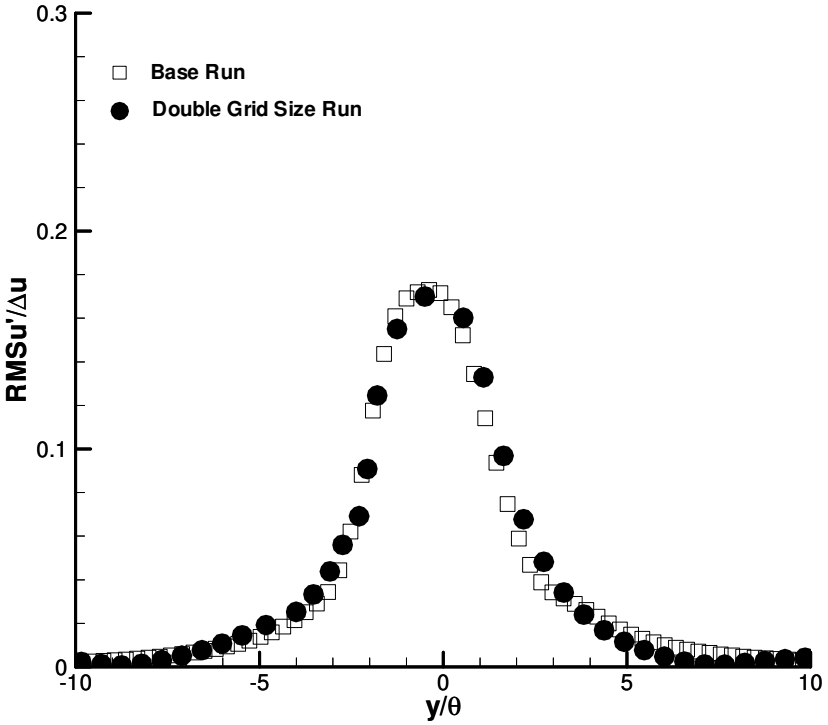

Fig. 6.28. Sensitivity of root mean square streamwise velocity fluctuations to grid size at $t\Delta u/\theta_o$=89.4.

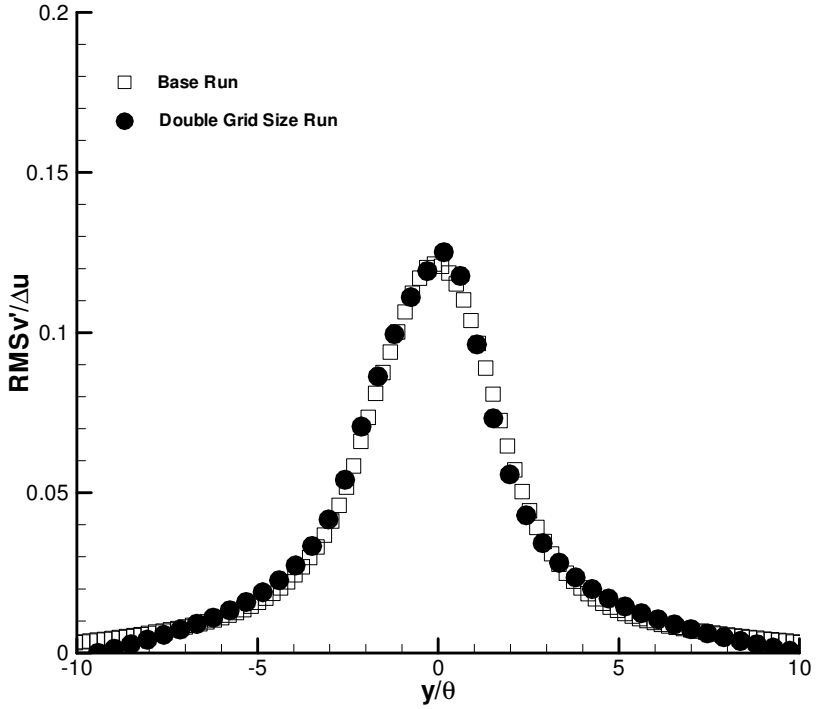

Fig. 6.29. Sensitivity of root mean square cross-stream velocity fluctuations to grid size at $t\Delta u/\theta_o$=89.4.

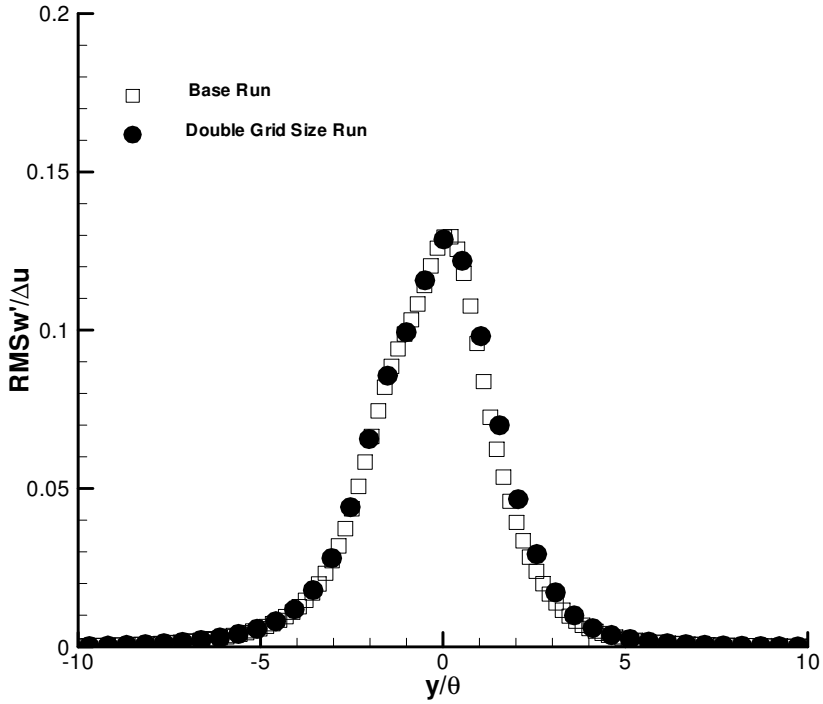

Fig. 6.30. Sensitivity of root mean square spanwise velocity fluctuations to grid size at $t\Delta u/\theta_o$=89.4.

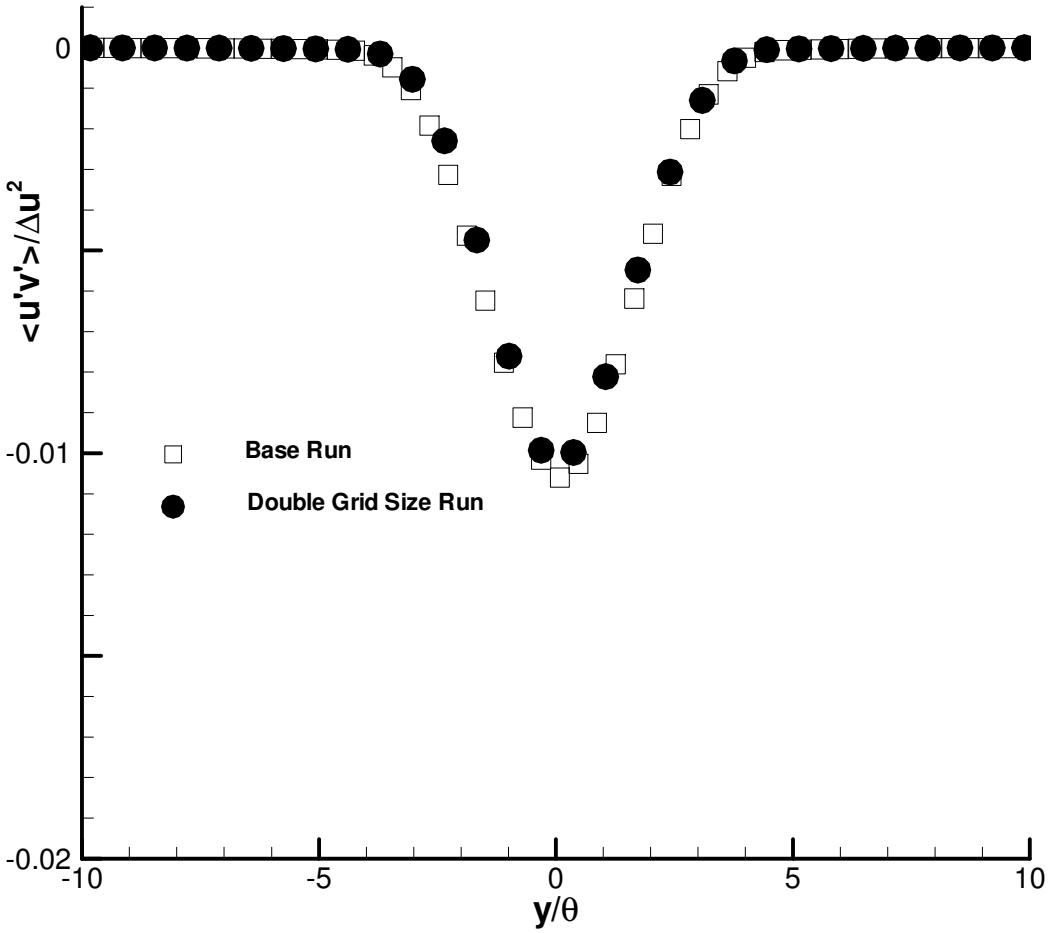

Fig. 6.31. Sensitivity of cross correlation $u'v'$ to grid size at $t\Delta u/\theta_o$=89.4.

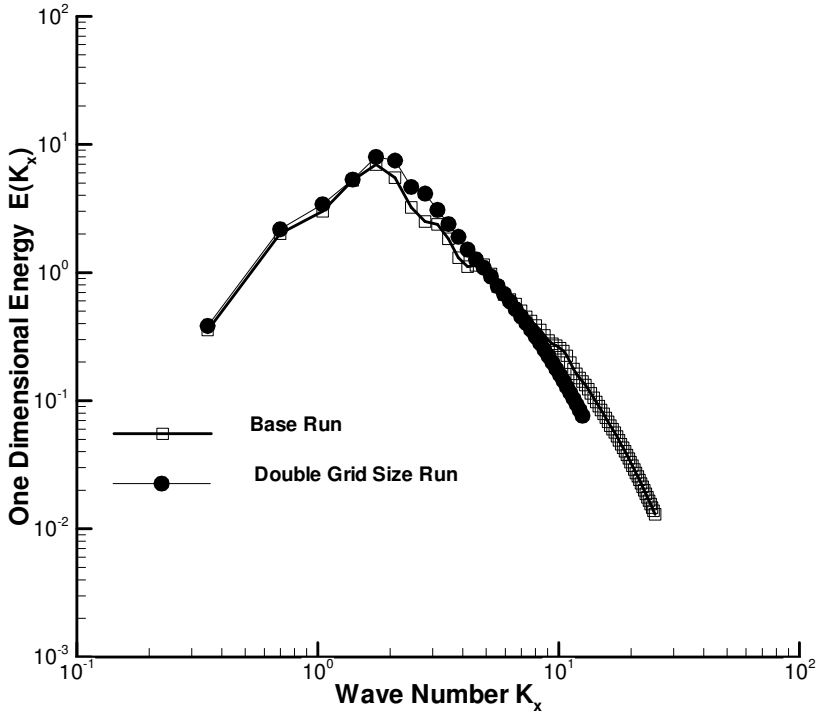

Fig. 6.32. Sensitivity of streamwise energy spectrum to grid size at $t\Delta u/\theta_o$=89.4.

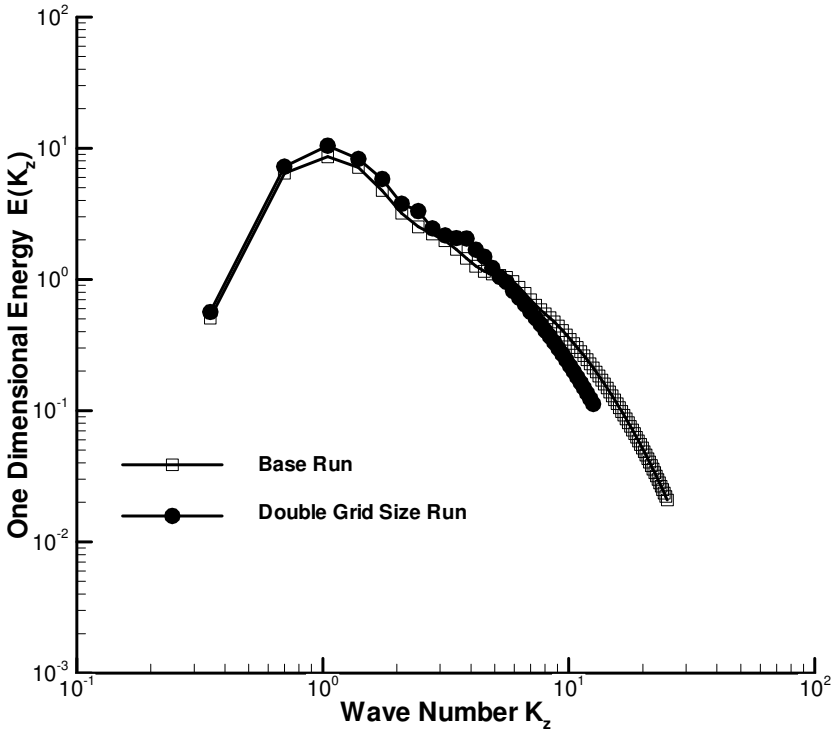

Fig. 6.33 Sensitivity of spanwise energy spectrum to grid size at $t\Delta u/\theta_o$=89.4.

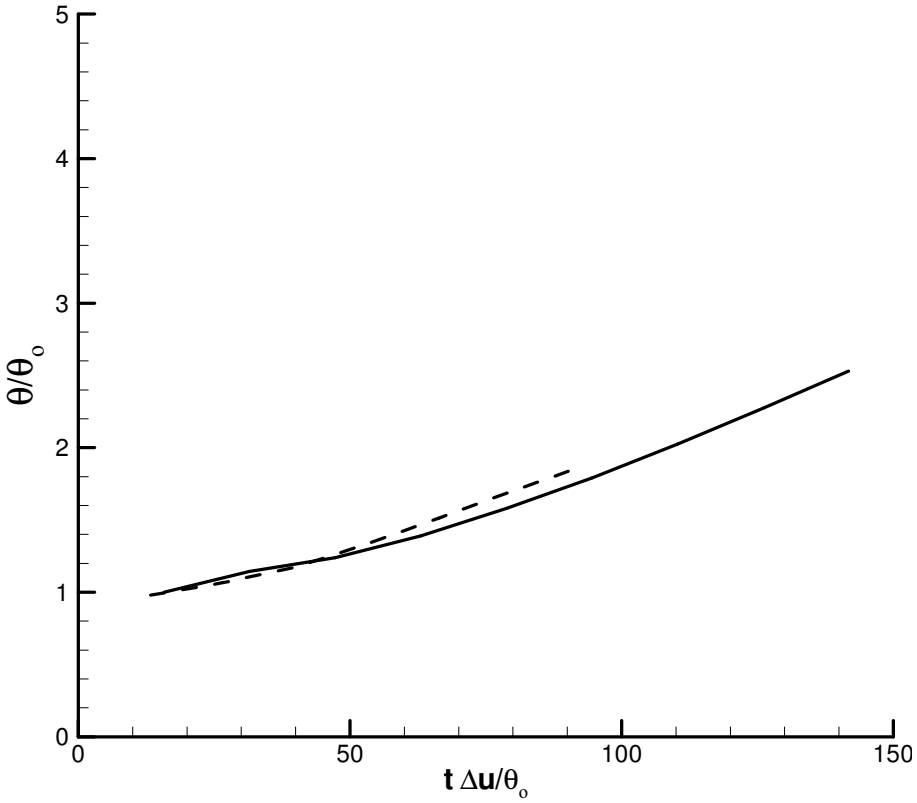

Fig. 6.34 Temporal growth of momentum thickness. ----- (invisid run), _____ (viscous run)

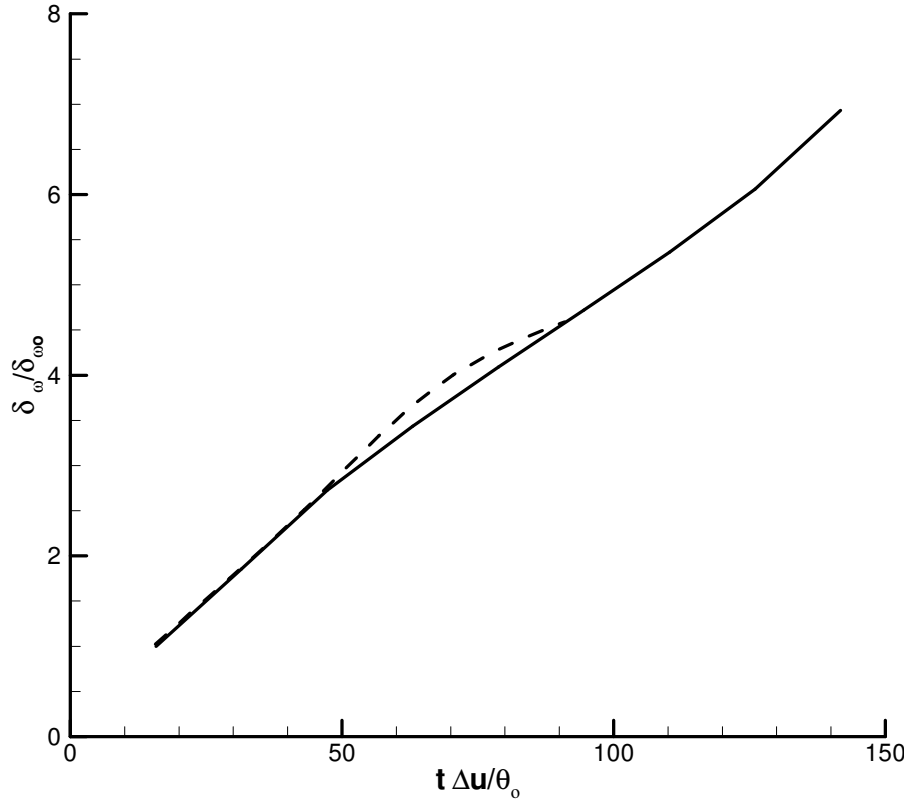

Fig. 6.35 Temporal growth of vorticity thickness. ---------- (invisid run), _____ (viscous run)

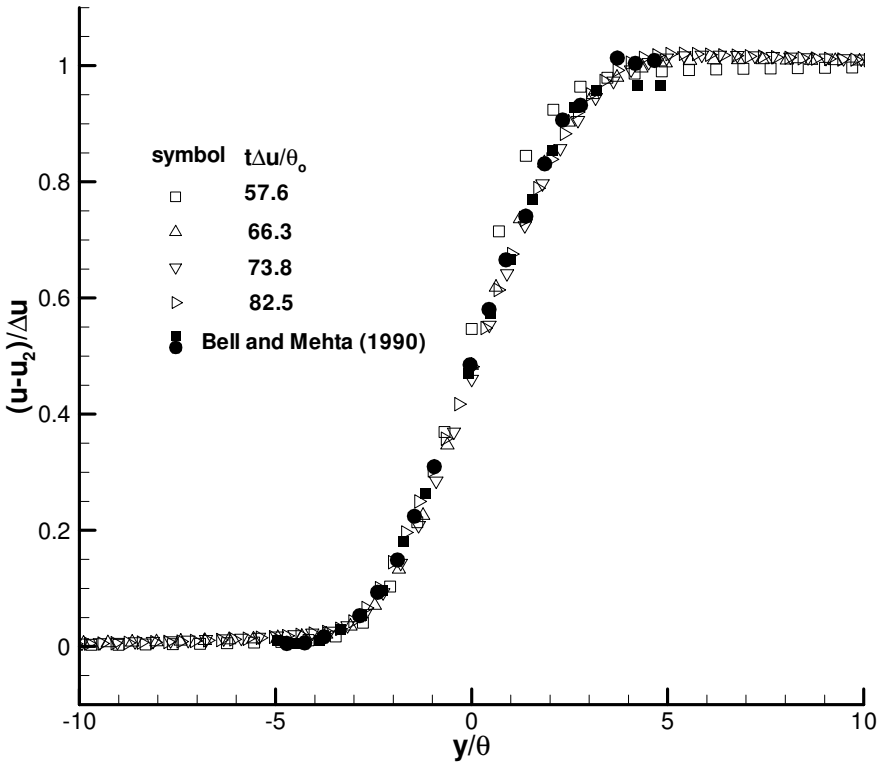

Fig. 6.36. Profiles of mean streamwise velocity in inviscid run at four times.

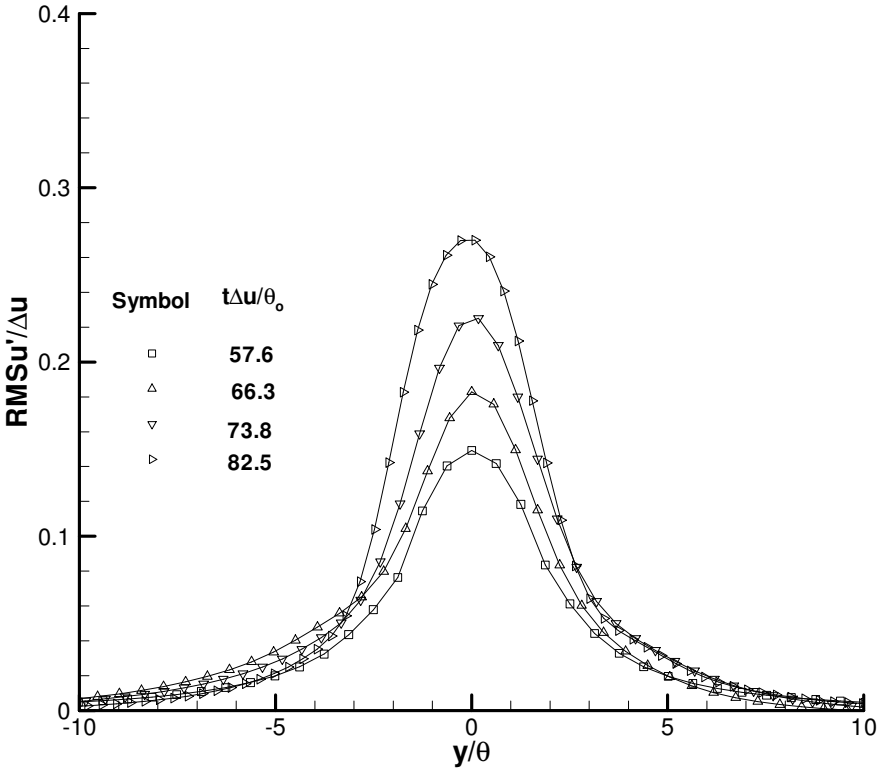

Fig. 6.37. Temporal evolution of root mean square streamwise velocity fluctuations in inviscid run at four times.

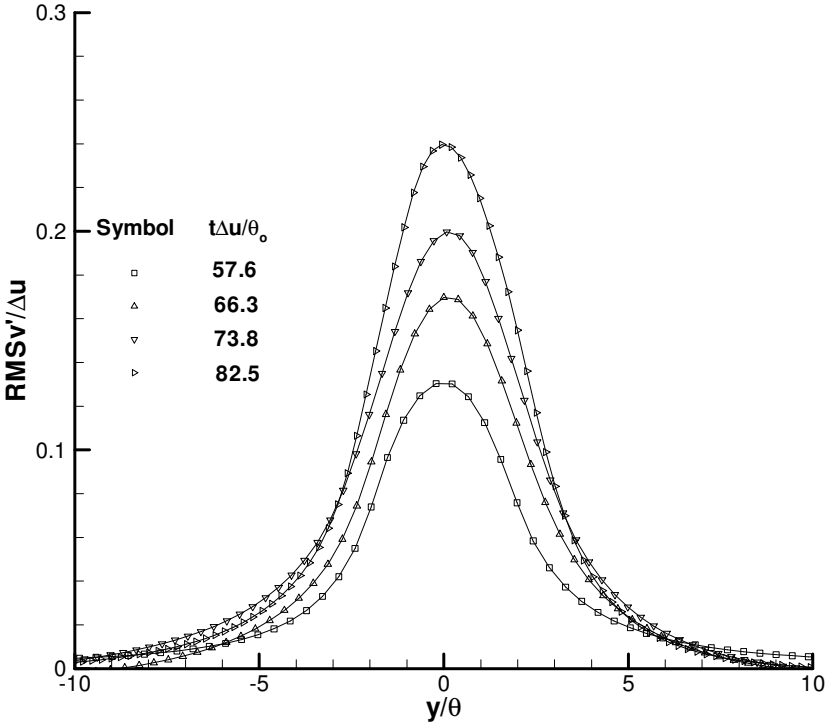

Fig. 6.38. Temporal evolution of root mean square cross-stream velocity fluctuations in inviscid run at four times.

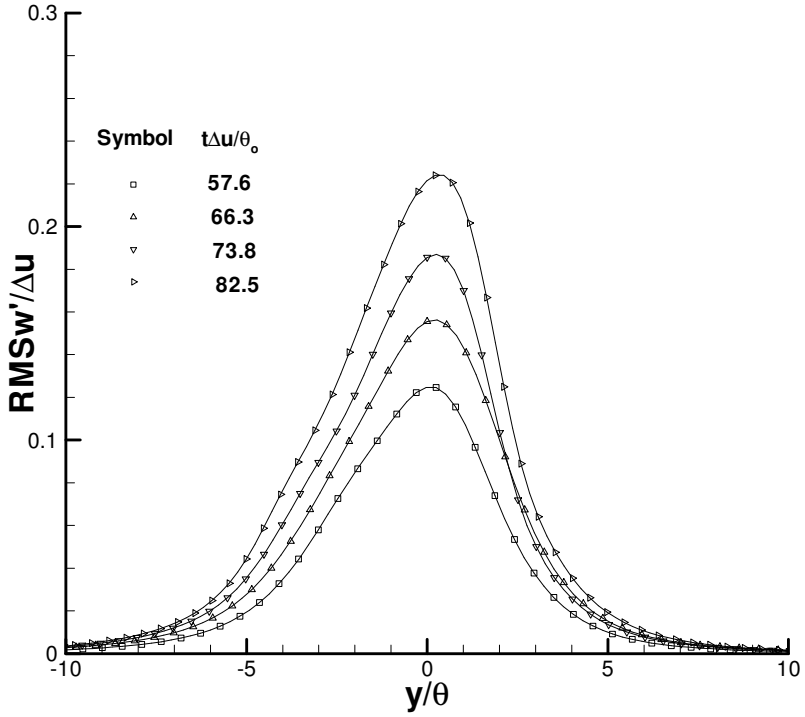

Fig. 6.39. Temporal evolution of root mean square spanwise velocity fluctuations in inviscid run at four times.

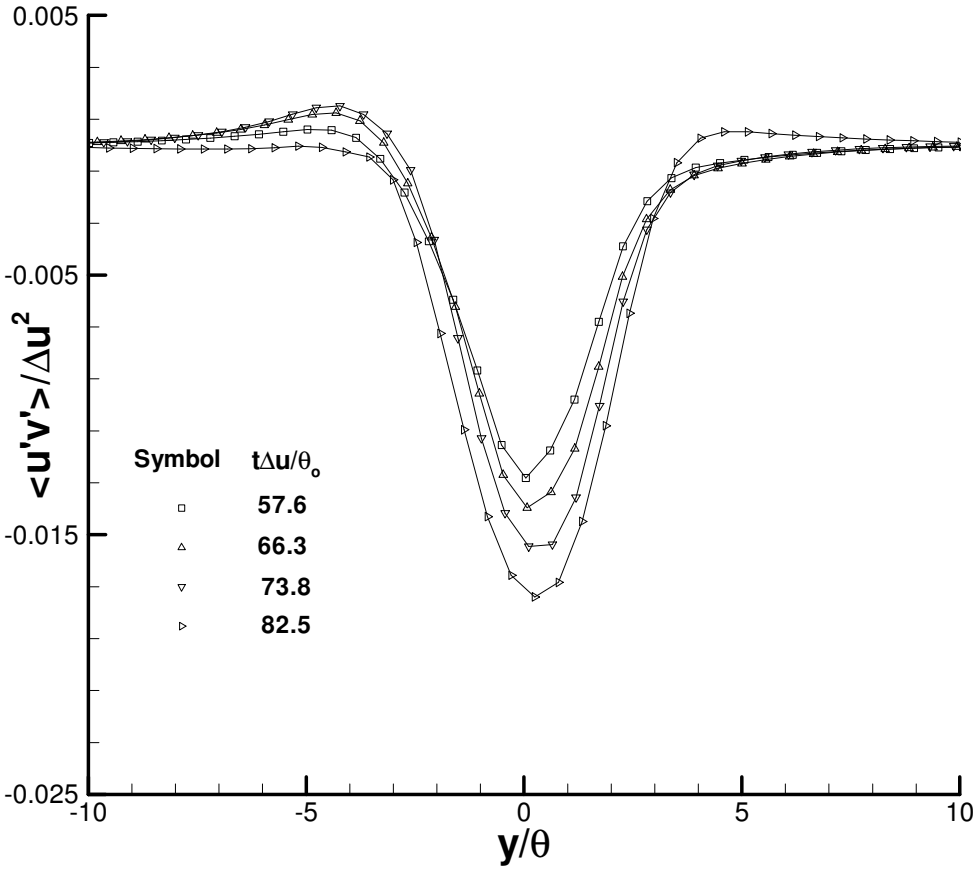

Fig. 6.40. Temporal evolution of cross correlation u'v' in inviscid run at four times.

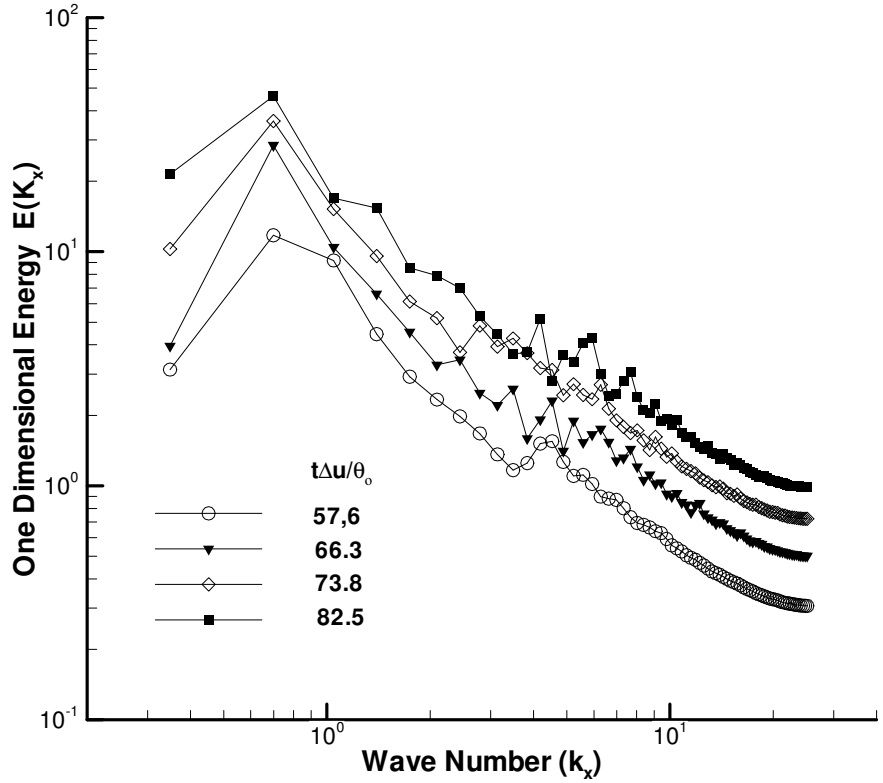

Fig. 6.41. Temporal evolution of streamwise energy spectrum in inviscid run at four times.

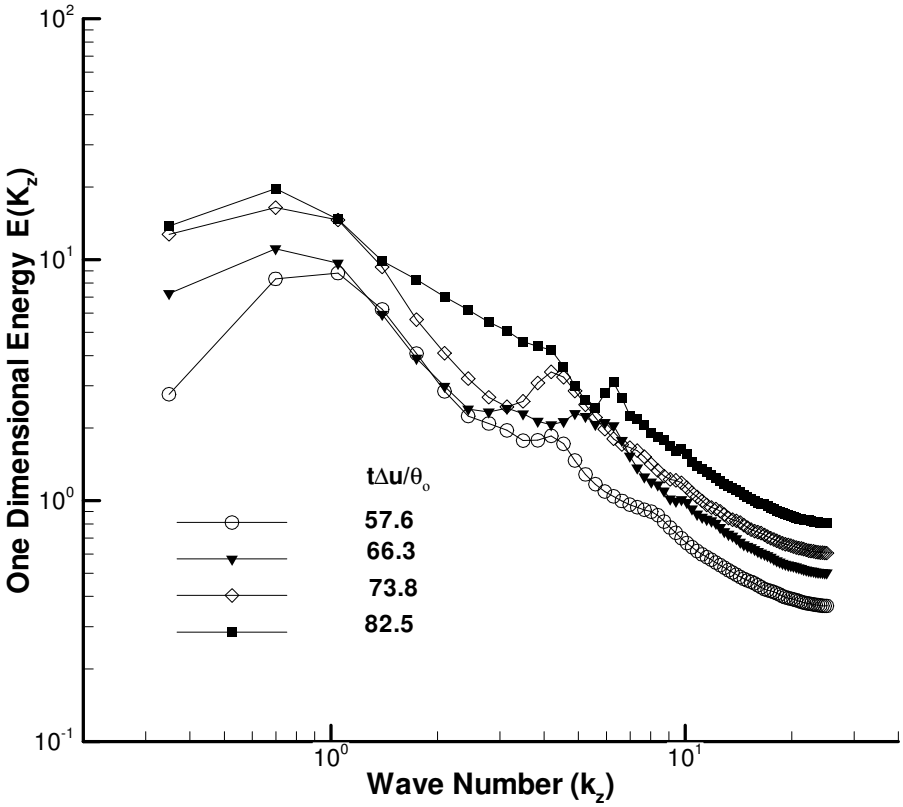

Fig. 6.42. Temporal evolution of spanwise energy spectrum in inviscid run at four times.

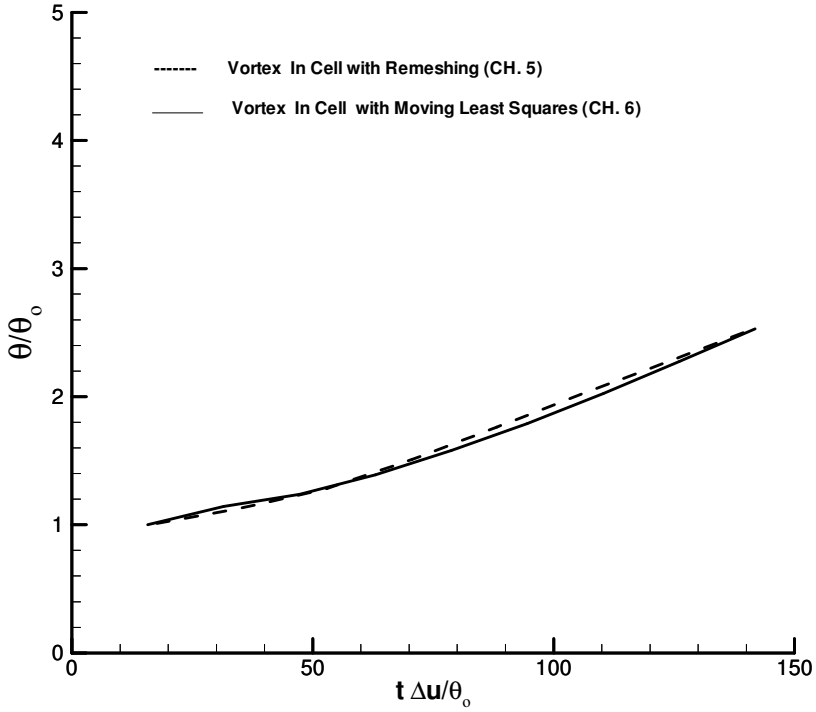

Fig, 7.1 Momentum Thickness

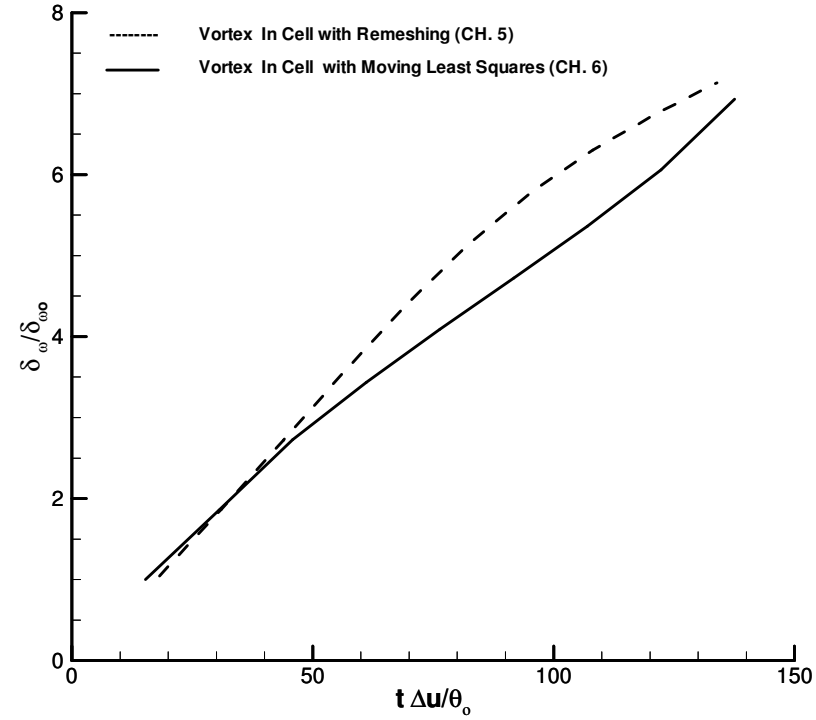

Fig. 7.2 Vorticity thickness

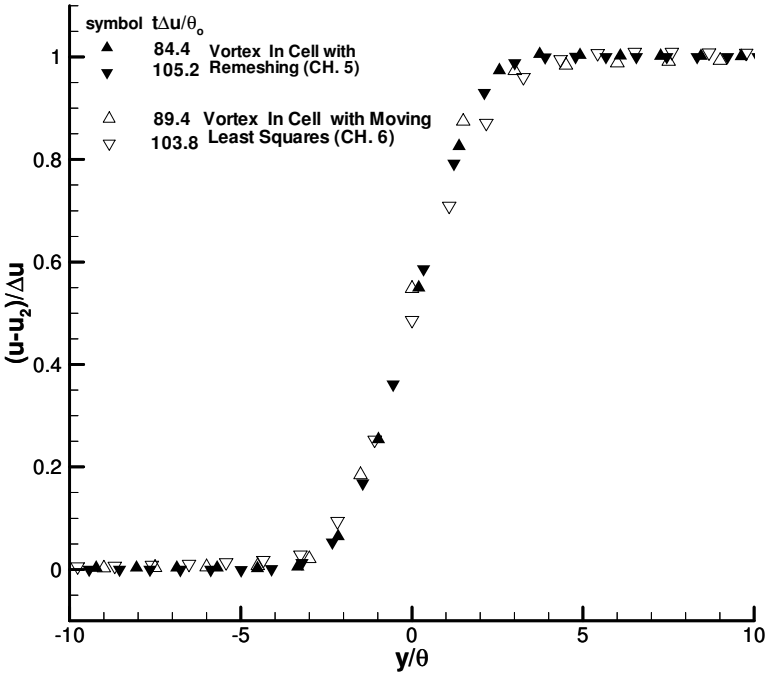

Fig. 7.3 Comparison of the profiles of mean streamwise velocity

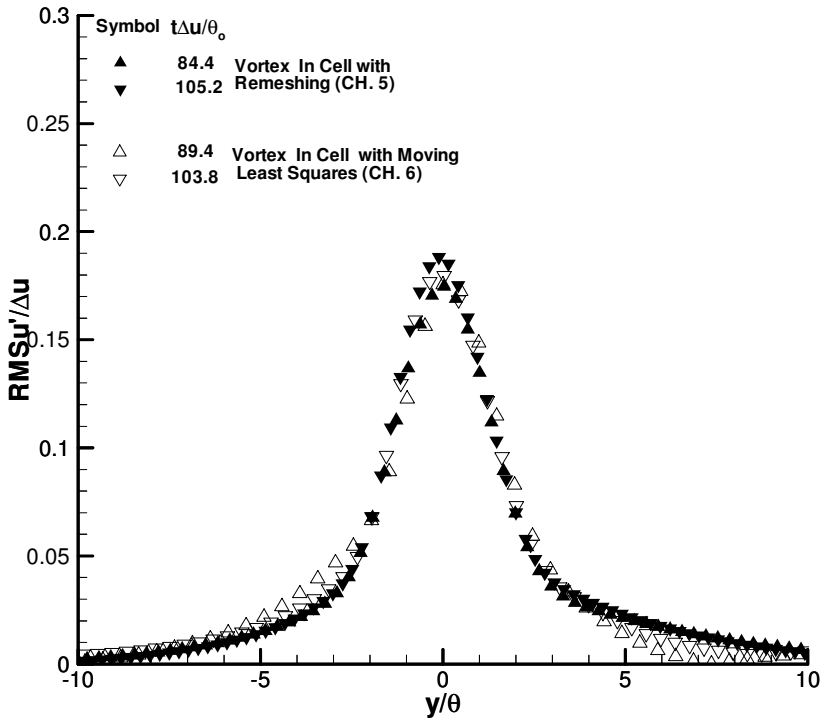

Fig. 7.4 Comparison of the profiles of root mean square streamwise velocity fluctuations.

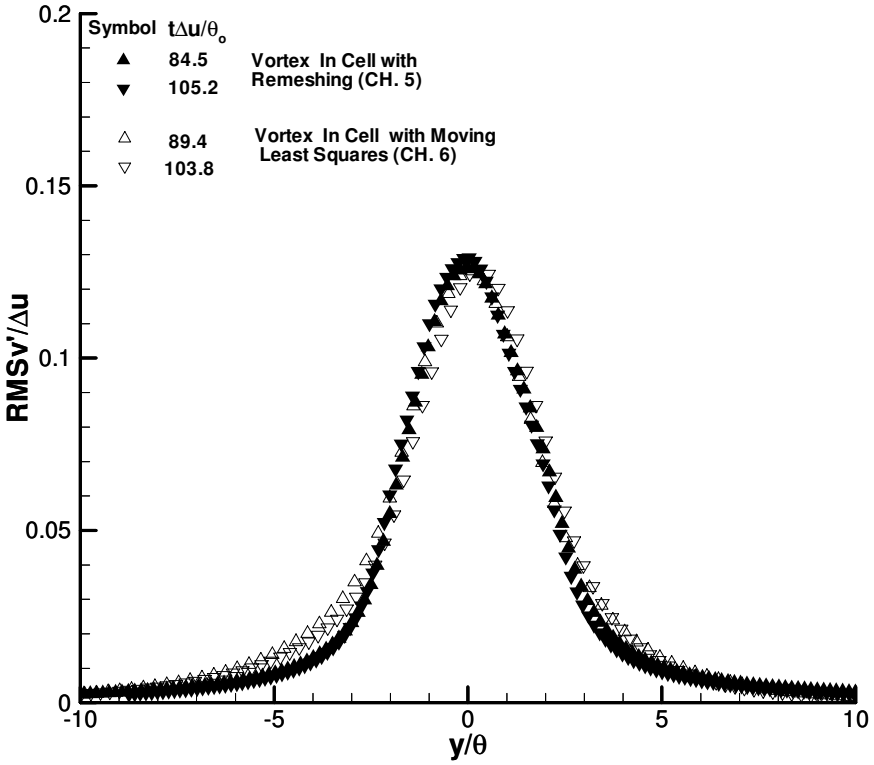

Fig. 7.5 comparison of profiles of root mean square cross-stream velocity fluctuations.

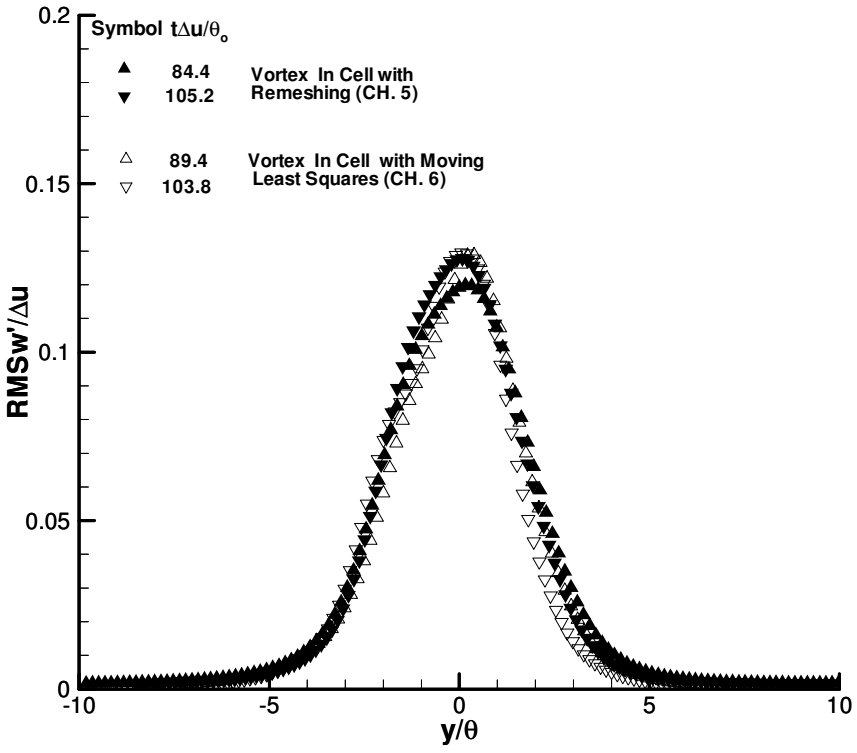

Fig. 7.6 Comparison of the profiles of root mean square spanwise velocity fluctuations.

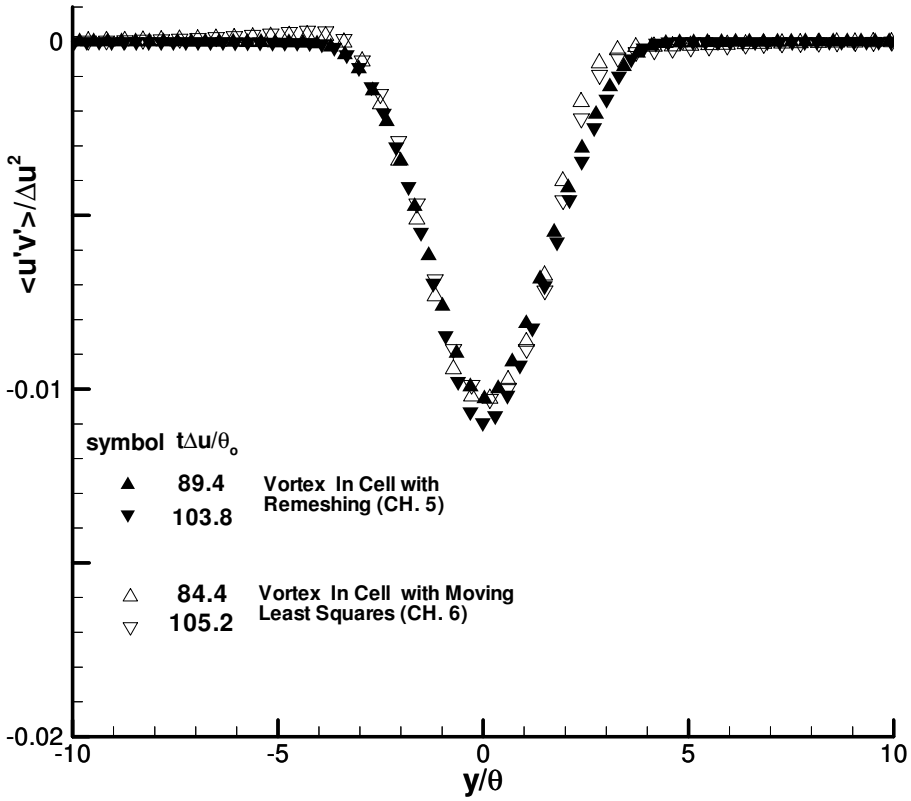

Fig. 7.7 Comparison of the profiles of *u'v'* cross-correlation

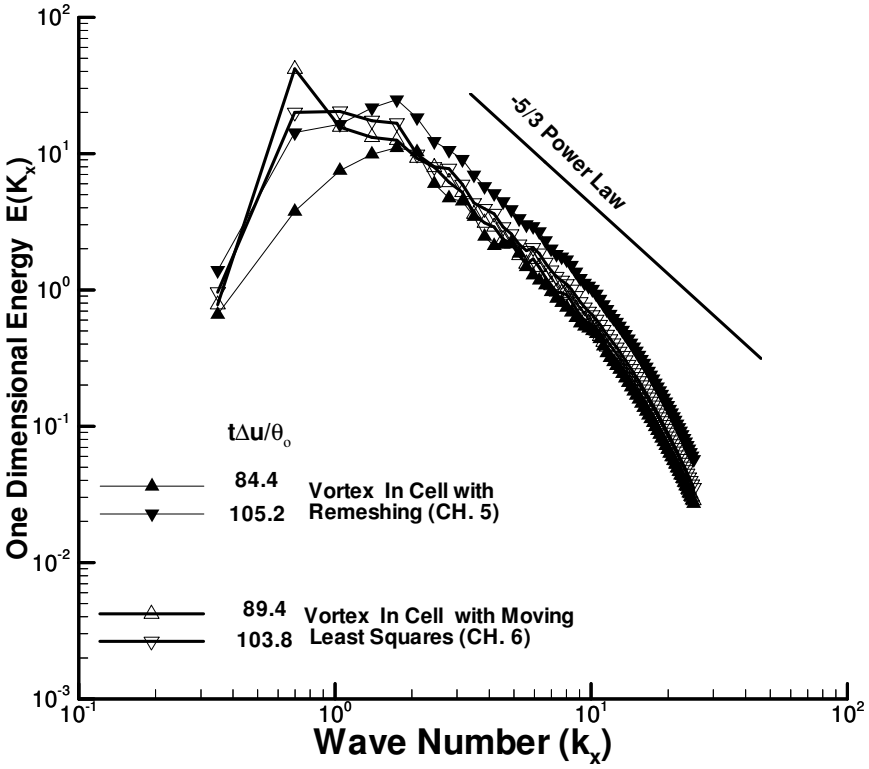

Fig. 7.8 Comparison of the one dimensional energy spectra

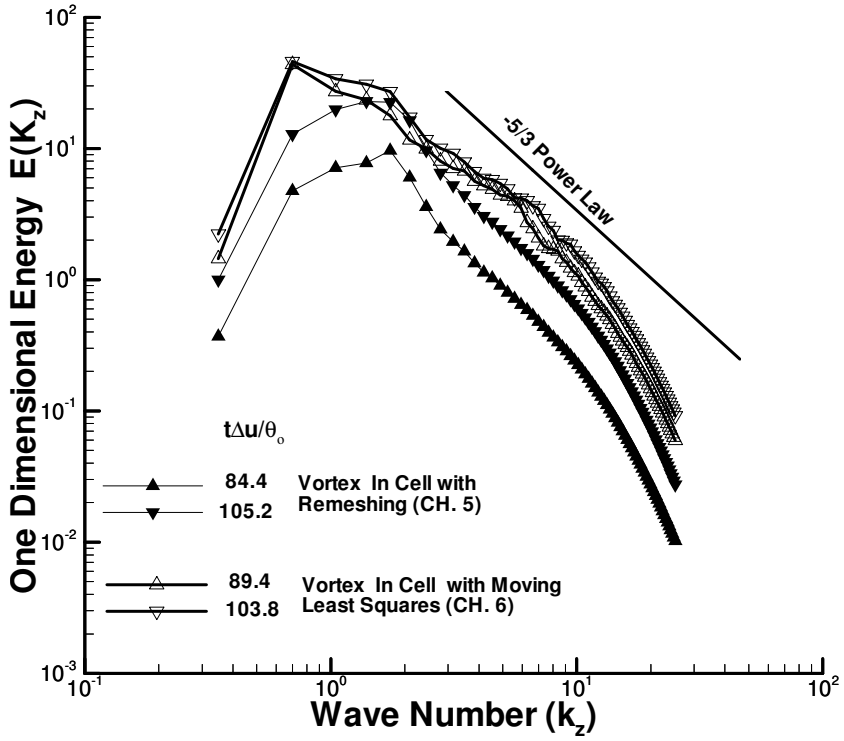

Fig. 7.9 Comparison of the one dimensional energy spectra

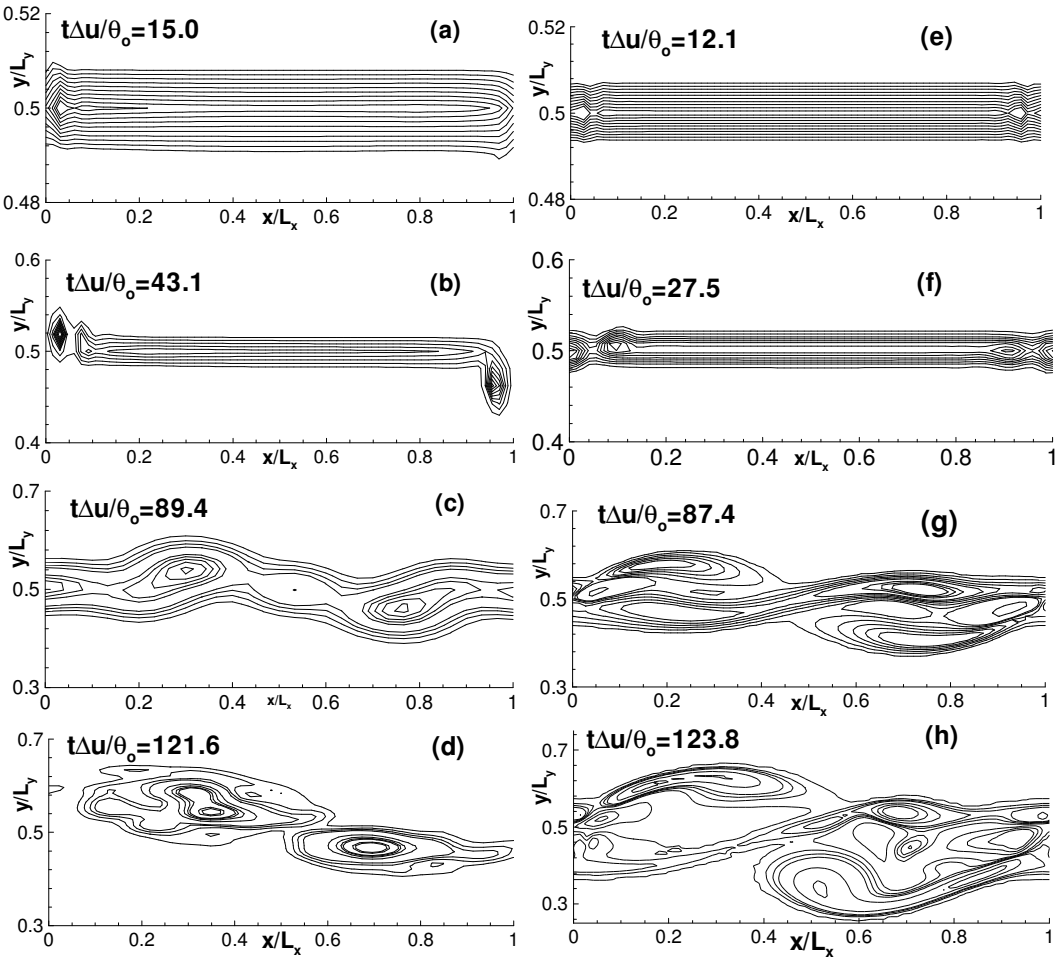

Fig. 7.10 Comparison of the development of spanwise vorticity structures. For captions see figures 5.14 and 6.12

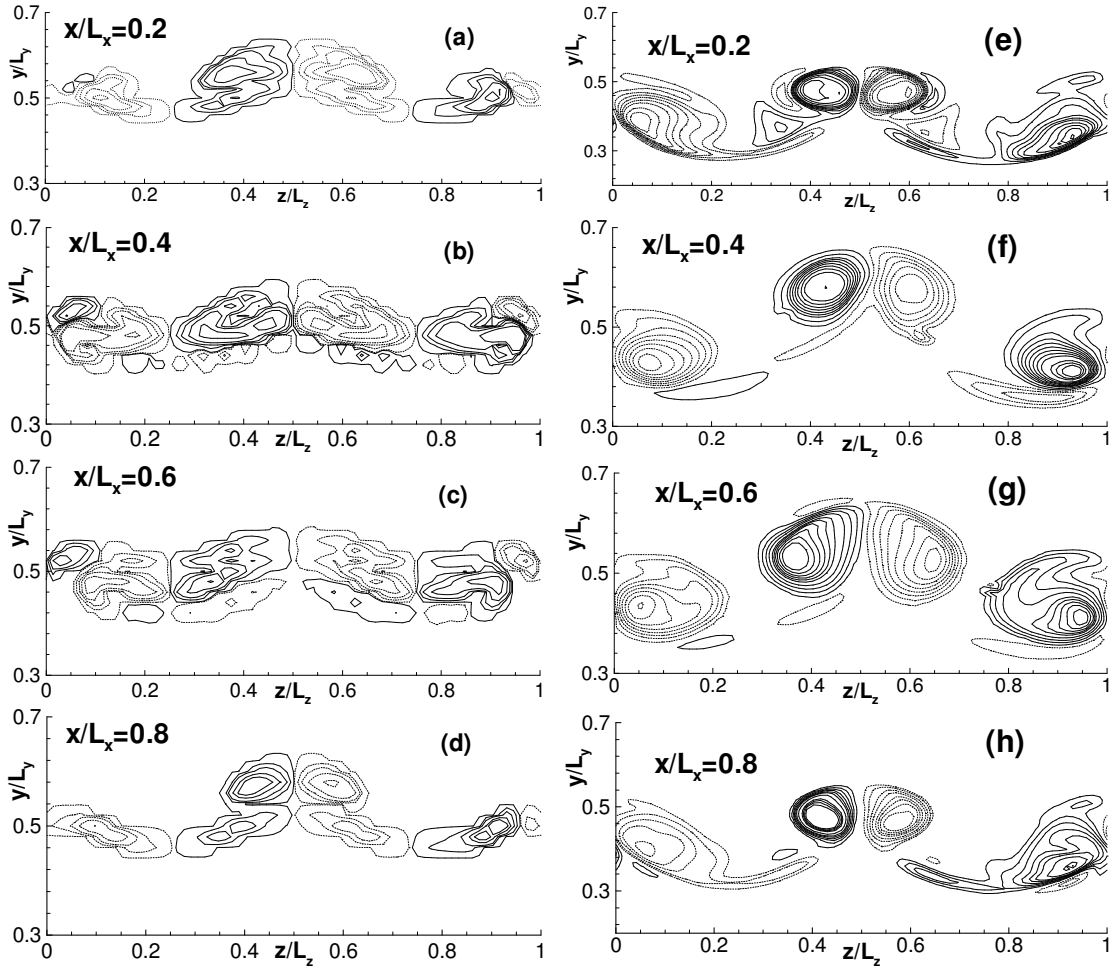

Fig. 7.11 Comparison of the streamwise vorticity structures. For captions see figures 5.20 and 6.19.

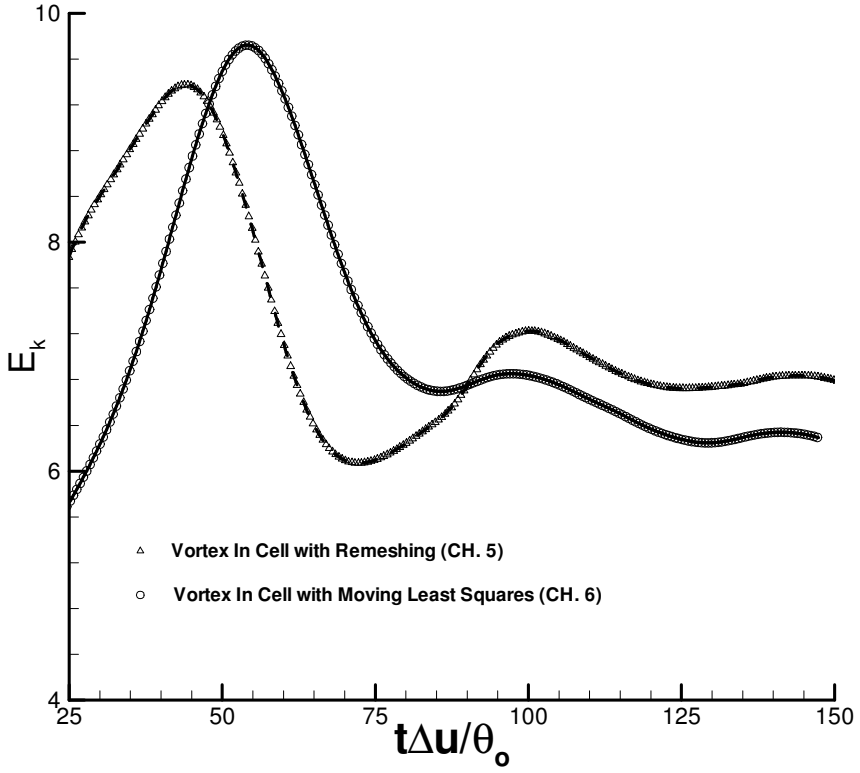

Fig. 7.12. Temporal development of kinetic energy for the two schemes

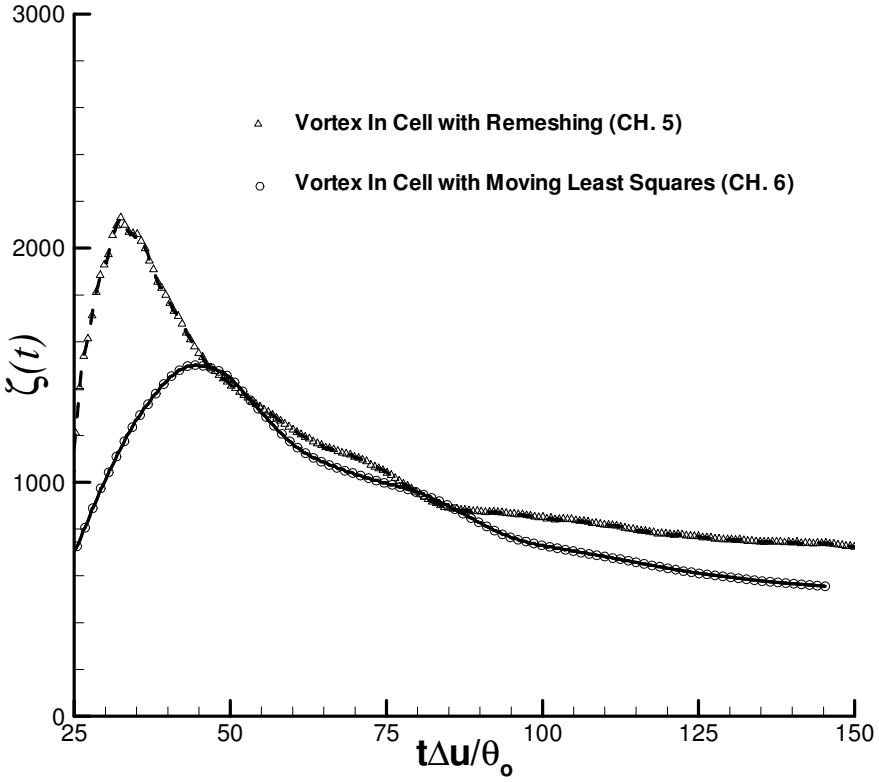

Fig. 7.13. Temporal development of enstrophy for the two schemes.

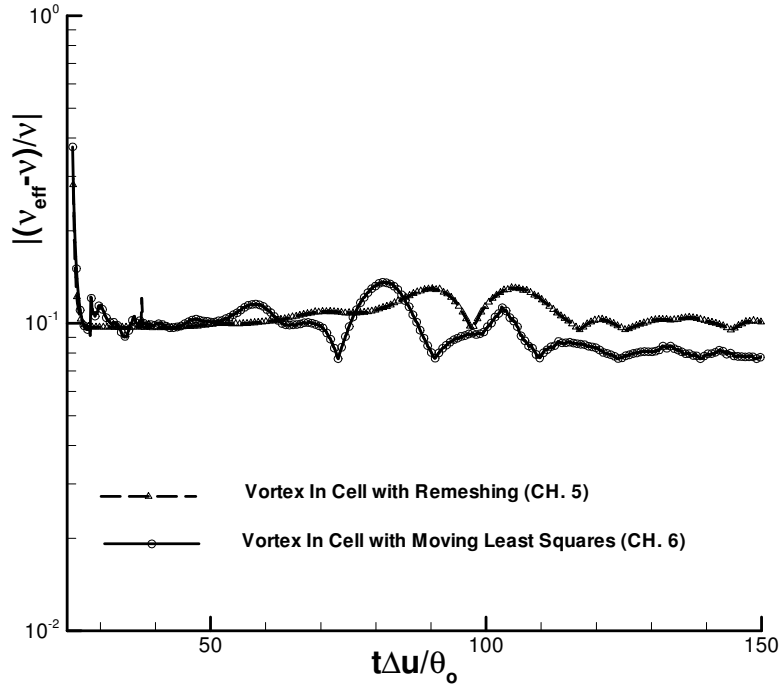

Fig. 7.14 Temporal development of relative diffusion error.

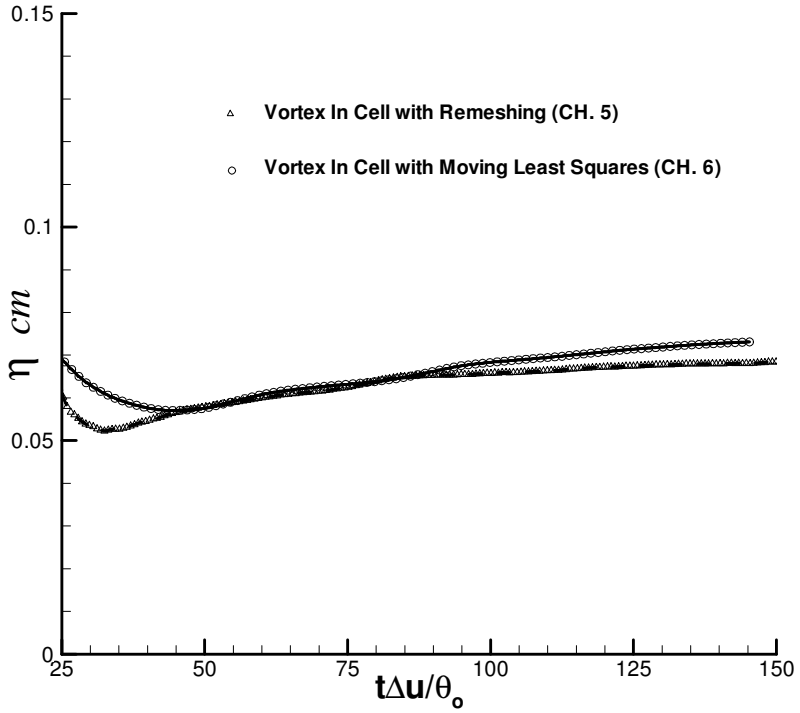

Fig. 7.15 Variation of the dissipation scales.

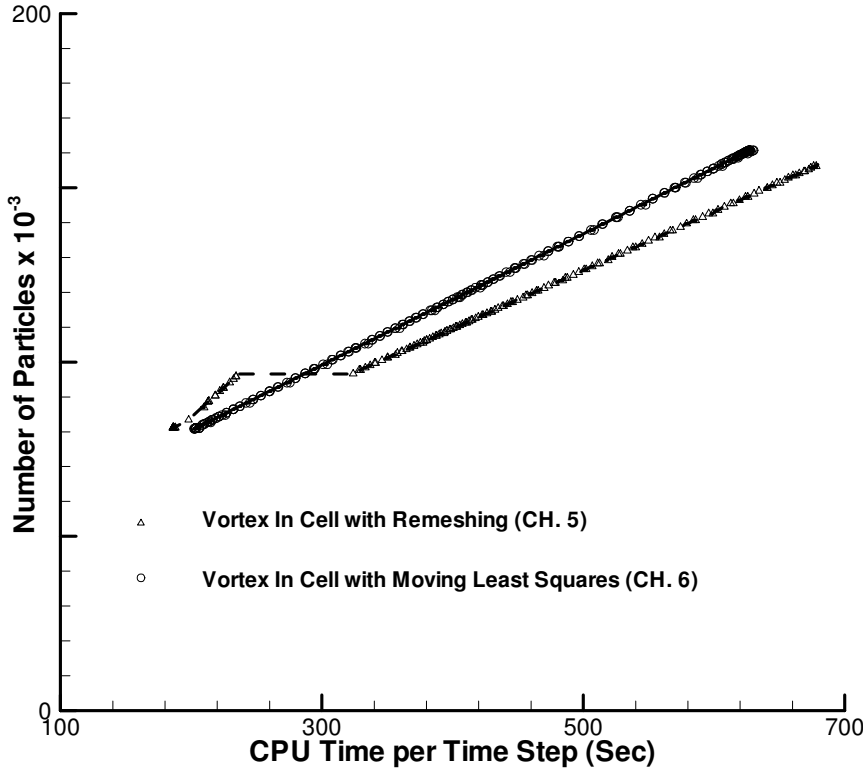

Fig. 7.16 Processing time for each time step.

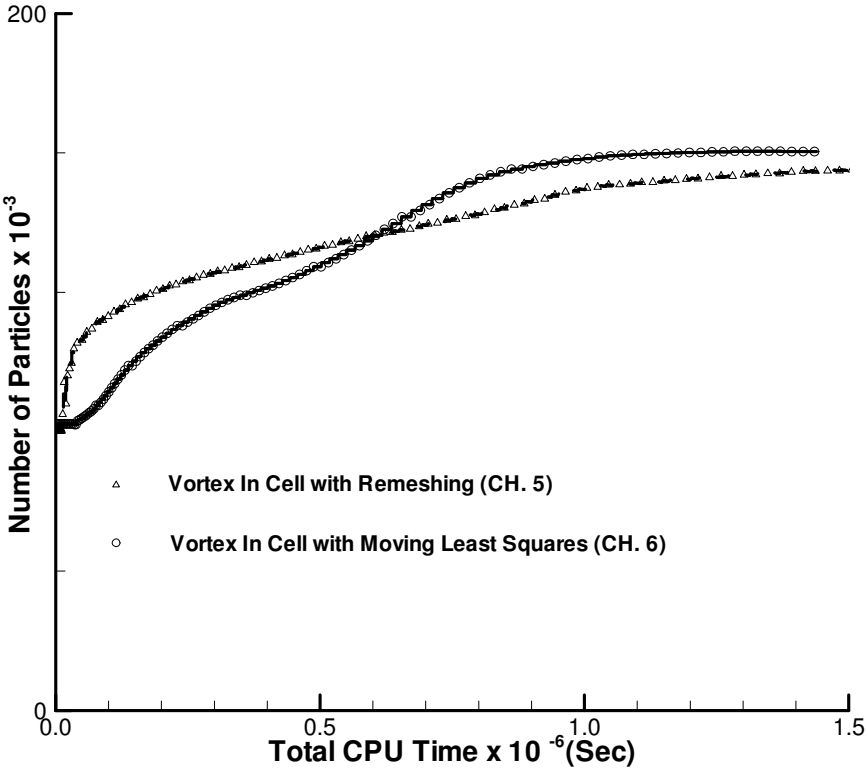

Fig. 7.17 Cumulative processing time.